

University of Windsor

Scholarship at UWindor

Electronic Theses and Dissertations

Theses, Dissertations, and Major Papers

2008

Characteristics of AA6061-T4 and -T6 extrusions under cutting deformation

Amitabha Majumder
University of Windsor

Follow this and additional works at: <https://scholar.uwindsor.ca/etd>

Recommended Citation

Majumder, Amitabha, "Characteristics of AA6061-T4 and -T6 extrusions under cutting deformation" (2008). *Electronic Theses and Dissertations*. 8115.
<https://scholar.uwindsor.ca/etd/8115>

This online database contains the full-text of PhD dissertations and Masters' theses of University of Windsor students from 1954 forward. These documents are made available for personal study and research purposes only, in accordance with the Canadian Copyright Act and the Creative Commons license—CC BY-NC-ND (Attribution, Non-Commercial, No Derivative Works). Under this license, works must always be attributed to the copyright holder (original author), cannot be used for any commercial purposes, and may not be altered. Any other use would require the permission of the copyright holder. Students may inquire about withdrawing their dissertation and/or thesis from this database. For additional inquiries, please contact the repository administrator via email (scholarship@uwindsor.ca) or by telephone at 519-253-3000ext. 3208.

CHARACTERISTICS OF AA6061-T4 AND -T6 EXTRUSIONS UNDER CUTTING
DEFORMATION

by

Amitabha Majumder

A Thesis
Submitted to the Faculty of Graduate Studies
Through Mechanical Engineering
in Partial Fulfillment of the Requirements for
the Degree of Master of Applied Science at the
University of Windsor

Windsor, Ontario, Canada

2008

© 2008 Amitabha Majumder



Library and
Archives Canada

Bibliothèque et
Archives Canada

Published Heritage
Branch

Direction du
Patrimoine de l'édition

395 Wellington Street
Ottawa ON K1A 0N4
Canada

395, rue Wellington
Ottawa ON K1A 0N4
Canada

Your file *Votre référence*
ISBN: 978-0-494-47070-1
Our file *Notre référence*
ISBN: 978-0-494-47070-1

NOTICE:

The author has granted a non-exclusive license allowing Library and Archives Canada to reproduce, publish, archive, preserve, conserve, communicate to the public by telecommunication or on the Internet, loan, distribute and sell theses worldwide, for commercial or non-commercial purposes, in microform, paper, electronic and/or any other formats.

The author retains copyright ownership and moral rights in this thesis. Neither the thesis nor substantial extracts from it may be printed or otherwise reproduced without the author's permission.

AVIS:

L'auteur a accordé une licence non exclusive permettant à la Bibliothèque et Archives Canada de reproduire, publier, archiver, sauvegarder, conserver, transmettre au public par télécommunication ou par l'Internet, prêter, distribuer et vendre des thèses partout dans le monde, à des fins commerciales ou autres, sur support microforme, papier, électronique et/ou autres formats.

L'auteur conserve la propriété du droit d'auteur et des droits moraux qui protègent cette thèse. Ni la thèse ni des extraits substantiels de celle-ci ne doivent être imprimés ou autrement reproduits sans son autorisation.

In compliance with the Canadian Privacy Act some supporting forms may have been removed from this thesis.

Conformément à la loi canadienne sur la protection de la vie privée, quelques formulaires secondaires ont été enlevés de cette thèse.

While these forms may be included in the document page count, their removal does not represent any loss of content from the thesis.

Bien que ces formulaires aient inclus dans la pagination, il n'y aura aucun contenu manquant.


Canada

AUTHOR'S DECLARATION OF ORIGINALITY

I hereby certify that I am the sole author of this thesis and that no part of this thesis has been published or submitted for publication.

I certify that, to the best of my knowledge, my thesis does not infringe upon anyone's copyright nor violate any proprietary rights and that any ideas, techniques, quotations, or any other material from the work of other people included in my thesis, published or otherwise, are fully acknowledged in accordance with the standard referencing practices. Furthermore, to the extent that I have included copyrighted material that surpasses the bounds of fair dealing within the meaning of the Canada Copyright Act, I certify that I have obtained a written permission from the copyright owner(s) to include such material(s) in my thesis and have included copies of such copyright clearances to my appendix.

I declare that this is a true copy of my thesis, including any final revisions, as approved by my thesis committee and the Graduate Studies office, and that this thesis has not been submitted for a higher degree to any other University of Institution.

ABSTRACT

The main focus of this research was to investigate force/displacement response and energy absorption performances of axially loaded AA6061-T4 and -T6 circular aluminum alloy extrusions under cutting deformation mode.

Quasi-static experimental investigation on load/displacement and energy absorption characteristics under cutting deformation mode was completed utilizing specially designed heat-treated 4140 steel alloy cutters and two different geometries of the cone-shaped deflectors, namely, straight and curved. An almost constant force during cutting was observed, which eliminated high peak crush force associated with progressive folding or global bending deformation modes. The average mean cutting force, as a result of the cutting deformation, was observed to be 29.8 kN and 43.2 kN for the AA6061-T4 and -T6 extrusions with a wall thickness of 3.175 mm respectively. For the extrusions with a wall thickness of 1.587 mm, the average mean cutting force was observed to be 14.9 kN for T4 temper and 19.6 kN for T6 temper tubes under the cutting deformation.

Additionally a dual stage cutting process was initiated using two cutters in series in this research. In addition to cutters and deflectors, spacers of different geometries between the cutters were also incorporated in this study. The force/displacement responses illustrated that the dual stage cutting was the superposition of two single-stage cutting processes. As spacing between the cutters increased the stability of the cutting progress degraded.

Additionally, controlling the load/displacement response through varying extrusions wall thickness along the length of the specimens was investigated. Results from the experimental testing illustrated that the force/displacement response was dependent upon the extrusion thickness and an almost linear relationship was observed to exist between wall thickness and the steady state cutting force.

Finally to this research, a numerical study of the axial cutting deformation process was simulated employing an Eulerian and Smoothed Particle Hydrodynamic (SPH) methods. Good predictive capabilities of the numerical model employing the Eulerian element formulation were observed.

*To my wife Shashwati, my daughters Depita and Rohita,
for their endless support, love and encouragement*

ACKNOWLEDGEMENTS

I would like to express my most sincere gratitude and profound appreciation to Dr. William Altenhof for his supervision, guidance and support. His knowledge and expertise has been of immeasurable assistance throughout my graduate studies and research.

My sincere thanks to Mr. Andrew Jenner and Mr. John Robinson for their technical assistance as well as my fellow researchers for their support and friendship.

TABLE OF CONTENTS

AUTHOR'S DECLARATION OF ORIGINALITY	iii
ABSTRACT	iv
DEDICATION	v
ACKNOWLEDGEMENTS	vi
LIST OF TABLES	xii
LIST OF FIGURES	xiv
LIST OF APPENDICES	xxv
NOMENCLATURE	xxvi
ABBREVIATIONS	xxvii
CHAPTER	
1. INTRODUCTION	1
2. LITERATURE REVIEW	5
2.1 Modes of deformation for axially loaded tubes	6
2.1.1 Axial plastic buckling	6
2.1.2 External inversion	11
2.1.3 Axial splitting/cutting	14
2.2 Factors that influence collapse mode	24
2.2.1 Cross-sectional geometry	24
2.2.2 Geometrical dimensions	27
2.2.3 Extrusion materials	30
2.3 Crush initiators	32
2.4 Analytical models of the axial crushing	40
2.5 Finite element modeling of the axial crushing of thin-walled tubes	44
2.5.1 Lagrangian FE formulation	45
2.5.2 Eulerian or arbitrary Lagrangian/Eulerian (ALE) element formulations	50
2.5.3 Smooth Particle Hydrodynamics (SPH)	53
3. FOCUS OF RESEARCH	56

4.	EXPERIMENTAL TESTING METHOD	58
4.1	Overview of tensile testing of aluminum alloy extrusion	58
4.2	Quasi-static axial crush tests	59
4.2.1	Specimens preparation for axial crush tests	60
4.2.2	Crush test methodology	61
4.3	Quasi-static axial cutting tests	62
4.3.1	Cutting tool design and manufacturing	63
4.3.2	Deflectors design and manufacturing	65
4.3.3	Fabrication Spacers	65
4.3.4	Test Specimens Preparation	66
4.3.4.1	Cutting tests using only a single cutter	66
4.3.4.2	Dual stage cutting in the presence of deflectors and spacers	69
4.3.4.3	Controlling the load/displacement response	70
4.3.5	Cutting test methodology	72
5.	PARAMETERS USED TO EVALUATE THE CRUSH CHARACTERISTICS OF THE EXTRUSIONS	74
5.1	Total energy absorption	74
5.2	Peak crush load	75
5.3	Mean crush force	75
5.4	Crush force efficiency	75
5.5	Specific energy absorption	76
5.6	Energy-absorbing effectiveness factor	76
6.	EXPERIMENTAL RESULTS AND DISCUSSION	77
6.1	Tensile testing results	77
6.2	Quasi-static crush testing results and discussion	78
6.2.1	Crush test results for the specimens in groups 1 through 4	78
6.2.2	Crush test results for the specimens in groups 5 through 12	81
6.2.3	Crush test results amongst all specimens	84
6.2.4	Comparison of crush performance parameters	86
6.2.4.1	The Peak crush force and the mean crush force	88
6.2.4.2	Total energy absorption and crush force efficiency	88
6.2.4.3	SEA and effectiveness factor	89
6.3	Quasi-static cutting tests results and discussion utilizing the single cutter	89
6.3.1	Cutting test results for the specimens in groups c-1 through c-4	89
6.3.2	Cutting test results for the specimens in groups c-5 through c-8	92
6.3.3	Cutting test results for the specimens in groups c-9 through c-12 and c-17	93

6.3.4	Cutting test results for the specimens in groups c-13 through c-16 and c-18	95
6.3.5	Cutting test results for the specimens in groups d-1 through d-4	97
6.3.6	Cutting test results for the specimens in groups d-5 through d-8	100
6.3.7	Cutting test results for the specimens in groups d-9 through d-12	101
6.3.8	Cutting test results for the specimens in groups d-13 through d-16	103
6.3.9	Cutting test results for the specimens in groups d-17 through d-20	104
6.3.10	Cutting test results for the specimens in groups d-21 through d-24	106
6.3.11	Cutting test results for the specimens in groups d-25 through d-28	108
6.3.12	Cutting test results for the specimens in groups d-29 through d-32	110
6.3.13	Cutting test results amongst all specimens	111
6.3.14	Comparison of crush performance parameters	116
6.3.14.1	The Peak crush force and the mean crush force	119
6.3.14.2	Total energy absorption and crush force efficiency	120
6.3.14.3	SEA and effectiveness factor	120
6.3.15	Cutting force analysis and comparison with the theoretical prediction	121
6.4	Cutting test results and discussion utilizing dual cutter configuration	125
6.4.1	Cutting test results for the specimens in groups m-1 through m-3	125
6.4.2	Cutting test results for the specimens in groups m-4 through m-6	128
6.4.3	Cutting test results for the specimens in groups m-7 through m-9	130
6.4.4	Cutting test results for the specimens in groups m-10 through m-12	133
6.4.5	Cutting test results for the specimens in groups m-13 through m-15	135
6.4.6	Cutting test results for the specimens in groups m-16 through m-18	137
6.4.7	Cutting test results for the specimens in groups m-19 through m-21	138
6.4.8	Cutting test results for the specimens in groups m-22 through m-24	140

6.4.9	Cutting test results for the specimens in groups s-1 through s-4	142
6.4.10	Cutting test results for the specimens in groups s-5 through s-8	143
6.4.11	Cutting test results amongst all specimens	144
6.4.12	Comparison of crush performance parameters	146
6.4.12.1	Peak crush force and mean crush force	148
6.4.12.2	Total energy absorption and <i>CFE</i>	148
6.4.12.3	SEA and effectiveness factor	149
6.5	Controlling the load/displacement response	150
6.5.1	Cutting test results for the specimen in groups a-T6 through d-T6	150
6.5.2	Cutting test results for specimen in groups e-1-T6 through e-4-T6	152
6.5.3	Cutting test results for the specimen in groups a-T6 through d-T6	154
6.5.4	Cutting test results for the specimen in groups e-1-T4 through e-4-T4	155
6.5.5	Cutting test results amongst all specimens	156
6.5.6	Comparison of crush performance parameters	157
6.5.6.1	Peak crush force and mean crush force	157
6.5.6.2	Total energy absorption and crush force efficiency	158
7.	FINITE ELEMENT MODELLING AND SIMULATION METHOD	159
7.1	Eulerian FE formulation	159
7.1.1	Model geometry and discretization	160
7.1.2	Modeling contact	162
7.1.3	Application of boundary conditions	162
7.1.4	Material models	163
7.1.5	Simulation procedure	163
7.2	Smooth Particle Hydrodynamic (SPH) Mesh Free Approach	164
7.2.1	Model geometry and discretization	164
7.2.2	Modeling contact	165
7.2.3	Application of boundary conditions	165
7.2.4	Material models	166
7.2.5	Simulation procedure	166
8.	FINITE ELEMENT SIMULATION RESULTS AND DISCUSSION	167
8.1	FE simulation results and discussion in presence of straight deflector	167
8.2	FE simulation results and discussion in presence of curved deflector	169
8.3	Total energy absorption and crush force efficiency	171
8.4	Mean cutting force and peak cutting force	173

9.	CONCLUSIONS	174
9.1	Conclusions for Quasi-static Axial Crushing Tests	174
9.2	Conclusions for Cutting Deformation Mode Utilizing Single Cutter	175
9.3	Conclusions for Dual Stage Cutting	177
9.4	Conclusions for Controlling Load/displacement Response	178
9.5.	Conclusions for FE Modeling	179
9.6	Future Works	179
	REFERENCES	180
	APPENDIX A: EXPERIMENTAL LOAD VERSUS DISPLACEMENT CURVES	186
	APPENDIX B: LS-DYNA EXTRUSION MATERIAL MODELS	199
	APPENDIX C: COPYRIGHT PERMISSION	203
	VITA AUCTORIS	219

LIST OF TABLES

Table		Page
4.1	Specimen geometry for AA6061-T4 and T6 specimens considered for axial crush tests (all dimensions are in mm).	61
4.2	Cutters hardness after heat treatment (Rockwell 'C' scale).	64
4.3	Cutting blades tip width dimensions (mm).	64
4.4	Specimen grouping information and geometric dimensions using cutters.	67
4.5	Specimen grouping information and geometric dimensions in the presence of cutters and defectors.	68
4.6	Specimen grouping information and geometric dimensions for the dual stage cutting of AA6061 extrusions.	69
4.7	Specimen grouping information and geometric dimensions for the dual stage cutting with spacers.	70
6.1	Material properties of the 6061-T4 and -T6 extrusions from tensile tests [38]	77
6.2	Calculated average values of the crush parameters for each group.	87
6.3	Calculated average values of TEA, SEA and EF for each group	87
6.4	Calculated average values of the crush parameters for each group utilizing different cutter sides, extrusions tempers and wall thicknesses.	117
6.5	Calculated average values of the crush parameters for each group utilizing the cutters and the straight or curved deflector.	118
6.6	Steady state cutting resistance force comparison between experimental findings and theoretical predictions.	124
6.7	Proportion energy dissipation for each mechanism.	124
6.8	Calculated average values of the crush parameters for each group in the dual stage cutting process using specimens with wall thicknesses of 1.587 mm and 3.175 mm.	146
6.9	Calculated average values of TEA, SEA and the effectiveness factor.	147

6.10	Calculated average values of the crush parameters for each group in the dual stage cutting process using spacers of various geometries.	147
6.11	Specimen grouping information and crush parameters for the specimens in group a through d and groups e-1 through e-4 with both temper.	157
8.1	Cutting characteristics for the AA6061-T6 extrusions summarized from experimental testing and numerical simulations in the presence straight and curved deflector.	173

LIST OF FIGURES

Figure		Page
1.1	Structural damage after frontal offset and side crush tests of Audi A6 2008 model. (a) view after frontal impact, (b) driver's survival space maintained well, (c) view of side impact and (d) driver dummy's head was protected from being hit by hard structures by the side curtain airbag [1].	2
1.2	Potential mass savings using advanced steel and aluminum compared to conventional steel in vehicle design [2].	3
2.1	Deformation modes during axial crushing of circular tubes. (a) progressive folding, (b) global bending and (c) mixed mode.	6
2.2	Classification chart for different deformation modes associated with circular 6060-T5 aluminum tubes [5].	7
2.3	Ratio between mean loads for extrusions with T4 and T6 tempered conditions [7].	8
2.4	Comparison between dynamic and static force versus displacement response for the extrusions with T6 tempered conditions [7].	9
2.5	Load/displacement profile for the axial crushing of HT-30 aluminum alloy tube under axisymmetric deformation mode [8].	10
2.6	Schematic representation of the external inversion of tubes using a die [12].	11
2.7	Load/displacement profile of copper and 70:30 brass tubes for quasi-static inversion process [10].	12
2.8	Various stages of the inversion of a copper tube in quasi-static method [10].	13
2.9	Comparison of experimental and theoretical results for the critical radius [14].	14
2.10	The load-displacement profiles with or without using stopper plate [17].	15
2.11	Sketch of the experimental set up. The bottom and top plates were attached to the base and crosshead of Instron machine [18].	16
2.12	Sketch of the experimental set-up, with 8 evenly spaced 5 mm initial saw-cuts around lower circumference [19].	17
2.13	Load/displacement curves for mild steel tubes with $D = 74.0$ mm and $t = 1.8$ mm against dies with semi-angle $\alpha = 45^\circ, 60^\circ$ and 75° respectively [19].	18

Figure	Page
2.14 Load/displacement curves for aluminum tubes with $D = 77.9$ mm and $t = 1.9$ mm against dies with semi-angle $\alpha = 45^\circ, 60^\circ$ and 75° respectively [19].	18
2.15 Typical force-displacement profiles for mild steel square tubes with $t = 2.5$ mm against dies with semi-angles of $45^\circ, 60^\circ$ and 75° respectively [20].	20
2.16 Photographs of typical mild steel specimens after test [20].	20
2.17 Load/displacement profile comparisons for cutting and global bending deformation modes [21].	21
2.18 Photographs of cutting process for AA6061-T6 square extrusions [21].	21
2.19 Load/displacement profile comparisons for cutting, progressive folding and global bending deformation modes [22].	22
2.20 Load/displacement response of AA6061-T6 round tubes under cutting deformation mode in presence of a cutter and a straight deflector [25].	23
2.21 Specific energy absorption for different combination of design aspects [27].	25
2.22 Proposed multi-cell cross-section of AA6063-T7 aluminum column [28].	25
2.23 Deformation shape of square and circular corner columns [28].	26
2.24 Crushing forces versus displacement profile comparison [28].	26
2.25 Experimental test set-up and controls: (a) test machine set-up; (b) collapse initiator geometry and (c) grooved end cap set for tube end constraints [29].	27
2.26 Deformed shapes of circular specimens. Both ends of the tube specimens were welded with aluminum panels [31].	29
2.27 Specific impact absorption versus thickness/width (or diameter) ratio for the circular and rectangular specimens [31].	30
2.28 Typical engineering stress-strain relationships for the three temper materials used in the study [7].	31
2.29 Comparison of load/displacement profiles for each extrusion materials considered [32].	32
2.30 Crush initiator geometry configurations studied by Krauss [34].	33

Figure	Page
2.31 Numerically calculated force versus deflection curves for specimens with each size of circular crush initiator [34].	34
2.32 Geometry and configurations of dents considered by Lee [36]. All dimensions are in millimetres.	35
2.33 The load-displacement profiles of specimens A through D [36].	36
2.34 Crush force efficiency of the extrusions consider in the investigation [38].	37
2.35 Geometry of the AA6061-T6 aluminum extrusion and discontinuities considered by Cheng at al. [39].	38
2.36 Photographs illustrate the crushing process from a representative group [39].	39
2.37 Comparison of load-displacement profiles of AA6061-T6 extrusions with elliptical discontinuity and without discontinuity [39].	39
2.38 Collapse element model used to analytically characterize the axial buckling of square tubes [4].	41
2.39 Photographs of different failure modes. (a) Concertina tearing failure by a blunt wedge, (b) Braided tearing of a plate by a narrow wedge and (c) Center 'clean cut' of a plate by a sharp wedge with stable flap buckled [23]	43
2.40 One quarter finite element model of 6060 aluminum alloy extrusions including trigger position [46].	46
2.41 Discretization of specimens ($L = 200$ mm, $D = 14.2$ mm, $t = 3.15$ mm). The inset shows a detail of the discretization of the circular hole discontinuity region [32].	48
2.42 Experimental and numerical crushing process for 6061-T6 extrusions [32].	49
2.43 Experimental and numerical crushing process for 6063-T5 extrusions [32].	50
2.44 Discretization of the AA6061-T6 round tubular extrusions ($L=60$ mm, $D=50.8$ mm, $t=3.175$ mm), the tube airmesh, and the cutter blade [52].	52
2.45 Load versus displacement observations from numerical and experimental testing procedures [52].	52
2.46 Computational cycle for SPH methodology in LS-DYNA [55]	53

Figure	Page	
2.47	Velocity histories of the rigid fragments for four impact simulations [56].	54
4.1	Arrangement of tensile test specimen, extensometer and wedge grips of the Instron tensile testing machine.	59
4.2	Geometry of AA6061-T4 and -T6 aluminum alloy extrusion specimens considered in this experimental test. L is the length of the extrusion specimen, D is the nominal external diameter of the specimen and t is the wall thickness of the specimen.	61
4.3	Arrangement of extrusion for axial crush test in Tinius-Olsen compression testing machine.	62
4.4	The geometry of a representative cutter.	64
4.5	Geometry of the straight and curved deflectors (all dimensions are in mm).	65
4.6	Geometry of the spacers	66
4.7	CNC finished geometries of AA6061-T6 round extrusion specimens under consideration in the experimental test. t is the original nominal wall thickness of the specimen (all dimensions in mm).	71
4.8	Arrangement of extrusion, cutter, deflector and round steel rod during experimental quasi-static axial cutting tests.	73
6.1	The engineering stress versus engineering strain curves of AA6061-T4 and T6 obtained from tensile testing [38].	78
6.2	The load/displacement observations from all the specimens in groups 1 and a representative specimen in Group 2.	80
6.3	The load/displacement responses of the representative specimen from Groups 3 and 4.	80
6.4	Photographs illustrate the progressive folding and global bending deformation modes for a representative specimen in Groups 3 and 4. (a) and (b) illustrate the progressive folding deformation mode; (c) and (d) represents the global bending deformation mode.	81
6.5	The load/displacement profiles from the representative specimens in Groups 6, 8 and 10	83
6.6	The load/displacement observations from the representative specimens in Groups 7, 11 and 12.	83

Figure	Page
6.7 The load/displacement observations for the extrusions with T6 and T4 temper and wall thicknesses of 3.175 mm and 1.587 mm under the progressive folding deformation mode.	84
6.8 Figure 6.8. The load/displacement observations for the extrusions with T6 and T4 temper and wall thicknesses of 3.175 mm and 1.587 mm under the global bending deformation mode.	85
6.9 Comparison of load/displacement behaviour between the progressive folding and the global bending deformation modes for the extrusions with T6 and T4 temper and 3.175 mm wall thickness.	86
6.10 Experimentally observed load/displacement profiles for AA6061-T4 representative specimens from Groups c-1 through c-4.	90
6.11 Photographs illustrating the experimental cutting process for a representative specimen in Group c-1 (top and bottom views).	91
6.12 The load/displacement response for the representative specimen from Group c-1, positions a, b, c and d correspond to photographs in Figure 6.11.	91
6.13 Experimentally observed load/displacement profiles for AA6061-T6 representative specimens from Groups c-5 through c-8.	92
6.14 Experimentally obtained load/displacement profiles for the specimens in Group c-10.	94
6.15 Photographs illustrating the experimental cutting process for a representative specimen in Group c-10 (top and bottom views).	94
6.16 Experimentally obtained load/displacement profile for the representative specimen in Group c-10, positions a, b, c and d correspond to photographs in Figure 6.15.	95
6.17 Experimentally obtained load/displacement profile for the specimens in Group c-16.	96
6.18 Petalled side wall cutting deformation characteristics of T4 and T6 tempered extrusions. (a) entire extrusions (b) close range image illustrating back and forth folding of sidewalls for T4 specimen (solid arrows) and smooth continuous cut (dashed arrows) for T6 specimen.	97
6.19 Experimentally obtained load/displacement responses for the specimens in Groups d-1 through d-4.	99

Figure	Page
6.20 Photographs illustrating the experimental cutting process for a representative specimen in Group d-1.	99
6.21 Experimentally obtained load/displacement responses for the representative specimen in Group d-1, positions a, b, c and d correspond to photographs in Figure 6.20.	100
6.22 Experimentally obtained load/displacement profiles for the specimens in Group d-5 through d-8.	101
6.23 Experimentally obtained load/displacement responses for the specimens in Group d-9 through d-12.	102
6.24 Experimentally obtained load/displacement profiles for the specimens in Group d- 13 through d-16.	103
6.25 The force/displacement responses for the specimen in Groups d-17 through d-20 in the presence of straight deflector.	105
6.26 Photographs illustrating the experimental cutting process for a representative specimen in Group d-17.	105
6.27 Experimentally obtained load/displacement profile for the representative specimen in Group d-17, positions a, b, c and d correspond to photographs in Figure 6.26.	106
6.28 The force/displacement responses for the specimen in Groups d-21 through d-24 in the presence of curved deflector.	107
6.29 Photographs illustrating the experimental cutting process for a representative specimen in Group d-22.	107
6.30 Experimentally obtained load/displacement profile for the representative specimen in Group d-22, positions a, b, c and d correspond to photographs in Figure 6.29.	108
6.31 The load/displacement responses for the tubes in Groups d-25 through d-28 in the presence of straight deflector.	109
6.32 Photographs illustrating the experimental cutting process for a representative specimen in Group d-22.	110
6.33 The load/displacement profile for the representative specimen from Group d-25, positions a, b, c and d correspond to photographs in Figure 6.32.	110

Figure	Page
6.34 The load/displacement responses for the specimen in Groups d-29 through d-32 in the presence of curved deflector.	111
6.35 Comparison of the load/displacement profiles between the specimens with the T6 and the T4 temper as well as wall thicknesses of 3.175 mm and 1.587 mm.	112
6.36 Comparison of the load/displacement responses among T6 round extrusions with a wall thickness of 3.175 mm in the presence and without the presence of deflectors.	113
6.37 Comparison of the load/displacement responses among T4 round extrusions with a wall of thickness 3.175 mm in the presence and without the presence of deflectors.	114
6.38 Comparison of load/displacement responses for the specimens with both wall thicknesses and T6 temper in presence of the straight and the curved deflectors.	115
6.39 Comparison of the load/displacement responses for the specimens with both wall thicknesses and T6 temper in presence of the straight and the curved deflectors.	116
6.40 Experimentally observed load/displacement responses for representative specimens from Groups m-1 through m-3.	126
6.41 Photographs illustrating the experimental cutting process for a representative specimen in Group m-2 (top and bottom views).	127
6.42 Experimentally obtained load/displacement profile for the representative specimen in Group m-2, positions a, b, c and d correspond to photographs in Figure 6.41.	127
6.43 The load/displacement profiles for the representative specimens from Groups m-4 through m-6 in presence of the straight deflector.	129
6.44 Photographs illustrating the experimental cutting process for a representative specimen in Group m-2 (top and bottom views).	129
6.45 The load/displacement response for the representative specimen from Group m-4, positions a, b, c and d correspond to photographs in Figure 6.44.	130
6.46 The load/displacement profiles for the representative specimens from Groups m-7 through m-9 in the presence of curved deflector.	131

Figure	Page
6.47 Photographs illustrating the experimental cutting process for a representative specimen in Group m-7 (top and bottom views).	132
6.48 The load/displacement response for the representative specimen from Group m-7, positions a, b, c and d correspond to photographs in Figure 6.47.	132
6.49 The load/displacement profiles for the representative specimens from Groups m-10 through m-12.	133
6.50 Photographs illustrating the experimental cutting process for a representative specimen in Group m-10.	134
6.51 The load/displacement profile for the representative specimen from Group m-10, positions a, b, c and d correspond to photographs in Figure 6.50.	134
6.52 The load/displacement profiles for the representative specimens from Groups m-13 through m-15.	135
6.53 Photographs illustrating the experimental cutting process for a representative specimen in Group m-13 (top and bottom views).	136
6.54 The load/displacement profile for the representative specimen from Group m-13, positions a, b, c and d correspond to photographs in Figure 6.53.	136
6.55 Experimentally obtained load/displacement profiles for the specimens in Group m-16 through m-18.	137
6.56 Photographs illustrating the experimental cutting process for a representative specimen in Group m-17.	137
6.57 The load/displacement profile for the representative specimen from Group m-17, positions a, b, c and d correspond to photographs in Figure 6.56.	138
6.58 Experimentally obtained load/displacement responses for specimens in Groups m-19 through m-21.	139
6.59 Photographs illustrating the experimental cutting process for a representative specimen in Group m-21 (top and bottom views).	139
6.60 The load/displacement profile for the representative specimen from Group m-21, positions a, b, c and d correspond to photographs in Figure 6.59.	140
6.61 Experimentally obtained load/displacement responses for specimens in Groups m-22 through m-24.	141

Figure	Page
6.62 Photographs illustrating the experimental cutting process for a representative specimen in Group m-22.	141
6.63 The load/displacement profile for the representative specimen from Group m-22, positions a, b, c and d correspond to photographs in Figure 6.62.	142
6.64 The load/displacement responses for representative specimen from Groups s-1 through s-4 utilizing spacers of different lengths.	143
6.65 The load/displacement responses for the representative specimen from Groups s-5 through s-8 utilizing spacers of different lengths and straight/curved deflector.	144
6.66 Comparison of the load/displacement responses among specimens without using any spacing and incorporating spacing of different lengths.	145
6.67 Experimentally obtained load/displacement profiles for representative specimens from Groups a-T6 through d-T6.	151
6.68 Photographs illustrating the cutting process for specimen a-T6-1.	152
6.69 The load/displacement profile for the representative specimen from Group a-T6-1, positions a, b, c and d correspond to photographs in Figure 6.68.	152
6.70 Experimentally obtained load/displacement profiles for representative specimens from Groups e-1-T6 through e-4-T6.	153
6.71 Experimentally obtained load/displacement profiles for representative specimens from Groups a-T4 through d-T4.	154
6.72 Experimentally obtained load/displacement profiles for representative specimens from Groups e-1-T4 through e-4-T4.	155
6.73 Comparison of load/displacement profiles for representative specimens from Group d and Group e-1 with T6 and T4 temper conditions.	156
7.1 Discretization of the AA6061-T6 specimen, the tube airmesh, the cutter blade and the straight deflector.	161
7.2 Discretization of the AA6061-T6 specimen, the tube airmesh, the cutter blade and the curved deflector.	165
8.1 The load/displacement behaviour from experimental testing and numerical simulation of axial cutting in presence of the straight deflector.	168

Figure	Page
8.2 Experimental (a) and numerical (b and c) axial cutting of the AA6061-T6 extrusions in presence of the straight deflector.	169
8.3 The load/displacement behaviour from experimental testing and numerical simulation of the axial cutting in presence of the curved deflector.	170
8.4 Experimental (a) and numerical (b and c) axial cutting of AA6061-T6 extrusions in presence of the curved deflector.	171
8.5 Energy absorbed versus displacement behaviour from experimental testing and numerical simulation of axial cutting with the presence of the straight deflector.	172
8.6 Energy absorbed versus displacement behaviour from experimental testing and numerical simulation of axial cutting with the presence of the curved deflector.	172
A.1 The force/displacement responses for AA6061-T4 circular specimens with a wall thickness of 3.175 mm in Group 4.	187
A.2 The force/displacement profiles for AA6061-T6 round specimens with a wall thickness of 1.587 mm in Group 5.	187
A.3 The experimental load/displacement curves for AA6061-T4 round specimens with a wall thickness of 3.175 mm in Group c-1.	188
A.4 The experimental load/displacement curves for AA6061-T6 round specimens with a wall thickness of 3.175 mm in Group c-5.	188
A.5 The load/displacement profiles for AA6061-T6 extrusions with a wall thickness of 3.175 mm in the presence of straight deflector in Group d-1.	189
A.6 The load/displacement profiles for AA6061-T6 extrusions with a wall thickness of 3.175 mm in the presence of curved deflector in Group d-5.	189
A.7 The load/displacement responses for AA6061-T4 extrusions with a wall thickness of 3.175 mm in the presence of straight deflector in Group d-9.	190
A.8 The load/displacement responses for AA6061-T4 extrusions with a wall thickness of 3.175 mm in the presence of curved deflector in Group d-13.	190
A.9 The load/displacement profiles for AA6061-T6 extrusions with a wall thickness of 1.587 mm in the presence of straight deflector in Group d-17.	191

Figure	Page
A.10 The load/displacement profiles for AA6061-T6 extrusions with a wall thickness of 1.587 mm in the presence of curved deflector in Group d-21.	191
A.11 The load/displacement curves for AA6061-T4 extrusions with a wall thickness of 1.587 mm in the presence of straight deflector in Group d-25.	192
A.12 The load/displacement curves for AA6061-T4 extrusions with a wall thickness of 1.587 mm in the presence of curved deflector in Group d-29.	192
A.13 The force/displacement profiles of AA6061-T6 round extrusions with a wall thickness of 3.175 mm under dual stage cutting from Group m-1.	193
A.14 The force/displacement profiles of AA6061-T6 round extrusions with a wall thickness of 3.175 mm under dual stage cutting from Group m-4.	193
A.15 The force/displacement profiles of AA6061-T6 round extrusions with a wall thickness of 3.175 mm under dual-stage cutting from Group m-7.	194
A.16 The force/displacement profiles of AA6061-T4 round extrusions with a wall thickness of 3.175 mm under dual stage cutting from Group m-11.	194
A.17 The force/displacement responses of AA6061-T6 round specimens with a wall thickness of 1.587 mm under dual stage cutting from Group m-13.	195
A.18 The force/displacement profiles of AA6061-T6 round specimens with a wall thickness of 1.587 mm under dual stage cutting from Group m-16.	195
A.19 The force/displacement profiles of AA6061-T6 round specimens with a wall thickness of 1.587 mm under dual stage cutting from Group m-19.	196
A.20 The force/displacement profiles of AA6061-T4 round specimens with a wall thickness of 1.587 mm under dual stage cutting from Group m-23.	196
A.21 The force/displacement profiles of the AA6061-T6 round specimens under the dual stage cutting using a 10 mm spacing between cutters in Group s-2.	197
A.22 The force/displacement profiles of the AA6061-T6 round specimens using a 10 mm spacing between cutters in presence of the straight deflector in Group s-5.	197
A.23 The force/displacement profiles of the AA6061-T4 round specimens with stepped wall in Group a-T4.	198

LIST OF APPENDICES

Appendix		Page
A	Axial Load/displacement profiles for each experimental test specimen within selected groups.	186
B	The partial input used in the FE simulation to simulate cutting tests in the presence of straight or curved deflector.	199
C	Copyright permission	203

NOMENCLATURE

B	One-half of the wedge shoulderwidth
C	Side width of square extrusion
D	Diameter of the round specimen
D_c	Critical damage value
E	Young's modulus
$E_{absorbed}$	Energy absorbed by a structure through plastic strain
H	Half the initial length of a folding element for a square tube
i	Index for the i^{th} data point
L	Length of a circular extrusion
M_o	Parameter defined in equation 2.6
P	Axial crushing force
P_m	Mean axial crushing force
P_{max}	Maximum load observed during axial crushing
S	Positive material damage parameter
t	Nominal wall thickness of a circular specimens
T	Blade tip width
σ_o	Plastic flow stress
δ	Crosshead displacement in the axial crushing direction
δ_t	Total crosshead displacement in the axial direction
σ_y	Yield strength
σ_u	Ultimate strength
θ	Half wedge semi-angle
ψ	Energy-absorbing effectiveness factor

ABBREVIATIONS

AA	Aluminum Alloy
AHSS	Advanced High Strength Steel
ALE	Arbitrary Lagrangian-Eulerian
ASTM	American Society for Testing and Materials
CFE	Crush Force Efficiency
CNC	Computer Numeric Control
FE	Finite Element
EF	Effectiveness factor
HSS	High Strength Steel
IIHS	Insurance Institute for Highway Safety
LVDT	Linear voltage differential transformer
NHTSA	National highway traffic safety administration
SEA	Specific Energy Absorption
SPH	Smooth particle hydrodynamics
TEA	Total energy absorption

1. INTRODUCTION

Vehicle occupant safety and addressing strict environmental regulations are significant challenges for automotive manufacturers. Over the years, safety, styling, comfort and handling were the primary concerns for consumers. However, environmental consciousness and dramatic increase of fuel prices in recent years shifted consumer choice towards more environment friendly fuel efficient vehicles. Globalization of auto industry, new government regulations and consumer demand has led to a greater emphasis towards more research on vehicle crashworthiness as well as incorporation of light weight materials in vehicle structures.

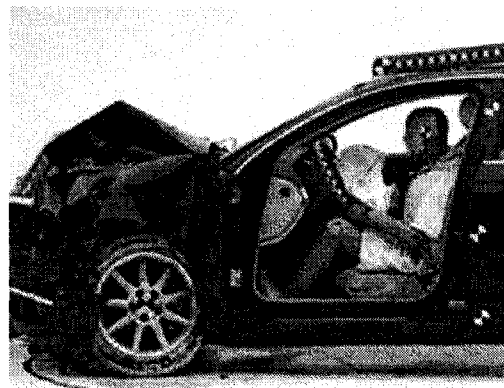
Government agencies, insurance underwriters, automotive manufacturers and the media provide consumers with significant amounts of safety information regarding vehicles. Most vehicles manufactured in recent years have incorporated safety features such as energy absorbing front and side structures, air bags, seats with integrated seat belts and various crash avoidance devices, such as anti-lock braking system, traction control devices, daytime running lamps, engine immobilizer, fog lamps, onboard monitoring system of tire pressures and rear view cameras to satisfy regulatory requirements. The National Highway Traffic Safety Administration (NHTSA) and the Insurance Institute for Highway Safety (IIHS) provide crashworthiness ratings of new vehicles and has ranked all tested vehicles in different categories according to crash test results. The IIHS conducts fully instrumented crash tests using the 50th percentile male Hybrid III dummy on a variety of new vehicle models each year. Frontal offset crash tests are a good assessment of a vehicle's structural design. Side impact crash tests are good assessments of occupant protection when vehicles are struck in the side by SUVs or pickups. Rear crash protection ratings focus on how well seat/head restraint combinations protect against whiplash injury. Photographs in Figure 1.1 illustrate the effectiveness of crashworthiness engineering during frontal offset crash and side impact crash tests conducted by the IIHS [1].

Depending upon the crash situation, different degrees of energy dissipation must occur in a controllable fashion to minimize the potential for injury to the occupants. In other words, energy dissipative structures are designed to absorb kinetic energy while

other structures are expected to maintain a safe survival region for the occupants. One way of achieving this objective is through use of structural members that absorb energy through plastic deformation. The frontal rails of the vehicle frame act as the main energy absorber during frontal impact and side A, B pillars and energy absorbing side door panels absorb a major portion of the kinetic energy during side impact. Efforts from industry and academic areas are trying to control the deformation mode of structural members and dissipation of energy in a controlled fashion during impact.



(a)



(b)



(c)



(d)

Figure 1.1. Structural damage after frontal offset and side crush tests of Audi A6 2008 model. (a) view after frontal impact, (b) driver's survival space maintained well, (c) view of side impact and (d) driver dummy's head was protected from being hit by hard structures by the side curtain airbag [1].

The other major challenge for the auto industry is to introduce more fuel efficient vehicles to address environmental concerns of their products through use of lightweight materials without compromising occupant safety. Material selection is critical to achieve the goals of weight versus strength. The basic requirements for automotive structural materials include good formability, lightweight, corrosion resistance and recyclability. Traditionally steels account for the majority of parts in a vehicle structure. Conventional high strength steel (HSS) (carbon-manganese, bake hardenable, high-strength interstitial-free, and high-strength, low-alloy steels) are replaced with the newer types of advanced high strength steel (AHSS) (dual phase, transformation-induced plasticity, complex phase, and martensitic steels) to achieve goals of mass reduction and improved material properties [2]. The strength to weight ratio and material properties of aluminum made it even more attractive in the design of vehicle structures. According to a study conducted by FKA [2], aluminum designs provide 5% to 20% mass savings compared to an advanced steel design as shown in Figure 1.2. Aluminum alloys have been widely used in vehicular structures as a result of the material's favourable strength to weight ratio, material and mechanical properties, recyclability, and relative low cost. In 2006, aluminum overtook iron to become the second most used material in new cars and trucks [3].

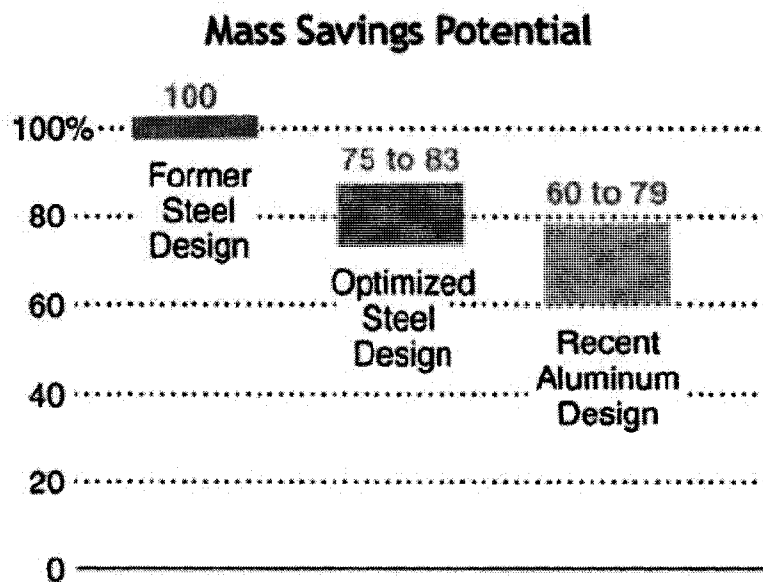


Figure 1.2. Potential mass savings using advanced steel and aluminum compared to conventional steel in vehicle design [2].

The research presented in this thesis involves the study of energy absorbing structural components made of extruded aluminum. The objective of this research is to examine the influence of geometrical parameters and temper conditions on the crashworthiness characteristics of axially loaded extruded AA6061 tubes. Experimental quasi-static crush tests have been used to determine the collapse mode, load/displacement characteristics, and energy absorption ability of round aluminum specimens. Specially designed cutters and deflectors have been utilized to achieve higher crush force efficiency and steady state load/displacement response under cutting deformation. Furthermore, investigations considering the use of cutters in series, as a potential adaptive energy absorber, and variations in the extrusion wall thickness (in the axial direction) have been considered in this research. The experimental results have been compared with the results of non-linear finite element (FE) simulations employing an Eulerian element formulation. A comparison between experimental results and analytical models developed by other researchers has been completed and will be presented for quasi-static axial cutting tests of round aluminum extrusions.

2. LITERATURE REVIEW

The ability to dissipate kinetic energy in the form of plastic deformation in a controlled manner by structural members of a vehicle is critical for occupant safety during an accident. A significant amount of theoretical, experimental and numerical research work has been performed on structural crashworthiness of thin-walled structures. The literature, related to the present study, dealing with energy absorption characteristics and crashworthiness of tubular structures are presented in this chapter. Section 2.1 discusses the collapse modes of axially loaded tubular structures under different loading conditions. Section 2.2 details the factors such as geometric variations, material properties and cross-sectional shape which influence the collapse mode of axially loaded tubes. Section 2.3 illustrates the influence of crush initiators in the form of geometric discontinuities and material imperfections on energy absorption characteristics. Section 2.4 discusses some of the analytical models developed by various researchers to predict peak buckling load and mean crush load for square tubes. Section 2.5 details the work performed by researchers using finite element analysis.

2.1 Modes of deformation for axially loaded tubes

The main physical mechanisms associated with energy absorption of metal structures are plastic deformation and fracture. The effectiveness of an energy absorbing device largely depends on its plastic deformation mode. A wide range of these modes exist, including, global bending, progressive folding, external inversion and axial splitting/cutting for thin-walled structures. Figure 2.1 illustrates the pattern of different deformation modes during axial crushing of circular tubes.

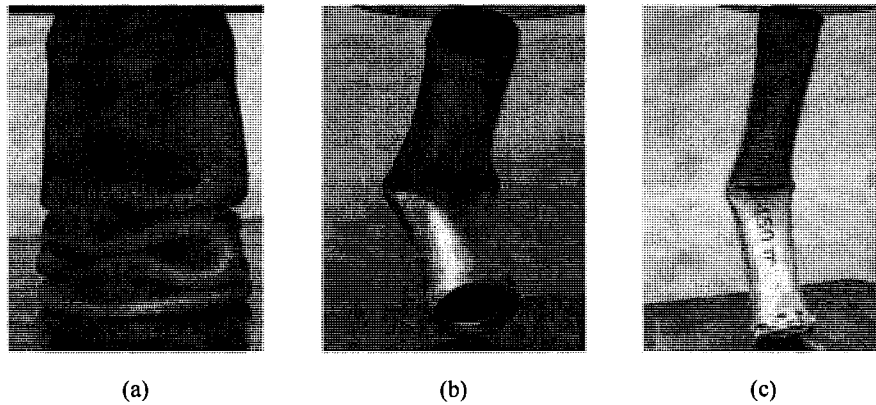


Figure 2.1: Deformation modes during axial crushing of circular tubes. (a) progressive folding, (b) global bending and (c) mixed mode.

2.1.1 Axial plastic collapse

There are a few possible patterns of collapse modes available during axial plastic collapse depending on geometrical parameters and material characteristics of the structure. The geometric parameters which govern the deformation mode are the ratios of L/D (length/diameter) and D/t (diameter/thickness) for circular tubes and L/C (length/width of side) and C/t (width of side/thickness of wall) for square tubes. The possible deformation modes within axial plastic collapse include progressive folding and global bending.

Abramowicz and Jones [4] characterized in detail the progressive collapse modes of axially loaded square tubes and divided the progressive collapse mode into three distinct crushing modes: symmetric, asymmetric, and transition. Possible symmetric

modes of deformation for square extrusions include (1) four individual lobes deforming inwards, (2) three lobes inwards and one outwards or (3) two opposite lobes deforming inwards with the other two opposite lobes deforming outwards. In contrast with symmetric mode, the asymmetric mode of deformation has the following deformation characteristics: (1) a layer of three individual lobes deforming outwards and one inwards or (2) two adjacent lobes deforming outwards with the other two adjacent lobes deforming inwards. The transition mode from progressive axial crushing to overall bending occurred when the asymmetry of the deformation gives rise to an inclination of the undeformed part of the column relative to the vertical axis.

Guillow et al. [5] experimentally investigated axial compression of thin-walled circular 6060 aluminum tubes with T5 tempered conditions and with different geometry variations. The range of D/t considered in these investigations was between 10 and 450 and L/D was selected ≤ 10 . The observed different modes of collapse corresponding to D/t and L/D ratios are presented in Figure 2.2.

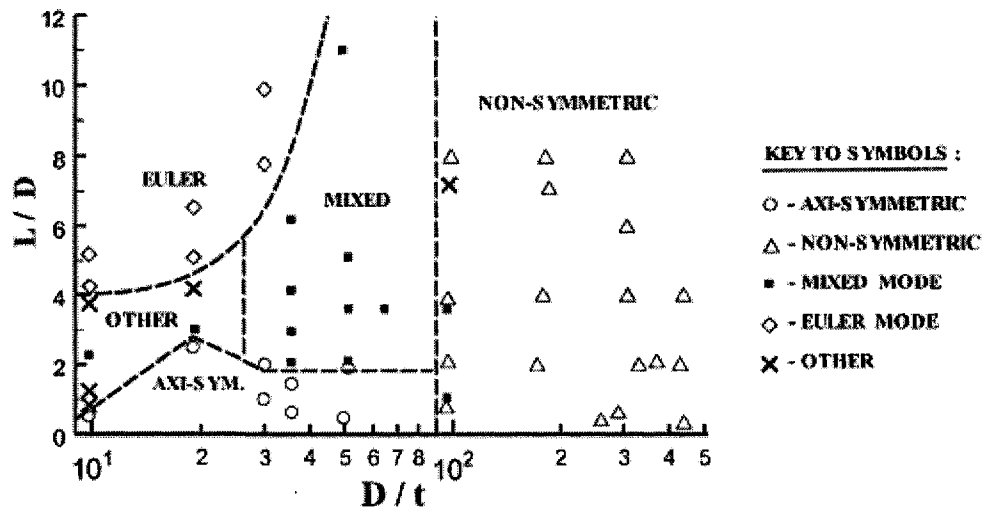


Figure 2.2. Classification chart for different deformation modes associated with circular 6060-T5 aluminum tubes [5].

They observed the ratio of maximum to average crush force increased substantially with an increase in the D/t ratio. They also found reasonable agreement between experimental findings and theory developed by Abramowicz and Jones [6] for axis-symmetric and non-symmetric modes.

Langseth and Hopperstad [7] experimentally investigated the crush behaviour of axially loaded square thin-walled AA6061 extrusions with T6 and T4 as well as modified T4 tempered conditions under static and dynamic loading. The geometry of the extrusions considered in this investigation had a length of 310 mm, width of 80 mm and wall thicknesses of 1.8 mm, 2.0 and 2.5 mm. All tubes considered in this study collapsed in a progressive symmetric deformation mode under static loading conditions regardless of wall thickness and tempered conditions. However, the number of lobes formed during the deformation process was found to be a function of the hardening properties of the material. When the specimens were fully compressed, approximately 6 lobes were formed in the tubes with T4 temper, between 6 and 7 lobes were formed in the tubes with modified T4 temper and 7 lobes were formed in the tubes with T6 temper.

The mean crush force and energy absorbed were reported higher for the tubes with T6 tempered condition. It was believed this finding was a result of the higher yield strength of the T6 temper. However, the ratio of the mean crush forces associated with T6 and T4 tempered conditions was observed highest for extrusions with 1.8 mm wall thickness and the ratio decreased with an increase of extrusion wall thickness. The authors attributed this towards difference hardening properties of two temper conditions. With the increase of wall thickness, strains are increased and thus gave a significant growth in the flow stress for T4 temper material which does not occur for T6 temper material due to low hardening modulus. Figure 2.3 illustrates the ratio between the mean loads for T4 and T6 tempered conditions as a function of wall thickness and axial displacement.

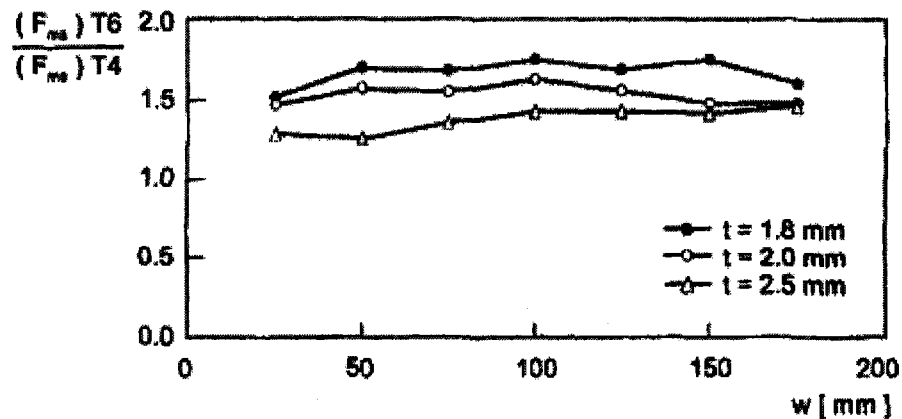


Figure 2.3. Ratio between mean loads for tubes with T4 and T6 tempered conditions [7].

Langseth and Hopperstad [7] also observed mixed mode of deformation during dynamic tests on similar extrusions used for static tests. The dynamic mean force was significantly higher than the corresponding static force for the same axial displacement. As the strain rate effects have minor importance, they indicated the observed difference had to be associated with inertia effects set up at the instant of impact due to lateral movement of sidewalls in order to initiate the folding process. A representative comparison between dynamic and static force versus displacement response for T6 tempered condition is presented in Figure 2.4.

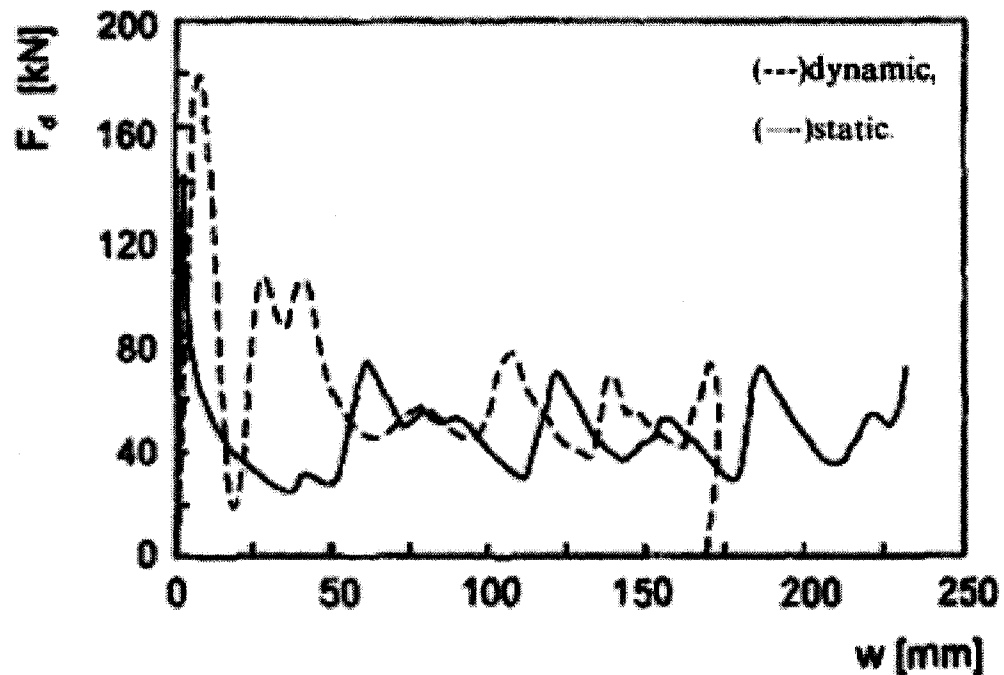


Figure 2.4. Comparison between dynamic and static force versus displacement response for the extrusions with T6 tempered conditions [7].

Singace [8] developed an analytical model. The theoretical work was also validated with experimental findings to evaluate the crushing load of tubes deformed in the multi-lobe mode using an eccentricity factor which is the proportion of the inside and the outside length of the fold. Singace reported analytical observations for the mean collapse load, value of eccentricity factor and the critical folding angles obtained for tubes of different materials and geometric ratios. These were in good agreement with those obtained from experimental results. It was discovered that the eccentricity factor

was independent of the tube's material and geometric ratio. Figure 2.5 represents the load/displacement profile for the axial crushing of HT-30 aluminum alloy tube with 50 mm outside diameter and 1.6 mm wall thickness crushed up to the fourth inward fold in axisymmetric deformation mode.

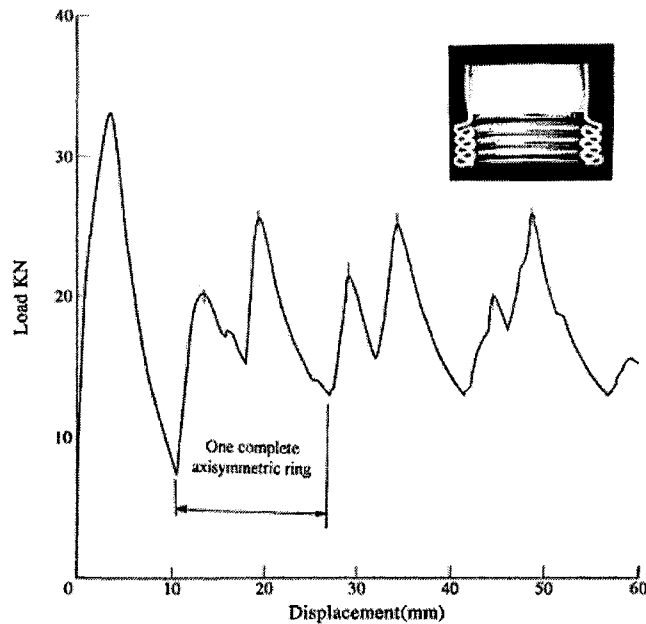


Figure 2.5. Load/displacement profile for the axial crushing of HT-30 aluminum alloy tube under axisymmetric deformation mode [8].

Hsu and Jones [9] conducted experimental investigations on the circular thin-walled 304 stainless steel, 6063-T6 aluminum alloy and mild steel tubes under quasi-static and dynamic loading conditions to identify critical slenderness ratios at the transition between progressive folding and global bending deformation modes. They reported that the stainless steel tubes absorbed the most energy, but they were the least efficient of the three materials for both quasi-static and impact loads according to energy absorption effectiveness factor. The effectiveness factor is the ratio of the energy absorbed by the extrusion to the product of the volume of the extrusion and the area below the σ/ϵ curve. The aluminum alloy tubes were the most efficient on the basis of energy absorption effectiveness factor. They also concluded that the specimen lengths for a transition from an energy efficient progressive folding to a potentially catastrophic global bending behaviour for quasi-static load were similar for the three materials.

2.1.2 External inversion

Tube inversion involves the turning inside out or outside in of a thin circular tube made of ductile material. There are two interesting stages in the tube inversion process, the first stage is the curling phase when the tube end is forced to conform to the shape of the curved die and begins to curl up. The second stage involves the formation of a second wall after the curling process. Inversion of tubes for energy absorbers was pioneered by General Motors as indicated in reference [10]. The main advantage of this mode of deformation is the constant load of axial compression and the axial shortening of the tube which can be achieved for a uniform tube. However, tube inversion is limited by die radius. If the die radius is small, progressive buckling of the tube will result and if the radius is larger than some limiting value, tube splitting will occur [11].

External inversion of a tube using a die is characterized by the axial compression of a tube over a die with appropriate radius as shown in Figure 2.6 [12]. The plastic deformation of the tube is the result of three different mechanisms: bending, stretching and friction [13]. Bending takes place at the point where the tube contacts the die, stretching along the circumferential direction progresses while the tube turns around the corner of the die and the interface friction occurs in the contact region between tube and die.

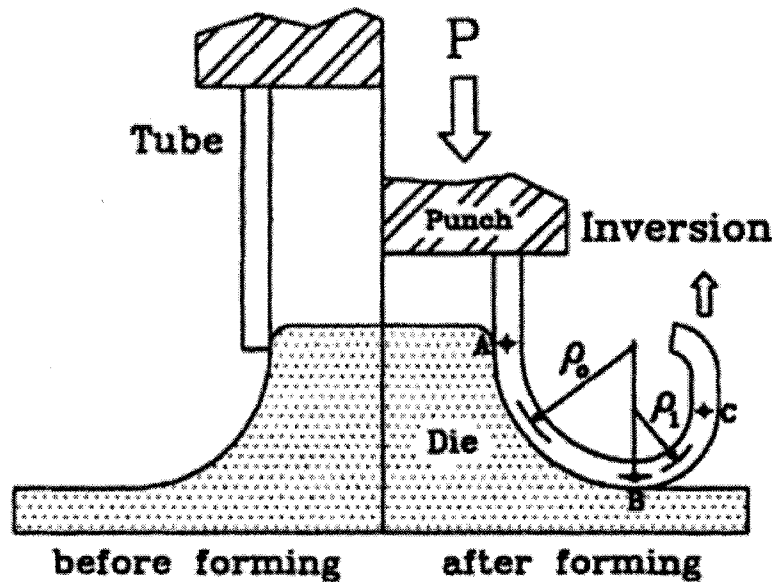


Figure 2.6. Schematic representation of the external inversion of tubes using a die [12].

Miscow and Al-Qureshi [10] performed an experimental and theoretical analysis of tube inversion under quasi-static and dynamic loading conditions. The specimens used in this investigation were copper and 70:30 brass tubes having an outside diameter of 50.8 mm, wall thickness of 1.58 mm and length of 88.9 mm. The quasi-static tests were carried out using a 200 kN capacity hydraulic testing machine at ram velocity of 20 mm/min. The die assembly was attached to the lower platen of the hydraulic testing machine and the hollow punch was fixed to the movable upper arm. A typical load versus displacement profile for copper and 70:30 brass tubes using a die radius of 4.76 mm is presented in Figure 2.7. From initial flaring of the material covering the die radius until the final steady-state inversion the tube passed through many stages. Typical samples of the tubes at various stages of external inversion are shown in Figure 2.8 for the quasi-static testing of copper tubes. Letters depicted in Figure 2.8 correspond with the stages that are shown in Figure 2.7.

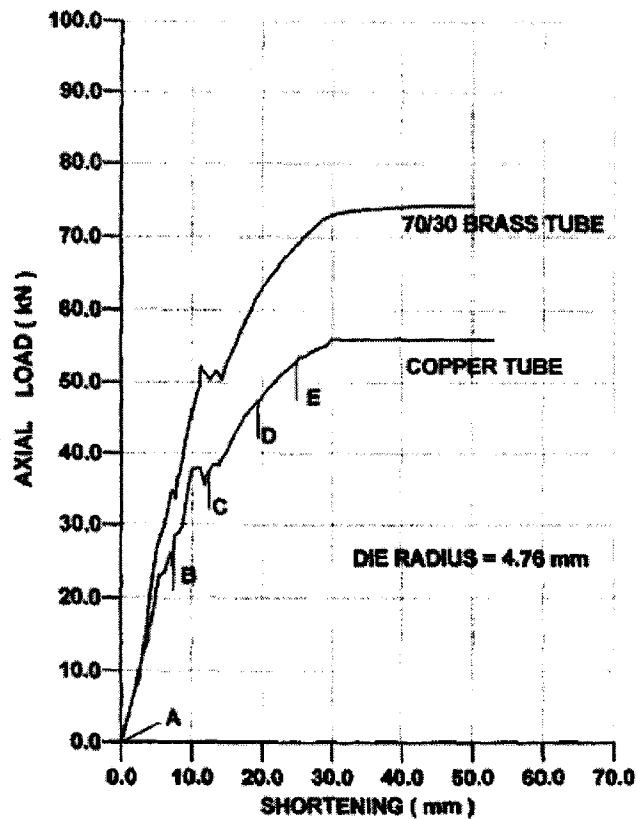


Figure 2.7. Load/displacement profile of copper and 70:30 brass tubes for quasi-static inversion process [10].

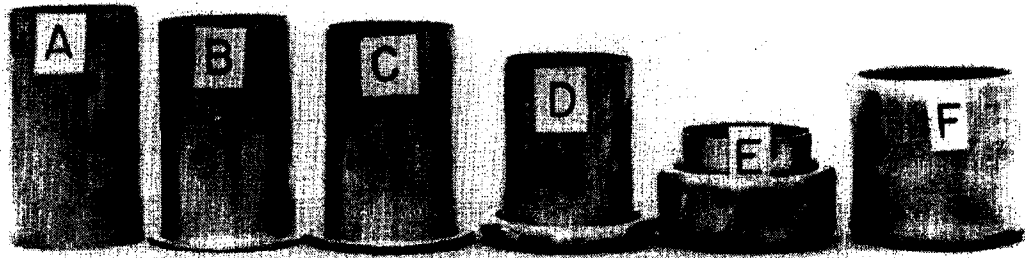


Figure 2.8. Various stages of the inversion of a copper tube in quasi-static method [10].

The authors concluded that materials in the as received and/or the partially work-hardened conditions were more appropriate to this technique than in annealed state, which generally demonstrated premature buckling. They also observed a considerable increase in the overall hardness along the inverted tube, in addition, an increase in wall thickness of approximately 8% throughout the inverted tube.

Leu [12] analyzed the curling behaviour of quasi-static inside-out inversion of tubes using a theoretical energy method technique on the critical condition for more precise design. The effects of geometric and material parameters, such as strain hardening exponent, friction coefficient and half-apex angle of die were investigated on the basis of the work by Kitazawa [14]. It was observed that the strain hardening exponent and half-apex angle of the die had a significant influence on critical bending radii. However, the friction coefficient dependence was not as great as that of the strain hardening exponent. Comparison between theoretical and experimental observations for the influence of half-apex angle of die on critical bending radius is presented in Figure 2.9.

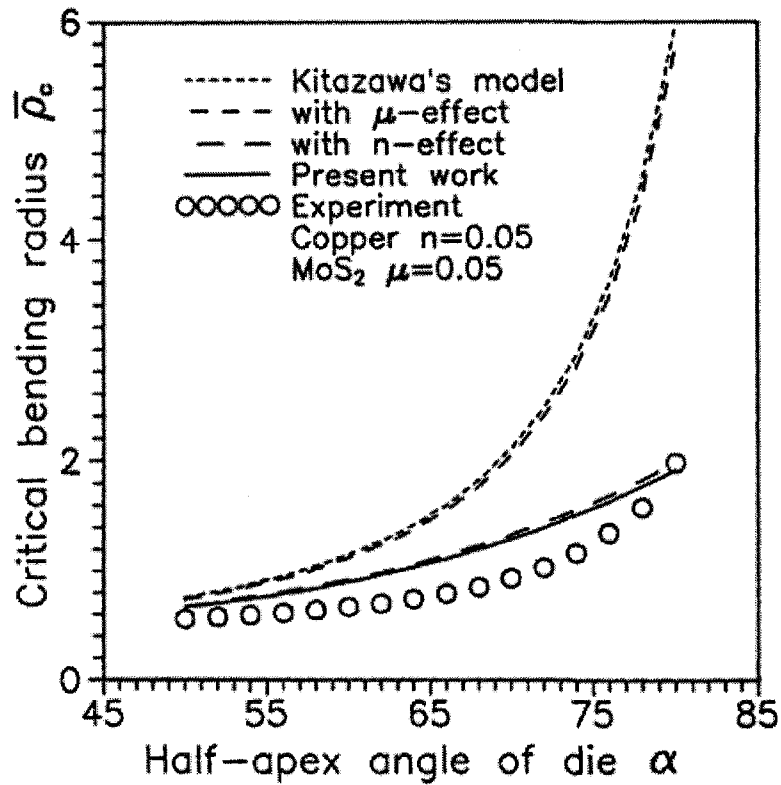


Figure 2.9. Experimental and theoretical results comparison for the critical radius [14].

2.1.3 Axial splitting/cutting

Splitting mode of deformation is a special case of tube inversion where the die radius is large enough to cause splitting instead of inversion [15]. The splitting deformation mechanism has advantages from the viewpoint of energy absorption capabilities. It has a long stroke of over 90 percent of the total length while maintaining a steady crush force after an initial transition period. The cutting deformation mode can be achieved by axially compressing the tube through specially designed cutters. The advantages of cutting deformation mode are the almost constant cutting force and the high CFE of over 95 percent that can be achieved.

Stronge et al. [16] conducted an experimental study on a passive crashworthy system that dissipates impact energy by fracture and plastic deformation. They considered square HE30 aluminum tubes having length of 50 mm and wall thicknesses of 1.6 mm as well as 3.2 mm. They reported three primary sources of energy dissipation

namely work done in plastic deformation, fracture propagation and curling during splitting and curling of tube by pressing the tube against flat plate.

Reddy and Reid [17] studied the splitting behaviour of circular cold drawn mild steel and HE30 aluminum tubes compressed axially between a plate and a die. They reported that different load levels can be achieved by varying the die radius and friction conditions as well as allowing the strips to curl, or being prevented from doing so. They also observed constant load/displacement profiles after an initial transition period and stroke efficiency of as high as 95 percent. The load/displacement profiles with or without using stopper plates are presented in Figure 2.10.

Lu et al. [18] conducted experimental studies on splitting square aluminum and mild steel tubes of thicknesses ranging from 0.47 mm to 1.67 mm. The experiments were carried out by driving four rollers, each attached to the side of the tube, leading to the bending of the wall to a constant curvature and, at the same time, tearing the material along the four corners. They determined tearing energy by pre-cutting some corners to a different length and found that the tearing energy per unit area may be related to the ultimate extrusion material stress and fracture strain. Figure 2.11 illustrates the experimental set up associated with this study

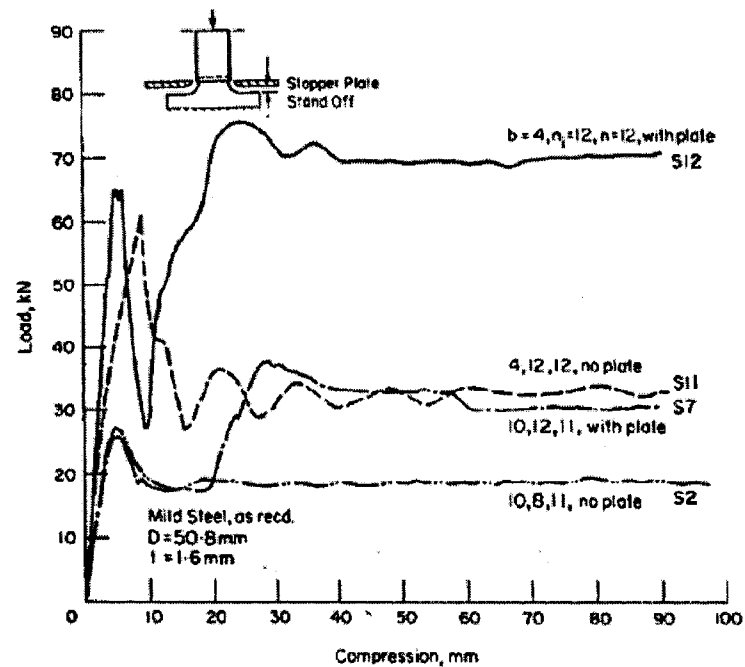


Figure 2.10. The load-displacement profiles with or without using stopper plate [17].

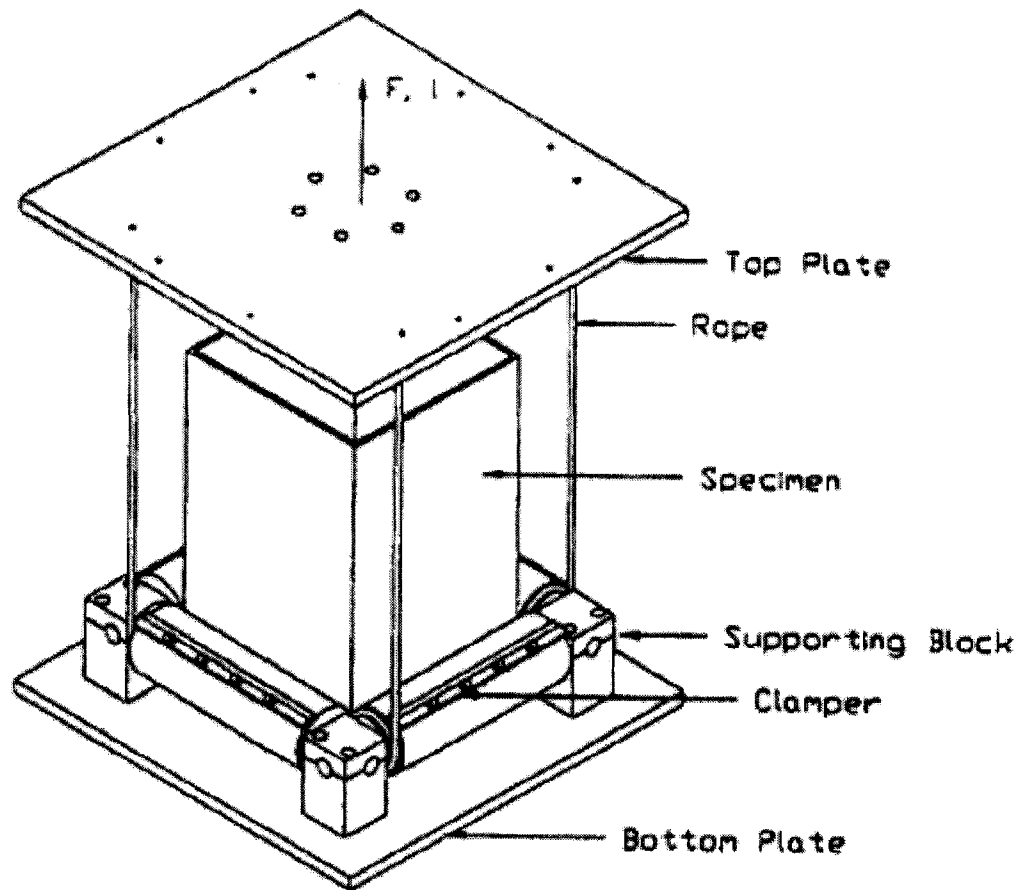


Figure 2.11. Sketch of the experimental set up. The bottom and top plates were attached to the base and crosshead of Instron machine [18].

Huang et al. [19] investigated the axial splitting and curling behaviour of mild steel and aluminum circular tubes by axially pressing the tubes onto a series of conical dies with different semi-angle (α). The specimens selected for this investigation were 200 mm long and the ratio of the diameter to thickness ranged from 15 to 60. In order to establish the split and curl mode while preventing other collapse modes, initial 5 mm saw-cuts were made into the specimen which were evenly spaced around the lower circumference. A cone-shaped die was fixed to the bottom bed of the testing machine and a short cylindrical mandrel was placed inside the tube to prevent the tube from tilting. Quasi-static testing conditions existed. Three different semi-angles of 45, 60 and 75 were selected for the conical die. The experimental set-up is illustrated in Figure 2.12.

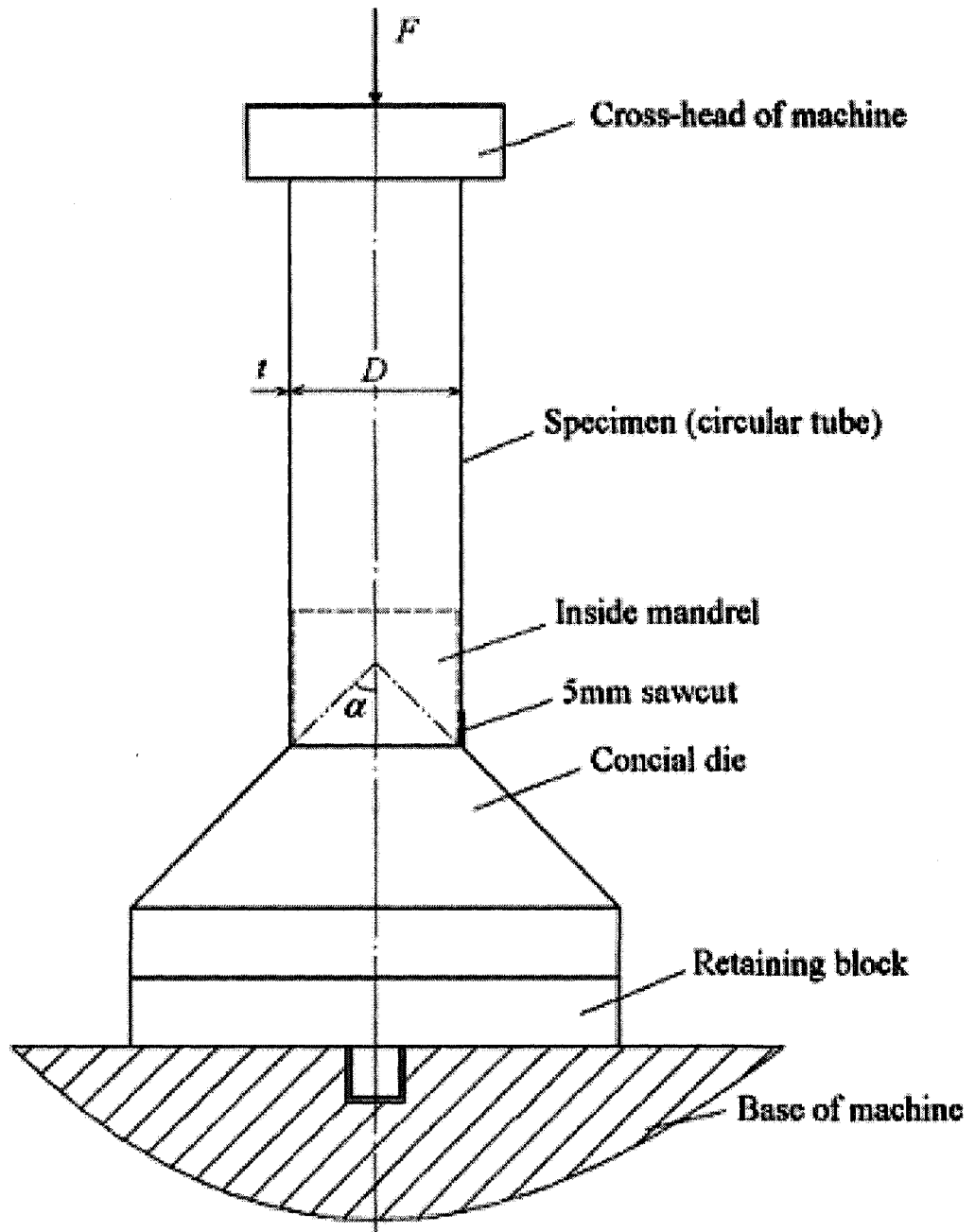


Figure 2.12. Sketch of the experimental set-up, with 8 evenly spaced 5 mm initial saw-cuts around lower circumference [19].

Typical force-compression curves for mild-steel tubes ($D = 74.0$ mm and $t = 1.8$ mm) and aluminum tubes ($D = 77.9$ mm and $t = 1.9$ mm) with three different dies are presented in Figure 2.13 and Figure 2.14 respectively.

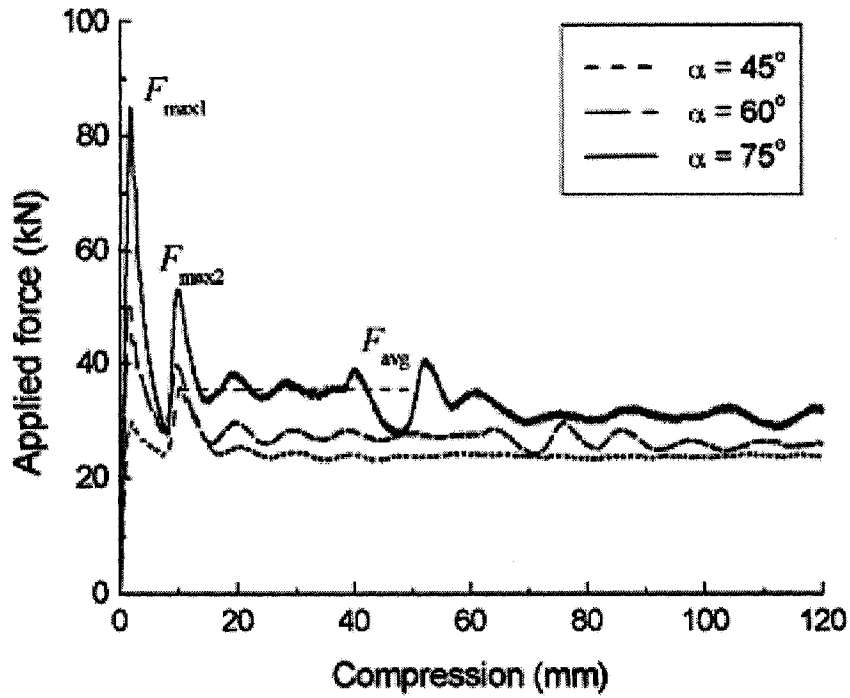


Figure 2.13. Load/displacement curves for mild steel tubes with $D = 74.0$ mm and $t = 1.8$ mm against dies with semi-angle $\alpha = 45^\circ$, 60° and 75° respectively [19].

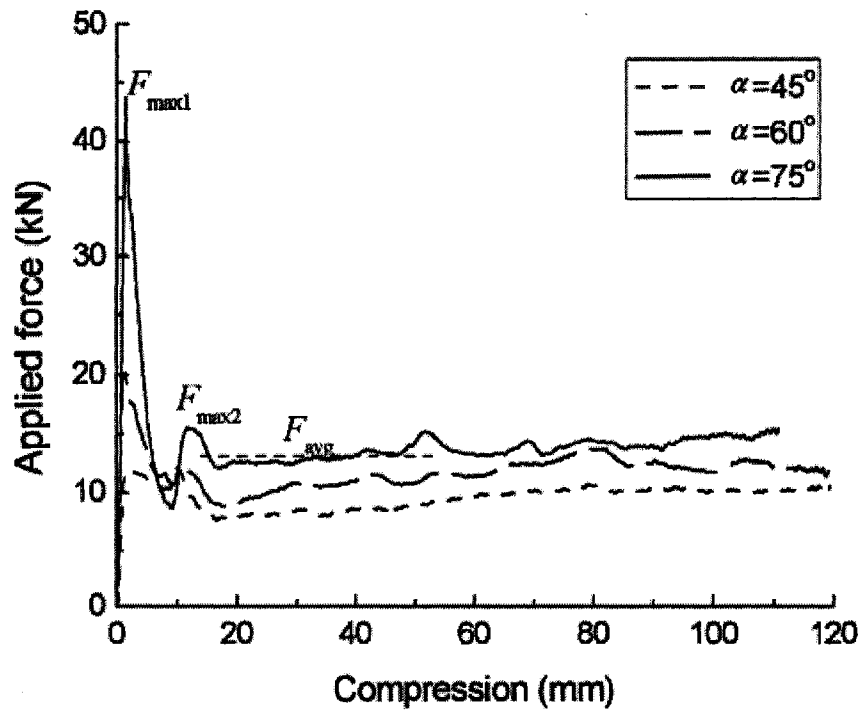


Figure 2.14. Load/displacement curves for aluminum tubes with $D = 77.9$ mm and $t = 1.9$ mm against dies with semi-angle $\alpha = 45^\circ$, 60° and 75° respectively [19].

The force initially increased with the cross-head movement until it reached the first peak, which corresponded to the onset of inversion of strips from the initial cut. A second peak force then occurred and this corresponded to the initiation of cracks. After approximately another 10 mm of displacement the force reached a steady state and remained almost constant. They found similar deformation modes for both mild steel and aluminum tubes, except that the average force was at the same level before and after the front edges of the curls touched the tube wall. The decrease in the applied force due to the increasing radius of the next roll was offset by an increase in friction between the tube and the inside mandrel.

Hung et al. [20] further investigated the energy absorbing behaviour of axially splitting square mild steel and aluminum tubes. Square tubes with a nominal side width of 50 mm, wall thicknesses ranging from 1.6 mm to 3.2 mm and length of 200 mm were selected for this study. The tubes were pushed slowly against rigid pyramid shaped dies, which had three different semi-angles of 45°, 60° and 75°. By pre-cutting 5 mm long slits at the four corners, the tube split along the corners and curled outward with a certain radius at a constant force. Typical force-displacement profiles for three different semi-angles of die are shown in Figure 2.15 and the corresponding specimens after testing are presented in Figure 2.16. The force initially increased with the cross-head movement until it reached a peak, which corresponded to the initiation of the four cracks at the corners. After that, the load decreased rapidly as the cracks propagated along the tube by ductile tearing. The four free sides then began to roll into curls. With increasing plastic deformation, the load again increased. Eventually, the curls formed with a constant radius as the plastic bending and load reached the steady state and the load remained constant with little fluctuation for the remainder of the test.

Hung et al. [19, 20] reported three forms of energy dissipating mechanism namely tearing energy, plastic deformation energy and frictional energy. They conducted theoretical analysis of three energy components and observed good agreement between theoretical predictions and experimental findings. The results showed that tubes which both split and curl may be used as efficient, long stroke energy absorbing devices.

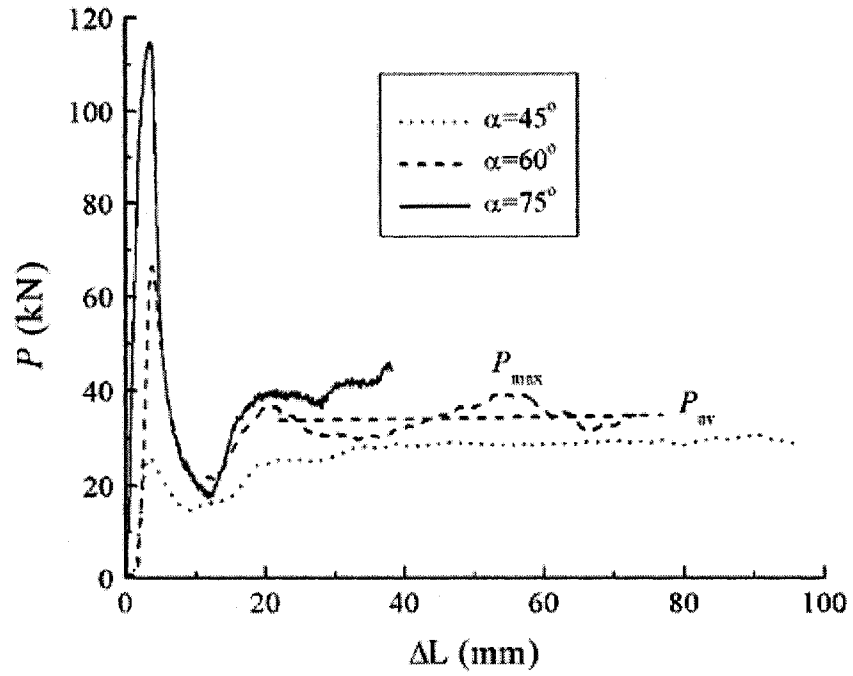


Figure 2.15. Typical force-displacement profiles for mild steel square tubes with $t = 2.5$ mm against dies with semi-angles of 45° , 60° and 75° respectively [20].

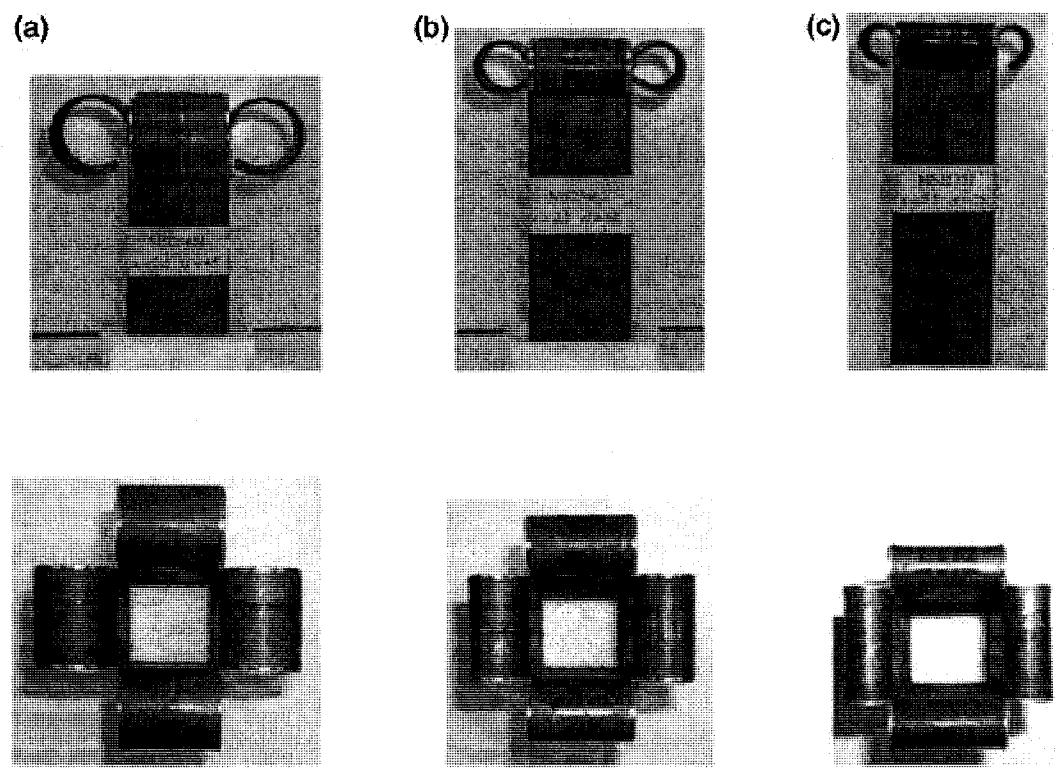


Figure 2.16. Photographs of typical mild steel specimens after test [20].

Chen and Altenhof [21] conducted an experimental study on the load-displacement and energy absorption characteristics of AA6061-T6 aluminum square extrusion under a cutting deformation mode utilizing specially designed cutters. Tube lengths of 200 mm and 300 mm with a wall thickness of 3.15 mm and nominal side width of 38.1 mm were used in this research. They observed an almost constant load/displacement response and a high CFE of 80 percent in the cutting mode compared to only 18 percent for 200 mm length extrusions in a global bending deformation mode. The force versus displacement profiles for cutting deformation and global bending deformation mode are presented in Figure 2.17. The photographs of corresponding cutting process are shown in Figure 2.18.

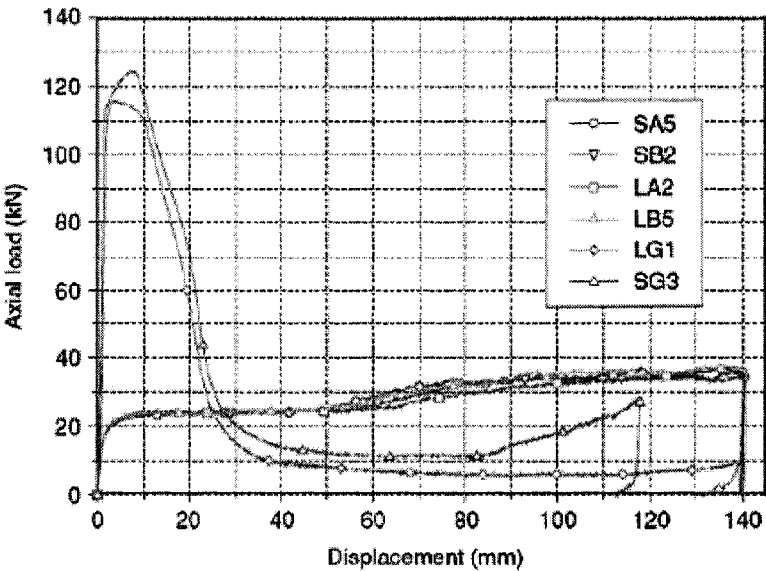


Figure 2.17. The load/displacement profile comparisons for cutting and global bending deformation modes [21].

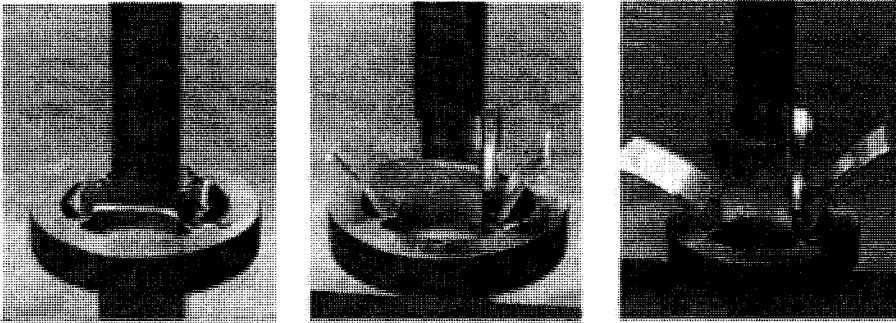


Figure 2.18. Photographs of cutting process for AA6061-T6 square extrusions [21].

They found no significant influence of tube length on the force/displacement response of the extrusions which experienced the cutting deformation mode. Three mode of energy dissipating mechanisms were observed, a cutting deformation mechanism and petalled sidewall outward bending mechanism and friction. The bending energy absorption mechanism appeared to initiate after approximately 50 mm crosshead displacement and accounted for approximately 25% of total energy absorption.

Jin et al. [22] studied the load/displacement and energy absorption characteristics of AA6061-T6 round extrusions under cutting deformation mode. A heat treated 4041 steel alloy cutter with four cutting blades of approximately average thickness of 1.18 mm was utilized in this investigation. The specimens used were round tubes of length 200 mm and 300 mm with a nominal wall thickness of 3.175 mm and an external diameter of 50.8 mm. They observed an almost constant cutting force during the cutting deformation mode. The cutting deformation exhibited a high average CFE of 95% compared to average values of 66% and 20% for progressive folding and global bending deformation modes. The load/displacement profiles comparison between different deformation modes shown in Figure 2.19.

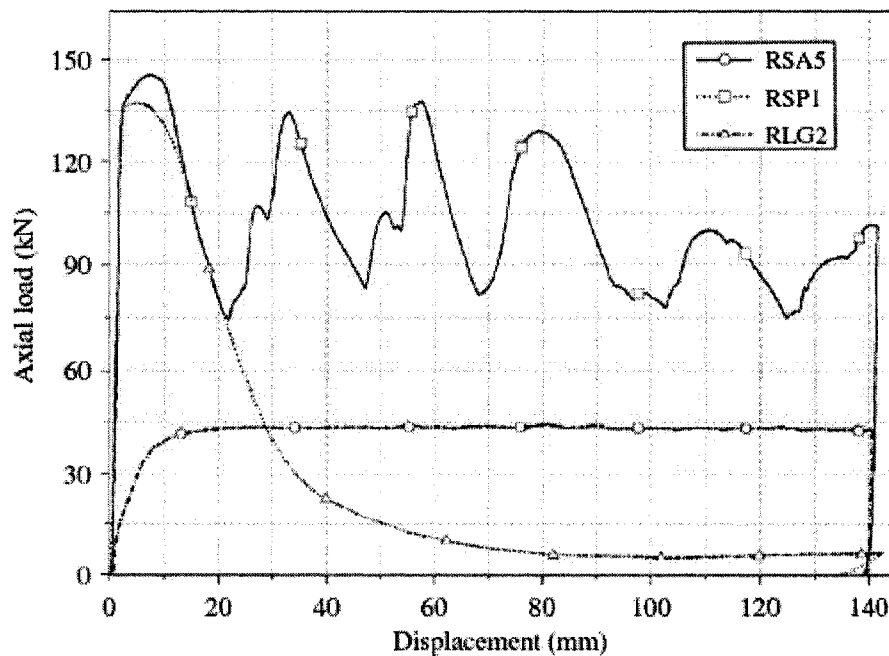


Figure 2.19. The load/displacement profile comparisons for cutting, progressive folding and global bending deformation modes [22].

The mean steady-state cutting force observed was 45.58 kN and a fair agreement was found between the experimental results and theoretical predictions utilizing the theoretical models developed by Zheng and Wierzbicki [23] and Simonsen and Wierzbicki [24]. The cutting deformation mode observed can be referred to a stable or clean cut [23]. Four energy dissipating mechanisms were observed, namely, a near blade tip cutting deformation mechanism, a circumferential membrane stretching, friction and a far field petalled sidewall outward bending.

Jin and Altenhof [25] further conducted experimental investigation on load/displacement and energy absorption characteristics of AA6061-T6 tubes under cutting deformation mode in presence of both cutters and deflectors. The specimens used in this investigation were similar to those used in reference [22]. Two different geometries of the cone-shaped deflectors, namely, straight and curved profile, were considered to control petalled side wall bending in addition to cutter similar to the cutters used in reference [22]. They found fluctuations in the cutting force when petalled sidewall hit the deflector but after 70 mm of crosshead displacement cutting force became steady-state. The load/displacement response in presence of a straight deflector is shown in Figure 2.20.

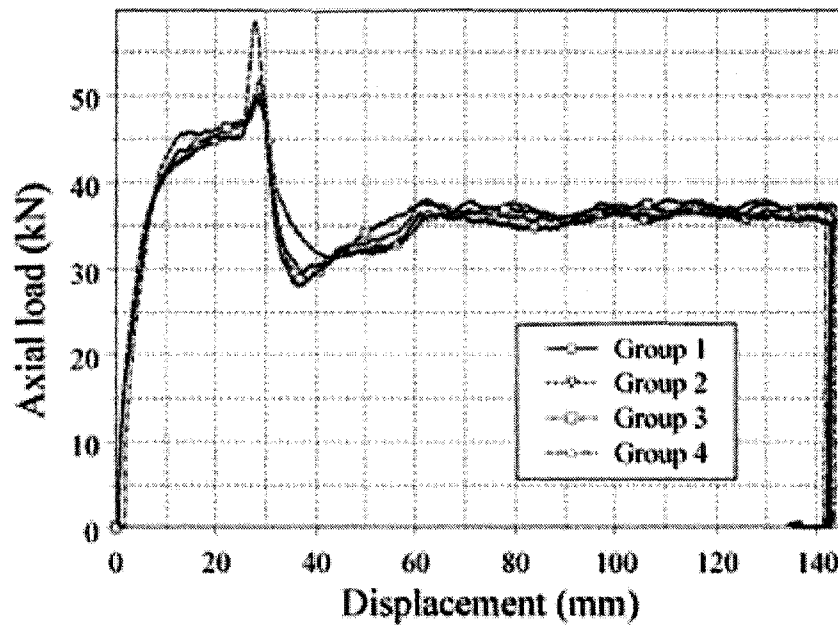


Figure 2.20. The load/displacement response of AA6061-T6 round tubes under cutting deformation mode in the presence of a cutter and a straight deflector [25].

2.2 Factors that influence collapse mode

The energy absorption of axially crushed tubes highly depends upon the collapse mode and the conditions governing the mode in which a tube will collapse are very important in this study. Significant research has been done in the past on different factors that influence tube collapse for a specific deformation mode. The major factors which have great influence on different deformation modes are extrusion geometry and material characteristics.

2.2.1 Cross-sectional geometry

The effect of cross-sectional shape on the crash resistance under bending-dominant collapse was extensively studied by Kim and Wierzbicki [26]. For the three-dimensional 'S' shaped frame, the crash energy absorption was shown to increase more than 200% without losing weight efficiency by redesigning the cross-sectional shape with a diaphragm. Kim and Wierzbicki [27] extended their numerical study to the 'S' frame with hat-type profile utilizing the nonlinear finite element code PAM-CRASH. They performed over 30 computer simulations in combination of several design aspects of closed hat-type 'S' frame, namely, type of hat-type cross-section, orientation of the cross-section, position of the internal stiffening member, aluminum foam-filling, hat type double cell profile with cut-out portion of the internal member and triggering dent. They found two types of design of the S-frame were superior over the remaining cases. The optimum design consisted of an internal stiffener positioned diagonally, and offered a high resistance to plastic bending but behaved poorly in axial compression. However, removing the two end portions of the inner stiffener and with the introduction of a triggering dent, this geometry exhibited an increase of total energy and specific energy absorption by 190% and 203% respectively. The second best optimum design used plastic stress of 3 MPa aluminum foam as a reinforcing agent. This structure exhibited a 160% increase in energy absorption and 184% increase in the specific energy absorption capability. The specific energy absorption of various models is compared in Figure 2.21.

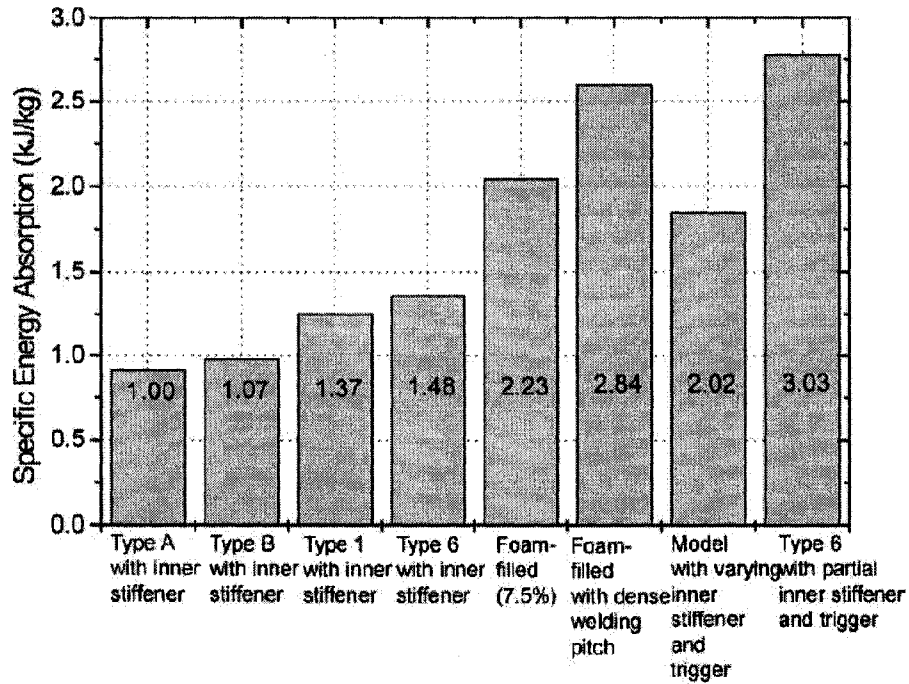


Figure 2.21. Specific energy absorption for different combination of design aspects [27].

Kim [28] has proposed two new multi-cell cross-sections with four square elements at the corner to maximize crash energy absorption and weight efficiency. The specimens considered in this investigation were thin-walled AA6063-T7 aluminum columns with cross-sectional dimension of 80X80 mm and length of 400 mm. The mechanical properties of the columns had an elastic modulus of 69 GPa, initial yield stress of 86.94 MPa and Poisson's ratio of 0.3. Numerical simulations of both cross-sections in Figure 2.22 were made for $b = 80$ mm, $C = 20$ mm and $r = 10$ mm cases. The uniform thickness over the entire cross-section, $t = 2$ were used.

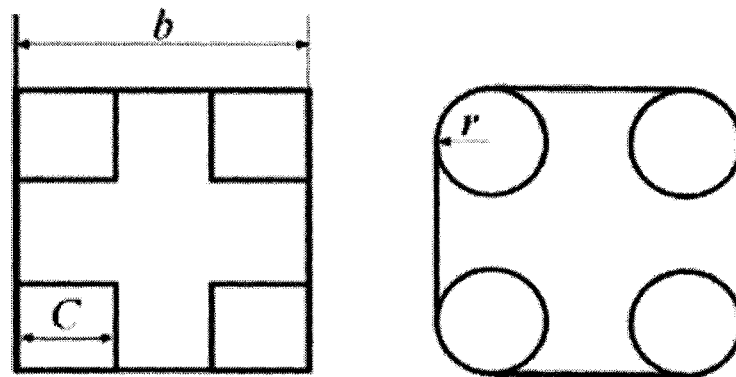


Figure 2.22. Proposed multi-cell cross-section of AA6063-T7 aluminum column [28].

The deformation shapes for square and circular corner columns are shown in Figure 2.23 and the crushing forces associated with different cross-sectional geometry are compared in Figure 2.24. The deformation mode was governed by the square or circular element on the corner part, so that the very short folding wave length was observed for both cases and the side flanges acted as the stabilizer between each corner element.

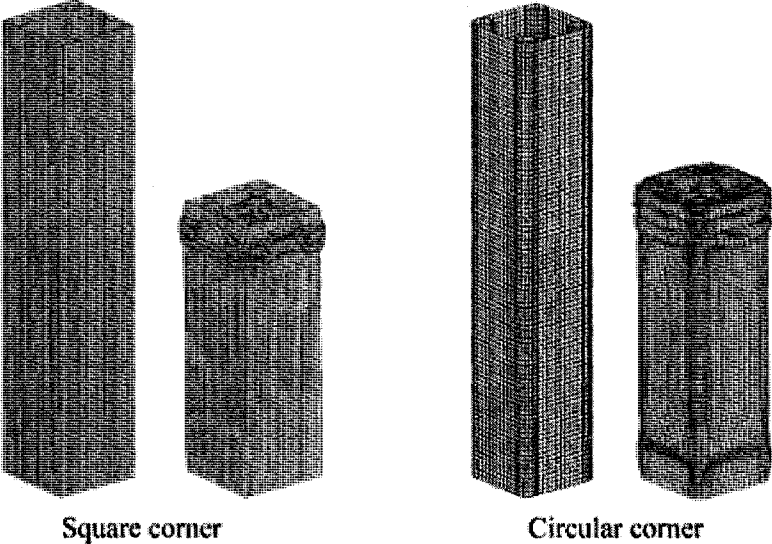


Figure 2.23. Deformation shape of square and circular corner columns [28].

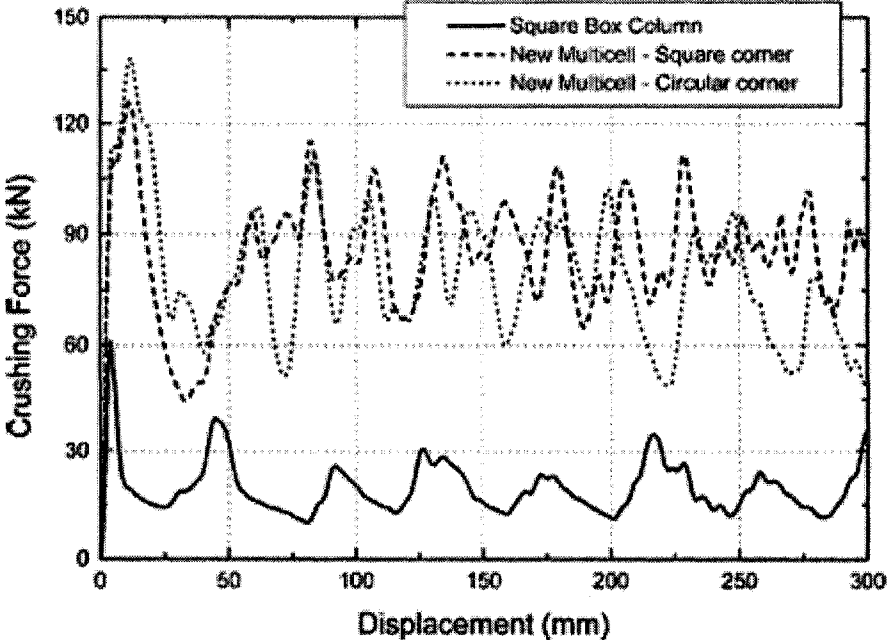


Figure 2.24. Crushing forces versus displacement profile comparison [28].

2.2.2 Geometrical dimensions

Further extrusion geometry other than cross-sectional geometry has a great influence on extrusion collapse modes and energy absorption capacities. A significant amount of research has been done to predict deformation mode based on geometric dimensions during axial loading. Abramowicz and Jones [29] have explored the critical parameters which govern the transition from global bending to progressive collapse, for circular and square thin-walled mild steel columns having a range of practical sizes and subjected to static and dynamic axial loading conditions. A total of 128 thin-walled mild steel columns with a wide range of lengths, widths and wall thicknesses were crushed in a quasi-static fashion in order to determine their collapse modes. Six different cross sections ($5.5 \leq C/t \leq 38$) for square tubes and five different cross sections ($9.6 \leq 2R/t \leq 48$) for circular tubes were selected for this investigation.

The experimental results are summarized in Figure 2.25 in terms of the dimensionless parameters $L/2R$ and $2R/t$, where L is the length of the tube, R is the outer radius of the tube, and t is the wall thickness. The solid line in Figure 2.25 approximately separates the experimentally determined progressive buckling and global bending regions (i.e. regions above the line represent geometries of tubes that collapse in the global bending mode and regions below the line represent geometries of tubes that collapse in the progressive buckling mode).

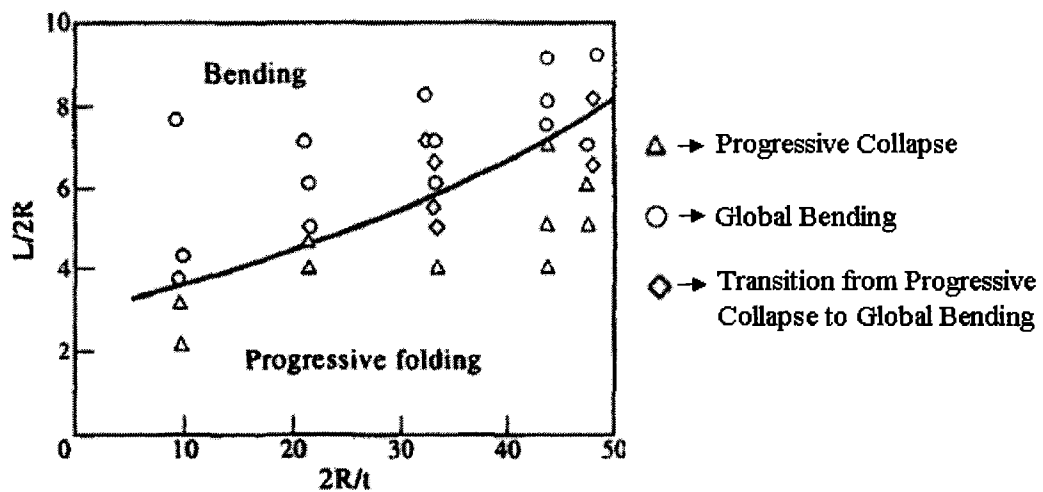


Figure 2.25. The deformation map for circular columns subjected to a quasi-static axial loading [29].

It was also noted in reference [29] that an accurate description of the transition process was difficult since it required detailed knowledge on the formation of a plastic folding mechanism as well as a precise distribution of the stresses in a column cross section. Although a complete solution to this problem was not available, a simplified model of a collapsing column was used to develop the theoretical relation for the transition boundary between the global bending mode and the progressive collapse mode for plastic buckling of circular and square tubes. Equation (2.1), which is an empirical relation describing the transition boundary between the global bending deformation mode and the progressive collapse mode for plastic buckling of circular tubes as a function of $(L/2R)$ was obtained by a curve fitting method.

$$\left(\frac{L}{2R}\right)_{cr} = 2.996 \exp\left(0.02 \frac{2R}{t}\right) \quad (2.1)$$

The critical length for which a column can be completely squeezed in a progressive mode was similar for both static and dynamic loading condition for square and circular tubes. The dynamic response of a column at the onset of the dynamic crushing process was significantly influenced by the inertia force. In an early stage of the deformation process, the inertia force inhibited the bending of the column and allowed the formation of few complete plastic lobes at the impacted end. As the crushing process progressed, the stabilizing effect of the inertia force gradually diminished.

Langseth and Hanssen [30], who have done extensive research on the axial crushing of aluminum extrusions, suggested a critical length to width ratio of 3 for a stable (progressive buckling) collapse mode. For small width-to-thickness ratios, this value is in reasonable agreement with the experimental and theoretical results.

Kim and Lee [31] conducted dynamic compressive tests on extruded 6061 aluminum tubes with varying cross-sectional shape, thickness, width, and edge tip radius to experimentally evaluate impact energy absorption. The specimens selected for this investigation had a length of 220 mm and thickness to diameter ratios for circular tubes ranged from 0.019 to 0.037 and thickness to width ratios for square tubes ranged from 0.022 to 0.039. Both ends of the tube were welded to aluminum panels in the exact vertical direction to the longitudinal specimen direction for even compressive loading and

a hole of 6 mm diameter was introduced at the center of the panel in order to exclude the effect of internal air compression. As the t/w or t/D ratios increased to a certain extent, more symmetric folds tend to be formed and thus specific impact energy absorption rose almost linearly. Under the same t/w ratio, the circular specimens showed higher specific impact absorption energy compared to the rectangular geometry. The authors credited this phenomenon towards the higher tendency of the symmetric fold formation in the circular specimens than in the rectangular. Photographs in Figure 2.26 demonstrate the deformed shapes after the test for a circular specimen. Figure 2.27 illustrates the correlation between specific impact energy absorption and t/w (or t/D) ratio for both rectangular and circular specimens. The difference in the specific impact energy absorption between circular and rectangular specimens reduced as the t/D ratio increased. It is expected that under higher t/w or t/D ratios (above 0.6), nearly constant specific impact energy absorption may be shown, irrespective of cross-sectional shape.

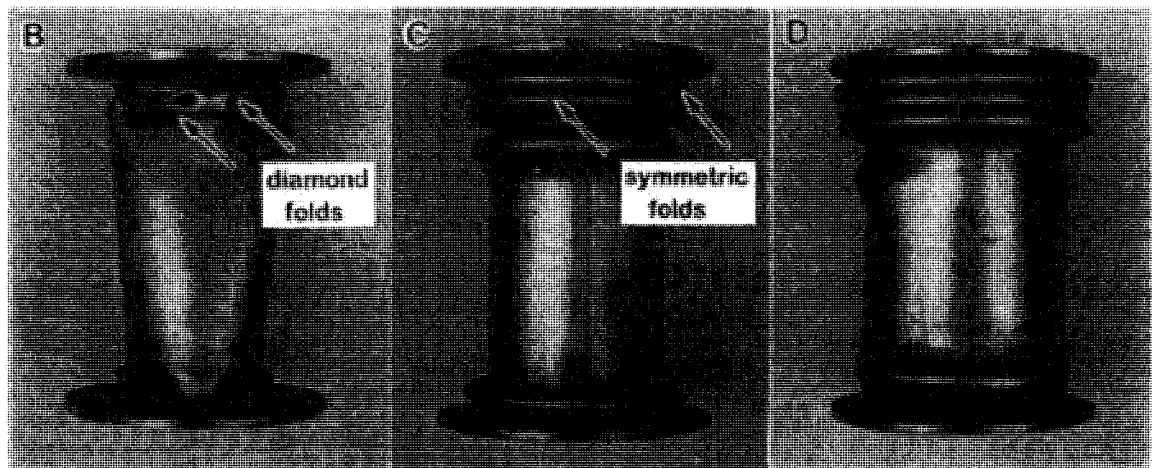


Figure 2.26. Deformed shapes of circular specimens. Both ends of the tube specimens were welded with aluminum panels [31].

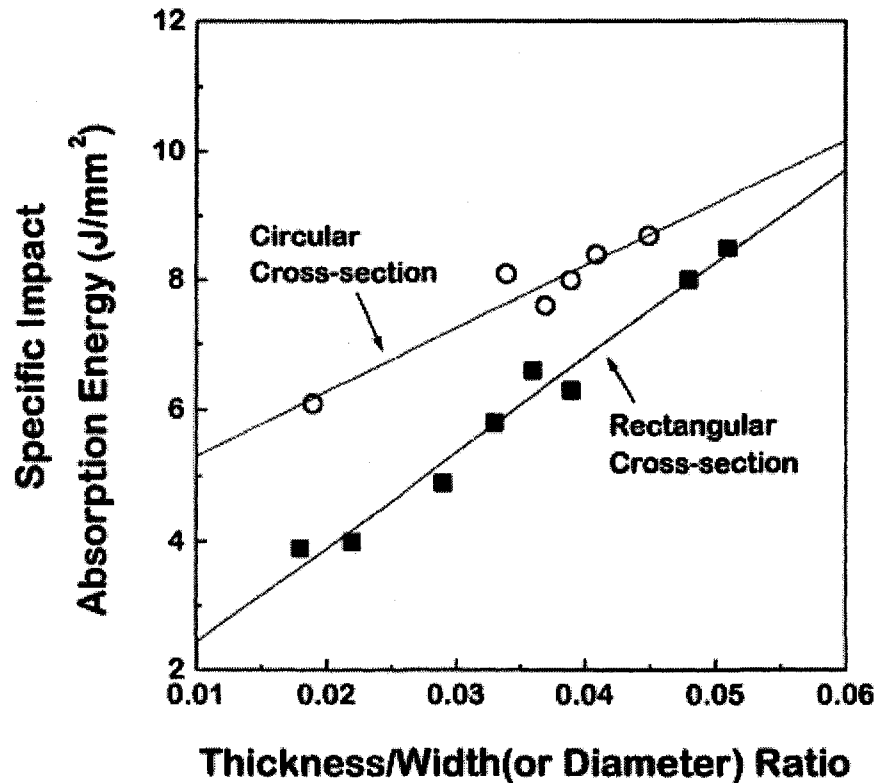


Figure 2.27. Specific impact absorption versus thickness/width (or diameter) ratio for the circular and rectangular specimens [31].

2.2.3 Extrusion materials

Extrusion material has an important role in specific deformation mode and energy absorption capability. A significant amount of research has been performed on circular and square tubes of commonly used materials including aluminum alloys, stainless steel, mild steel and high strength steel. Langseth and Hopperstad [7] also investigated the influence of extrusion material on crush performance of axially loaded square thin-walled AA6061 aluminum alloy extrusions with T6 and T4 as well as modified T4 tempered (T4*) conditions. The engineering stress versus strain relationship for different temper materials are presented in Figure 2.28. The authors observed that the number of lobes formed during the deformation process as well as the way the different lobes were formed was a function of the hardening properties of the materials. The lobes were formed successively for T6 temper while for T4 temper two successive lobes formed first apart

from each other and then the third lobe formed between the first two. The average effective crushing distance to form a complete lobe was 32 mm for T6 temper, while the corresponding value for T4 temper was 37 mm. The deformation pattern for modified T4 temper was something between those of T4 and T6 tempers.

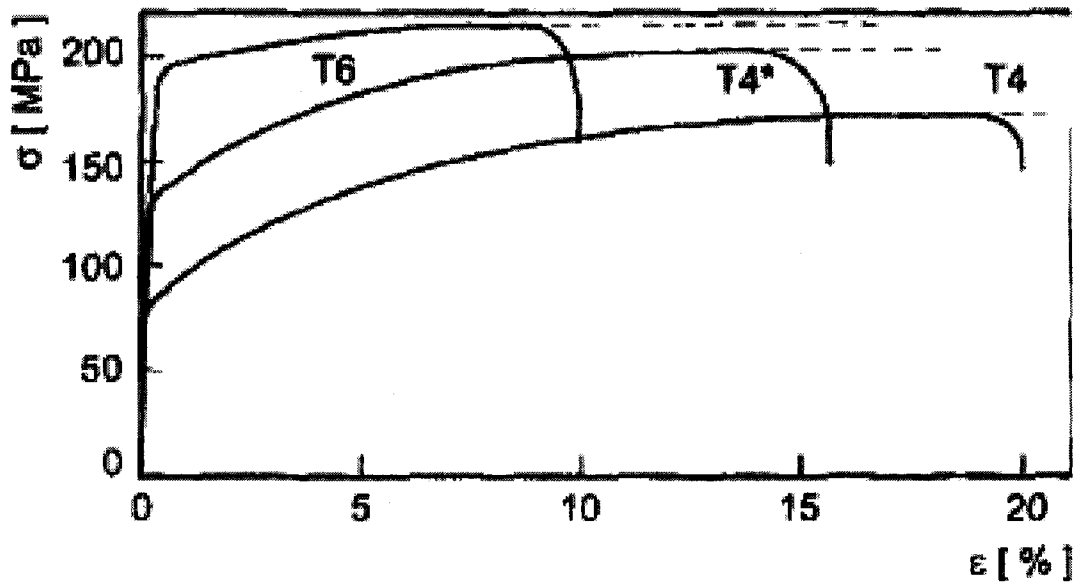
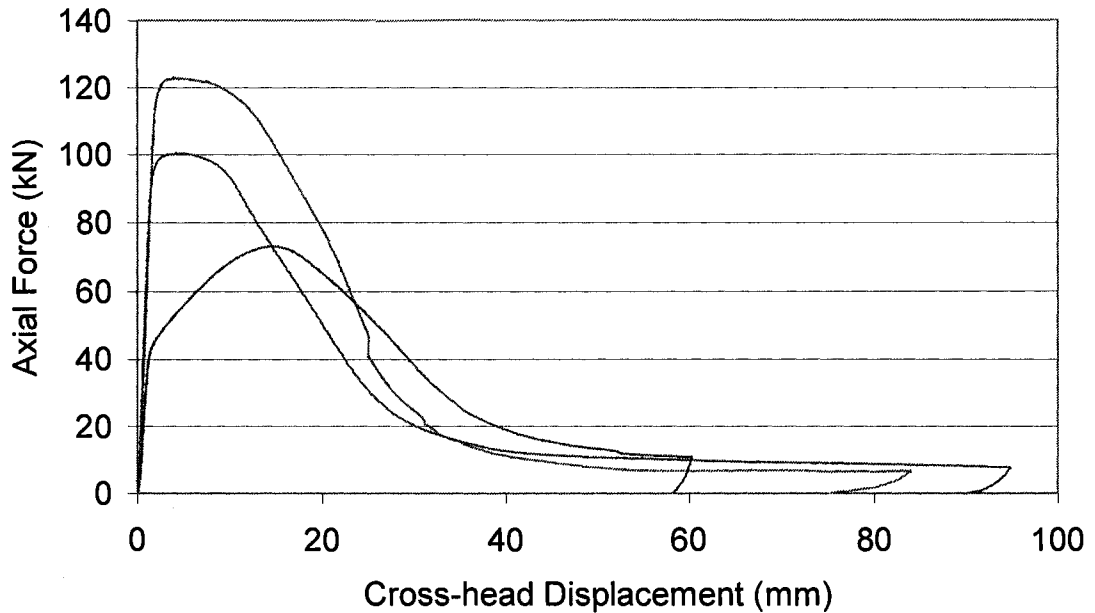


Figure 2.28. Typical engineering stress-strain relationships for the three temper materials used in the study [7].

Arnold and Altenhof [32] studied the energy absorption capabilities of axially loaded square aluminum alloy extrusions. The specimens selected for this study were AA6061-T4 and T6 as well as AA6063-T5 with nominal wall thickness of 3.15 mm and width of 38.1 mm. The Load versus displacement profiles for specimens made from each of the three extrusion materials are illustrated in Figure 2.29. Due to the large hardening capacity of the AA6061-T4 extrusion material, the uniform plastic compression phase of the load versus displacement curve was extended for a longer amount of crosshead displacement than the specimens of the other two materials. They found a significantly larger crush force efficiency for the specimens made from AA6061-T4 than for the specimens made from the other two materials. This was attributed towards the larger area under the load versus displacement curve for the AA6061-T4 specimens relative to the peak buckling load than the tubes made from the other two materials.



— AA6061-T4 (group D) — AA6061-T6 (group I) — AA6063-T5 (group N)

Figure 2.29. Comparison of load/displacement profiles for each extrusion materials considered [32].

2.3 Crush initiators

Crush initiators are stress concentrations introduced into structural members in the form of material imperfection or part geometry to initiate a specific axial collapse mode, stabilize the collapse process and minimize variations in crush load. The use of crush initiators can considerably reduce the peak plastic buckling load, improve crush performance parameters and trigger deformation at a specific location.

Use of crush initiators to enhance the performance of an energy absorbing structure through changing material properties can be achieved by localized heat-treating at the regions of interest. But the more common method of introducing crush initiators is through the use of a geometric discontinuity located somewhere along the length of the absorber. This discontinuity usually takes the form of a hole or notch, and when applied to an axially loaded square tube, is usually located at the corners or middle of the tube. Geometric initiators can be easily controlled by changing location, shape, dimension and quantity of the initiator.

Gupta and Gupta [33] studied the influence of length to diameter and diameter to thickness ratios as well as cut-outs in the form of circular holes on deformation behaviour of round aluminum and mild steel tubes. The discontinuities were introduced through laterally drilled holes and varied in diameter, number and position. It was observed that the presence of holes in the tubes altered their mode of collapse.

The effect of geometric discontinuities on reducing peak buckling loads and promoting a stable collapse mode was studied by Krauss [34]. Krauss introduced circular and diamond shaped holes and cross-sectional beads in square steel tubes. The geometries of the initiators are illustrated in Figure 2.30. A parametric study was also conducted on the effect of crush initiator geometry and size on the peak buckling load and mean crushing load supported by the tube. Area reduction geometries of 5%, 10% and 15% were studied for each of the crush initiator geometries. Experimental dynamic crush tests as well as numerical simulations were completed. It was observed that each type of initiator effectively reduced the peak crushing load. The load versus displacement curves obtained from the numerical studies for each size of circular holes as well as the specimen with no initiator are shown in Figure 2.31. For the circular and diamond shaped notches, the peak buckling load decreased as the size of the initiator increased.

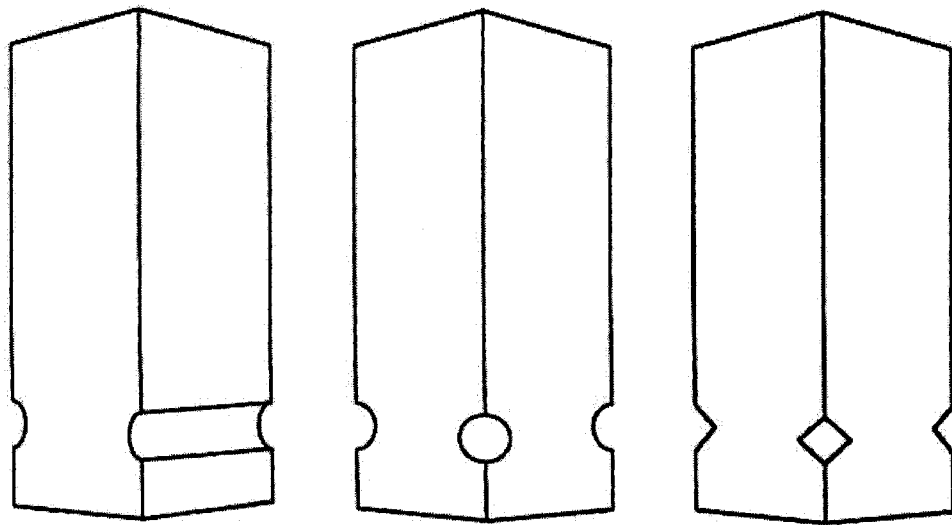


Figure 2.30. Crush initiator geometry configurations studied by Krauss [34].

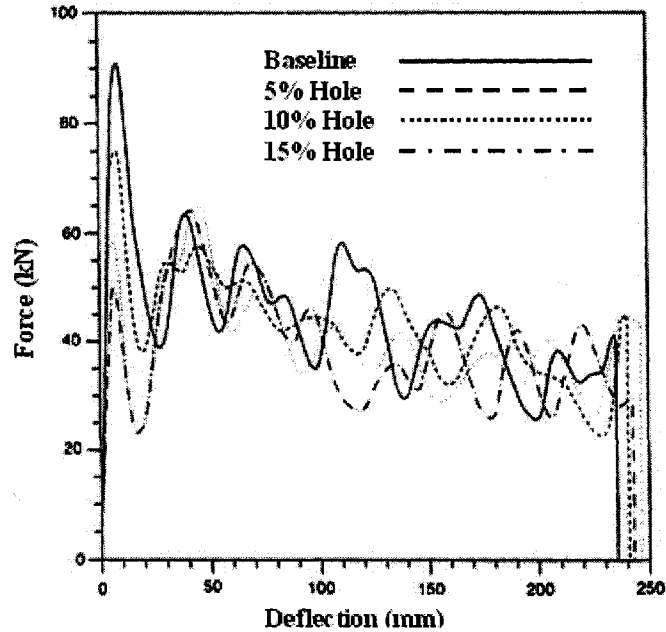


Figure 2.31. Numerically calculated force versus deflection curves for specimens with each size of circular crush initiator [34].

In order to reduce the peak crushing load and initiate collapse, Abah et al. [35] introduced circular holes at the corners of thin-walled extruded aluminum tubes. The specimens utilized in this investigation had a length of 200 mm, width of 48 mm and a thickness of 1 mm. Crush initiator diameter ranged from 2 mm to 12 mm. Using experimental axial crushing tests and FE simulations, Abah et al. obtained similar findings to those of Krauss. The holes caused a peak crushing load decrease proportional to the initiator size, while the mean crush load remained relatively constant. Lee et al. [36] also studied the effect of crush initiators on the energy absorption of axially loaded square tubes. Lee et al. introduced rows of grooves into dynamically loaded aluminum tube extrusions. The energy absorption performance of the tubes was evaluated under quasi-static crushing tests on a 10-ton Instron compressive testing machine using a crosshead speed of 20mm/min. FE simulations were also conducted using the FE simulation program PAM-CRASH. The groove geometries considered by Lee et al. are illustrated in Figure 2.32. Two types of grooves, referred to as the full dent and the half dent, were used as initiators in the study. As illustrated in Figure 2.32, the grooves were 1mm deep and 2mm wide and extended across the full side width of the tube or half the side width.

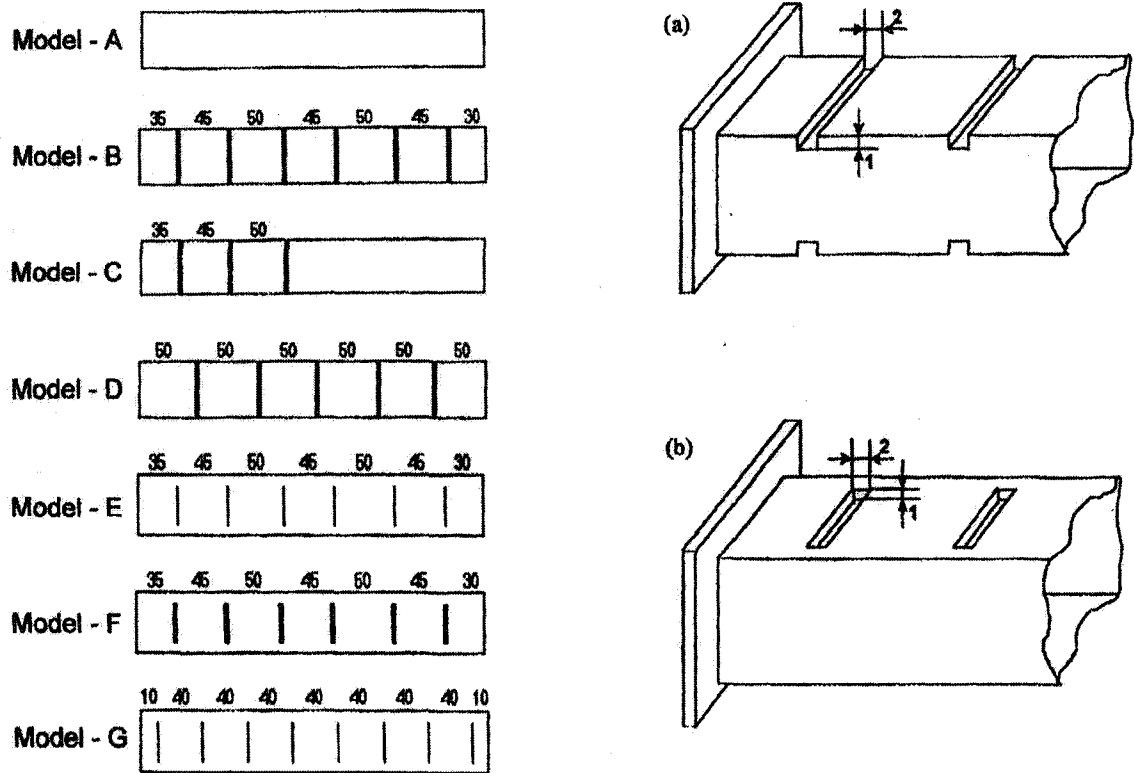


Figure 2.32. Geometry and configurations of dents considered by Lee [36]. All dimensions are in millimeters.

Six dent configurations were considered, in addition to one baseline tube with no dents. The dented configurations of models B, C, E and F were based on the predicted or pre-estimated folding sites and the dent configurations of models D and G were spaced at even intervals at locations that did not correspond to the natural folding sites. A good correlation was observed between the results of the experimental tests and numerical simulations. The results showed that the tubes with dent configurations corresponded to the estimated folding sites in the same mode as the baseline model (symmetric). The models with dent locations not corresponding to pre-estimated folding sites exhibited a non-uniform crushing mode accompanied by global bending in both the experimental testing and the FE simulations. Figure 2.33 illustrates the load/displacement relationship of specimens A through D. Similar maximum crush forces of dented specimens B through D were observed. However, the maximum crush force was reported for the undented specimen A.

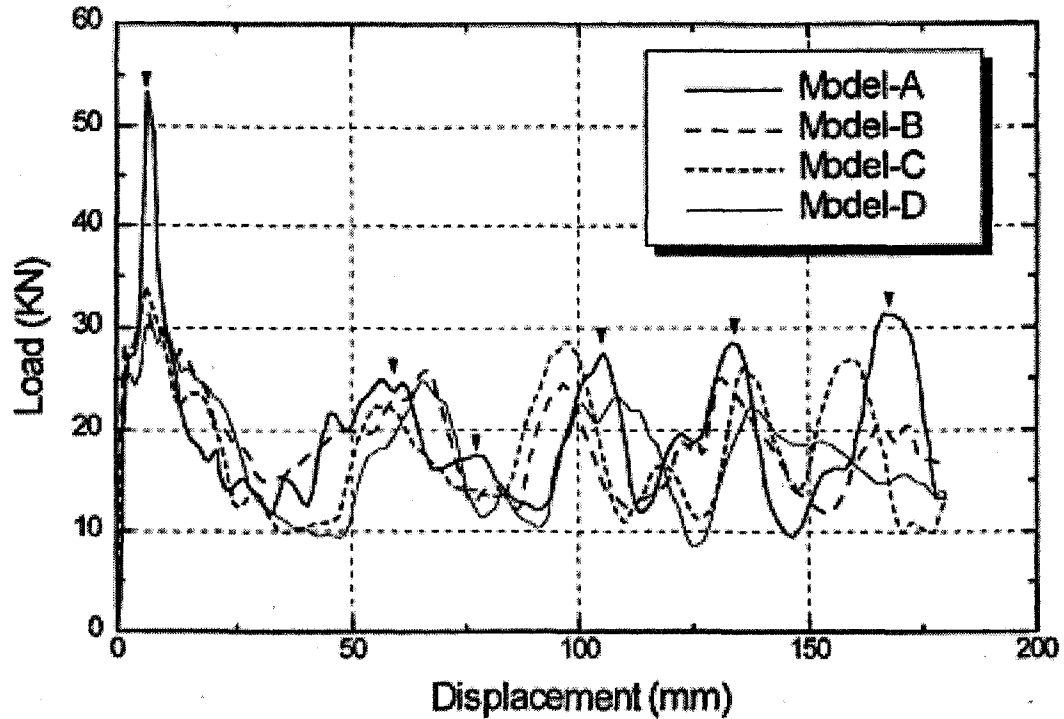


Figure 2.33. The load-displacement profiles of specimens A through D [36].

The use of crush initiators in automotive side rail members has been investigated by Kitigawa et al. [37]. Beading was introduced in side rails at estimated folding sites in an effort to obtain a more desirable collapse mode and increase energy absorption. Edge beads, concave beads and convex beads were fabricated into the side of a hat-section automotive side rail member. The edge bead was placed at the site of the first fold and concave and convex beads were placed at the predicted sites of inward and outward folds respectively. It was observed that the initiators effected a significant improvement in collapse mode, which caused a large increase in energy absorption. This work illustrates that the collapse mode of an automotive structural member can be beneficially changed with a small and inexpensive change in geometry, having a significant positive effect on energy absorption.

Arnold and Altenhof [38] experimentally investigated the crush characteristics of AA6061-T4 and T6 structural square tubes with and without presence of circular discontinuities. The tubular geometries selected had lengths of 200 mm and 300 mm, nominal side width of 38.1 mm and wall thickness of 3.15 mm. Centrally located circular holes with diameter 7.1 mm and 14.2 mm, machined into the two opposite walls of the

tube, were used as crush initiators to commence the plastic buckling process. It was reported that collapse modes and energy absorption of the structure depended largely on material properties and to a lesser extent on the diameter of the discontinuity. Significant increase in the crush force efficiency, up to a maximum of approximately 22%, was observed for 200 mm length tube geometry as illustrated in Figure 2.34. Energy absorption capabilities were substantially improved for specimens containing circular discontinuity relative to specimens without discontinuity.

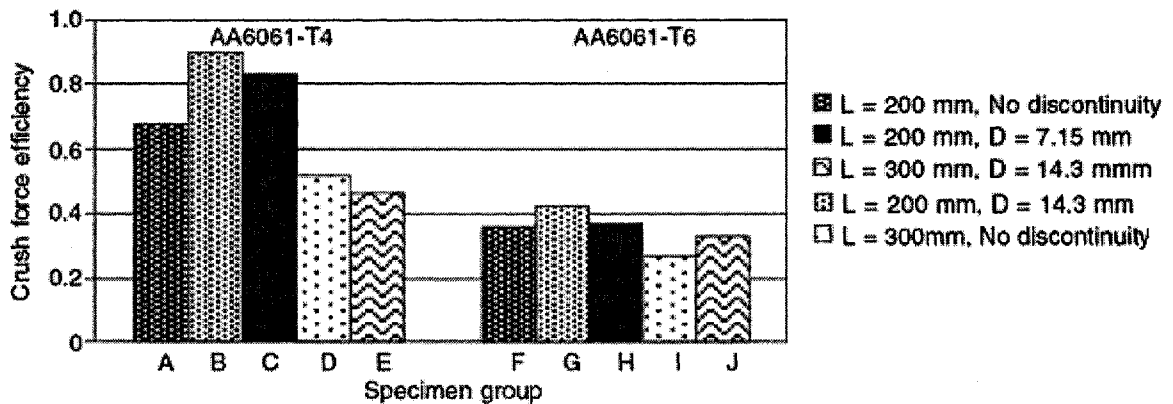


Figure 2.34. Crush force efficiency of the extrusions consider in the investigation [38].

Cheng et al. [39] studied influence of different shapes and sizes crush initiators on crush performance of AA6061-T6 square tubes. Three different types of geometrical discontinuities, namely, circular, slotted and elliptical holes and three different aspect ratios (1.33, 2.0 and 3.0) were fabricated into the center of the two opposite side walls of the extrusion as shown in Figure 2.35. The authors reported that a splitting and cutting deformation mode was generated by introducing crush initiators into the structural members where as global bending deformation which was observed for specimens without discontinuity which is demonstrated in Figure 2.36.

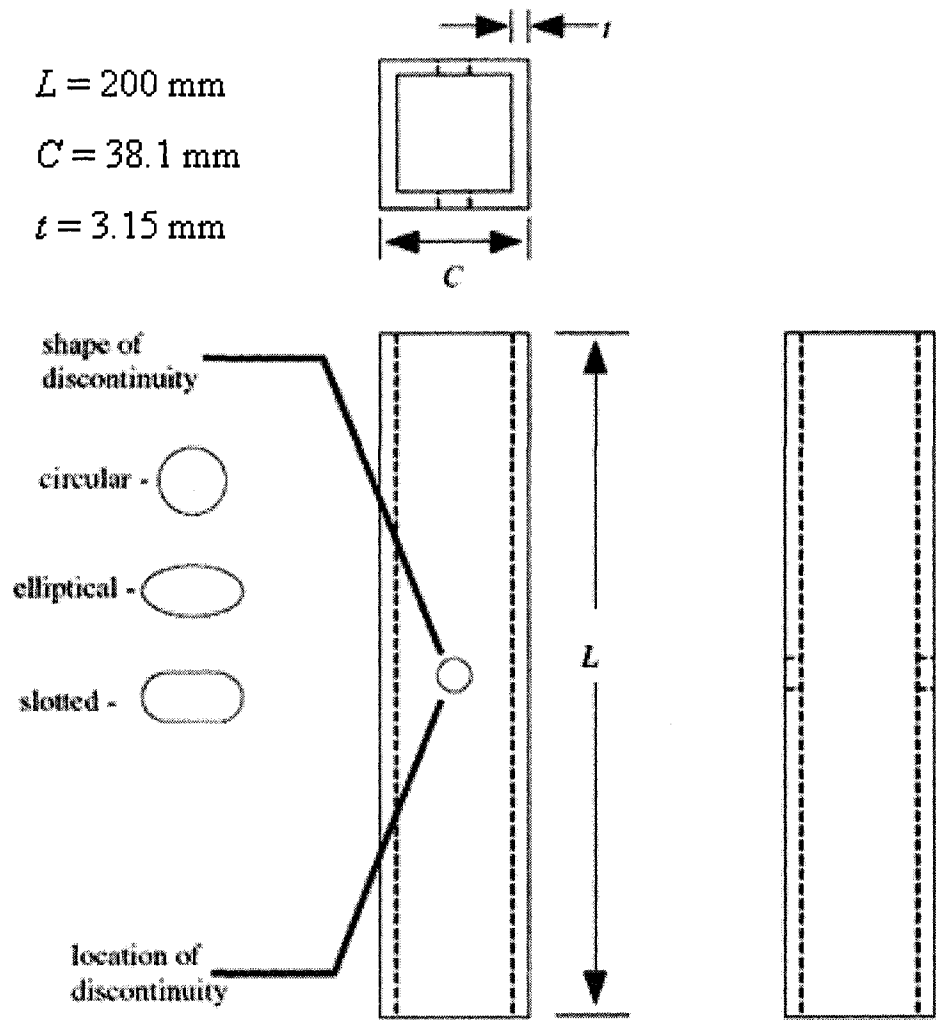


Figure 2.35. Geometry of the AA6061-T6 aluminum extrusion and discontinuities considered by Cheng at al. [39].

By incorporating the through hole crush initiators, the peak load was reduced within a range of 5.2% to 18.7% and total energy absorption was increased in the range of 26.6% to 74.7%. The most significant improvement was reported for crush force efficiency in the range of 54.5% to 95.8%. The peak crush load and total energy absorption was to be independent of initiator geometry and aspect ratio for the extrusions with major axis length of 7.14 mm. However, for specimens with a major axis length of 10.72 mm and 14.29 mm and aspect ratio of 3, a geometrical influence on the peak load and total energy absorption was apparent. Figure 2.37 illustrates the load-displacement profiles of extrusions with large elliptical discontinuity and different aspect ratios.



Figure 2.36. Photographs illustrating the crushing process from a representative group [39].

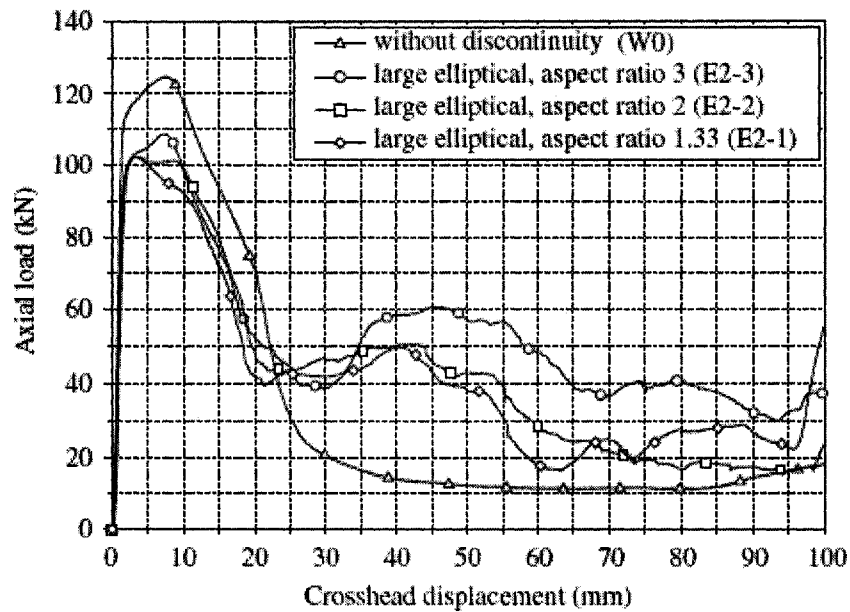


Figure 2.37. Comparison of load-displacement profiles of AA6061-T6 extrusions with elliptical discontinuity and without discontinuity [39].

The influence of cutouts on the energy absorption capabilities of circular aluminum and steel tubes under quasi-static and dynamic loading conditions was studied by Han et al. [40]. They conducted parametric studies on the influence of material properties, including yield and ultimate strength of material, strain rate effect, location of cutout, tube length and impact speed. They first developed a numerical model using LS-DYNA and subsequently, experimental tests were conducted to validate the numerical model. The energy absorption efficiency of both aluminum and steel tubes was improved when the cutout location was moved from mid-height to the top end.

2.4 Analytical models of the axial crushing

Analytical models are valuable for a quick estimation to the mean crushing force of extrusions during the design stages of a component. Simplified models for predicting axial crushing of thin-walled structures were developed by Ohkubo et al. [41], Wierzbicki [42] and Hayduk and Wierzbicki [43]. Abramowicz and Jones [1, 3] made comparisons between the theoretical predictions for the mean crushing loads of square tubes and experimental results. The theoretical analyses completed in references [1, 3] used quasi-inextensional and extensional collapse elements to describe the collapse behaviour of the tubes. These models gave a fairly good agreement with the experimental results.

Wierzbicki and Abramowicz [44] developed an analytical model for the axial progressive crushing of thin-walled rectangular column using the super folding element method. The expression for the average mean crush load was derived from the energy balance by equating the external work done by the crush load with energies dissipated in different types of deformation mechanisms as they occurred in a folding process. The mean crushing force P_m can be calculated by

$$P_m = 13.06\sigma_0 b^{1/3} t^{5/3} \quad (2.2)$$

where σ_0 denotes the flow stress of the section width, t is the wall thickness and b is the sectional width.

The half wavelength H for the folding deformation can be calculated by

$$H = 1.176b^{2/3} t^{1/3} \quad (2.3)$$

The flow stress σ_0 for material with power law hardening can be approximated by an energy equivalent stress [42]

$$\sigma_0 = \sqrt{\frac{\sigma_y \sigma_u}{1+n}} \quad (2.4)$$

where σ_y and σ_u denote the yield stress and the ultimate tensile stress of the material, respectively, n is the exponent of the power law constitutive model.

Abramowicz and Jones [4] developed analytical models to analyze the behaviour of tubes as they collapse in each of the three progressive collapse modes discussed in section 2.1.1. The procedure for analyzing the symmetric collapse mode involved a basic collapse element as shown in Figure 2.38. The variables illustrated in Figure 2.38 include

H , being half the initial length of the folding element, α , being the angle between the vertical axis and the walls of the element and C , being the mean width of a side wall.

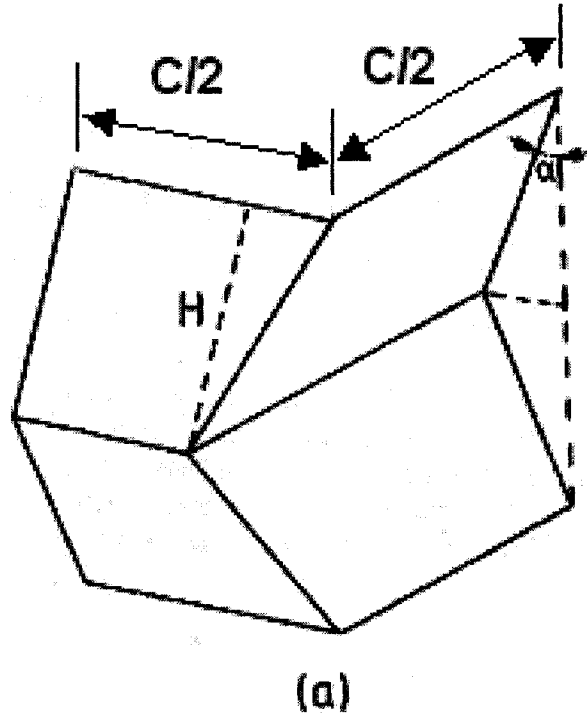


Figure 2.38. Collapse element model used to analytically characterize the axial buckling of square tubes [4].

The symmetric crushing mode was modelled using four of the elements shown in Figure 2.38. The mean crushing force for each mode was obtained by equating the external work done by the applied force to the internal strain energy needed to form one complete layer of lobes, under the assumption of elastic/ perfectly plastic material behaviour. The mean crushing force (P_m) for the symmetric mode was found to be:

$$P_m = M_o 52.22 \left(\frac{C}{H} \right)^{\frac{1}{3}} \quad (2.5)$$

where,

$$M_o = \sigma_o H^2 / 4 \quad (2.6)$$

here σ_o is the plastic flow stress.

Abramowicz and Jones also developed the following relation for the effective crushing distance for one complete fold:

$$\delta_1 = 0.73(2H) \quad (2.7)$$

Equation 2.7 gives the axial length of one fold formed in a square tube undergoing the progressive symmetric collapse mode.

Singace [5] also presented an analytical model to examine the collapse of tubes in the formation of multi-lobes and to evaluate the crushing load using the eccentricity factor. The analysis produced a distinctive value for the eccentricity factor that simplifies the expression for the mean collapse load, which is a function of tube geometry and number of lobes. He verified the analytical model with the experimental results that were discussed in section 2.1.1. Equation 2.8 represents the normalized crushing load as a function of the number of lobes as well as tube geometry.

$$\frac{P_m}{M_p} \cong -\frac{\pi}{3}N + \frac{4\pi^2}{N} \tan\left(\frac{\pi}{2N}\right) \frac{R}{t} \quad (2.8)$$

where

$$M_p = \frac{\sigma_y t^2}{2\sqrt{3}} \quad (2.9)$$

Here, σ_y is the material yield strength, R is the mean radius of the tube, t is the wall thickness and N represents the number of triangular folds.

In addition to axial crushing, analytical models to predict cutting force, which is an important aspect of this study, were also developed by various researchers. Zheng and Wierzbicki [23] developed a simple and realistic model of steady state cutting of a wedge through a steel plate and derived a closed form solution for the cutting force by applying the upper bound theorem of plasticity. They identified three different failure modes. Photographs in Figure 2.39 illustrate all three failure modes observed during plate cutting process.

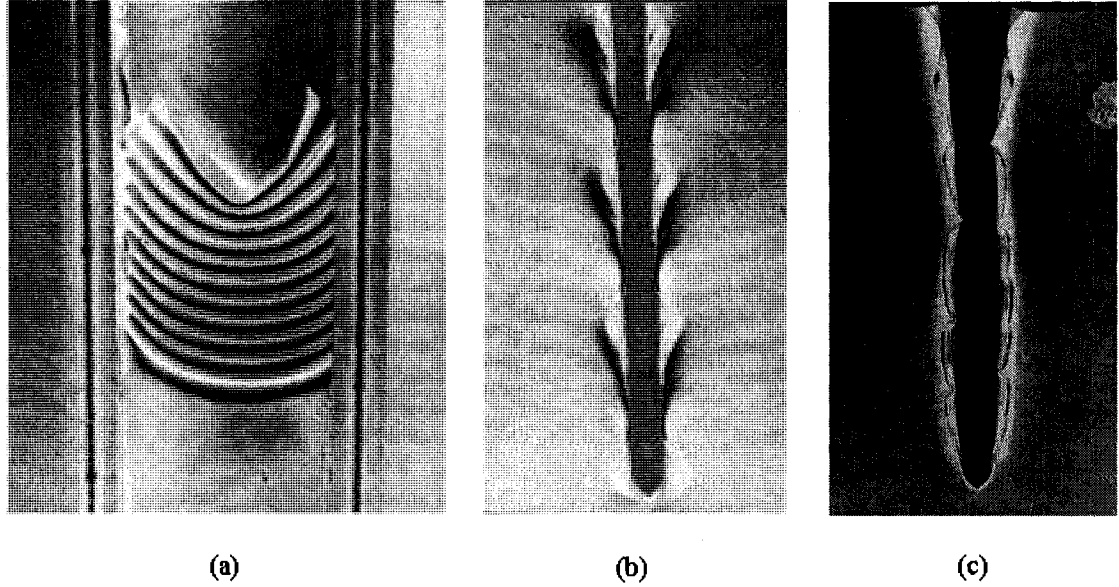


Figure 2.39. Photographs of different failure modes. (a) Concertina tearing failure by a blunt wedge, (b) Braided tearing of a plate by a narrow wedge and (c) Center 'clean cut' of a plate by a sharp wedge with stable flap buckled [23].

The steady-state wedge cutting force of steel plate was given by:

$$F = \left(1.268 \frac{R}{t} \cos \theta \frac{\sigma_0 t^2}{4} + 2 \frac{R+B}{R} \frac{\sigma_0 t^2}{4} + 1.28 \theta^2 \frac{(R+B)^2}{Rt} \cos(\theta/2) \frac{\sigma_0 t^2}{4} \right) \cdot (1 + \mu \cot \theta) \quad (2.10)$$

where R is the rolling radius expressed in equation (2.11),

$$R = B \sqrt{\frac{2(t/B) + 1.28 \theta^2 \cos(\theta/2)}{1.268 \cos \theta + 1.28 \theta^2 \cos(\theta/2)}} \quad (2.11)$$

In equation (2.10), B is one-half of the wedge shoulder width, σ_0 is the flow stress, t is the plate thickness and θ is the half wedge semi-angle.

Simonsen and Wierzbicki [24] presented a closed form solution to the problem of steady-state wedge cutting through ductile metal plate. This new kinematic model greatly simplified the analysis of strain and displacement fields. The mechanics of the cutting process is complicated and involves plastic flow of the plate in the vicinity of the wedge tip, friction between the wedge and plate, membrane deformation of the plate and large

scale bending of the plate flaps. The resistance force during steady-state cutting process was found to be

$$F = \left(\frac{0.64}{\sqrt{3}} \sigma_0 t R \cos^2 \theta (1 + 0.55\theta^2) + \frac{\sigma_0 t^2 (B + R)}{\sqrt{3} R \cos \theta} + \frac{2}{\sqrt{3}} \sigma_0 t B \theta \right) \cdot \left(1 - \frac{\mu}{\sin \theta + \mu \cos \theta \cos(\theta/2)} \right)^{-1} \quad (2.12)$$

where the roll radius R determined through equation (2.12)

$$R = \sqrt{\frac{Bt}{0.64(1 + 0.55\theta^2) \cos^3 \theta}} \quad (2.13)$$

2.5 Finite element modeling of the axial crushing of thin-walled tubes

Computational mechanics is an important tool in the assessment of the crash behaviour of individual structural components as well as the complete structure. All manufacturers today employ numerical simulations as a support in their design process in order to reduce the number of prototype testing and to increase safety. Furthermore, numerical simulations enable new designs and materials to be evaluated without extensive testing and provide a framework for implementing new knowledge gained through experiments and improvement of theory of materials and structures. However, an essential ingredient in the development and use of numerical tools is the validation of the codes by comparison with precision tests [45].

The FE method subdivides a continuous body into finite size elements interconnected by nodal points on the element edges. Time integration techniques predict a real-life continuous phenomenon by approximating the displacement of nodes in the discrete body at finite time interval. The main five steps involved in non-linear FE analysis are model development, formulation of governing equations, discretization of equations, solution of equations and interpretation of results. There are a number of element formulation techniques available in commercial large deformation FE packages including, Lagrangian, Eulerian, Arbitrary Lagrangian-Eulerian (ALE), meshfree Lagrangian (SPH) and element free Galerkin (EFG).

2.5.1 Lagrangian FE formulation

Lagrangian FE formulations are most common in the majority of numerical simulations employing the FE method. When a Lagrangian mesh undergoes deformation, the nodes of the mesh remain fixed to the material coordinate, therefore the Lagrangian mesh moves with the material.

Langseth et al. [46] numerically simulated the axial crushing of thin-walled square AA6060 aluminum alloy extrusions with T4 and T6 tempered conditions using non-linear finite element code LS-DYNA. The validation of the numerical model was accomplished through experimentation of the similar event used in the numerical study. Due to symmetry observed in experimental testing, only one quarter of the specimens was modeled using the Belytschko-Lin-Tsay shell element with nine integration points through the thickness and one point in the plane of the elements. The initial imperfections were represented by a trigger at the top or at mid-section to initiate a symmetric deformation mode. A total of 2500 elements were utilized in the quarter model with an element size of 3 x 3 mm. A specimen length of 310 mm was used in the numerical simulation as shown in Figure 2.40. A rigid block modelled with brick elements was used to apply the load at the upper end of the specimen. Full boundary constraints were prescribed at the bottom of the specimen and rotational degrees of freedom were fixed at the upper end of the specimens to avoid unrealistic deformation modes. A material model (*MAT 103 within LS-DYNA) developed by Berstad et al. [47] was utilized for the extrusion model. This material model uses isotropic elastic plastic behaviour, the von-Mises yield criterion, associated flow rule and non-linear isotropic hardening. The contact between the rigid block and the extrusion was modelled using a node-to-surface contact algorithm with a friction coefficient of 0.25. To account for the contact between the lobes during deformation, a single surface contact algorithm without friction was prescribed. The analyses were performed using 125000 time-steps for a period of 25 s with a maximum displacement of 250 mm, giving a deformation velocity of 10 mm/s.

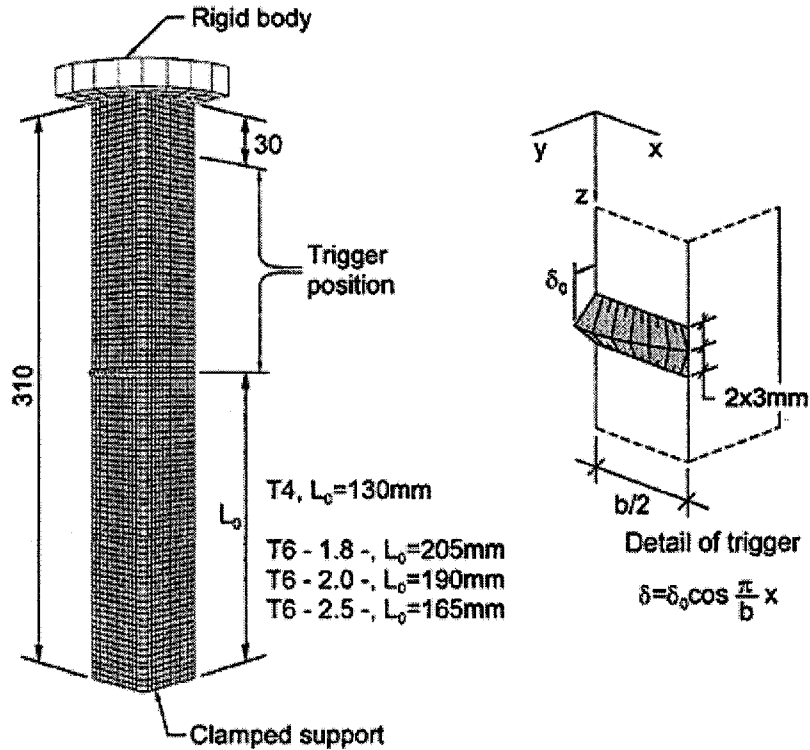


Figure 2.40. One quarter finite element model of 6060 aluminum alloy extrusions including trigger position [46].

The quasi-static simulation results from numerical modeling of axial crushing of aluminum alloy extrusions correlated well with the experimental results of reference [4]. The numerical results showed that six lobes were formed in the model with the T4 tempered condition while seven lobes were formed in the model with the T6 tempered condition, which were inline with experimental findings. The peak load and the mean load as a function of the axial displacement from numerical simulations were predicted within 10% of the experimental data. Furthermore, the study of influence of using mass scaling in numerical simulation of axial buckling showed an increased mass of the tube will increase the initial buckling load as well as the mean load level during axial deformation.

In another study, Hanssen et al. [48] validated material models for aluminum foams and extrusions for creating FE models of foam-filled extrusions. In order to take into account the ductile failure of the extrusions, material model 104 in LS-DYNA was used. This model incorporates damage mechanics to model ductile failure. When used for simulating the axial crushing of foam-filled extrusions, they found that the model

effectively predicted the rupture of the extrusion, but contributed to an under prediction of the mean crushing load.

Yamazaki and Han [49] used the non-linear FE code LS-DYNA to study the dynamic axial crushing of square tubes. Four different tube geometries, all with a constant mass of 0.53 kg were considered in the study. Three of the four tubes were modelled using 4-node shell elements and the remaining tube with relatively thick wall thickness was modelled using 8-node brick elements. Crush initiators were incorporated into the tube model by moving one node out of its side-wall plane by a magnitude of 1% of the wall thickness. In order to provide enough kinetic energy to crush the tube, a concentrated mass equal to 500 times the mass of the tubes was attached to the non-impacted end of the tube model. The tube was prescribed an initial velocity of 10 m/s to impact onto the rigid wall. The material model used by Yamazaki and Han had employed the von Mises yield criterion and assumed bi-linear stress-strain characteristics; failure was not modeled. The collapse modes observed in this numerical study are in good agreement with the theoretical and empirical predictions of reference [27] for progressive buckling and global bending. Han and Yamazaki [50] expanded study on this by considering square extrusions with axial “stiffeners”, which were strips added to each side wall in the direction orthogonal to the side wall. The modelling techniques used in [50] were similar to those used in [49].

Mamalis et al. [51] implemented the explicit FE code LS-DYNA to simulate the crush behaviour and energy absorption characteristics of steel thin-walled tubes of octagonal cross section subjected to axial loading. The tube was modeled using 4-node shell elements (Belytschko-Tsai shell element) with three integration points through thickness. Penalty based nodes to surface contact algorithm was prescribed between nodes of tube and nodes of the base. The single surface type of interface was selected to simulate the situation during the collapse, when elements of the tube wall contact each other creating a new interface. An isotropic elastic-plastic material, characterized by a bi-linear elastoplastic behaviour with strain hardening, was introduced to the model. The collapse procedure was successfully simulated and the simulation results were found to be in good agreement with experimental observations.

Arnold and Altenhof [32] further developed a numerical model to study the influence of circular discontinuities and material properties on axial crush behaviour of aluminum alloy extrusions under quasi-static loading situation. Only one quarter of the extrusion was modelled using solid and shell elements due to symmetry observed in experimental testing. The discretization of the extrusion was carried out using the parametric mesh generation software TrueGrid. As shown in Figure 2.41, the mesh density was finer in the region of the structure surrounding the circular hole discontinuity to accurately capture the stress distribution resulting from stress concentration due to the presence of discontinuity. Four elements through the thickness of the tube were utilized. The axial crushing process of the absorber specimens was modeled by prescribing a constant velocity of 2 m/s to the rigid plate in the axial direction of the tube (the negative Z-direction in Figure 2.41). Contact was modeled between the rigid plate and the extrusion using a surface-to-surface contact algorithm available in LS-DYNA. Contact between the walls of the tube was implemented using a single-surface contact algorithm. Material model 105 in LS-DYNA was used to model the extrusion tube materials. This material model allows the direct input of the true stress versus true plastic strain data in the form of a piecewise linear curve. During the simulation, LS-DYNA performs a curve fit of the data and determines the strain hardening properties. This material model also allows the implementation of failure mechanism. An iterative calibration process was capable to determine the numerical failure parameters D_c and S .

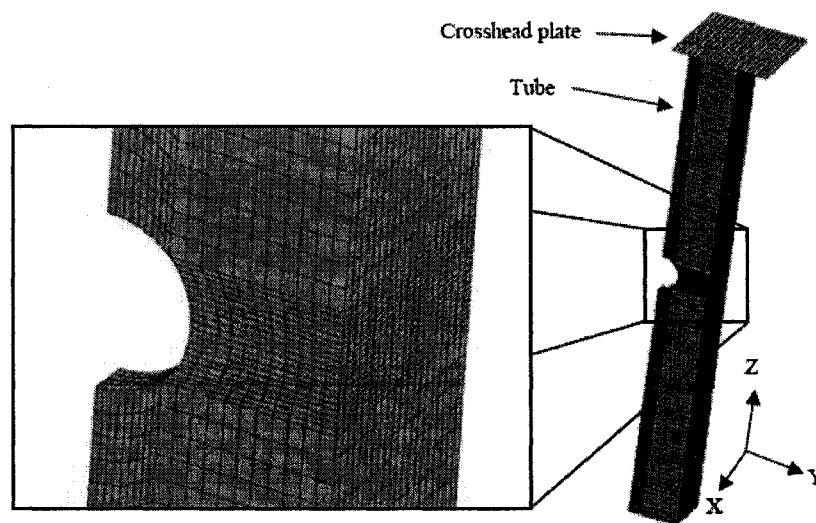
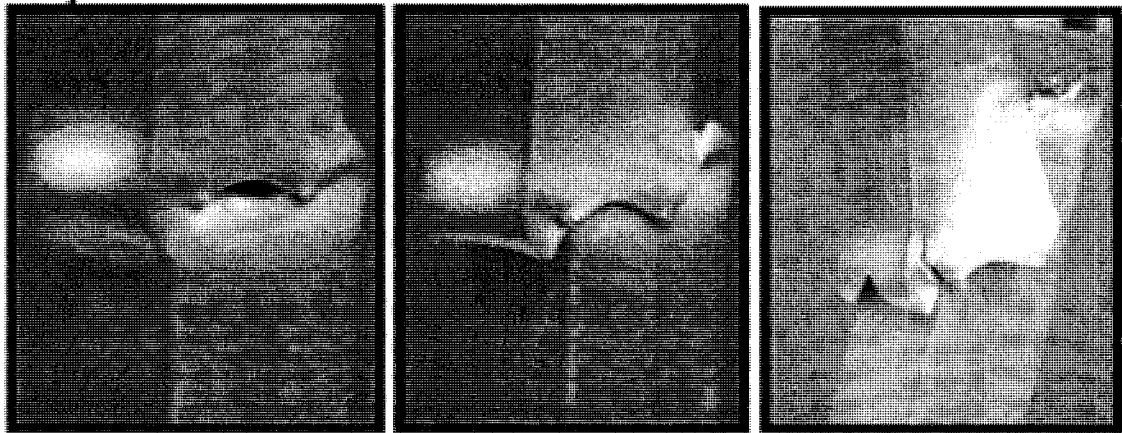


Figure 2.41. Discretization of specimens ($L = 200$ mm, $D = 14.2$ mm, $t = 3.15$ mm). The inset shows a detail of the discretization of the circular hole discontinuity region [32].

A good correlation was observed between the results of FE simulations and the results of quasi-static crush testing of extrusion absorber structures. Material model 105 in LS-DYNA, which incorporates non-linear plasticity and employs damage mechanics theory, successfully predicted the cracking and complex splitting collapse modes that were observed in experimental testing of the AA6061-T6 and AA6063-T5 tube specimens as shown in Figure 2.42 and Figure 2.43 respectively.

Experimental:

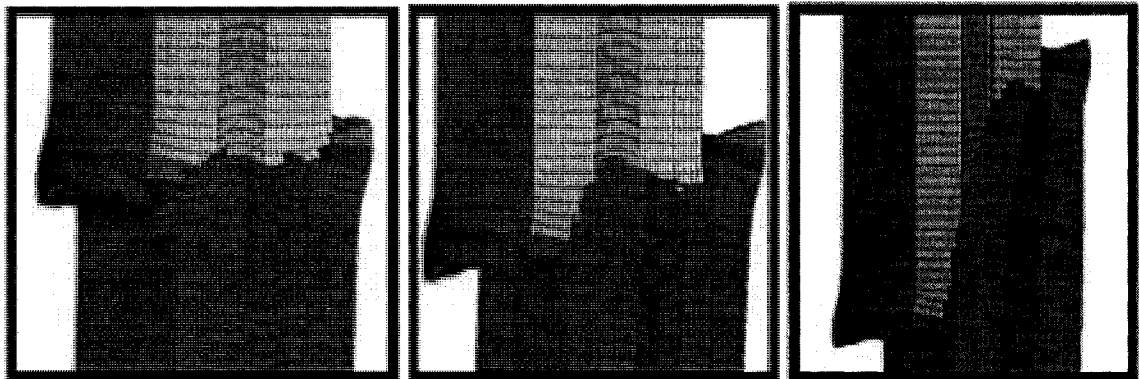


a) $\delta=9\text{mm}$

b) $\delta=19\text{mm}$

d) $\delta=55\text{mm}$

Numerical:



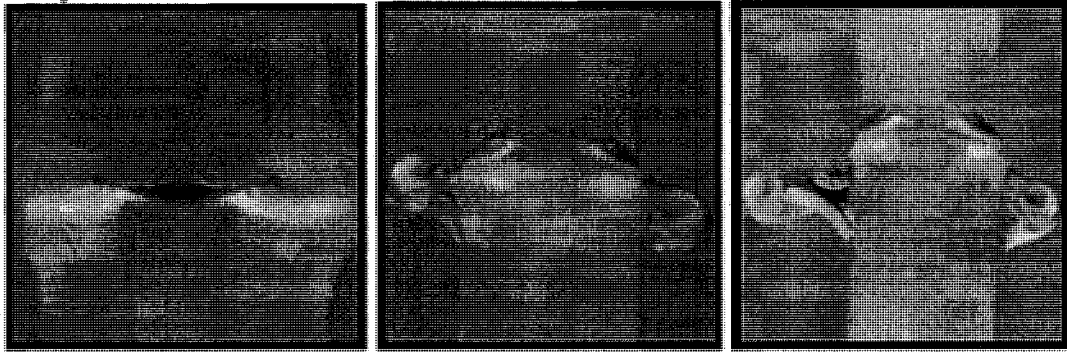
e) $\delta=9\text{mm}$

f) $\delta=19\text{mm}$

(h) $\delta = 54\text{mm}$

Figure 2.42. Experimental and numerical crushing process for 6061-T6 extrusions [32].

Experimental:

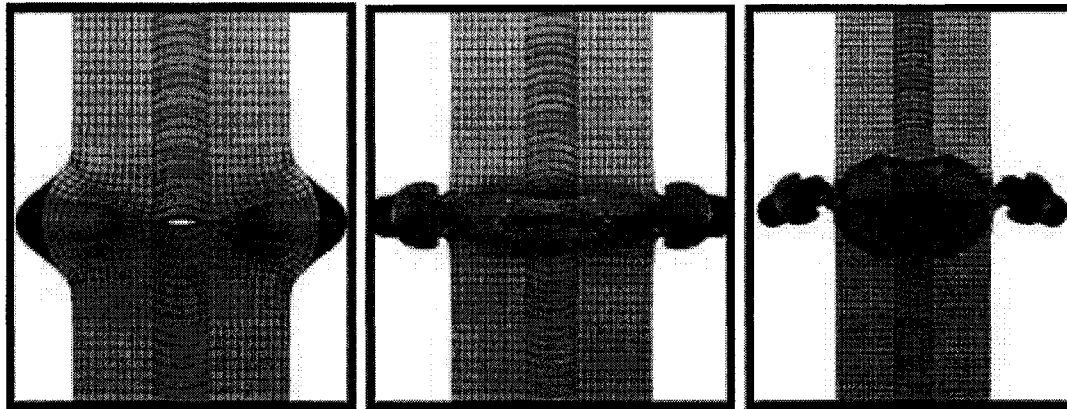


a) $\delta=14.0\text{mm}$

b) $\delta=35.0\text{mm}$

c) $\delta=47.0\text{mm}$

Numerical:



e) $\delta=14.0\text{mm}$

f) $\delta=35.0\text{mm}$

g) $\delta=47.0\text{mm}$

Figure 2.43. Experimental and numerical crushing process for 6063-T5 extrusions [32].

2.5.2 Eulerian or arbitrary Lagrangian/Eulerian (ALE) element formulations

In the Eulerian element formulation the material coordinates and spatial coordinates of the FE mesh are disassociated and the material moves through the FE mesh. In the explicit time integration scheme, during every cycle (time step) of the simulation each Eulerian element completes a Lagrangian analysis, however, prior to the next cycle the spatial coordinates of the FE mesh is remapped to its original position in a process referred to as advection. While the FE mesh is remapped to its original position, the material coordinates are not and will move through the FE mesh. Therefore, an airmesh must surround the original material location of the extrusion material for evaluation of the deformed material state. At the start of the simulation, the airmesh

contains no material and its only purpose is to accommodate deformed material. Special care must be taken to model the airmesh large enough to provide space around the workpiece for any possible material flow.

Jin and Altenhof [52] numerically studied crush characteristics of AA6061-T6 round tubes during a cutting deformation utilizing an Eulerian element formulation. Due to the symmetry observed in the experimental quasi-static cutting process of the extrusions, only one quarter of the tubular specimen and one corresponding cutter blade were considered in the FE model. Eight-noded solid elements were utilized for the tubular extrusion and the airmesh. A single point quadrature Eulerian element was selected for both entities. As shown in Figure 2.44, the mesh density of the tube in the vicinity of the region of contact between the cutter and extrusion was finer than all other regions. Belytschko-Tsay shell elements employing a rigid material model were used to model the cutter blade. Contact between the Eulerian extrusion and airmesh and the Lagrangian FE cutter blade was completed through Eulerian/Lagrangian coupling by employing a single `CONSTRAINED_LAGRANGE_IN_SOLID` contact definition available within LS-DYNA. A hydrodynamic material model (referred to as `MAT_ELASTIC_PLASTIC_HYDRO` within LS-DYNA) was selected for the extrusion and airmesh. A rigid material definition was applied to the cutter. At the lower end of the extrusion, full boundary constraints were applied to all nodes. To ensure symmetry, nodes lying in the symmetry planes of the tube were constrained to move only within the corresponding symmetry plane. The axial cutting process of the tubular specimens was modeled by prescribing a penetration of 35 mm in the axial direction in 5 ms, which is equivalent to an average axial cutting speed of 7 m/s. Load/displacement profiles presented in Figure 2.45 illustrated that the FE model predicted the transient and steady state cutting process well with an over prediction of approximately 20% of the experimental steady state constant cutting force. The authors indicated that the over prediction of the FE simulation observations were most likely a result of the lack of material failure consideration in the material model for the extrusion.

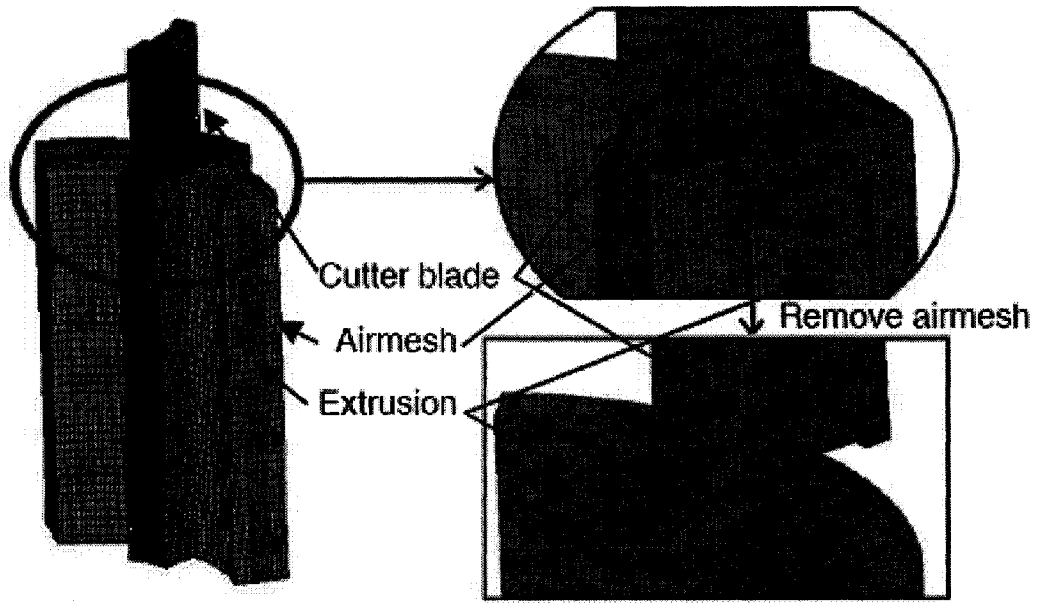


Figure 2.44. Discretization of the AA6061-T6 round tubular extrusions ($L=60$ mm, $D=50.8$ mm, $t=3.175$ mm), the tube airmesh, and the cutter blade [52].

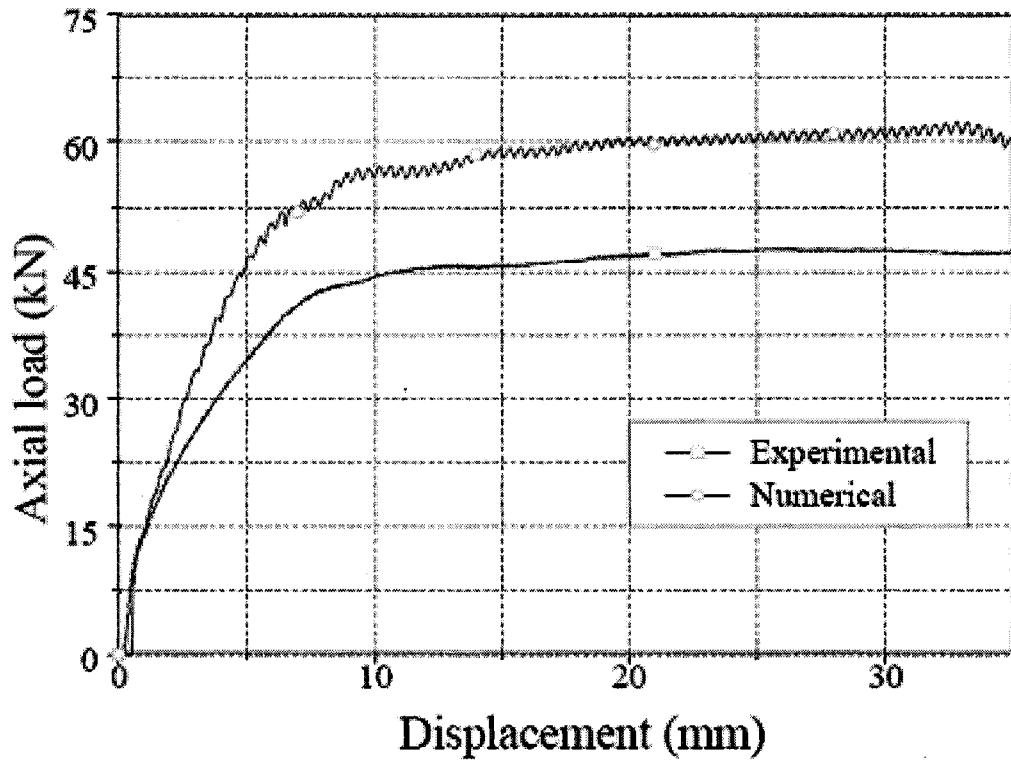


Figure 2.45. Load versus displacement observations from numerical and experimental testing procedures [52].

2.5.3 Smooth particle hydrodynamics (SPH)

Smoothed Particle Hydrodynamics is a mesh-free Lagrangian numerical technique, originally developed to simulate astrophysical problems by Lucy [53], Gingold and Monaghan [54], which is a possible alternative to numerical techniques currently used to analyze large deformation events. The technique has some special advantages over the traditional grid-based numerical methods, the most significant one among which is the adaptive nature of the SPH method. This adaptability of SPH is achieved at the very early stage of the field variable approximation that is performed at each time step based on a current local set of arbitrarily distributed particles. Because of this adaptive nature of the SPH approximation, the formulation of SPH is not affected by the arbitrariness of the particle distribution. Therefore, it can naturally handle problems with extremely large deformation. The basic steps of SPH method used in LS-DYNA are presented in Figure 2.46 [55]. The calculation cycle is similar to that for a classical FE computation except for the steps where a kernel approximation is used. Kernel approximations are used to compute forces from spatial derivatives of stresses and spatial derivatives of velocity are required to compute strain rates. In addition SPH requires a sort of the particles in order to locate current neighbouring particles (neighbours search).

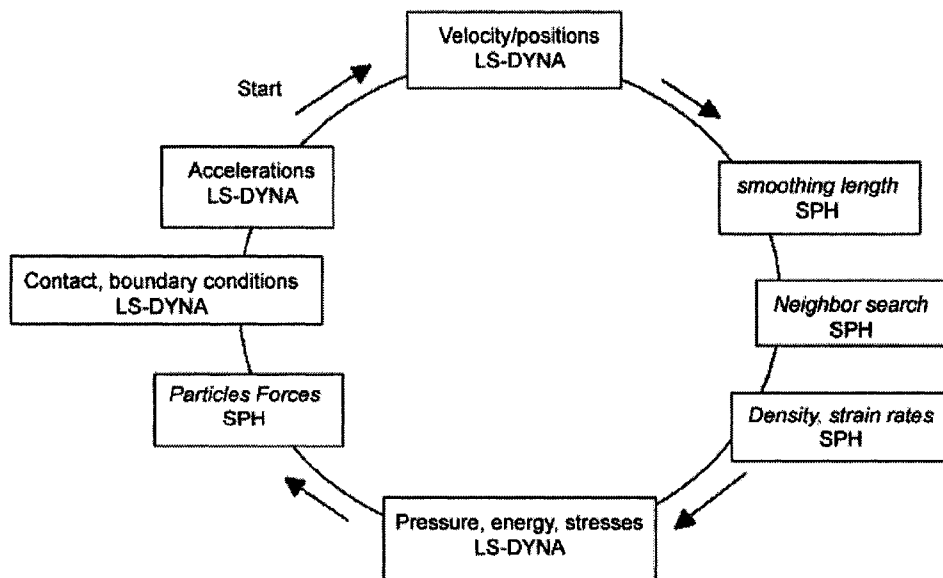


Figure 3.46. Computational cycle for SPH methodology in LS-DYNA [55].

Schwer [56] studied the impact of fragments on concrete wall utilizing Lagrangian, Eulerian and SPH formulations. The primary focus of this study was to perform a preliminary assessment of a relatively new class of numerical methods, referred to as mesh free methods, for ballistic problems and compare the results with traditionally used Lagrangian and Eulerian techniques. The modeled concrete panel was square with a span to thickness ratio of 3.33. The fragment was a 5.8 gram steel cylinder with a length to diameter ratio of 1.268 assumed to impact the center of the panel at 1068 m/s. Figure 2.47 shows a comparison of fragment velocity histories for the simulations including Lagrangian with erosion and no erosion, Eulerian and SPH techniques. The velocity history of the SPH simulations seemed to have an early time problem coupling with the rigid Lagrange fragment, however the SPH velocity history then tracks the velocity history of other three simulations until about 0.01 ms. After this time the SPH velocity history indicates the concrete material provides less resistance to penetrate than in the other simulations; the final depth of penetration was 38.6 mm which was greater than the values associated with other simulations. The author did not provide any explanation for this behaviour of SPH technique, however he indicated 'tensile instability' associated with SPH technique a possible reason.

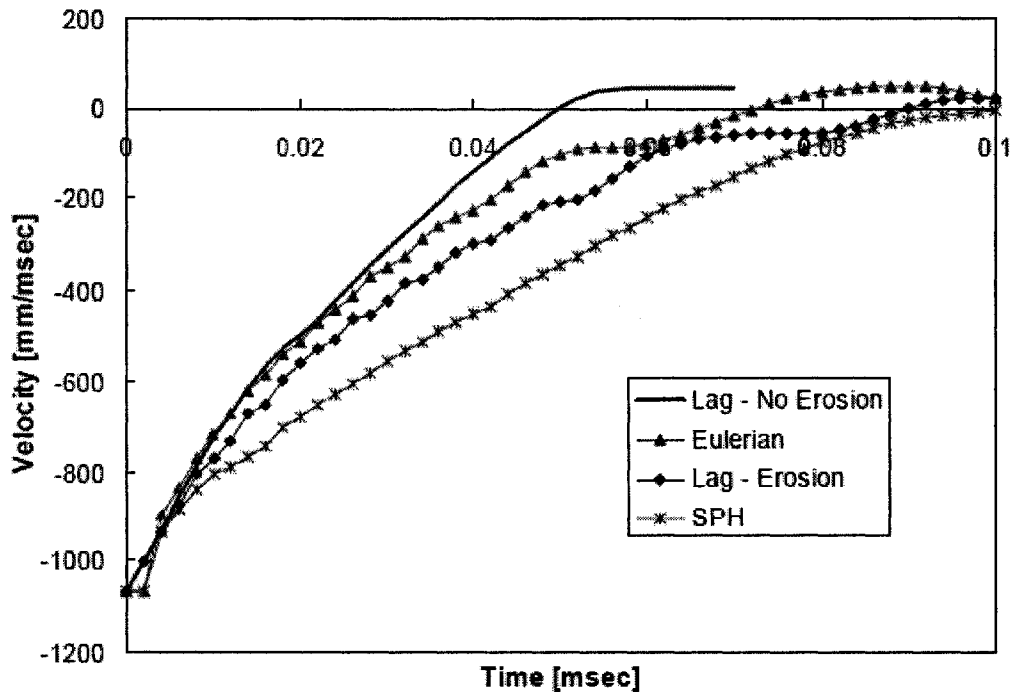


Figure 2.47. Velocity histories of the rigid fragments for four impact simulations [56].

In order to assess the possible application of SPH technique in ballistic impact applications, Schwer et al. [57] numerically investigated perforation of metal plates and compared with experimental findings. They found that the SPH analysis formulation worked well at velocities greater than the ballistic limit for the two plate thicknesses. However, the SPH analysis formulation results became suspect when there was significant bending and membrane stretching of the target plate, i.e. relative thin plates impacted at or below the ballistic limit. In this response range of the target plates, the SPH analysis techniques suffered from the so called 'tensile instability' and the simulated plate appeared to have less ballistic resistance than the corresponding experiment.

3. FOCUS OF RESEARCH

The reviewed literature indicated that the axial splitting or cutting modes provide exceptional load/displacement and energy absorption capabilities. A steady state splitting force can be achieved after an initial high transitional force in splitting mode. The cutting deformation mode was observed to be the best with respect to all crush parameters investigated in the literature. A constant load/displacement profile can be obtained after initial transition period and a CFE as high as 96% can be achieved under this deformation mode. However, these past investigations have only considered the T6 temper applied to the AA6061 alloy. No investigation considering a temper with significant work hardening has been completed. Additionally, only extrusion wall thickness of 3.175 mm has been considered. Although theoretical predictions indicate a non-linear relationship to the wall thickness, no experimental studies have been completed to validate these models. Consequently, this research will focus on these shortcomings. Specially, the following investigations will be detailed in this thesis:

1. Quasi-static axial cutting of AA6061-T4 and -T6 round extrusions with uniform wall thicknesses of 3.175 mm and 1.875 mm will be detailed. Additionally two different conical deflectors will also be utilized to control petalled side wall bending during cutting.
2. Experimental testing on similar aluminum alloy extrusions with both tempered conditions will be completed under progressive folding and global bending deformations modes to demonstrate the potential improvement in performance of the cutting deformation mode.
3. To control the load-displacement of response of AA6061 extrusions with both temper conditions, variations in the wall thickness along the axial direction of the extrusions will be detailed. Observations of the crush performance of these extrusions under cutting deformation will be provided.
4. Additionally, to control the load/displacement response during cutting two cutters positioned in series and spaced through a distance will be considered. Experimental cutting tests incorporating this configuration of cutters and

deflectors will be presented. The presence of a spacer slug between both cutters will be used to control the onset of the second cutting process.

5. FE models of the cutting deformation mode in the presence of cutters and deflectors will be developed and validated using the results of the experimental tests.

4. EXPERIMENTAL TESTING METHOD

The experimental testing considered in this research included the quasi-static axial crushing or cutting of AA6061-T4 and -T6 circular aluminum alloy extrusions. Extrusion wall thicknesses of 3.175 mm and 1.587 mm with a nominal external diameter of 50.8 mm and lengths ranging from 200 mm to 450 mm were utilized. Quasi-static axial cutting tests on extrusions with different wall thicknesses and tempered conditions were accomplished through employing of specially designed cutters, deflectors as well as spacers in between two cutters in the event of the dual stage cutting process. Specimens investigated under cutting deformation mode had lengths of 200 mm and 300 mm. An overview of the tensile testing of specimens extracted from the extrusion stock material completed by Arnold and Altenhof [38] is presented in this section as the material properties obtained from their tensile testing were used for FE simulations.

4.1 Overview of tensile testing of aluminum alloy extrusion

Tensile tests were performed to acquire material properties of 6061-T4 and -T6 stock aluminum alloy extrusions. Eight tensile specimens were extracted from the side walls of the square 3.175 mm thickness tube stock in the direction of extrusion for each temper of the AA6061 material. Although these extrusions are not those considered in the experimental part of this research, through a comparison of the engineering stress-strain response with tests conducted by other researchers [58] good agreement between the mechanical material behaviour was found. The tensile test specimens were prepared in accordance with ASTM standard E8M [59]. The tensile tests were performed according to ASTM standard E8M on an Instron tensile testing machine equipped with a 100 kN load cell. The elongation in the specimen was measured using an extensometer with a gauge length of 25.4 mm. The extensometer was fastened to the specimen in the centre region of the gauge using elastic bands. Figure 4.1 illustrates the arrangement of extensometer, tensile specimen and wedge grips of the testing machine. Data from the load cell and extensometer were acquired using a personal computer. Load and extension measurements were recorded at a sampling rate of 5 Hz. The tests were conducted using a constant crosshead speed of 5 mm/min at room temperature.

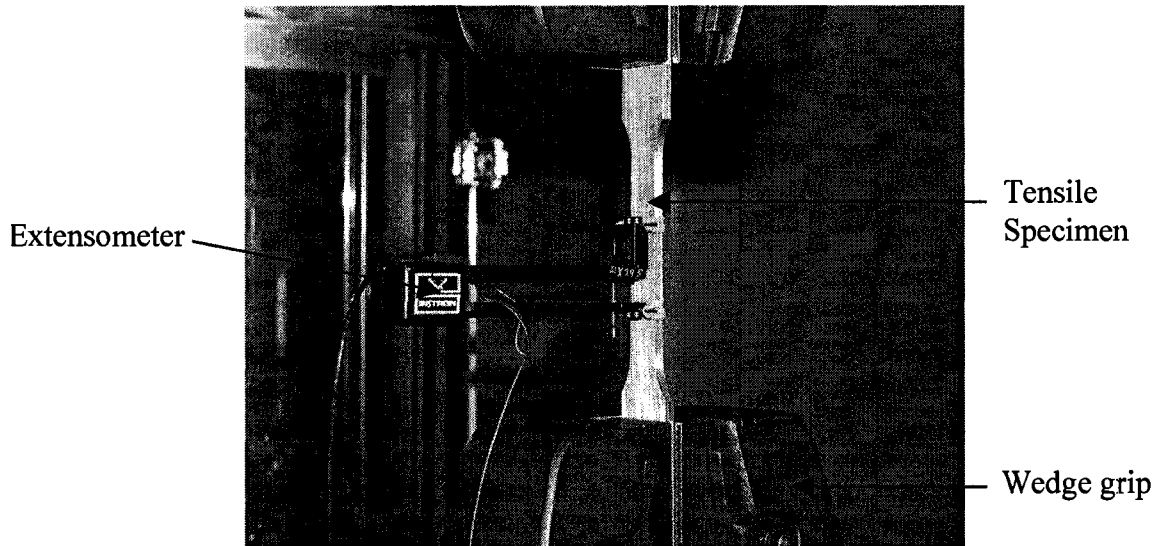


Figure 4.1. Arrangement of tensile test specimen, extensometer and wedge grips of the Instron tensile testing machine.

4.2 Quasi-static axial crush tests

The quasi-static axial crush tests were performed to evaluate the effect of uniform wall thickness and temper conditions on the deformation behaviour of aluminum extrusions. The specimens considered in this investigation were aluminum alloy AA6061-T4 and T6 round extrusions with a nominal external diameter (D) of 50.8 mm and wall thicknesses (t) of 3.175 mm as well as 1.875 mm. Figure 4.2 illustrates the geometry of the round extrusions. Length (L) of the extrusions with both temper conditions and 3.175 mm wall thickness were selected as 200 mm and 300 mm. However, the length of the extrusions with 1.587 mm wall thickness and both temper conditions were selected as 200 mm, 300mm, 400 mm and 450 mm. The extrusions for both wall thicknesses were selected under consideration of L/C and C/t ratios that resulted in a prediction of progressive folding and global bending deformation modes according to reference [30]. Although the extrusion stock material used in reference [30] (mild steel) is not consistent with the AA6061-T4 and -T6 extrusion material used in this investigation, it has been observed previously completed research [21, 22, 38] that the prediction of global bending and progressive folding deformation modes are generally consistent with the findings of reference [30].

4.2.1 Specimens preparation for axial crush tests

The stock aluminum alloy extrusions were received in the T6 tempered condition and in length of 6 m from the supplier. The stock lengths were cut down to the appropriate specimen lengths, making sure that the end faces were perpendicular to the axial direction of the absorber (i.e., that the specimens were square). The AA6061-T4 specimens were obtained through solution heat treating of AA6061-T6 tubes which were fabricated from the commercially obtained stock. To obtain the T4 condition, the specimens were placed in an oven at a temperature of 530°C for one hour and removed from the oven using steel tongs at the end of the heating period and immediately quenched in water at room temperature in accordance to ASTM standard B918 [60].

Test specimens were organized into twelve groups and three specimens were tested in each group. A summary of the extrusion geometries and tempers considered in this research is presented in Table 4.1. The identification system for each specimen in Table 4.1 follows the convention $R\alpha\text{-}\beta\text{-}\gamma\text{-}\mu\text{-}\xi\text{-}\delta$.

Where R indicates the extrusion had round cross-sectional geometry.

α indicates the length of the extrusion.

β represents the cutter side (for single cutter deformation) or the combination of cutter sides (for dual stage cutting). If progressive folding, global bending or a combination of both these modes existed 'P', 'G' or 'GP' are utilized.

γ represents the geometry of the deflector (DS for straight deflector and DC for curved deflector) if cutting deformation was imposed.

μ indicates the spacer geometries (10, 20 and 30) if dual stage cutting was performed utilizing spacers.

ξ represents the temper condition (either T4 or T6)

δ indicated whether the extrusion had a thinner wall ('tw' corresponding to a wall thickness of 1.587 mm) or wall thickness of 3.175 mm.

If any variable was not applicable to the deformation mode then the symbol 'xx' is used to indicate absence of this information.

It is important to note that the majority of the extrusions considering tempers and lengths at a wall thickness of 1.587 mm (as mentioned in Table 4.1) were selected in this study, as these combinations have not been considered in any previously completed research.

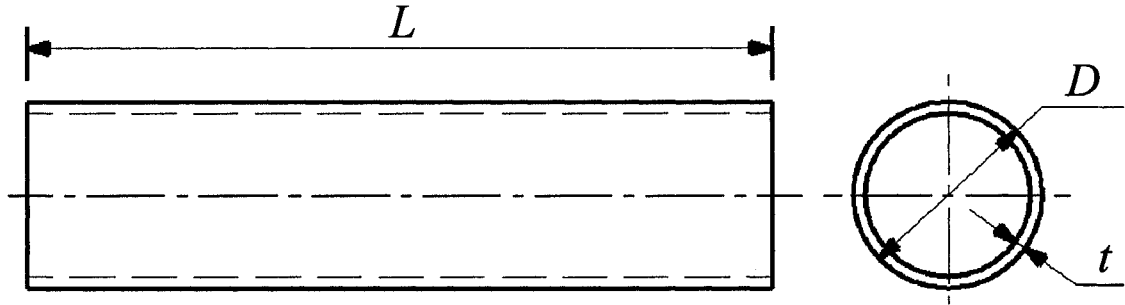


Figure 4.2. Geometry of AA6061-T4 and -T6 aluminum alloy extrusion specimens considered in this experimental test. L is the length of the extrusion specimen, D is the nominal external diameter of the specimen and t is the wall thickness of the specimen.

Table 4.1. Specimen geometry for AA6061-T4 and -T6 specimens considered for axial crush tests (all dimensions are in mm).

Group	Specimen ID	External Diameter D (mm)	Wall Thickness t (mm)
1	R200-P-xx-xx-T6	50.8	3.175
2	R300-G-xx-xx-T6	50.8	3.175
3	R200-P-xx-xx-T4	50.8	3.175
4	R300-G-xx-xx-T4	50.8	3.175
5	R200-P-xx-xx-T6-tw	50.8	1.587
6	R300-P-xx-xx-T6-tw	50.8	1.587
7	R400-GP-xx-xx-T6-tw	50.8	1.587
8	R450-P-xx-xx-T6-tw	50.8	1.587
9	R200-P-xx-xx-T4-tw	50.8	1.587
10	R300-P-xx-xx-T4-tw	50.8	1.587
11	R400-GP-xx-xx-T4-tw	50.8	1.587
12	R450-GP-xx-xx-T4-tw	50.8	1.587

4.2.2 Crush test methodology

Thirty-six quasi-static axial crushing tests for both tempers and thicknesses of the AA6061 extrusions were performed to evaluate the progressive folding and global

bending deformation modes. Axial compressive testing was performed using a hydraulic Tinius-Olsen compression testing machine. The specimens were placed with its extrusion direction parallel to the direction of crushing at the centre of the translating platen of the testing machine as shown in Figure 4.3. A fixed platen was located above the test specimen. The load cell used to determine the compressive force during crushing had a range of 150 kN. Displacement of the translating crosshead was measured using a linear voltage differential transformer (LVDT) with a range of 150 mm. A personal computer equipped with data acquisition software was used to record the measurements from the load cell and LVDT at a sampling rate of 60 Hz. The specimens were crushed at a constant crosshead speed of approximately 2.2 mm/s at room temperature, which was considered acceptable to evaluate the deformation behaviour as quasi-static [61]. It is generally accepted, and noted in reference [61], that dynamic loads applied at velocities on the order of 10 m/s or lower may be considered quasi-static. Furthermore, strain rate effects for the aluminum extrusions can be neglected, since it is well accepted that these alloys are considered strain rate insensitive [46].

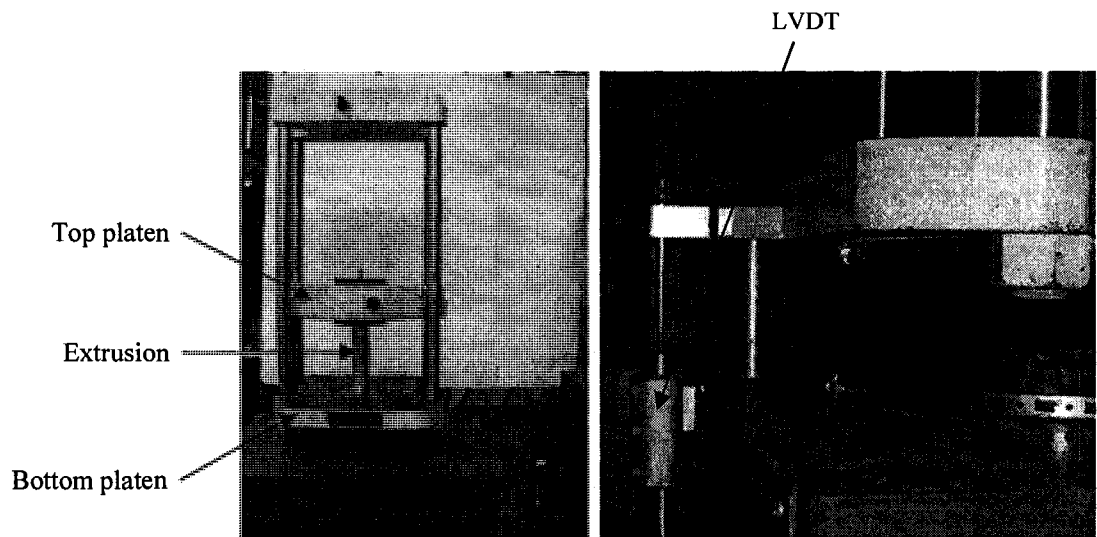


Figure 4.3. Arrangement of extrusion for axial crush test in Tinius-Olsen compression testing machine.

4.3 Quasi-static axial cutting tests

The aluminum alloy extrusions considered in the axial cutting tests were AA6061-T4 and -T6 circular tubes of lengths 200 mm and 300 mm. The extrusion

lengths of 200 mm and 300 mm were selected to minimize wastage of extrusions as energy absorption and the load/displacement characteristics of tubes under this deformation mode are independent of tube length [21]. The thicknesses of the extrusions were 3.175 mm and 1.587 mm as well as variable wall thicknesses machined from 3.175 mm wall thickness extrusions was utilized to investigate influence of wall thickness on the load/displacement profile. Specially designed cutters, identical to those used in references [21, 22], were employed. Two geometrically different conical deflectors in series with the cutters were used to control the bending of petalled side walls. Dual stage cutting, by placing two cutters in series with and without the presence deflectors, also utilizing separation between the cutters, through use of a spacer slug, was investigated.

4.3.1 Cutting tool design and manufacturing

As previously indicated the cutting tools used in this research are identical to those used in references [21, 22]. A brief overview of the manufacturing process is presented for the reader's interest. The cutting tools had four thin cutting blades. These blades were designed with widths that would initiate stresses in a tubular member that should exceed the ultimate stresses of both tempers of the AA6061 aluminum alloy without deformation or failure of the cutting blades. The geometry of one representative cutter is presented in Figure 4.4. The both cutting tools had an outside diameter of 101.6 mm and a thickness of 20 mm. Each cutter had four tapered blades 7 mm in length with a nominal blade shoulder width ($2 \cdot B$) of 3 mm. The blade tip width (T) was nominally 1.0 mm.

The cutters were machined on a computer numeric controlled (CNC) machining centre from AISI 4140 round bar stock followed by a two stage heat treatment process as detailed in reference [62]. In the first stage, the cutter was heated to 843°C and held at this temperature for one hour to ensure the completeness of the austenitic transformation. The second stage involved oil quenching to room temperature. Oil quenching provided a fast cooling rate to produce a martensitic structure. After hardening, tempering was completed at a temperature of 225°C for one hour to reduce residual stresses induced during quenching. The cutters were then cleaned using a sand blasting machine for removal of any film from the heat treatment process.

The hardness of the cutters after heat treatment, at the rim and centre locations, was determined and is listed in Table 4.2. The tip widths of the cutting blades, after manufacturing and heat treatment, were measured using a Vernier caliper. A summary of measured values of the tip widths for each blade is listed in Table 4.3.

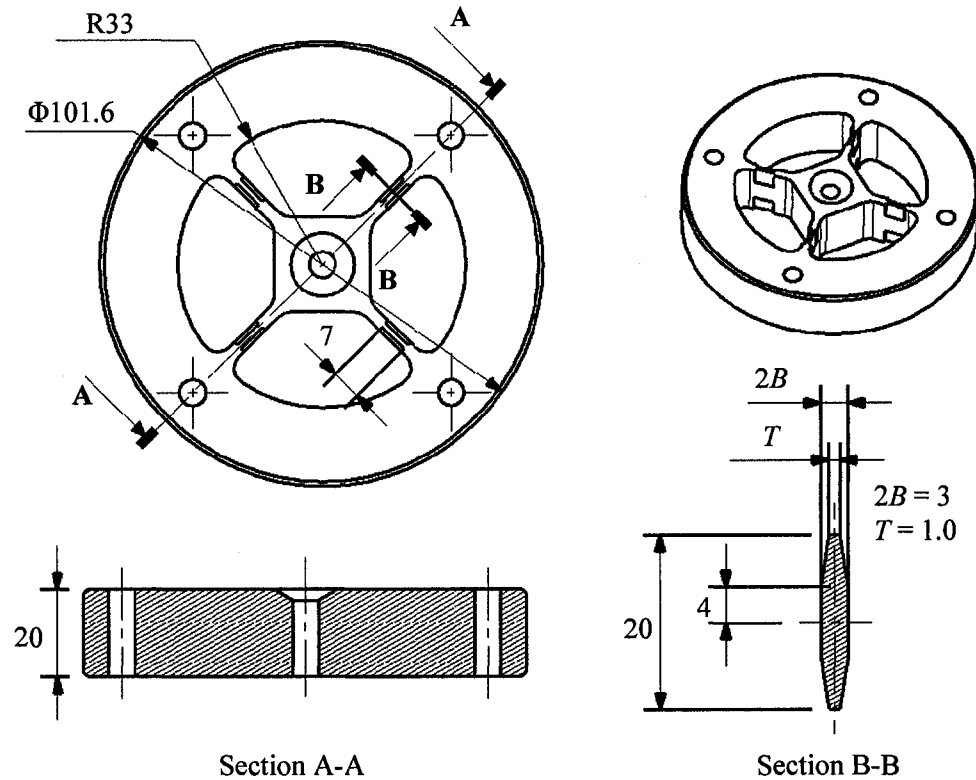


Figure 4.4. The geometry of a representative cutter.

Table 4.2. Cutters hardness after heat treatment (Rockwell 'C' scale).

Surface hardness	Rim	Centre
Cutter 1	54.0	54.7
Cutter 2	52.9	53.3

Table 4.3. Cutting blades tip width dimensions (mm).

	Blade 1	Blade 2	Blade 3	Blade 4	Average
Side A	0.87	1.2	0.81	1.14	1.01
Side B	1.11	0.87	1.14	0.87	1.00
Side C	1.27	1.08	1.24	1.08	1.17
Side D	1.09	0.97	1.06	0.96	1.02

4.3.2 Deflector design and manufacturing

The deflectors used in this research are identical to those used in references [25]. A brief overview of the manufacturing process is presented for the reader's interest. The deflectors had an outside diameter of 108 mm and a thickness of 50 mm. The straight deflector had a straight surface profile with an angle of 41.4° to the horizontal and the curved deflector had curved surface profile with a curvature radius of 50.8 mm as detailed in Figure 4.5.

The deflectors were machined on a computer numeric controlled (CNC) machining centre from AISI 4140 round bar stock followed by same two stage heat treatment process as described in section 4.3.1.

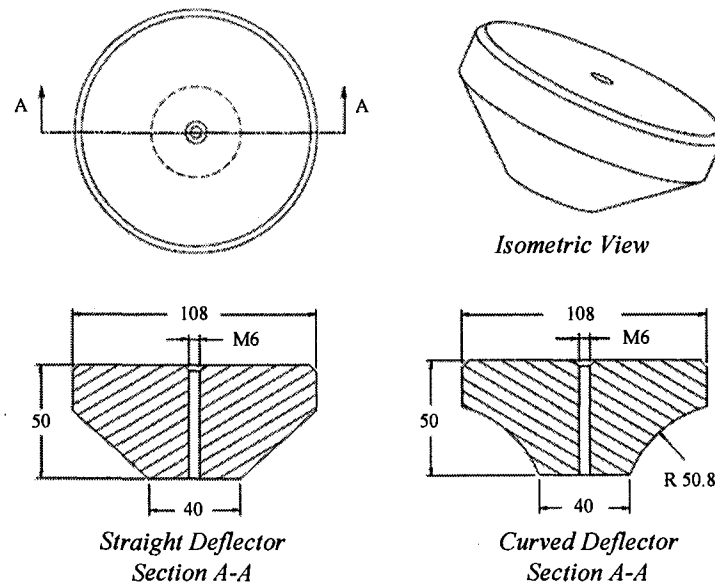


Figure 4.5. Geometry of the straight and curved deflectors (all dimensions are in mm).

4.3.3 Fabrication of spacers

Three different spacing geometries (L_{spacer}) of 10 mm, 20 mm and 30 mm investigated during the dual stage cutting tests. The geometry of a typical spacer is shown in Figure 4.6. The spacer slugs were machined on a CNC centre from an AISI 4140 solid circular shaft. The extended conical shaped edges at the centre of both ends of the spacers, matched with the centrally located grooves on both sides of cutter. These spacer geometries were used to minimize lateral shift of the cutters relative to each other.

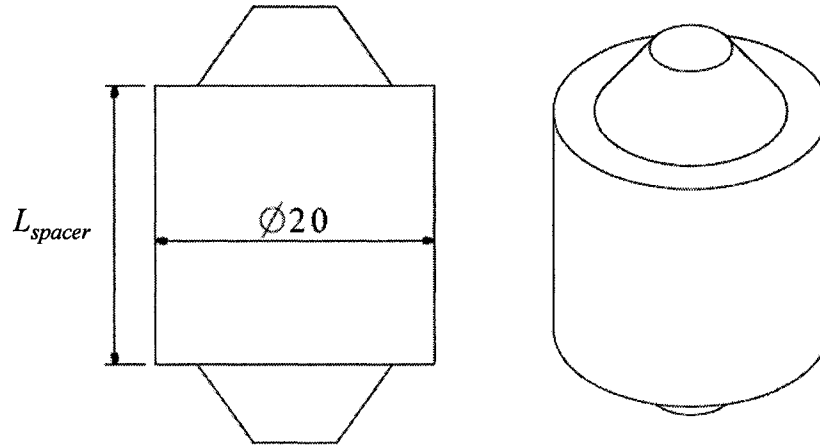


Figure 4.6. Geometry of the spacers

4.3.4 Test specimen preparation

The extrusion geometry and specimen grouping information were different for various experiments conducted to study the influence of tube geometry, extrusion temper and wall thickness on the load-displacement behaviour and crush performance of round aluminum alloy extrusions. The following sections detail the specimen grouping for a specific tests condition.

4.3.4.1 Cutting tests using only a single cutter

The specimens used in this testing condition were AA6061-T4 and -T6 round cross sectional extrusions with a nominal external diameter (D) of 50.8 mm, wall thicknesses (t) of 1.587 mm and 3.175 mm and various tube lengths (L). Figure 4.2 illustrates the critical dimensions D , t , and L of the round extrusions. Test specimens utilizing only the cutter during experiments were organized into eighteen groups and three specimens were tested in each group. Detailed specimen grouping information and extrusion geometries are presented in Table 4.4. The identification system for each specimen in Table 4.4 follows the similar convention mentioned in section 4.2.1.

Extrusion lengths considered were 200 mm and 300 mm for the 1.587 mm and 3.175 mm extrusion thicknesses respectively. Additionally, cutting deformation was imposed on 400 mm length extrusion with a wall thickness of 1.587 mm for both T4 and

T6 treated conditions. The 300 mm and 400 mm lengths were specifically selected to see if imposing cutting deformation would eliminate the global bending deformation mode. The 200 mm length was selected so as to reduce waste of material once it was understood that cutting of the extrusions eliminated global bending deformation. The AA6061-T4 specimens were obtained through similar solution heat treating of AA6061-T6 tubes detailed under section 4.2.1.

Table 4.4. Specimen grouping information and geometric dimensions using cutters.

Group	Specimen ID	External Diameter D (mm)	Wall Thickness t (mm)
c-1	R300-A-xx-xx-T4	50.8	3.175
c-2	R300-B-xx-xx-T4	50.8	3.175
c-3	R300-C-xx-xx-T4	50.8	3.175
c-4	R300-D-xx-xx-T4	50.8	3.175
c-5	R300-A-xx-xx-T6	50.8	3.175
c-6	R300-B-xx-xx-T6	50.8	3.175
c-7	R300-C-xx-xx-T6	50.8	3.175
c-8	R300-D-xx-xx-T6	50.8	3.175
c-9	R200-A-xx-xx-T4-tw	50.8	1.587
c-10	R200-B-xx-xx-T4-tw	50.8	1.587
c-11	R200-C-xx-xx-T4-tw	50.8	1.587
c-12	R200-D-xx-xx-T4-tw	50.8	1.587
c-13	R200-A-xx-xx-T6-tw	50.8	1.587
c-14	R200-B-xx-xx-T6-tw	50.8	1.587
c-15	R200-C-xx-xx-T6-tw	50.8	1.587
c-16	R200-D-xx-xx-T6-tw	50.8	1.587
c-17	R400-A-xx-xx-T4-tw	50.8	1.587
c-18	R400-A-xx-xx-T6-tw	50.8	1.587

In order to study the influence of the presence of the deflector during cutting, to control the cut petalled side walls deformation, a series of tests were performed with both geometries of deflectors. The test specimens were organized into thirty-two groups and three specimens were tested in each group. Identical extrusions used in experiments in presence of cutters only were selected in this study with a length of 200 mm. Extrusion of length 300 mm were not considered for the cutting deformation modes in presence of deflectors since the energy absorption and load/displacement characteristics of tubes

under this form of deformation was independent of tube length [21]. Specimen grouping information and extrusion geometries are presented in Table 4.5. The identification system for each specimen follows exactly the same convention indicated in section 4.2.1.

Table 4.5. Specimen grouping information and geometric dimensions in the presence of cutters and defectors.

Group	Specimen ID	External Diameter D (mm)	Wall Thickness t (mm)
d-1	R200-A-DS-xx-T6	50.8	3.175
d-2	R200-B-DS-xx-T6	50.8	3.175
d-3	R200-C-DS-xx-T6	50.8	3.175
d-4	R200-D-DS-xx-T6	50.8	3.175
d-5	R200-A-DC-xx-T6	50.8	3.175
d-6	R200-B-DC-xx-T6	50.8	3.175
d-7	R200-C-DC-xx-T6	50.8	3.175
d-8	R200-D-DC-xx-T6	50.8	3.175
d-9	R200-A-DS-xx-T4	50.8	3.175
d-10	R200-B-DS-xx-T4	50.8	3.175
d-11	R200-C-DS-xx-T4	50.8	3.175
d-12	R200-D-DS-xx-T4	50.8	3.175
d-13	R200-A-DC-xx-T4	50.8	3.175
d-14	R200-B-DC-xx-T4	50.8	3.175
d-15	R200-C-DC-xx-T4	50.8	3.175
d-16	R200-D-DC-xx-T4	50.8	3.175
d-17	R200-A-DS-xx-T6-tw	50.8	1.587
d-18	R200-B-DS-xx-T6-tw	50.8	1.587
d-19	R200-C-DS-xx-T6-tw	50.8	1.587
d-20	R200-D-DS-xx-T6-tw	50.8	1.587
d-21	R200-A-DC-xx-T6-tw	50.8	1.587
d-22	R200-B-DC-xx-T6-tw	50.8	1.587
d-23	R200-C-DC-xx-T6-tw	50.8	1.587
d-24	R200-D-DC-xx-T6-tw	50.8	1.587
d-25	R200-A-DS-xx-T4-tw	50.8	1.587
d-26	R200-B-DS-xx-T4-tw	50.8	1.587
d-27	R200-C-DS-xx-T4-tw	50.8	1.587
d-28	R200-D-DS-xx-T4-tw	50.8	1.587
d-29	R200-A-DC-xx-T4-tw	50.8	1.587
d-30	R200-B-DC-xx-T4-tw	50.8	1.587
d-31	R200-C-DC-xx-T4-tw	50.8	1.587
d-32	R200-D-DC-xx-T4-tw	50.8	1.587

4.3.4.2 Dual stage cutting in the presence of deflectors and spacers

In order to achieve higher cutting force, a two stage cutting process on the concentric extrusions was accomplished. The specimens utilized in these tests were identical with those used in section 4.3.4.1 and the geometries illustrated in Figure 4.2.

Specimens with wall thickness of 1.587 mm and 3.175 mm were organized into twenty-four groups for the dual stage cutting process. The detailed specimen grouping information and the extrusion geometries are presented in Table 4.6.

Table 4.6. Specimen grouping information and geometric dimensions for the dual stage cutting of AA6061 extrusions.

Group	Specimen ID	External Diameter D (mm)	Wall Thickness t (mm)
m-1	R200-AC-xx-xx-T6	50.8	3.175
m-2	R200-BD-xx-xx-T6	50.8	3.175
m-3	R200-CA-xx-xx-T6	50.8	3.175
m-4	R200-AC-DS-xx-T6	50.8	3.175
m-5	R200-BD-DS-xx-T6	50.8	3.175
m-6	R200-CA-DS-xx-T6	50.8	3.175
m-7	R200-AC-DC-xx-T6	50.8	3.175
m-8	R200-BD-DC-xx-T6	50.8	3.175
m-9	R200-CA-DC-xx-T6	50.8	3.175
m-10	R200-AC-xx-xx-T4	50.8	3.175
m-11	R200-AC-DS-xx-T4	50.8	3.175
m-12	R200-AC-DC-xx-T4	50.8	3.175
m-13	R200-AC-xx-xx-T6-tw	50.8	1.587
m-14	R200-BD-xx-xx-T6-tw	50.8	1.587
m-15	R200-CA-xx-xx-T6-tw	50.8	1.587
m-16	R200-AC-DS-xx-T6-tw	50.8	1.587
m-17	R200-BD-DS-xx-T6-tw	50.8	1.587
m-18	R200-CA-DS-xx-T6-tw	50.8	1.587
m-19	R200-AC-DC-xx-T6-tw	50.8	1.587
m-20	R200-BD-DC-xx-T6-tw	50.8	1.587
m-21	R200-CA-DC-xx-T6-tw	50.8	1.587
m-22	R200-BDtoPF-xx-xx-T4-tw	50.8	1.587
m-23	R200-BDtoPF-DS-xx-T4-tw	50.8	1.587
m-24	R200-BDtoPF-DC-xx-T4-tw	50.8	1.587

The specimens for dual stage cutting of the AA6061-T6 extrusions incorporating spacers were organized into seven groups and two specimens were tested within each group from s-1 to s-6. One specimen was tested within groups s-7 and s-8. The detailed specimen grouping information and the extrusion geometries are presented in Table 4.7.

Table 4.7. Specimen grouping information and geometric dimensions for the dual stage cutting with spacers.

Group	Specimen ID	External Diameter D (mm)	Wall Thickness t (mm)
s-1	R200-BD-xx-10-T6	50.8	3.175
s-2	R200-CA-xx-10-T6	50.8	3.175
s-3	R200-CA-xx-20-T6	50.8	3.175
s-4	R200-CA-xx-30-T6	50.8	3.175
s-5	R200-CA-DS-10-T6	50.8	3.175
s-6	R200-CA-DS-20-T6	50.8	3.175
s-7	R200-CA-DC-10-T6	50.8	3.175
s-8	R200-CA-DC-20-T6	50.8	3.175

4.3.4.3 Controlling the load/displacement response

To control the load-displacement response of AA6061 aluminum alloy extrusions with both temper conditions, variations in the wall thickness along the axial direction of the extrusions were considered by material removal through use of a CNC lathe with minimal material removal in the final cut of the specimen. The geometries of the machined specimens considered in this investigation are presented in Figure 4.7. The x -coordinate indicates the location and direction of initial cutting (in the axial direction) for all extrusions. Both stepped and tapered variations of the wall thickness profile along the length of the extrusion were considered. Figures 4.7(a) and 4.7(d) illustrate the stepped profiles while Figures 4.7(b), 4.7(c) and 4.7(e) illustrate the tapered sections considered in this investigation. All extrusions exhibited a final step profile to the nominal wall thickness at x equal to approximately 125 mm. Figure 4.7(e) indicates that a linear variation in wall thickness, with initial thicknesses of $t/4$, $t/2$, $3t/4$ and t , from the initial cutting location to 125 mm through the extrusion. The case where $W = t$ is

equivalent to a non-tapered tube. Extrusion wall thickness in the x direction was not always increased as indicated in Figure 4.7. However, careful selection of the minimum wall thickness, after a maximum thickness of t through the x direction and prior to $x=125$ mm, was necessary to ensure that the later reduced section did not switch deformation modes (to a local progressive folding mode in the later reduced section) during cutting. Test specimens were organized into five groups for each temper condition as presented in Figure 4.7. Two specimens were tested in groups a through d and one specimen was tested for each configuration in group e.

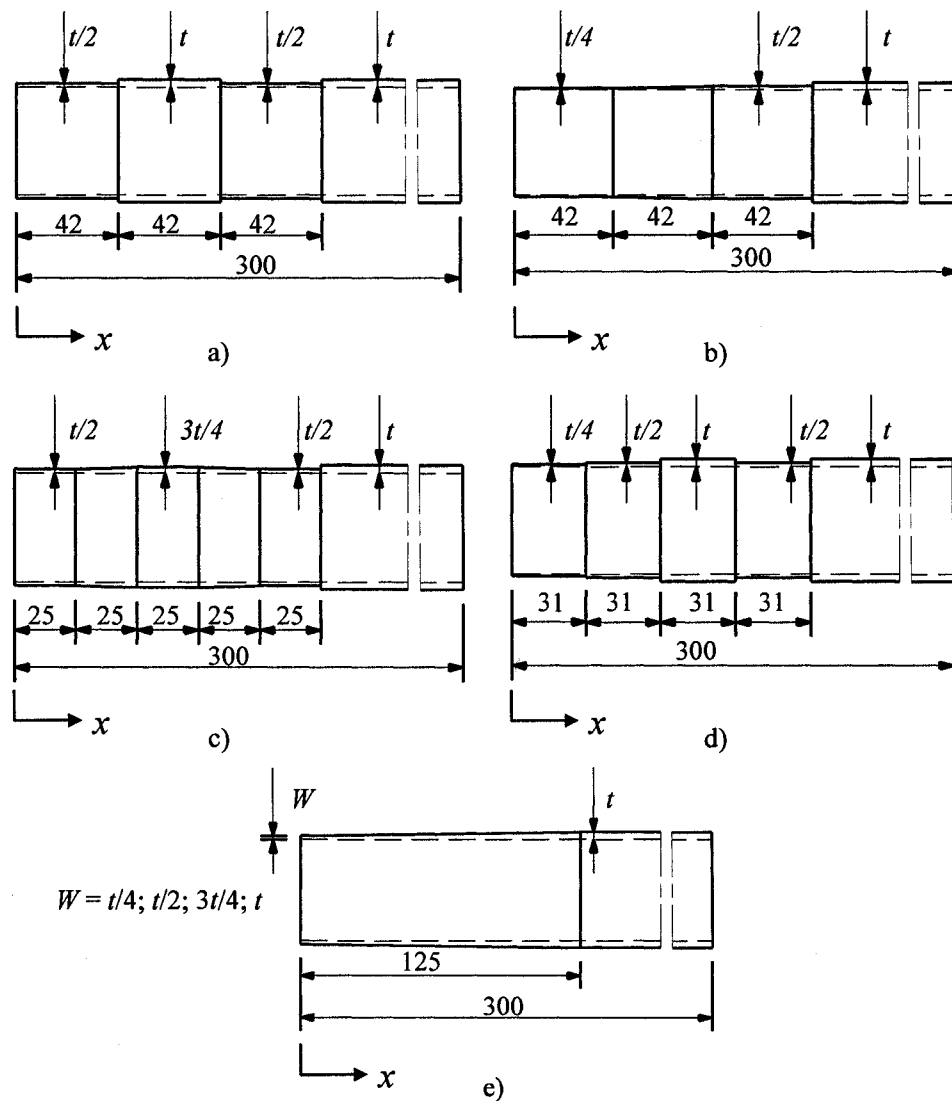


Figure 4.7. CNC finished geometries of AA6061-T6 round extrusion specimens under consideration in the experimental test. t is the original nominal wall thickness of the specimen 3.175mm (all dimensions in mm).

4.3.5 Cutting test methodology

All the quasi-static axial cutting tests were performed using a hydraulic Tinius-Olsen compression testing machine. The specimen was placed with its extrusion direction parallel to the direction of cutting at the centre of the fixture of the testing machine. For the tests employing only the cutter, manual placement of the cutter at the top end of the extrusion was completed prior to testing. A round steel rod with a diameter of 25.4 mm was manually placed on the top end of the cutter, and appropriately centred as illustrated in Figure 4.8 (a). This rod was used to push the cutter through the extrusion specimens.

The dual stage cutting process was accomplished by placing two cutters in series with careful alignment to be sure the blades of the top cutter lied in the mid-span of the two blades of the bottom cutter. The cutters were then manually placed at the top end of the extrusion with careful alignment to ensure that the cutter was centred to the specimen. A round steel rod with a diameter of 25.4 mm was manually placed on the top end of the cutter assembly, and appropriately centred as demonstrated in Figure 4.8 (b). The dual stage cutting process utilizing spacers was completed in the similar fashion as mentioned in dual stage cutting with the exception of spacers of different lengths were manually placed in between the two cutters.

In the event of the cutting tests utilizing both cutters and deflectors, the cutter(s) and the deflector were fastened together and the extrusion was manually placed on the cutter(s) with careful alignment. The deflector and cutter(s) along with the extrusion were placed at the centre of the bottom platen of the testing machine as shown in Figure 4.8 (c).

The load cell used to determine the compressive force during axial cutting had a range of 150 kN. Displacement of the translating crosshead was measured using a LVDT with a range of 150 mm. A personal computer equipped with data acquisition software was used to record the measurements from the load cell and LVDT at a sampling rate of 60 Hz for all the tests except tests for controlling load/displacement response detailed in section 4.3.4.3. For the tests of controlling load/displacement response, a personal (laptop) computer equipped with National Instruments Labview SignalExpress data acquisition software was used to record the measurements from a National Instruments

CompactDAQ data acquisition hardware systems using a voltage measurement module (NI 9215) which the two transducers were attached to. A data sampling rate of 30 Hz was used for all experimental tests. All the specimens were cut at a constant crosshead speed of approximately 2.2 mm/s at room temperature, which was considered acceptable to evaluate the deformation behaviour as quasi-static [61].

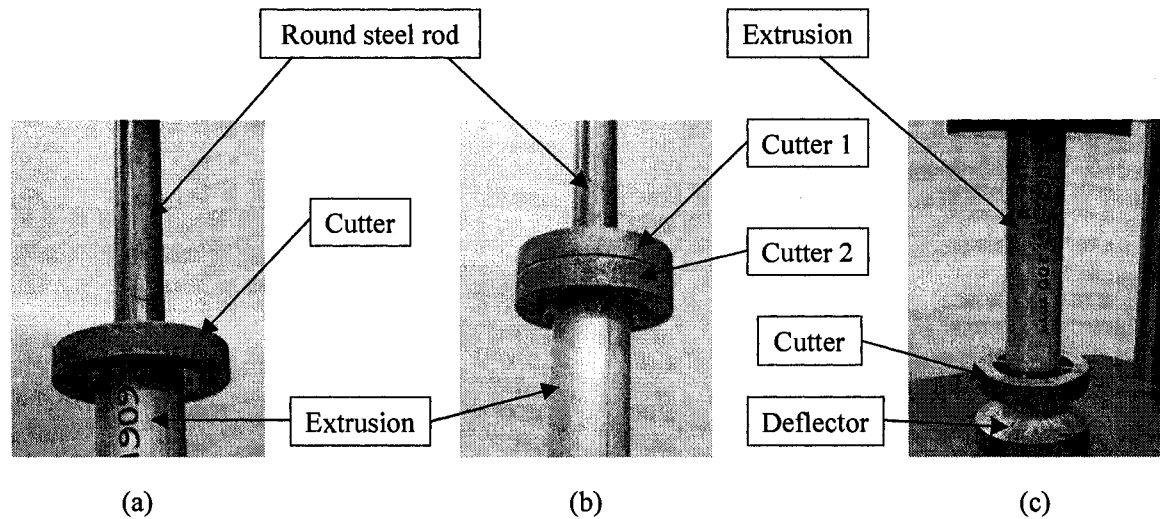


Figure 4.8. Arrangement of extrusion, cutter, deflector and round steel rod during experimental quasi-static axial cutting tests.

5. PARAMETERS USED TO EVALUATE THE CRUSH CHARACTERISTICS OF THE EXTRUSIONS

Different crush performance parameters developed by a number of researchers are used to quantify the load/displacement and energy absorption characteristics of the extrusions. Hsu and Jones [9] introduced an energy-absorbing effectiveness factor (ψ) to assess the efficiencies of tubes made of different materials under quasi-static and dynamic loading. Magee and Thornton [63] used the peak buckling load and mean crush load to characterize the crush behaviour of axially loaded square tubes that collapsed in symmetric mode. Mahmood and Paluszny [64] developed the concept of the crush force efficiency to compare the performance of energy absorbers of different shapes, sizes and strength. The total energy absorbed (TEA), peak crush load (P_{max}), mean crush force (P_m), crush force efficiency (CFE) and specific energy absorption (SEA) are described in this section as an assessment of crush behaviour and will be used in subsequent sections.

5.1 Total energy absorption

The energy absorbed by a specimen is determined experimentally as the work done by the crushing force and is calculated using equation (5.1).

$$E_{absorbed} = \int \vec{P} \cdot \overline{d\delta} = \int (P_x, P_y, P_z) \cdot (d\delta_x, d\delta_y, d\delta_z) = \int P_x \cdot d\delta_x \quad (5.1)$$

Where P_x is the crushing force in the axial direction and δ_x is the crosshead displacement in the axial direction. This quantity is represented as the area under the axial force versus axial displacement curve. In order to calculate the energy absorbed based on the experimental data, a numerical integration scheme is employed. The scheme presented in equation (5.2) is the rectangular rule which was utilized in this research to calculate the total energy absorbed. Other numerical integration techniques, such as trapezoidal or Simpson rules can also be implemented.

$$E_{absorbed} = \sum_{i=2}^{N-1} P_i \cdot \left(\frac{\delta_{i+1} - \delta_{i-1}}{2} \right) \quad (5.2)$$

5.2 Peak crush load

The peak crush load, P_{max} , is the maximum load experienced by the structure in the axial direction observed throughout the crushing process.

5.3 Mean crush force

Based on the total energy absorption defined in equation (5.2), the mean crush force, P_m , is defined by dividing equation (5.2) by the total crush displacement, δ_t , in the axial direction as presented in equation (5.3).

$$P_m = \frac{\sum_{i=2}^{N-1} P_i \cdot \left(\frac{\delta_{i+1} - \delta_{i-1}}{2} \right)}{\delta_t} = \frac{E_{absorbed}}{\delta_t} \quad (5.3)$$

5.4 Crush force efficiency

The crush force efficiency (CFE), which is defined as the ratio of the average crush force to the peak crush load as presented in equation (5.4). A value of unity represents the most desirable value of the CFE, corresponding to a constant load versus displacement profile.

$$CFE = \frac{P_m}{P_{max}} \quad (5.4)$$

5.5 Specific energy absorption

The specific energy absorption (SEA) of a structure is the energy absorbed by a structure divided by its mass as defined in equation (5.5).

$$SEA = \frac{TEA}{m} \quad (5.5)$$

Where, m is the mass of the absorber. This is a useful parameter that provides a method for comparing energy-absorbing structures with different masses.

5.6 Energy-absorbing effectiveness factor

The energy-absorbing effectiveness factor is the ratio of the energy absorbed by the extrusion to the product of the volume of the extrusion and the area below the σ/ϵ curve.

$$\psi = \frac{TEA}{V \cdot A} \quad (5.6)$$

Where, V is the volume of the extrusion and A is area under the σ/ϵ profile of the extrusion material.

6. EXPERIMENTAL RESULTS AND DISCUSSION

Results of the experimental testing conducted in this research are presented in this chapter. An overview is given in the first section of the tensile tests which were conducted by Arnold and Altenhof [38] to obtain material properties of the aluminum extrusions. The second section details the results of the quasi-static crush testing of the extrusion specimens with different wall thicknesses and temper conditions. The third section discusses the results of the axial cutting tests in the presence of cutters and deflectors as well as utilizing the cutter only. The fourth section details the dual stage cutting test results in the presence of deflectors and spacers. The fifth section provides detail discussion on controlling the load/displacement response.

6.1. Tensile testing results

The engineering stress versus the engineering strain profiles of one representative AA6061-T4 and -T6 tensile specimen are illustrated in Figure 6.1. It can be seen that there are significant differences in the yield point and hardening properties between each of the materials considered. AA6061-T6 illustrated a minimal level of strain hardening and an approximate mean strain to failure of 14% while AA6061-T4 illustrated a greater amount of strain hardening and an approximate mean strain to failure of 21%. The areas under these curves were calculated employing numerical integration technique. The calculated areas were utilized to determine the effectiveness factor. The material properties of the AA6061-T4 and -T6 averaged over the eight tensile specimens are summarized in Table 6.1. The yield strength presented in Table 6.1 is the 0.2% proof strength of the extrusion material.

Table 6.1. Material properties of the 6061-T4 and -T6 extrusions from tensile tests [38]

Properties	AA6061-T6	AA6061-T4
E (GPa)	68.1	65.3
σ_y (Mpa)	277.5	116.2
σ_u (Mpa)	320.2	258.3
% elongation	14.1	21.4

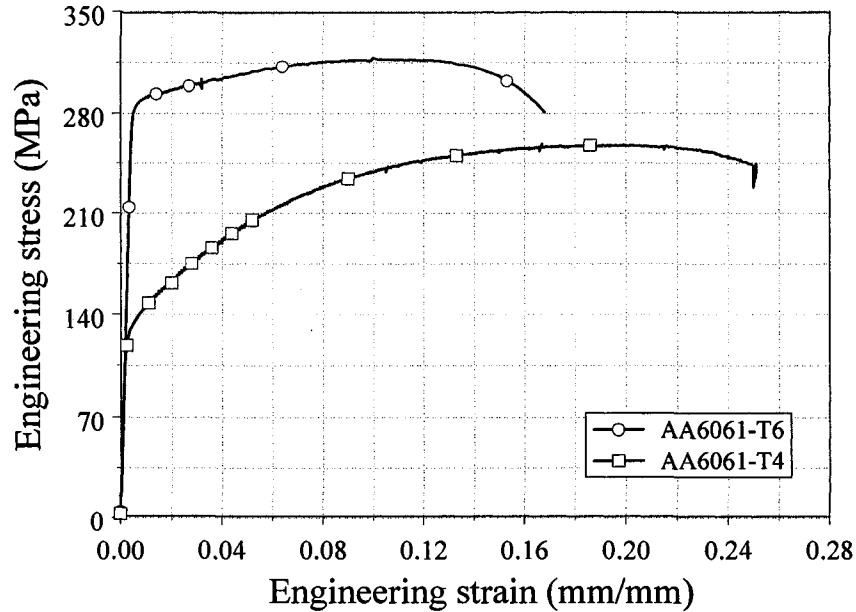


Figure 6.1. The engineering stress versus the engineering strain curves of AA6061-T4 and -T6 obtained from tensile testing [38].

6.2 Quasi-static crush testing results and discussion

The results are presented in the form of load/displacement profiles and collapse modes for each specimen group. Although three experimental tests were completed for each group the load/displacement observations for all the specimens within each group were fairly consistent if not indicated otherwise. For this reason and for greater clarity, only a representative specimen from each group was selected for illustration and discussion purposes. The load/displacement profiles of all three tests within group 4 and group 5 are presented in Appendix A to demonstrate the repeatability of the tests. A qualitative and quantitative examination of crush tests observations for each specimen group was completed through analysis of photographs and crush parameters.

6.2.1 Crush test results for the specimens in groups 1 through 4

The axial compressive crush tests of AA6061-T6 round tubes were performed for three specimens in group 1, which had a length of 200 mm, and three specimens in group 2, which had a length of 300 mm. The observed load/displacement profiles of each

specimen in group 1 and a representative specimen within group 2 are illustrated in Figure 6.2. All specimens within group 2 demonstrated global bending and very similar load/displacement profiles. It can be seen that the first specimen in group 1 collapsed in progressive folding mode as expected [30]. The second specimen initially deformed in a similar manner; however, after approximately 28mm a switch to global bending deformation occurred. The third specimen collapsed within a combination of progressive folding followed by a switch to global bending after a crosshead displacement of approximately 100 mm. All the specimens in group 1 illustrated an approximate peak crush load of 146 kN after approximately 8mm crosshead displacement. For the majority of specimens in group 1, a variable crush force corresponding to the development of material folding was observed following the peak crush load. Specimens in group 1 had L/D and D/t ratios of 3.94 and 16, respectively, which were approximately equal to the critical L/D value of 4.071 for a D/t ratio of 16 as indicated in reference [30] for a switch from progressive folding to global bending. Experimental testing illustrated that the specimens with geometries very similar to the critical geometrical dimensions from reference [30] may experience very unstable deformation during axial crush. Minor variations in specimen geometry and/or material characteristics could also contribute to the transition of progressive folding into a global bending mode of deformation. All the specimens in group 2 collapsed in the global bending mode and illustrated similar load/displacement responses. As the bending of the specimens within this group progressed, cracking occurred within the region of the kink near the mid-span of the extrusion. The global bending and cracking caused the force displacement profiles to have a large negative slope after the peak crush load. An approximate average peak crush load of 137 kN was observed for specimens in group 2. After the development of a mid-span kink, which occurred after approximately 40mm crosshead displacement, the magnitude of the crush force was approximately 8 kN.

Specific to the specimens with a T4 temper and a wall thickness of 3.175 mm, lengths of 200 mm (group 3) and 300 mm (group 4) were considered which illustrated a progressive folding and a global bending respectively. These deformation modes were consistent with observations from reference [30]. Variation in observations within each group were found to be negligible. Figure 6.3 illustrates the load/displacement responses

for the representative specimens from groups 3 and 4. Photographs of the progressive folding and global bending deformation modes for a representative AA6061-T4 specimen from group 3 and group 4 are illustrated in Figure 6.4(a)-(d).

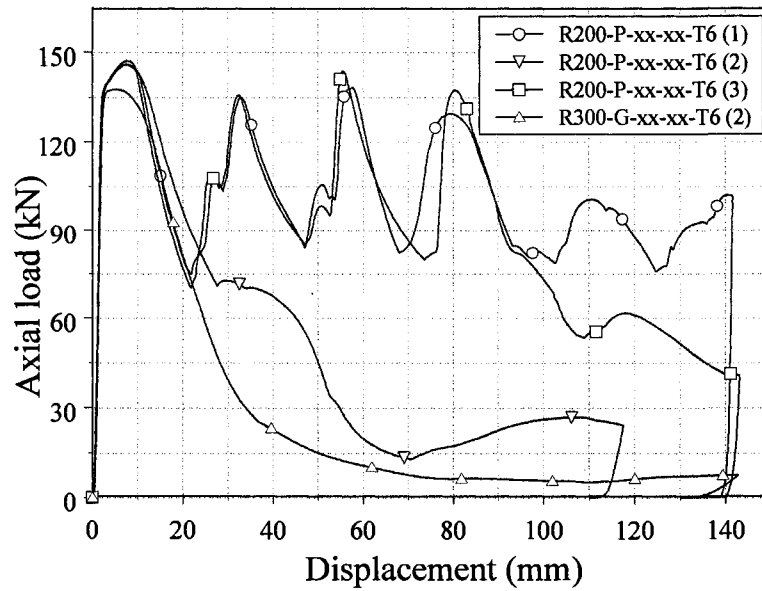


Figure 6.2. The load/displacement observations from all the specimens in Groups 1 and a representative specimen in group 2.

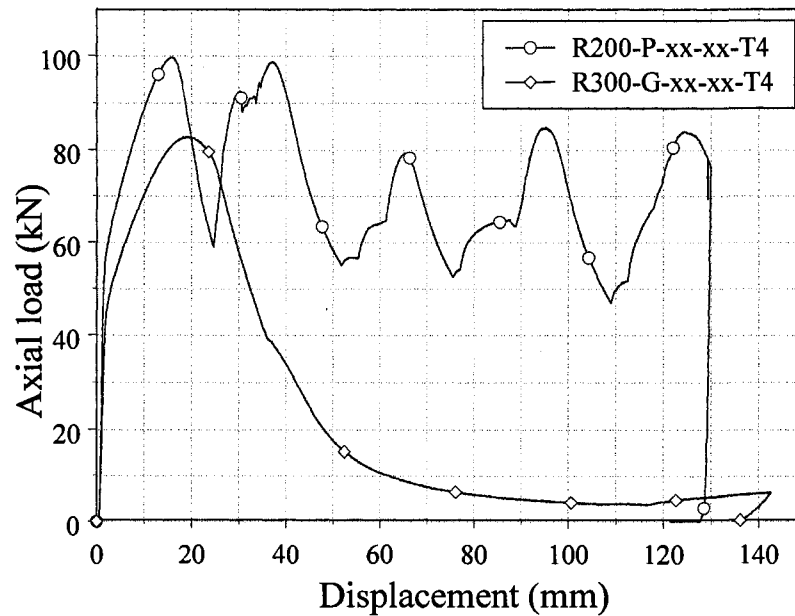


Figure 6.3. The load/displacement responses of the representative specimen from Groups 3 and 4.

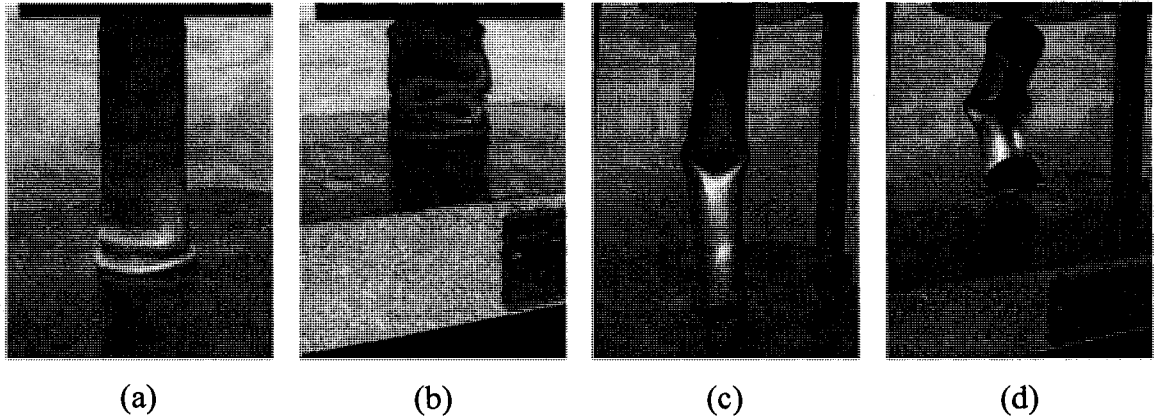


Figure 6.4. Photographs illustrate the progressive folding and global bending deformation modes for a representative specimen in Groups 3 and 4. (a) and (b) illustrate the progressive folding deformation mode; (c) and (d) represents the global bending deformation mode.

6.2.2 Crush test results for the specimens in groups 5 through 12

For specimens within groups 6 and 10, which were geometrically identical, with specimens in group 6 having a T6 temper and specimens in group 10 having a T4 temper, illustrated a progressive folding behaviour as predicted from reference [30]. However, all the specimens in group 6, illustrated significant local plasticity during the formation of folds which resulted in material failure and the generation of a large number of fragmented pieces of the extrusion. For all the specimens in group 10 no material failure was observed. Consistent load/displacement observations were found for the specimens within each group. It was observed that all specimens within group 8, which were 450 mm in length, of T6 temper, and had a wall thickness identical to specimens in groups 6 and 10, consistently illustrated a progressive folding deformation mode. This behaviour was not expected considering the findings of Abramowicz and Jones [30]. The deformation and the load/displacement response was generally identical to specimens in group 6, with a minor exception that the stiffness of the extrusions prior to plastic collapse was larger for the shorter specimens as one would expect. The load/displacement responses are presented in Figure 6.5 for the representative specimens from groups 6, 8, and 10.

Specimens in groups 7, 11, and 12, illustrated either progressive folding, global bending, or a combination of these two deformation modes amongst all three specimens tested within each group. One specimen, from group 7, illustrated a progressive folding behaviour, with fracturing of the side walls during formation of folds. This deformation was consistent throughout the entire test and similar to the findings from group 8. The remaining two specimens in group 7 illustrated global bending behaviour. The peak crushing forces were almost identical for all three specimens tested. The load/displacement observations for a specimen which experienced global bending in group 7 are illustrated in Figure 6.6.

In group 11, one specimen deformed in a global bending mode while the remaining two specimens illustrated progressive folding behaviour with similar load/displacement findings from group 10. An increase of approximately 10% in the peak crushing load was observed for the specimen which illustrated global bending. Figure 6.6 illustrates the observation for a specimen which experienced global bending from group 11.

Two specimens within group 12 deformed in a global bending mode having observations similar to the specimen in group 11 which also deformed in global bending. The remaining specimen in group 12 initially deformed in a progressive folding mode for approximately 85 mm of the total approximate crush displacement of 150 mm and then switched to a global bending deformation behaviour. It is worthy to note that the progressive folding process shifted slightly to the opposite side of the extrusion where global bending eventually occurred. There was only a very minor variation (approximately 3%) in the peak crush force between all three specimens in group 12. Presented in Figure 6.6 is the load/displacement response of the extrusion in group 12 which switched deformation modes during crushing.

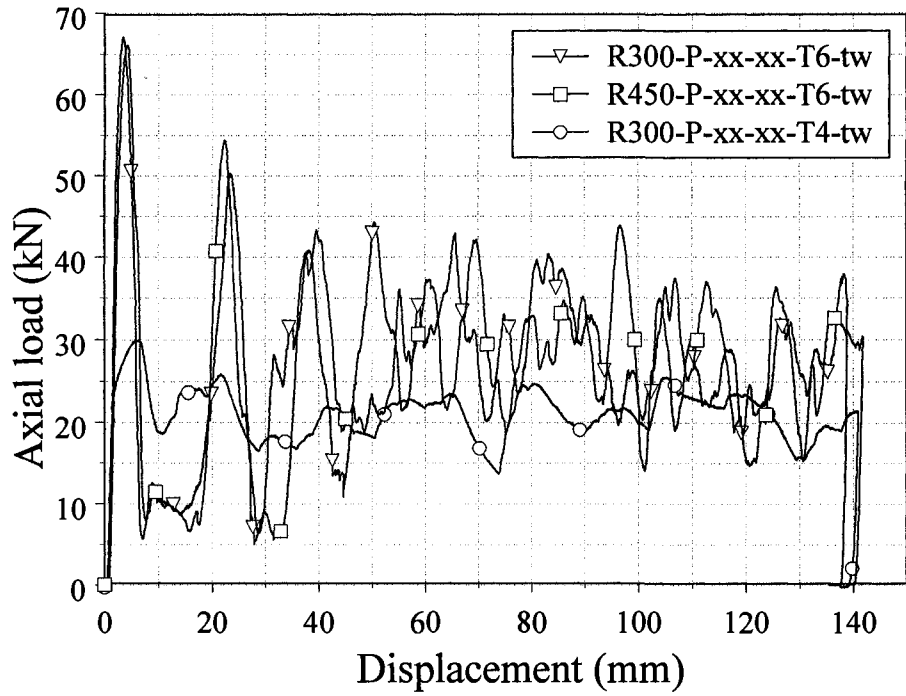


Figure 6.5. The load/displacement profiles from the representative specimens in Groups 6, 8 and 10.

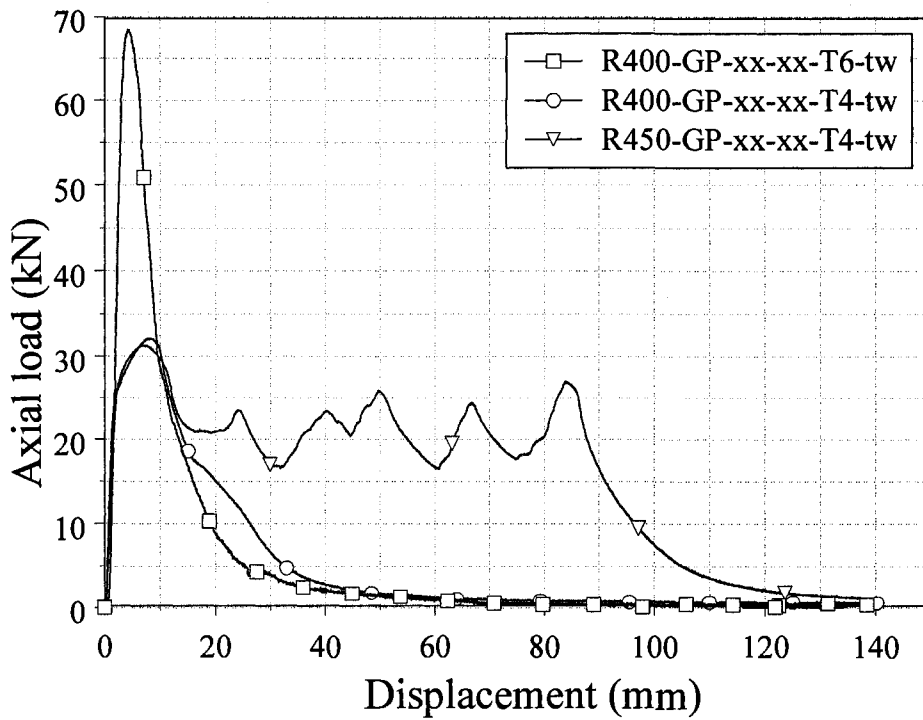


Figure 6.6. The load/displacement observations from the representative specimens in Groups 7, 11 and 12.

6.2.3 Crush test results amongst all specimens

The load/displacement responses for AA6061-T4 and -T6 round aluminum extrusions with wall thicknesses of 1.587 mm and 3.175 mm under progressive folding deformation mode are presented in Figure 6.7. The peak crush forces for the extrusions with both temper conditions and 3.175 mm wall thickness were almost double compared with corresponding extrusions with 1.587 mm wall thickness. The peak crush forces for the extrusions with a wall thickness of 3.175 mm and T6 and T4 temper conditions were 146.1 kN and 98.12 kN respectively. A 32.8% reduction of the peak crush force associated with the T4 temper extrusion was due to strain hardening. Extrusions with a T4 temper had a lower yield strength compared to the T6 temper specimens. Similar findings were also observed for specimens with a wall thickness of 1.587 mm.

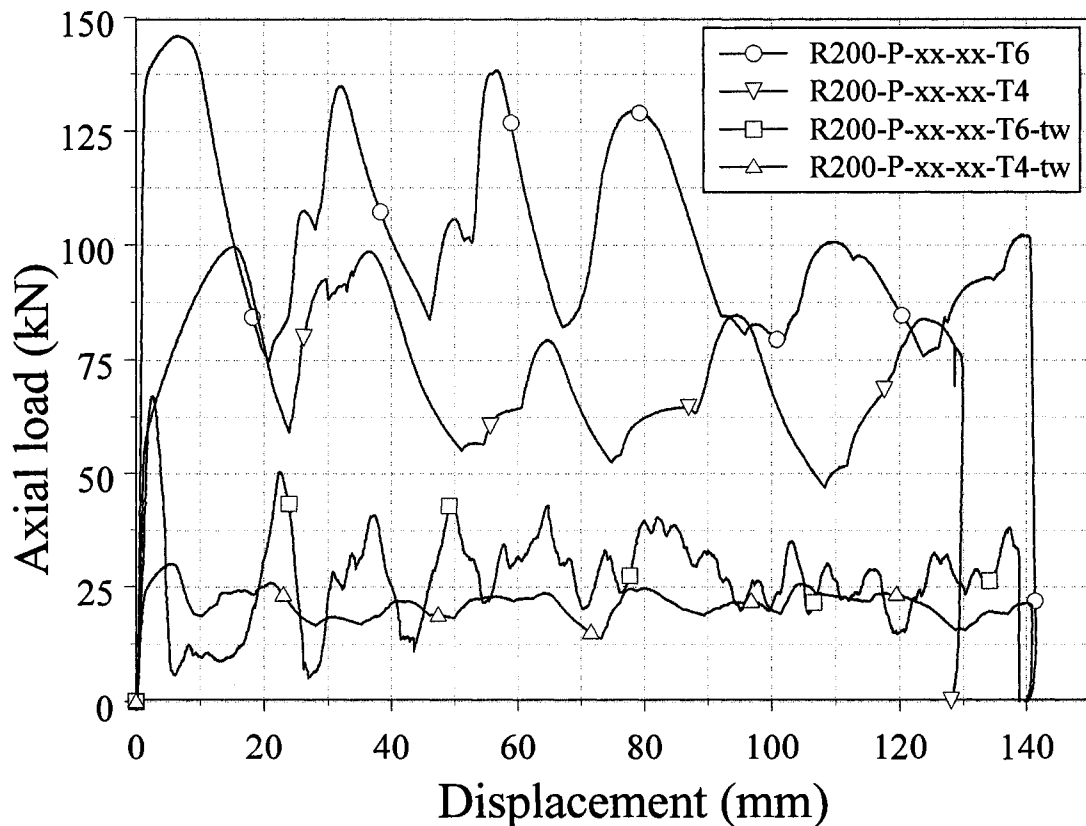


Figure 6.7. The load/displacement observations for the extrusions with T6 and T4 temper and wall thicknesses of 3.175 mm and 1.587 mm under the progressive folding deformation mode.

Figure 6.8 illustrates the load/displacement behaviour of AA6061 round aluminum alloy extrusions with both temper and wall thicknesses of 1.587 mm and 3.175 mm under global bending deformation mode. The magnitude of the peak buckling force for the specimens with the same temper but with a wall thickness of 3.175 mm was observed to approximately twice compared to the corresponding specimen with a wall thickness of 1.587 mm. Approximately 39.4% higher peak buckling force was observed for extrusions with 3.175 mm wall thickness and T6 temper compared to T4 temper specimen with similar wall thickness. The peak crush force for extrusions with a wall thickness of 3.175 mm but T6 and T4 temper conditions under progressive folding deformation mode was observed to be 5.7% and 14.8% higher respectively compared to global bending deformation mode as illustrated in Figure 6.9.

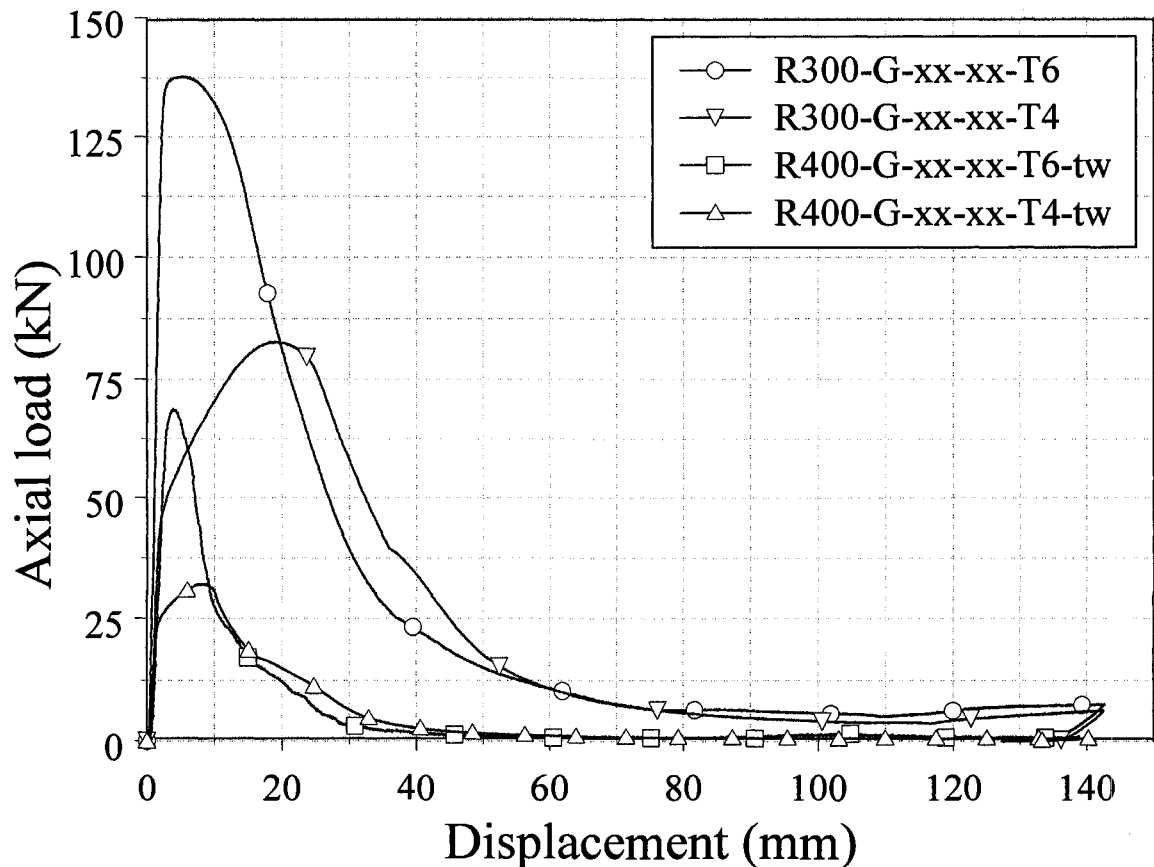


Figure 6.8. The load/displacement observations for the extrusions with T6 and T4 temper and wall thicknesses of 3.175 mm and 1.587 mm under the global bending deformation mode.

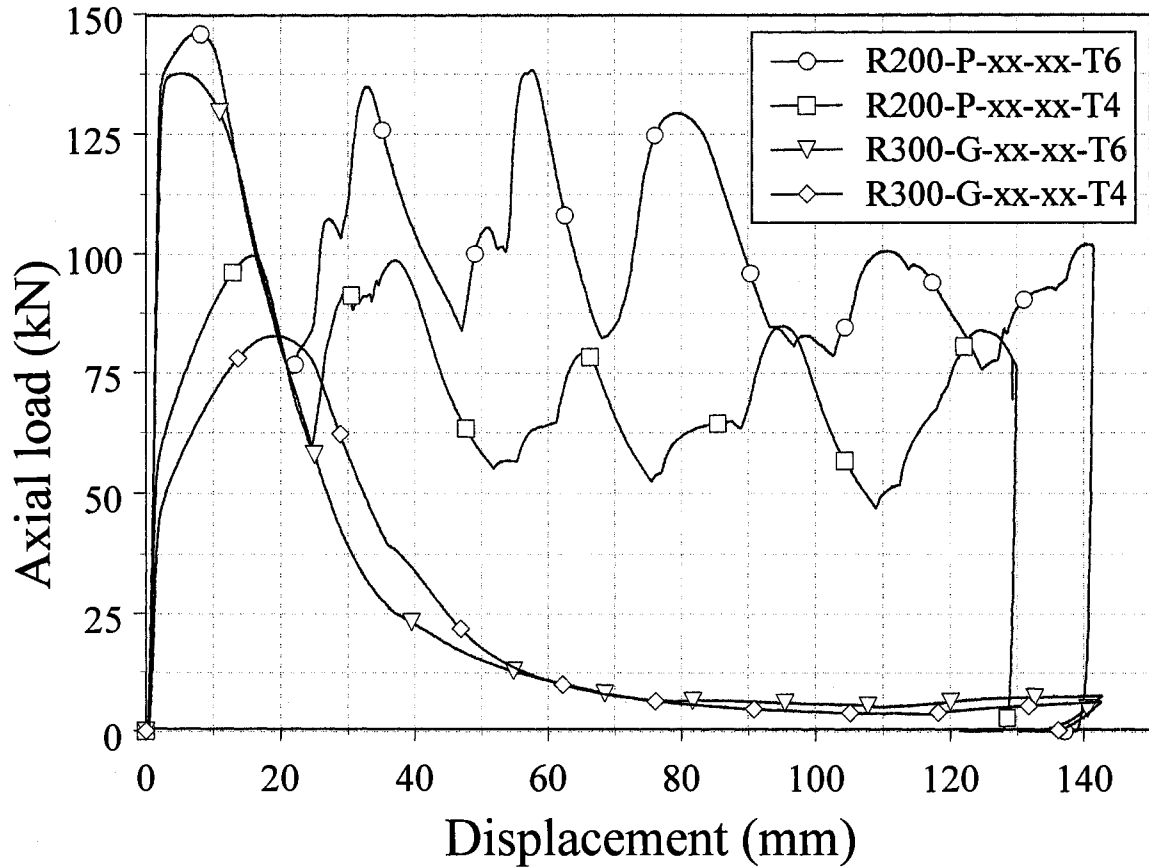


Figure 6.9. Comparison of load/displacement behaviour between the progressive folding and the global bending deformation modes for the extrusions with T6 and T4 temper and 3.175 mm wall thickness.

6.2.4 Comparison of crush performance parameters amongst all specimens

This section compares the crush performance parameters of each group considered in this research. For each specimen tested, the crushing force and the crosshead displacement were recorded. Post-testing data analysis was completed to determine the peak crush load, the mean crush force, CFE, total energy absorption, SEA and the effectiveness factor (ψ). The mean values of crush parameters for each group are presented in Table 6.2 and 6.3

Table 6.2. Calculated average values of the crush parameters for each group

Group	Specimen ID	Average P_m (kN)	Average P_{max} (kN)	Average CFE (%)
1	R200-P-xx-xx-T6	96.54	146.10	66.08
2	R300-G-xx-xx-T6	28.34	137.80	20.60
3	R200-P-xx-xx-T4	68.76	98.12	70.07
4	R300-G-xx-xx-T4	23.74	83.57	28.40
5	R200-P-xx-xx-T6-tw	26.48	67.55	39.23
6	R300-P-xx-xx-T6-tw	27.34	67.77	40.34
7	R400-GP-xx-xx-T6-tw	5.72 (G)	68.79 (G)	8.32 (G)
		26.23 (P)	68.57 (P)	38.23 (P)
8	R450-P-xx-xx-T6-tw	26.98	65.68	42.33
9	R200-P-xx-xx-T4-tw	22.35	32.99	67.73
10	R300-P-xx-xx-T4-tw	21.48	30.65	70.08
11	R400-GP-xx-xx-T4-tw	5.09 (G)	32.09 (G)	15.87 (G)
		21.40 (P)	28.86 (P)	74.19 (P)
12	R450-GP-xx-xx-T4-tw	5.06 (G)	30.88 (G)	16.40 (G)
		15.56 (P→G)	31.21 (P→G)	49.84 (P→G)

Table 6.3. Calculated average values of TEA, SEA and EF for each group

Group	Specimen ID	Average TEA (kJ)	Average SEA (kJ/kg)	Average EF ψ
1	R200-P-xx-xx-T6	10.54	41.85	0.401
2	R300-G-xx-xx-T6	3.73	9.70	0.095
3	R200-P-xx-xx-T4	9.28	36.16	0.428
4	R300-G-xx-xx-T4	3.29	8.54	0.101
5	R200-P-xx-xx-T6-tw	3.70	27.96	0.276
6	R300-P-xx-xx-T6-tw	3.79	28.57	0.186
7	R400-GP-xx-xx-T6-tw	0.79 (G)	5.98 (G)	0.028 (G)
		3.64 (P)	27.48 (P)	0.134 (P)
8	R450-P-xx-xx-T6-tw	3.79	12.67	0.124
9	R200-P-xx-xx-T4-tw	3.15	23.74	0.295
10	R300-P-xx-xx-T4-tw	3.02	16.01	0.190
11	R400-GP-xx-xx-T4-tw	0.71 (G)	2.66 (G)	0.026 (G)
		2.98 (P)	10.91 (P)	0.106 (P)
12	R450-GP-xx-xx-T4-tw	0.71 (G)	2.39 (G)	0.028 (G)
		2.17 (P→G)	7.27 (P→G)	0.086 (P→G)

6.2.4.1 The peak crush force and the mean crush force

Table 6.2 clearly illustrates that the difference of the peak crush load for the specimens which underwent the progressive folding deformation mode were slight higher compared to the specimens that experienced a global bending deformation mode for a similar temper condition and wall thickness. However, the mean crush force for the specimens which underwent a progressive folding deformation mode was observed to be approximately 240% and 190% higher compared to the specimens which experienced a global bending deformation mode for T6 and T4 temper respectively. The of peak crush load and the mean crush force for specimens in group 5, which were 200 mm in length, was observed to be 67.55 kN and 26.48 kN respectively. The magnitude of the peak and the mean crush forces observed in group 5 were very similar to the magnitude of the peak and the mean crush forces observed for the specimens in group 6, which were 300 mm in length. Similar findings were also observed between the specimens in groups 9 and 10 which were T4 temper and 1.587 mm wall thickness.

6.2.4.2 Total energy absorption and crush force efficiency

The total energy absorbed by the specimens in group 1, which underwent progressive folding deformation mode, and group 2, which experienced global bending deformation mode, was observed to be 10.54 kJ and 3.73 kJ respectively. A higher crush force efficiency of approximately 220% was also observed for the specimens in group 1 compared to the specimens in group 2. The total energy absorbed by the specimens with the T6 temper condition was observed to be approximately 45% higher compared to the specimens with the T4 temper condition under progressive folding deformation mode and with similar wall thickness. However, a higher crush force efficiency of approximately 5% was observed for specimens with the T4 temper condition compared to specimens with the T6 temper condition. The magnitude of the total energy absorption and the crush force efficiency for the specimens in group 5 was observed to be very similar for the specimens in group 6. Similar findings were also observed between specimens in group 9 and 10.

6.2.4.3 Specific energy absorption and effectiveness factor

The comparison of the specific energy absorption and effectiveness factor between different specimen groups is presented in Table 6.3. A higher specific energy of approximately 45% was observed for specimens in group 1, which were in the T6 temper condition, compared to the specimens in group 3, in the T4 temper. A higher specific energy absorption was observed for the specimens which were underwent progressive folding deformation mode compared to the specimens which experienced global bending deformation mode for similar temper condition. The effectiveness factors for the specimens with a wall thickness of 3.175 mm, which underwent progressive folding mode, were observed to be approximately 0.428 and 0.401 for the T4 and the T6 temper tubes respectively. An almost four times higher effectiveness factor was noticed for the specimens experienced progressive folding deformation mode compared to the extrusions with identical geometry and temper which went through global bending mode.

6.3 Quasi-static cutting tests results and discussion utilizing the single cutter

Although three experimental tests were completed for each group the load/displacement observations for all the specimens within each group were fairly consistent. For this reason and for greater clarity, only a representative specimen from each group was selected for illustration and discussion purposes. The load/displacement profiles of all three tests within groups c-1, c-5, d-1, d-5, d-9, d-13, d-17, d-21, d-25 and d-29 are presented in Appendix A to demonstrate repeatability of the tests.

6.3.1 Cutting test results for the specimens in groups c-1 through c-4

The observed load/displacement profiles for a representative specimen from groups c-1 through c-4 are illustrated in Figure 6.10. Photographs of the experimental cutting process for a representative AA6061-T4 specimen from group c-1 are illustrated in Figure 6.11(a)-(d). The load/displacement observations for the corresponding images in Figure 6.11(a)-(d) are presented in Figure 6.12.

Experimental tests showed that the cutter penetrated through the sidewall of the specimens and develop highly localized plastic deformation in the vicinity of the cutting blades where cutting chips were formed. No crack propagation was observed in any tests. As cutting progressed, petalled sidewalls bent slightly outwards as a result of the interaction between the cutter blade shoulder and the tube sidewalls.

It is evident from the force/displacement responses that the cutting phenomena can be referred to stable or clean curling cut [24]. At the transient cutting stage, occurring from the point of initial contact between the blade tip and tube sidewall to the point where the resistance force reaches a constant level, the resistance cutting load continued to increase. After an approximate 15 mm penetration of the cutter blade, the cutting process transferred to a steady state cutting stage with a constant resistance force of approximately 26 kN to 36 kN for all tests in groups c-1 through c-4. A notably larger cutting force was observed for all the specimens tested within group c-3, which is a result of the approximately 20% larger mean cutter blade tip width of 1.17 mm compared to all other sides of the cutters used in this experimental program.

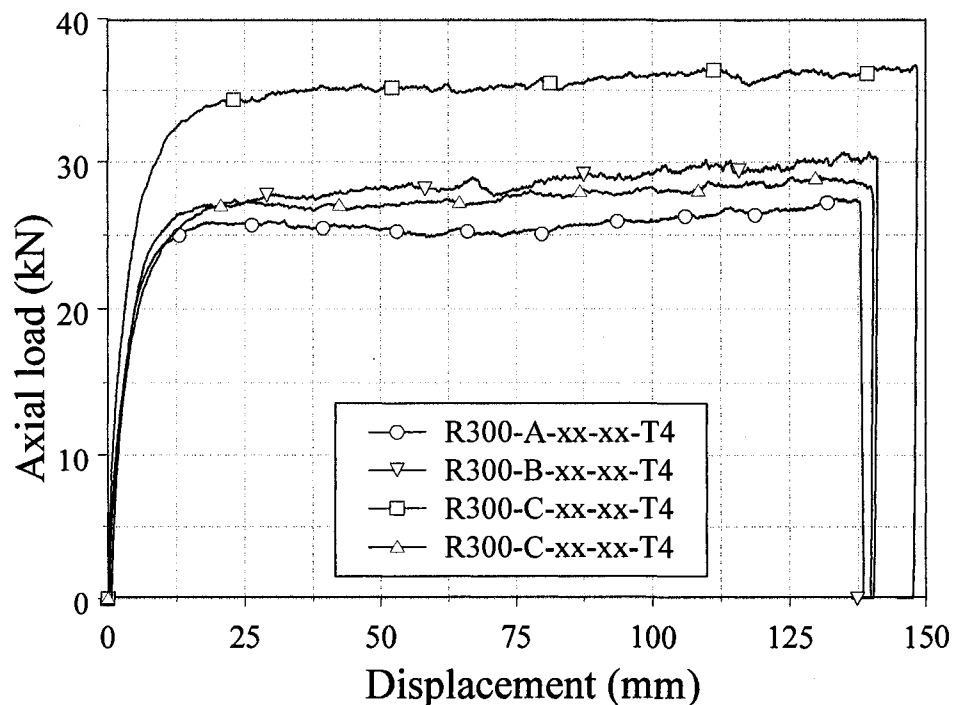


Figure 6.10. Experimentally observed load/displacement profiles for AA6061-T4 representative specimens from Groups c-1 through c-4.

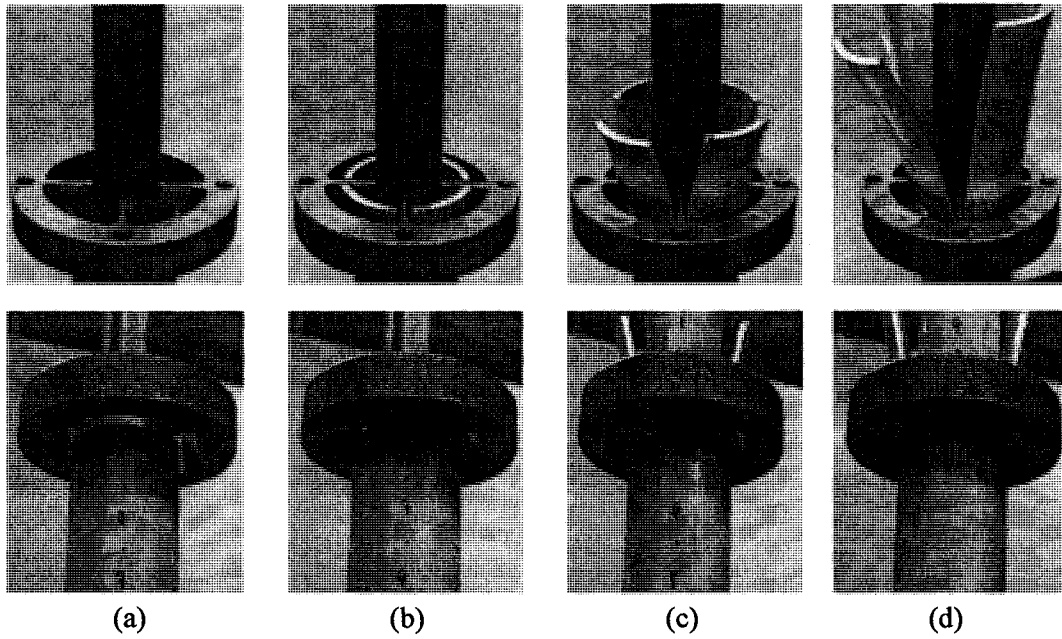


Figure 6.11. Photographs illustrating the experimental cutting process for a representative specimen in Group c-1 (top and bottom views).

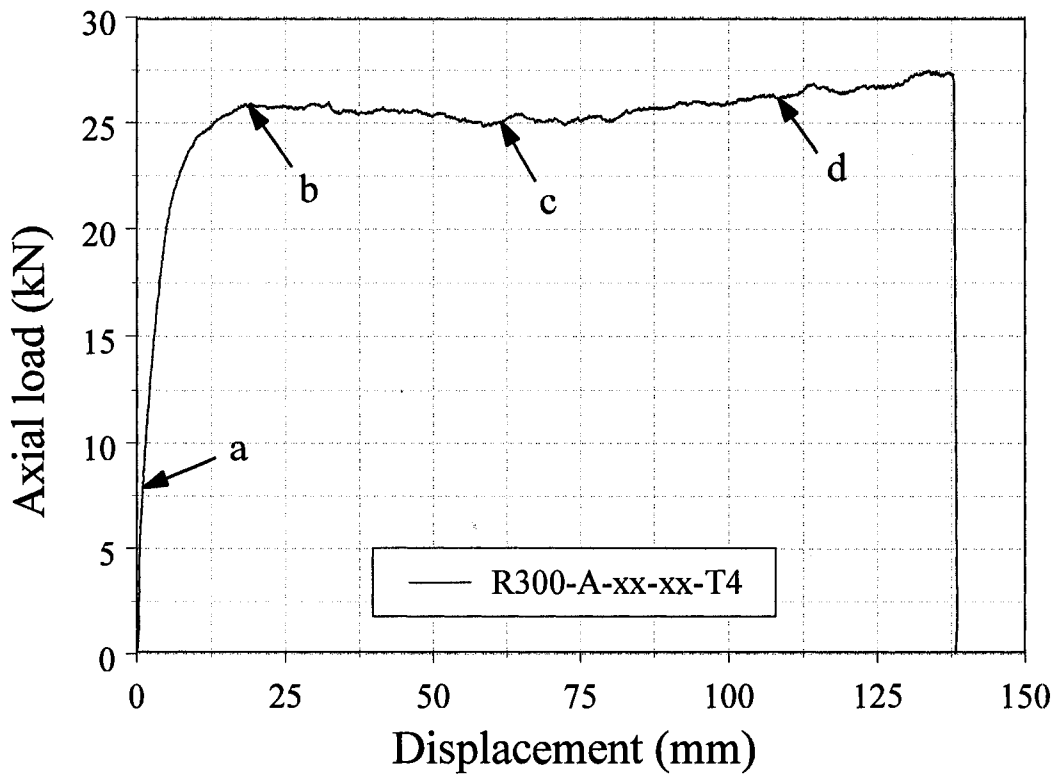


Figure 6.12. The load/displacement response for the representative specimen from Group c-1, positions a, b, c and d correspond to photographs in Figure 6.11.

6.3.2 Cutting test results for the specimens in groups c-5 through c-8

Specimens in groups c-5 through c-8 had the same tube length of 300 mm and were cut by cutter side A, B, C and D, respectively. The force/displacement profiles for representative specimens of each group are shown in Figure 6.13. The stability of the cutting process and the load/displacement profiles for the specimens in groups c-5 through c-8 appeared to be very similar to the observations from the specimens in groups c-1 through c-4. However, the magnitude of the cutting force for the specimens in groups c-5 through c-8, which were T6 temper, was significantly higher compared with the magnitude of cutting force for the specimens in groups c-1 through c-4, which are T4 temper conditions. No significant difference in the magnitude of the cutting force using different cutter blade tip widths for specimens with a T6 temper was observed. This was not consistent with observations for specimens with a T4 temper.

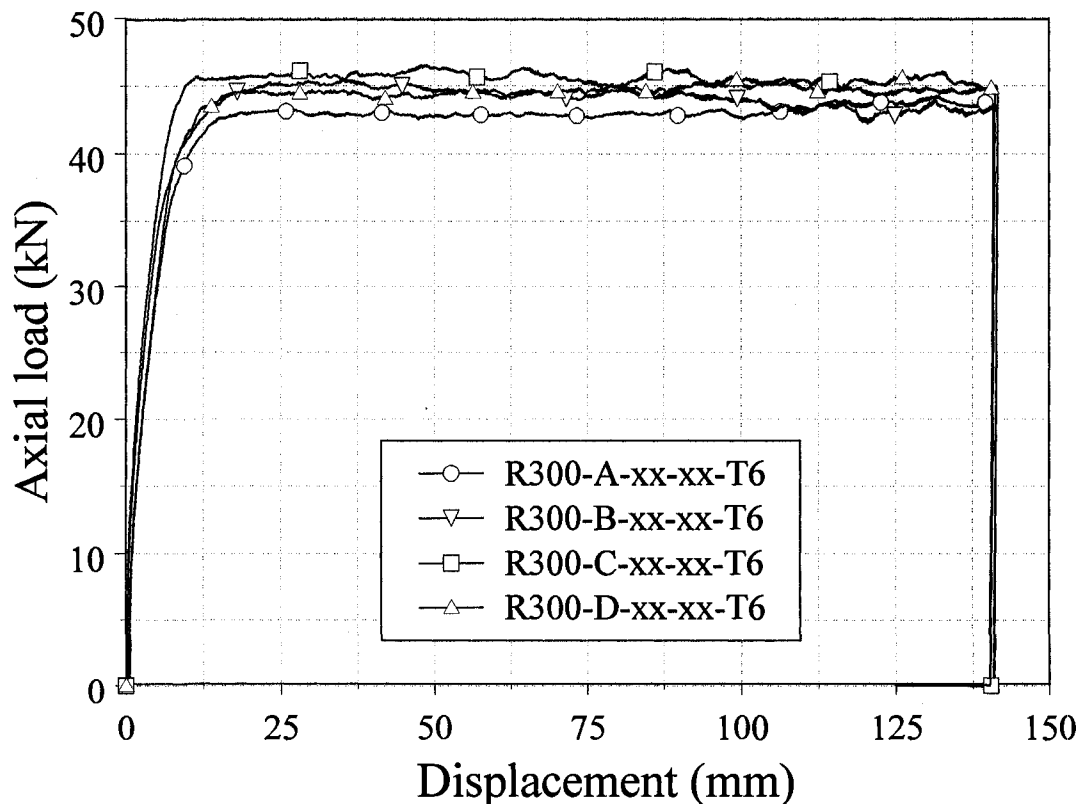


Figure 6.13. Experimentally observed load/displacement profiles for AA6061-T6 representative specimens from Groups c-5 through c-8.

6.3.3 Cutting test results for the specimens in groups c-9 through c-12 and c-17

The specimens tested within group c-17 were of identical temper and cross-sectional geometry to the specimens in groups c-9 through c-12, however, all specimens in group c-17 had lengths of 400 mm to investigate if use of the cutter switched the deformation mode from either progressive folding or global bending to a cutting behaviour.

It was observed that the cutting deformation associated with specimens in groups c-9 through c-12 and c-17 behaved as braided cut [24] with a very minor degree of tearing. The corresponding load/displacement response was typical of this type of cutting deformation as indicated in reference [24] where notable variations in the load were observed throughout the displacement domain. Fluctuations in the load/displacement behaviour, for specimens with a T4 temper and wall thickness of 1.587 mm irregardless of length, were observed to be significant compared with all other testing completed in this experimental program. This was a result of the minor “back and forth” folding of the cut petalled side walls during cutting which was not observed for all other specimens subjected to cutting deformation. Variations in the cutting forces were most notable after approximately 50 mm crosshead displacement. Figure 6.14 illustrates the load/displacement behaviour of all specimens within group c-10. Responses of other specimens within groups c-9, c-11, c-12, and c-17 were generally consistent with the fluctuations presented in Figure 6.14. Photographs of the experimental cutting process for a representative AA6061-T4 specimen from group c-10 are illustrated in Figure 6.15(a)-(d). Load/displacement observations for the corresponding images in Figure 6.15(a)-(d) are presented in Figure 6.16

Increasing the length of the test specimen from 200 mm to 400 mm and incorporating the cutter in the axial testing resulted in a switching to cutting deformation from the expected global bending mode . Specimens within group c-17 illustrated similar load/displacement responses as specimens within group c-9.

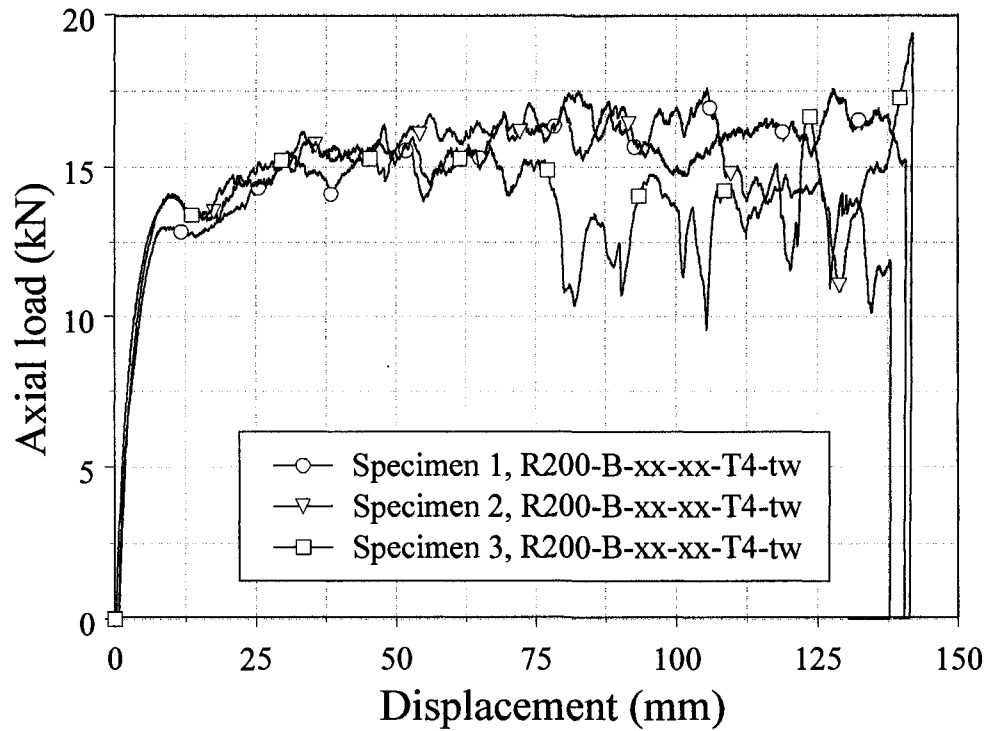


Figure 6.14. Experimentally obtained load/displacement profiles for the specimens in Group c-10.

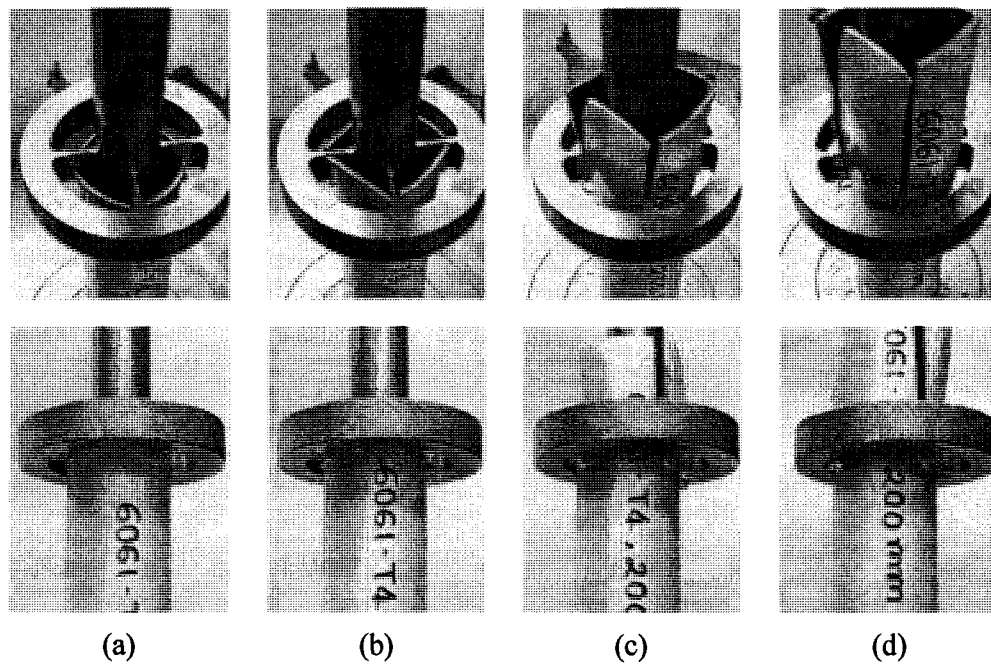


Figure 6.15 Photographs illustrating the experimental cutting process for a representative specimen in Group c-10 (top and bottom views).

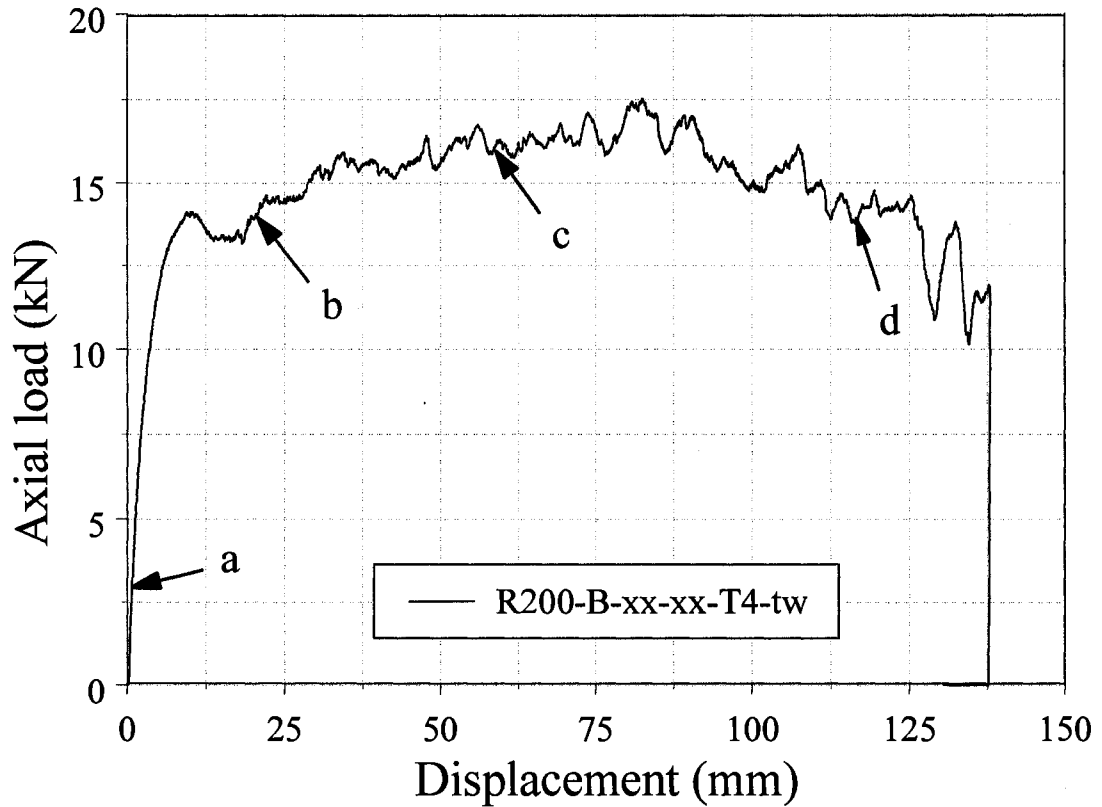


Figure 6.16. Experimentally obtained load/displacement profile for the representative specimen in Group c-10, positions a, b, c and d correspond to photographs in Figure 6.15.

6.3.4 Cutting test results for the specimens in groups c-13 through c-16 and c-18

Figure 6.17 illustrates the observed load/displacement response of all three specimens within group c-16. These findings are typical of results discovered in groups c-13 through c-15 and c-18. The cutting deformation behaviour was more representative of stable or clean curling cut [24] with generally only minor fluctuations in the cutting load within the displacement domain. Any significant variations in load were observed to occur over a longer cutting distance compared with results described in section 6.3.3 regarding the geometrically identical extrusions with a T4 temper. Thus the material characteristics in the T4 and the T6 temper conditions resulted in the differences in cutting deformation behaviour and variations in the load/displacement findings. The lower degree of strain hardening, for the T6 temper condition, permitted highly localized plasticity in the vicinity of the cutter, and for the extrusions with a 1.587 mm wall

thickness, did not appear to generate “back and forth” folding of the cut petalled side walls during cutting. Figure 6.21 illustrates the cut petalled side walls of extrusions after testing from specimens with the T4 and the T6 tempers, having a wall thickness of 1.587 mm. For both of these specimens, nondestructive methods were used to remove the cutter after testing. The specimen with the T4 temper presented in Figure 6.18 illustrates the “back and forth” folding of the cut petalled side walls and a small degree of sidewall tearing. This deformation was observed to be very notable in the specimen with the T4 temper, however, the specimen with a T6 temper did not illustrate any highly localized folding or tearing of the petalled side walls.

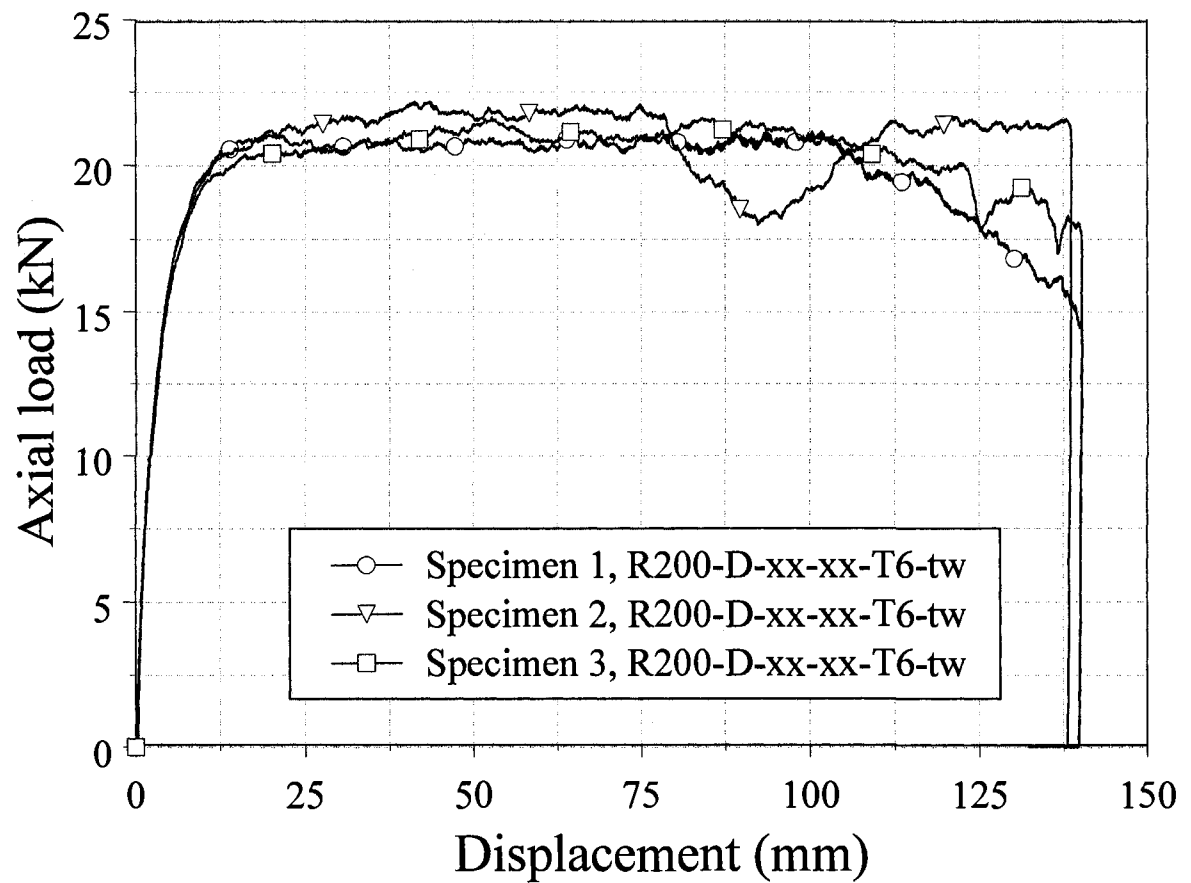


Figure 6.17. Experimentally obtained load/displacement profile for the specimens in Group c-16.

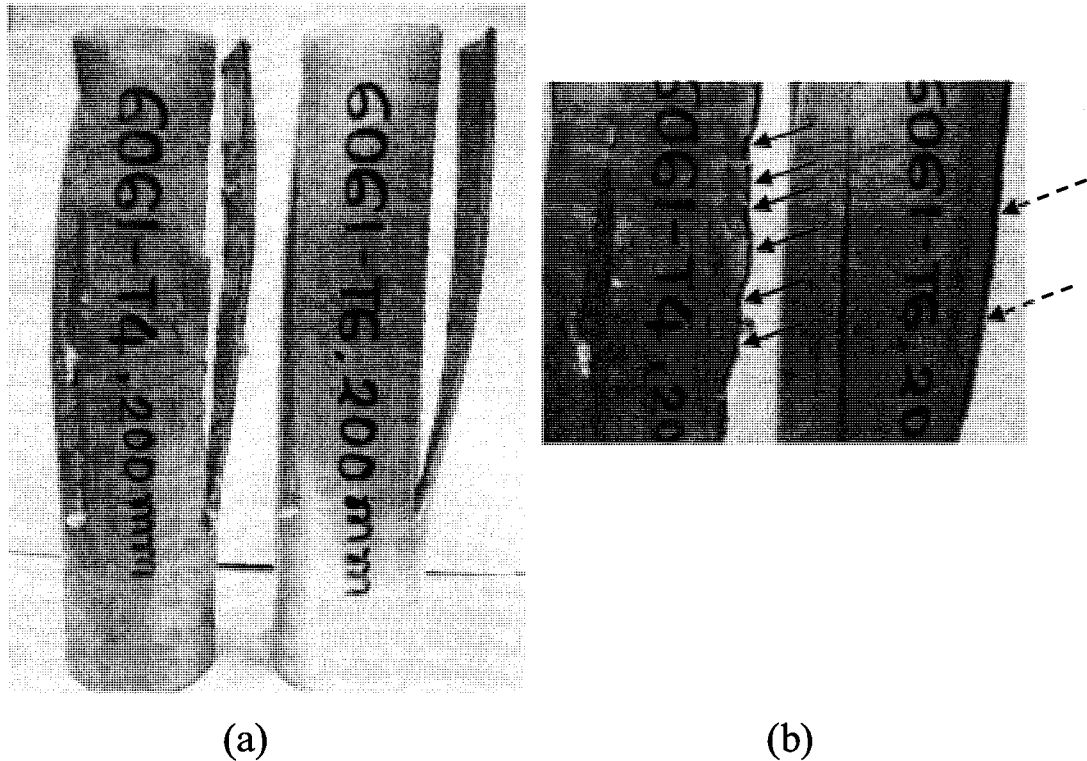


Figure 6.18. Petalled side wall cutting deformation characteristics of T4 and T6 tempered extrusions. (a) entire extrusions (b) close range image illustrating back and forth folding of sidewalls for T4 specimen (solid arrows) and smooth continuous cut (dashed arrows) for T6 specimen.

6.3.5 Cutting test results for the specimens in groups d-1 through d-4

The observed load/displacement profiles for representative specimens from groups d-1 through d-4 are illustrated in Figure 6.19. Photographs of the cutting process for specimen in presence of the straight deflector from group d-3 are illustrated in Figures 6.20(a)–(d). The load/displacement observations for the corresponding images in Figures 6.20(a)–(d) are presented in Figure 6.21. Photographs of the deformation process utilizing the straight deflector illustrated that the cutter penetrated through the sidewall of the specimens and developed highly localised plastic deformation in the vicinity of the cutting blades. No crack propagation was observed in any tests. As the cutting process proceeded, the petalled sidewalls contacted the deflector and flared outwards, forming a continuous region of contact with the deflector. Circumferential stretching of the tube was observed to occur after cutting but prior to contact with the deflector. After contact

between the deflector and petalled sidewalls commenced, a combination of circumferential stretching and large bending was observed to occur within the petalled sidewalls. From the load/displacement profiles in Figures 6.19 and 6.21, the first transient cutting phase, which was observed to occur for displacements in the range of 0 mm to 24 mm, exhibited a nonlinear increase in the cutting load from 0 kN to approximately 45 kN. As the petalled sidewalls contacted the deflector, the load surged to approximately 56 kN and resulted in a second transient cutting phase which was observed to occur with displacements in the range from approximately 25 mm to 65 mm. This increase in load in the second transient cutting phase, which was observed to be within the range from 7 kN to 12 kN for all specimens, was a result of the additional force necessary to initiate the flaring process of the vertical cut sidewalls. Experimental observations from all specimens indicated that this load increase was not consistent but the sharp increase in the load repeatedly occurred at a crosshead displacement of approximately 28 mm and significantly decreased with increasing displacement up to approximately 38 mm. The sharp reduction in load was believed to occur as a result of the flaring process of the aluminum extrusion and hence a reduction in the vertical component of the contact force between the deflector and the tube. The cutting force was observed to increase slightly after a crosshead displacement of approximately 38 mm until 65 mm, which was believed to be because of large plastic bending occurring within the petalled sidewalls near the contact region of the extrusion and deflector. Finally, the deformation process reached a steady state cutting phase after a crosshead displacement of approximately 65 mm with an approximate resistance force of 38 kN for all tests considered with the straight deflector. The cutting force in this phase was maintained constant until testing was completed. The reduction in steady state cutting force from approximately 45 kN to 38 kN was a result of the stretching imposed on the petalled sidewalls of the extrusion from the deflector. A minor influence of cutter blade tip width was observed during first transient phase but after that it was not noticeable. The specimens in group d-3, which utilized cutter side C with blade tip width of 1.17 mm, experienced cutting force approximately 44 kN and the specimens in group d-1, which utilized cutter side A with blade tip width of 1.01 mm, experienced cutting force of approximately 46 kN.

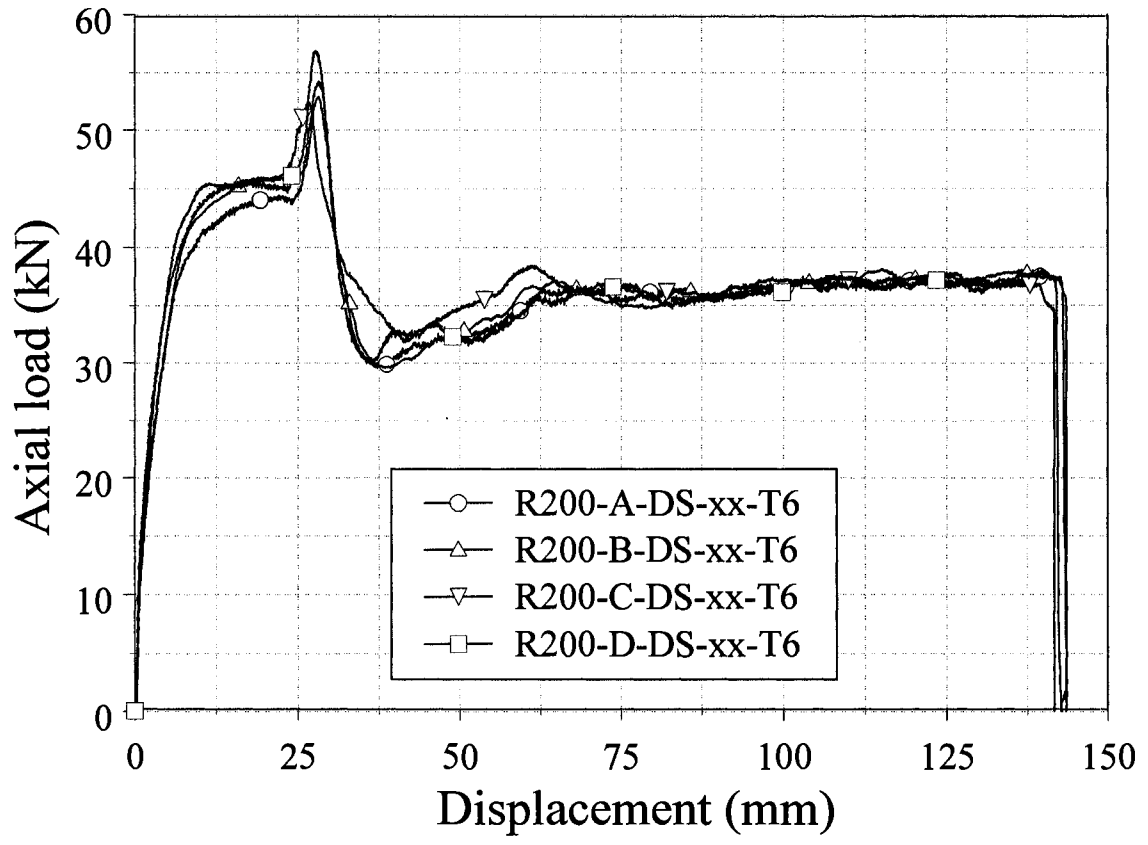


Figure 6.19. Experimentally obtained load/displacement responses for the specimens in Groups d-1 through d-4.

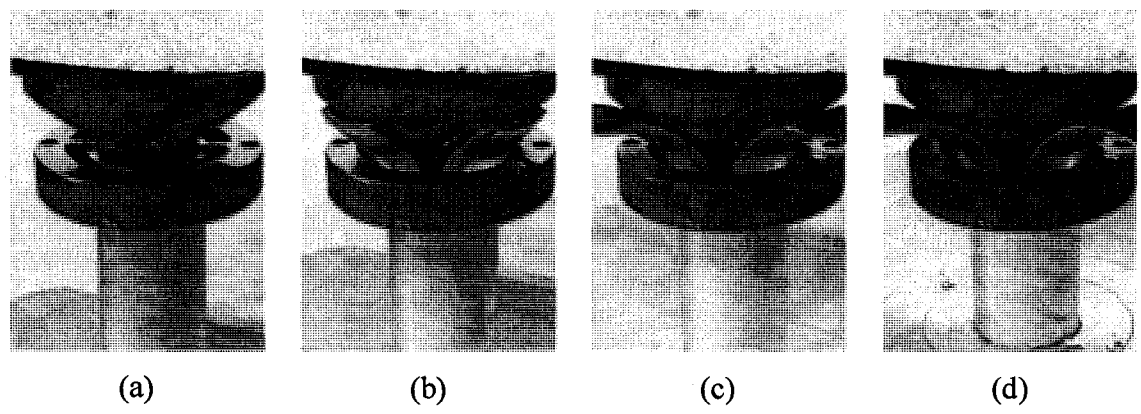


Figure 6.20. Photographs illustrating the experimental cutting process for a representative specimen in Group d-1.

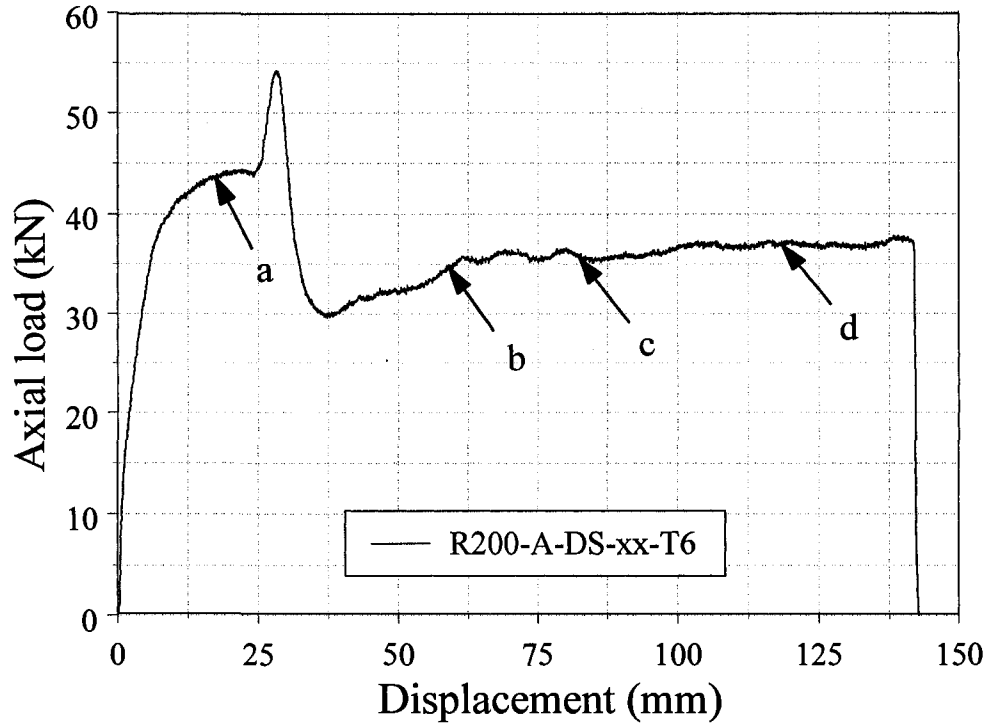


Figure 6.21. Experimentally obtained load/displacement responses for the representative specimen in Group d-1, positions a, b, c and d correspond to photographs in Figure 6.20.

6.3.6 Cutting test results for the specimens in groups d-5 through d-8

Fairly consistent load/displacement responses were observed for specimens within groups d-5 through d-8. The force/displacement profiles for representative specimens of each group are shown in Figure 6.22. The specimens in groups d-5 through d-8 exhibited similar load/displacement responses and cutting phenomenon to the specimens in groups d-1 through d-4. However, it was observed that the significant increase in cutting force previously observed in groups d-1 through d-4, when contact with the deflector was initiated, no longer existed with the use of the curved deflector. The elimination of the sharp increase in cutting force was caused by the curvature associated with the curved deflector. In addition, the reduction in cutting force after initial contact with the deflector occurred over a longer displacement with the curved deflector compared to the findings of the specimens within groups d-1 through d-4. Flaring of the specimens within groups d-5 through d-8 were more gradual than observed for the specimens within groups d-1 through d-4. This observation explained why the reduction in cutting force occurred over

a longer displacement. Finally, the cutting process reached a steady-state phase after a crosshead displacement of approximately 70 mm with an approximate resistance force of 38 kN for all specimens within these groups. The cutting force in this phase was maintained constant until testing was completed. The influence of cutter blade tip width observed to be more prominent in presence of the curved deflector compared to the straight deflector. The average cutting force for specimens in group d-7, which utilized cutter side C with blade tip width of 1.17 mm, was observed to be approximately 39.8 kN and specimens in group d-5, which utilized cutter side A with blade tip width of 1.01 mm, was observed to be approximately 36.6 kN.

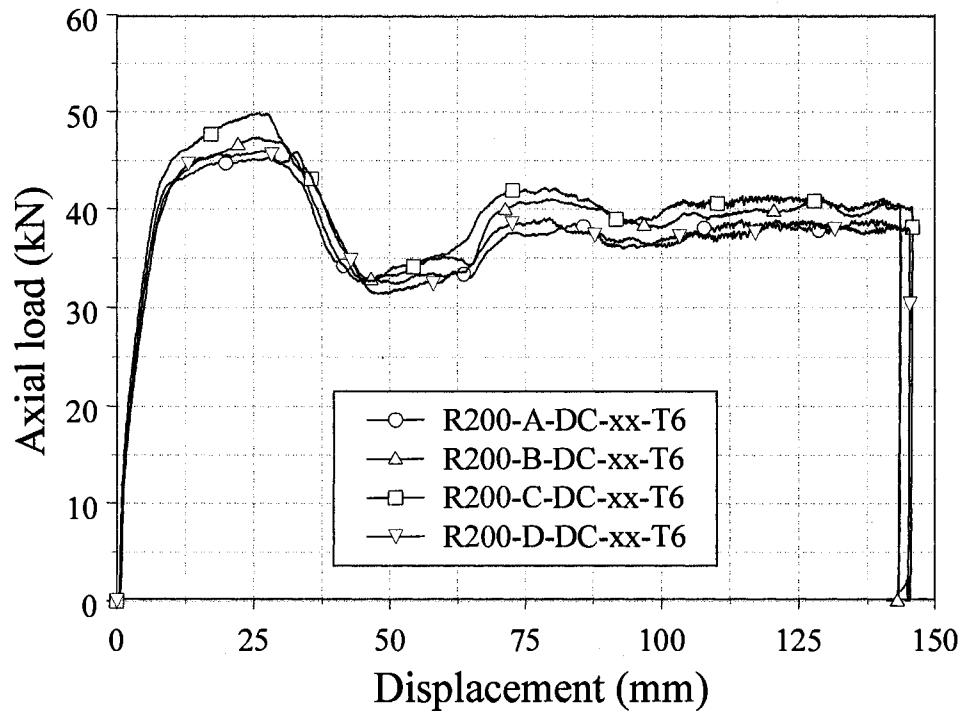


Figure 6.22. Experimentally obtained load/displacement profiles for the specimens in Group d-5 through d-8.

6.3.7 Cutting test results for the specimens in groups d-9 through d-12

The observed load/displacement profiles for representative specimens from groups d-9 through d-12 are illustrated in Figure 6.23. The specimens in groups d-9 through d-12 exhibited similar load/displacement responses and cutting phenomenon to

the specimens in groups d-1 through d-4. However, the significant increase in cutting force previously observed in groups d-1 through d-4 for specimens with the T6 temper no longer existed with use of the T4 temper specimens in groups d-9 through d-12 in presence of the straight deflector. The elimination of the sharp increase in cutting force was caused due to reduction of material strength of the T4 temper specimens. A significant difference of the cutting force was observed through use of different cutter blade tip width for specimens in group d-9 through d-12 which was not significant for specimens in group d-1 through d-4. The specimens in group d-11, which went through cutter side C, experienced the highest cutting force of approximately 40 kN at 27 mm cross-head displacement. The specimens in groups d-9 and d-10, which underwent through cutter sides A and B respectively, experienced the least cutting force of approximately 29 kN at the same cross-head displacement. This finding demonstrates the influence of cutter blade geometry on crush performance of aluminum extrusions.

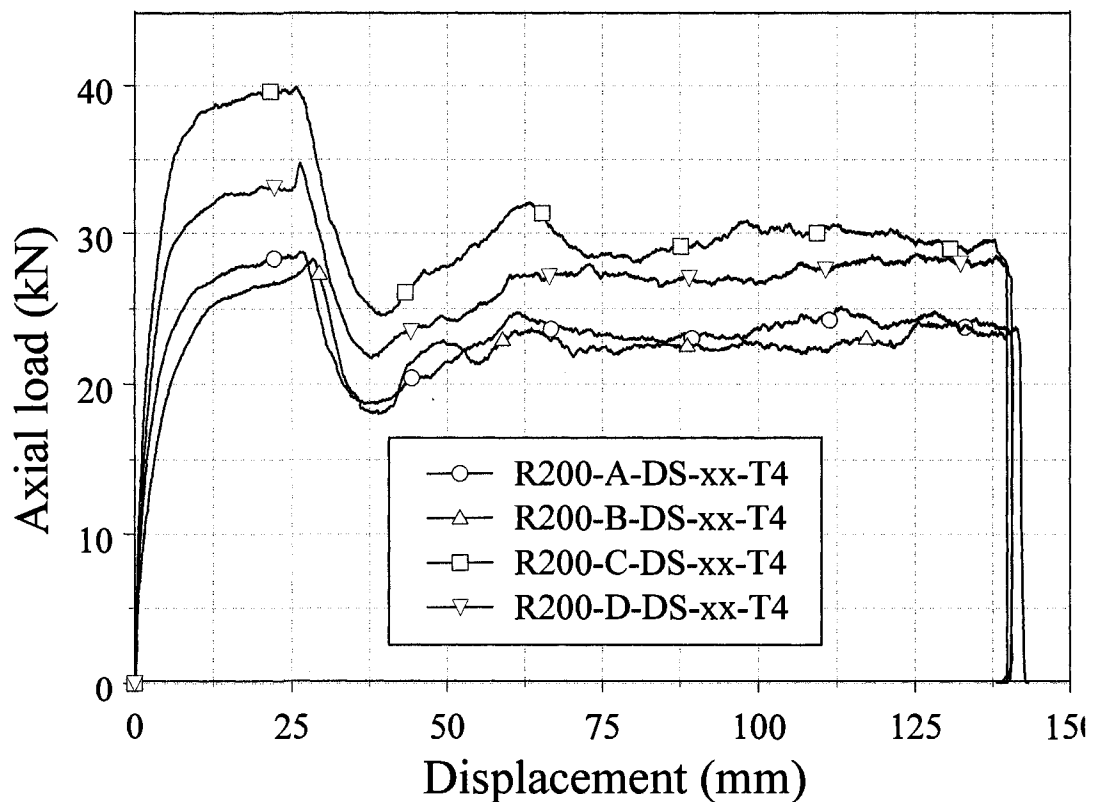


Figure 6.23. Experimentally obtained load/displacement responses for the specimens in Group d-9 through d-12.

6.3.8 Cutting test results for the specimens in groups d-13 through d-16

Figure 6.24 illustrates the force/displacement responses for representative specimens from groups d-13 through d-16. The specimens in groups d-13 through d-16 exhibited similar load/displacement responses and cutting phenomenon to the specimens in groups d-5 through d-8. However, the magnitude of the cutting force experienced by the specimens in groups d-13 through d-16, which were a T4 temper, was approximately 35% lower compared to the specimens in group d-5 through d-8 which were a T6 temper. The reduction of cutting force was due to lower material strength of the T4 temper specimens. A significant difference of cutting force was also observed through use of different cutter blade tip width for the specimens in group d-13 through d-16. The specimens in group d-15, which went through cutter side C, experienced the highest cutting force of approximately 37 kN at the cross-head displacement of 30 mm. The specimens in groups d-13 and d-14, which underwent through cutter sides A and B respectively, experienced the least cutting force of approximately 31 kN at similar crosshead displacement.

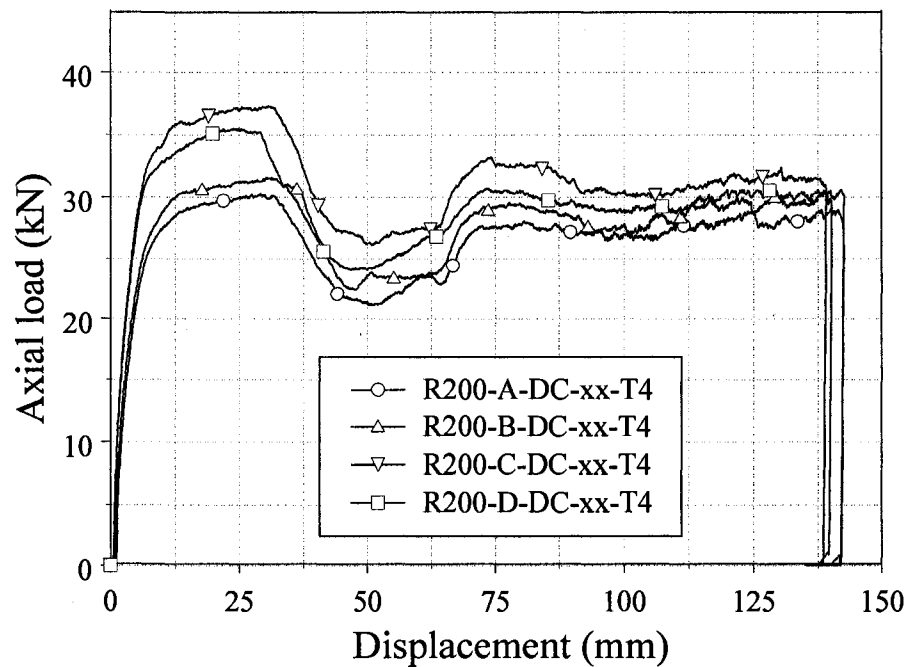


Figure 6.24. Experimentally obtained load/displacement profiles for the specimens in Group d-13 through d-16.

6.3.9 Cutting test results for the specimens in groups d-17 through d-20

Figure 6.25 illustrates the load/displacement profiles for representative specimens from groups d-17 through d-20. Photographs of the cutting process for specimen in presence of the straight deflector from group d-17 are illustrated in Figures 6.26(a)–(d). The load/displacement observations for the corresponding images in Figures 6.26(a)–(d) are presented in Figure 6.27. Photographs of the deformation process utilizing the straight deflector illustrated that the cutter penetrated through the sidewall of the specimens and developed highly localised plastic deformation in the vicinity of the cutting blades. Significant crack formation on petalled side walls was observed in all tests for the specimens with a T6 temper and wall thickness of 1.587 mm. From the load/displacement profiles in Figure 6.25, the first transient cutting phase, which was observed to occur for displacements in the range of 0 mm to 25 mm, exhibited a nonlinear increase in the cutting load from 0 kN to approximately 20 kN. As the petalled sidewalls contacted the deflector, the load surged to approximately 25 kN and resulted in a second transient cutting phase which was observed to occur with displacements in the range from approximately 25 mm to 35 mm. This increase in load in the second transient cutting phase, which was observed to be within the range from 3 kN to 5 kN for all specimens, was a result of the additional force necessary to initiate the flaring process of the vertical cut sidewalls. Experimental observations from all specimens indicated that this load increase was not consistent but the sharp increase in load repeatedly occurred at a crosshead displacement of approximately 28 mm and significantly decreased with increasing displacement up to approximately 38 mm. The sharp reduction in load was believed to occur as a result of the flaring process of the aluminum extrusion and hence a reduction in the vertical component of the contact force between the deflector and the tube. The cutting force was observed to fluctuate afterward until testing was completed. The fluctuation of cutting force was due to massive fracture occurred on petalled side walls after the side wall came in contact with the straight deflector. No significant influence of cutter blade tip width was observed for the T6 specimens with a wall thickness of 1.587 mm as shown in Figure 6.28.

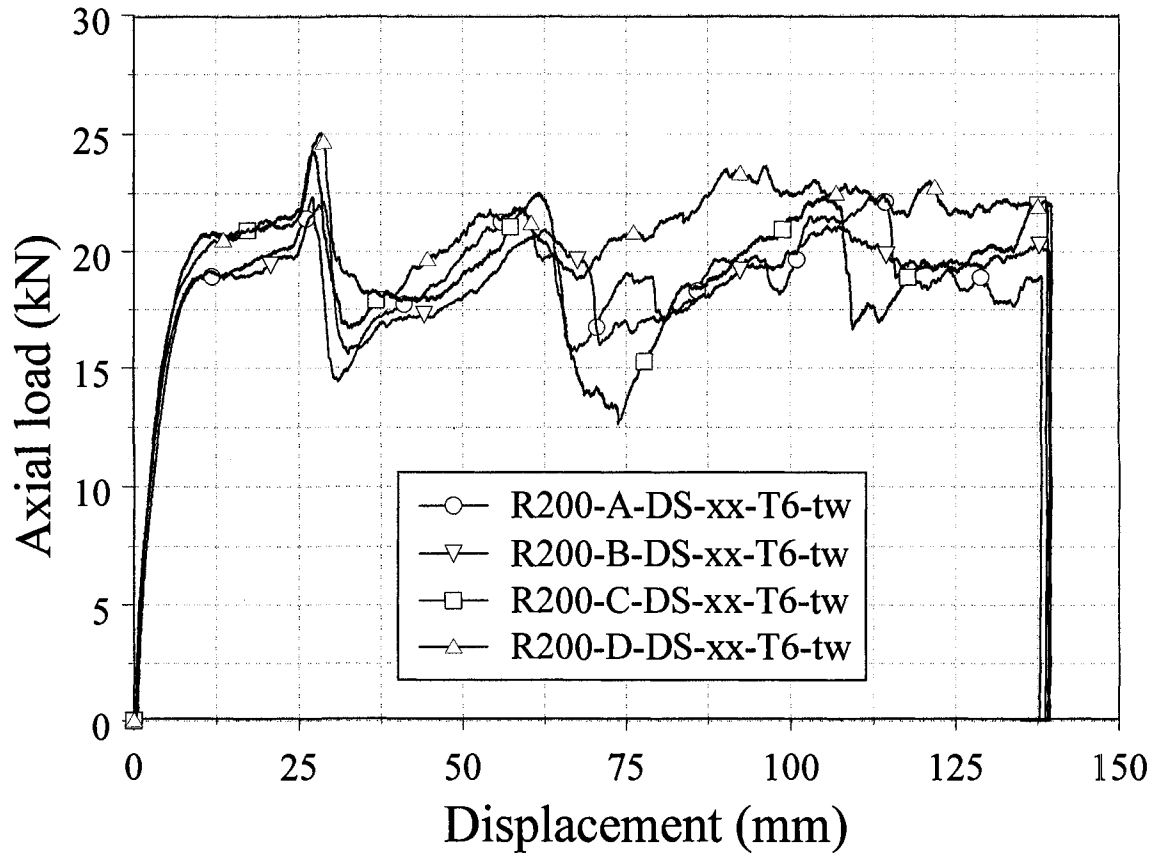


Figure 6.25. The force/displacement responses for the specimen in Groups d-17 through d-20 in the presence of straight deflector.

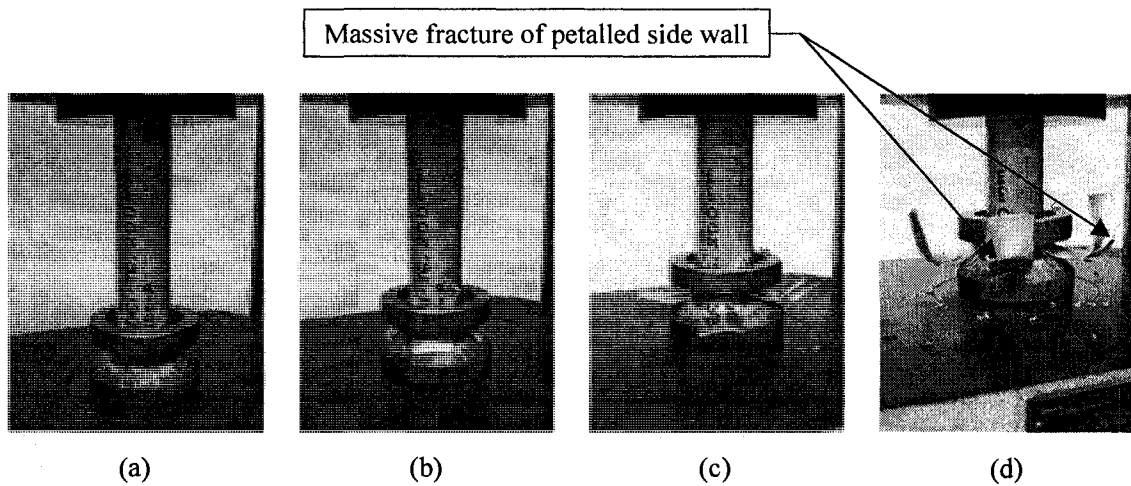


Figure 6.26. Photographs illustrating the experimental cutting process for a representative specimen in Group d-17.

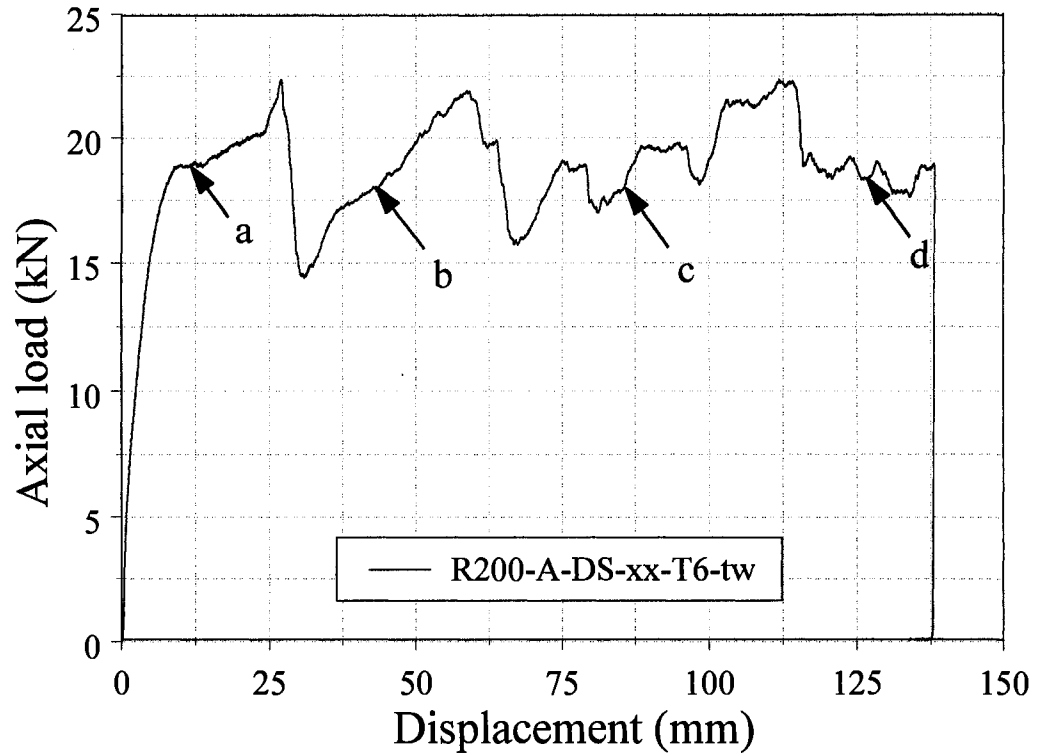


Figure 6.27. Experimentally obtained load/displacement profile for the representative specimen in Group d-17, positions a, b, c and d correspond to photographs in Figure 6.26.

6.3.10 Cutting test results for the specimens in groups d-21 through d-24

Fairly consistent load/displacement responses up to crosshead displacement of 30 mm were observed for the specimens within the groups d-21 through d-24. The force/displacement profiles for representative specimens of each group are shown in Figure 6.28. Photographs of the cutting process for specimen in presence of the curved deflector from group d-22 are illustrated in Figures 6.29(a)–(d). The load/displacement observations for the corresponding images in Figures 6.29(a)–(d) are presented in Figure 6.30. Specimens in groups d-21 through d-24 exhibited similar load/displacement responses and cutting phenomenon to the specimens in groups d-5 through d-8 which were similar temper but wall thickness of 3.175 mm. However, the fluctuation of the cutting force observed for specimens in groups d-21 through d-24 was not observed for specimens in groups d-5 through d-8. This fluctuation of cutting force was due to minor fracture of petalled side wall after side wall came in contact with the curved deflector.

The fracture observed utilizing the curved deflector was less significant compared to the fracture observed using the straight deflector. This phenomenon may be attributed towards the curvature associated with the curved deflector. Very minor influence of cutter blade tip width was observed as shown in Figure 6.28.

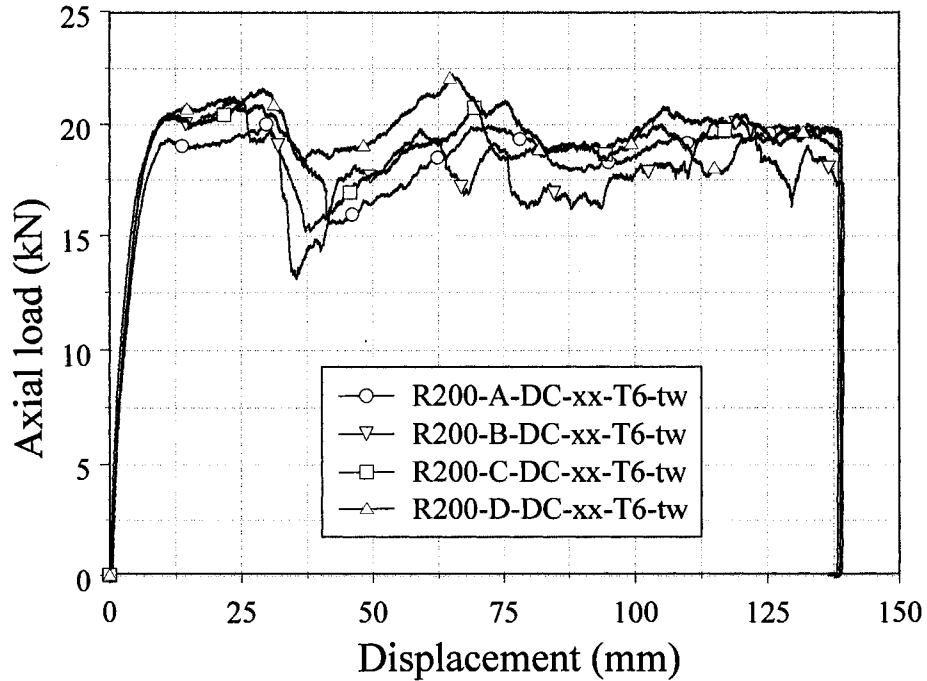


Figure 6.28. The force/displacement responses for the specimen in Groups d-21 through d-24 in the presence of curved deflector.

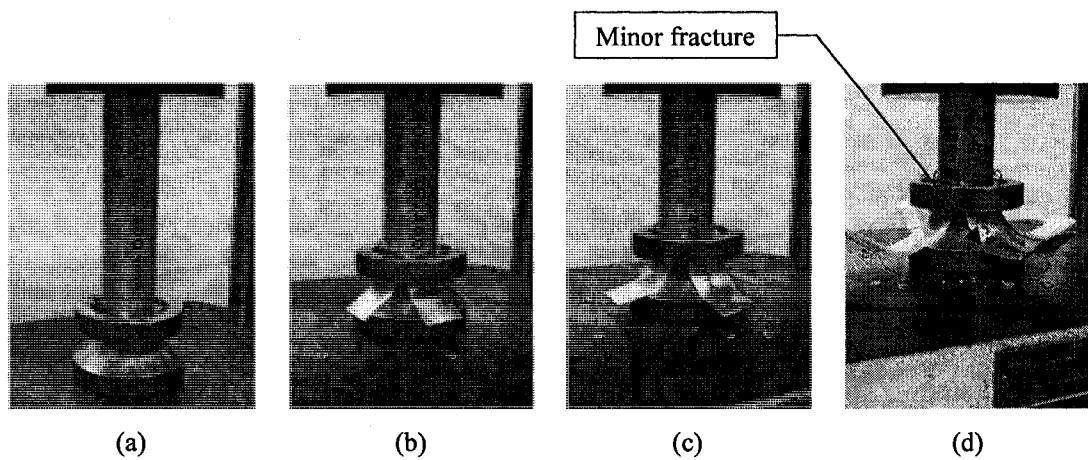


Figure 6.29. Photographs illustrating the experimental cutting process for a representative specimen in Group d-22.

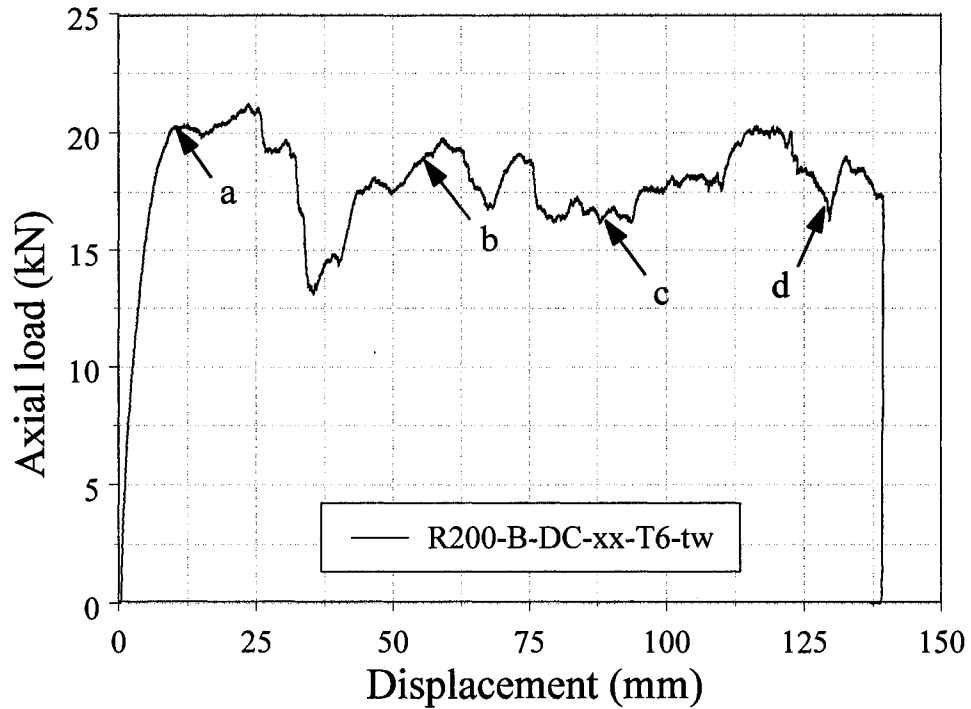


Figure 6.30. Experimentally obtained load/displacement profile for the representative specimen in Group d-22, positions a, b, c and d correspond to photographs in Figure 6.29.

6.3.11 Cutting test results for the specimens in groups d-25 through d-28

The force/displacement profiles for representative specimens from groups d-25 through d-28 are illustrated in Figure 6.31. Photographs of the cutting process for specimen with T4 temper and a wall thickness of 1.587 mm in presence of the straight deflector from group d-25 are illustrated in Figures 6.32(a)–(d). The load/displacement observations for the corresponding images in Figures 6.32(a)–(d) are presented in Figure 6.33. The specimens in groups d-25 though d-28 exhibited similar load/displacement responses and cutting phenomenon to the specimens in groups d-17 through d-20 which were a T6 temper. However, the surge of cutting force when the cut petalled side walls hit the deflector was not significant compared to the observations for the T6 temper specimens. No crack formation on petalled side walls was observed for the T4 temper specimens in the presence of the straight deflector. However, crack formation was observed to be massive for the T6 specimens in groups d-17 through d-20. The first transient cutting phase as noted in Figure 6.31 was observed to occur for

displacements in the range of 0 mm to 18 mm and exhibited a nonlinear increase in the cutting load from 0 kN to approximately 14 kN. As the petalled sidewalls contacted the deflector, the load surged to approximately 19.5 kN and resulted in a second transient cutting phase which was observed to occur with displacements in the range from approximately 19 mm to 30 mm. This increase in load in the second transient cutting phase, which was observed to be within the range from 2 kN to 3 kN for all specimens, was a result of the additional force necessary to initiate flaring process of the vertical cut sidewalls. A notable difference of cutting force was also observed through use of different cutter blade tip widths for the specimens in group d-25 through d-28. The specimens in group d-27, which went through cutter side C, experienced the highest cutting force of approximately 17 kN at cross-head displacement of 24 mm. The specimens in groups d-13 and d-14, which underwent through cutter sides A and B respectively, experienced the least cutting force of approximately 15.3 kN at similar cross-head displacement.

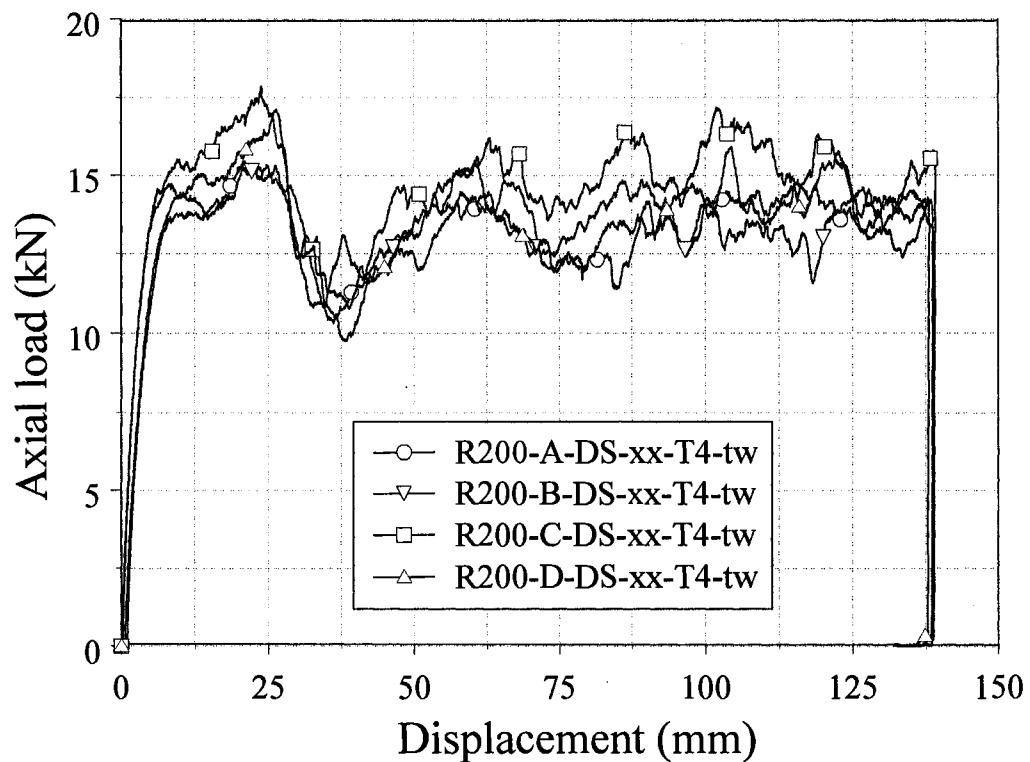


Figure 6.31. The load/displacement responses for the tubes in Groups d-25 through d-28 in the presence of straight deflector.

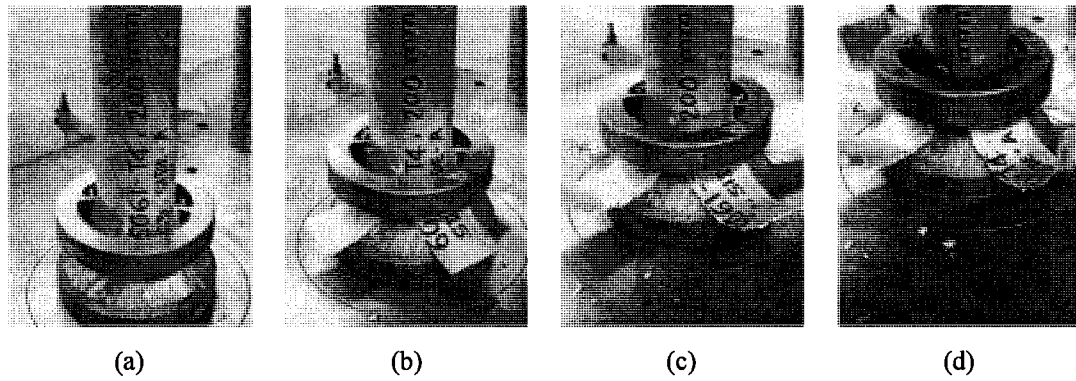


Figure 6.32. Photographs illustrating the experimental cutting process for a representative specimen in Group d-22.

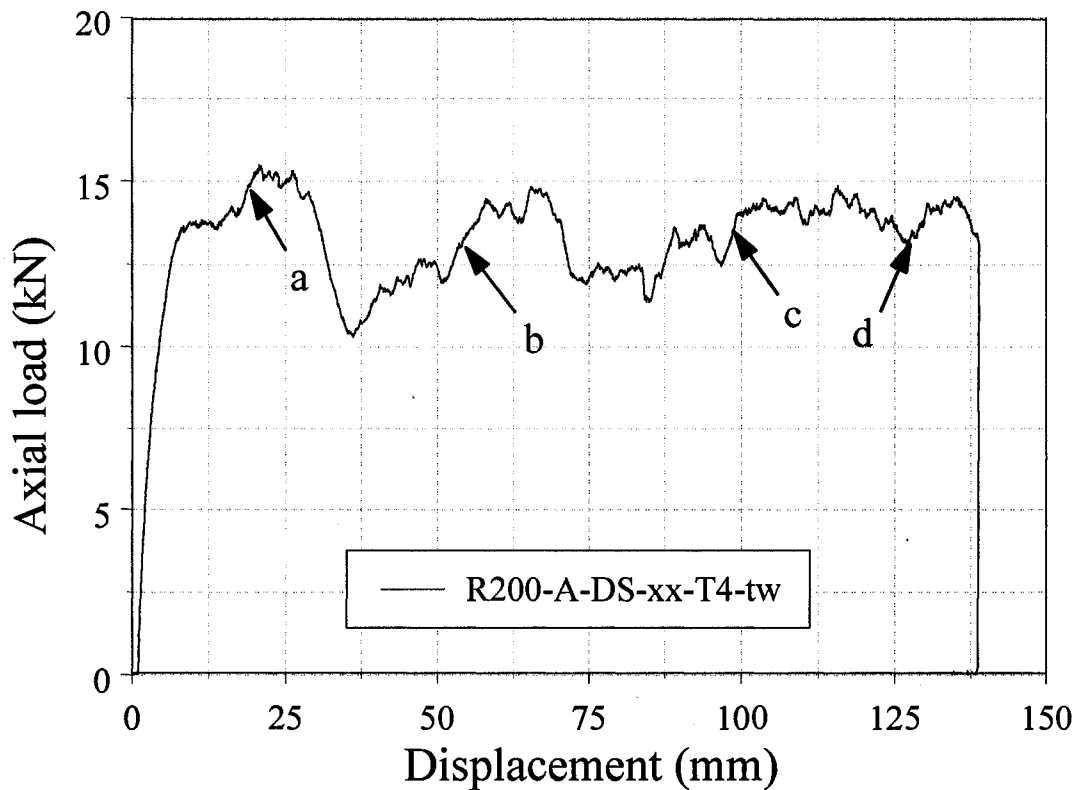


Figure 6.33. The load/displacement profile for the representative specimen from Group d-25, positions a, b, c and d correspond to photographs in Figure 6.32.

6.3.12 Cutting test results for the specimens in groups d-29 through d-32

Fairly consistent load/displacement responses were observed for specimens within groups d-29 through d-32. The force/displacement profiles for representative specimens

from each group are shown in Figure 6.34. The specimens in groups d-29 through d-32 exhibited similar load/displacement responses and cutting phenomenon to the specimens in groups d-21 through d-24 which were the T6 temper conditions. However, the fluctuation of cutting force observed for the specimens in groups d-21 through d-24 was not observed for specimens in groups d-29 through d-32 as no crack formation was observed for specimens with the T4 temper. A notable difference of cutting force was also observed through use of different cutter blade tip widths for the specimens in group d-29 through d-32 as shown in Figure 6.34.

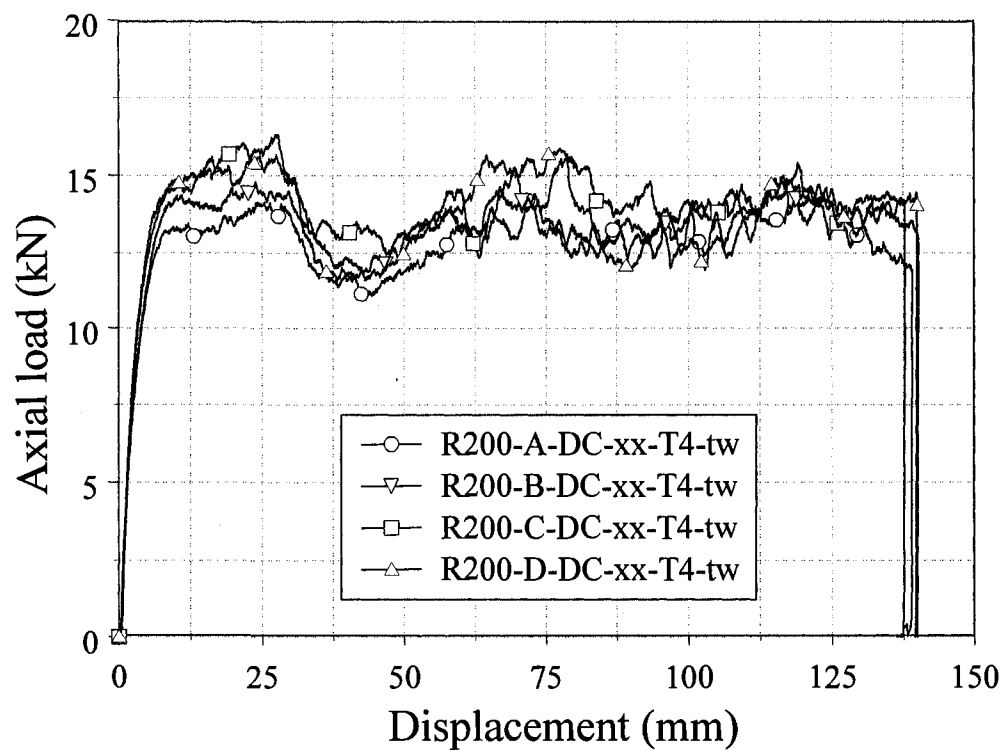


Figure 6.34. The load/displacement responses for the specimen in Groups d-29 through d-32 in the presence of curved deflector.

6.3.13 Cutting test results among all specimens

The load/displacement responses for AA6061-T4 and -T6 round aluminum extrusions with wall thicknesses of 1.587 mm and 3.175 mm under cutting deformation mode utilizing cutter side C are presented in Figure 6.35. The mean cutting forces for

extrusions with both temper conditions and a wall thickness of 3.175 mm were almost double compared with that for the extrusions with a wall thickness of 1.587 mm. The peak cutting forces for the extrusions with wall thickness of 3.175 mm and the T6 and T4 temper conditions were 47.14 kN and 36.4 kN respectively. The approximately 29.5 % reduction of the peak cutting force associated with the T4 temper extrusion was due to lower strength of material in T4 temper. Similar findings were observed for the specimens with a wall thickness of 1.587 mm.

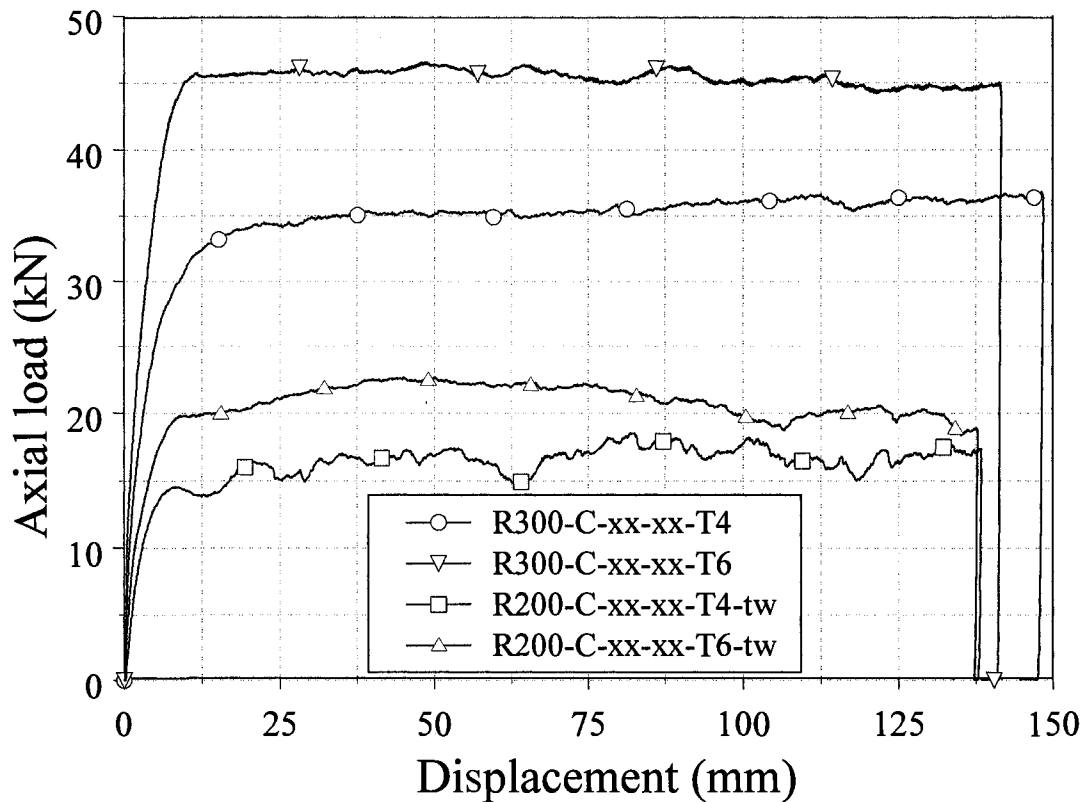


Figure 6.35. Comparison of the load/displacement profiles between the specimens with the T6 and the T4 temper as well as wall thicknesses of 3.175 mm and 1.587 mm.

Comparison of the load/displacement responses for AA6061-T6 round aluminum extrusions with a wall thickness of 3.175 mm utilizing the straight and curved deflector as well as only the cutter are illustrated in Figure 6.36. The maximum peak cutting force of approximately 52.3 kN was observed for the extrusions utilizing the straight deflector. However, the maximum mean cutting force of approximately 43.76 kN was observed for

the specimens using only the cutter. The mean cutting forces in the presence of the straight and curved deflector were 36.47 kN and 38.5 kN respectively. Figure 6.36 clearly illustrates that constant cutting force was observed after initial transition period for the specimens utilizing only the cutter but a massive reduction of the cutting force was observed after petalled side walls contacted the deflectors. The reduction of cutting force during the second phase was more prominent in presence of the straight deflector compared to the curved deflector. This was due to the curvature associated with the curved deflector.

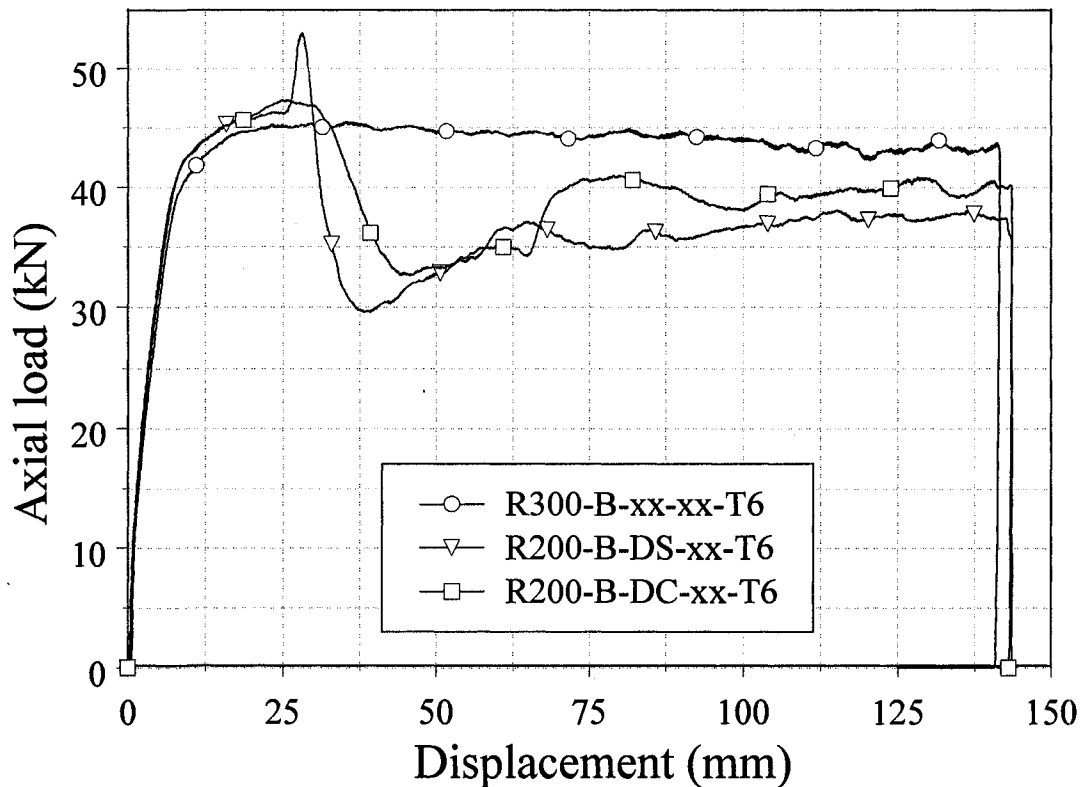


Figure 6.36. Comparison of the load/displacement responses among T6 round extrusions with a wall thickness of 3.175 mm in the presence and without the presence of deflectors.

Comparison of the load/displacement responses for the T4 extrusions with a wall thickness of 3.175 mm utilizing the straight and curved deflectors as well as only the cutter are illustrated in Figure 6.37. Similar trends of the peak and mean cutting forces were also observed for the specimens with the T4 temper compared to the T6 temper

extrusions. The maximum peak cutting force of approximately 39.91 kN was observed for the extrusions utilizing the straight deflector. However, the maximum mean cutting force of approximately 34.21 kN was observed for the specimens using only the cutter. The mean cutting forces in the presence of the straight and curved deflectors were 28.12 kN and 29.62 kN respectively.

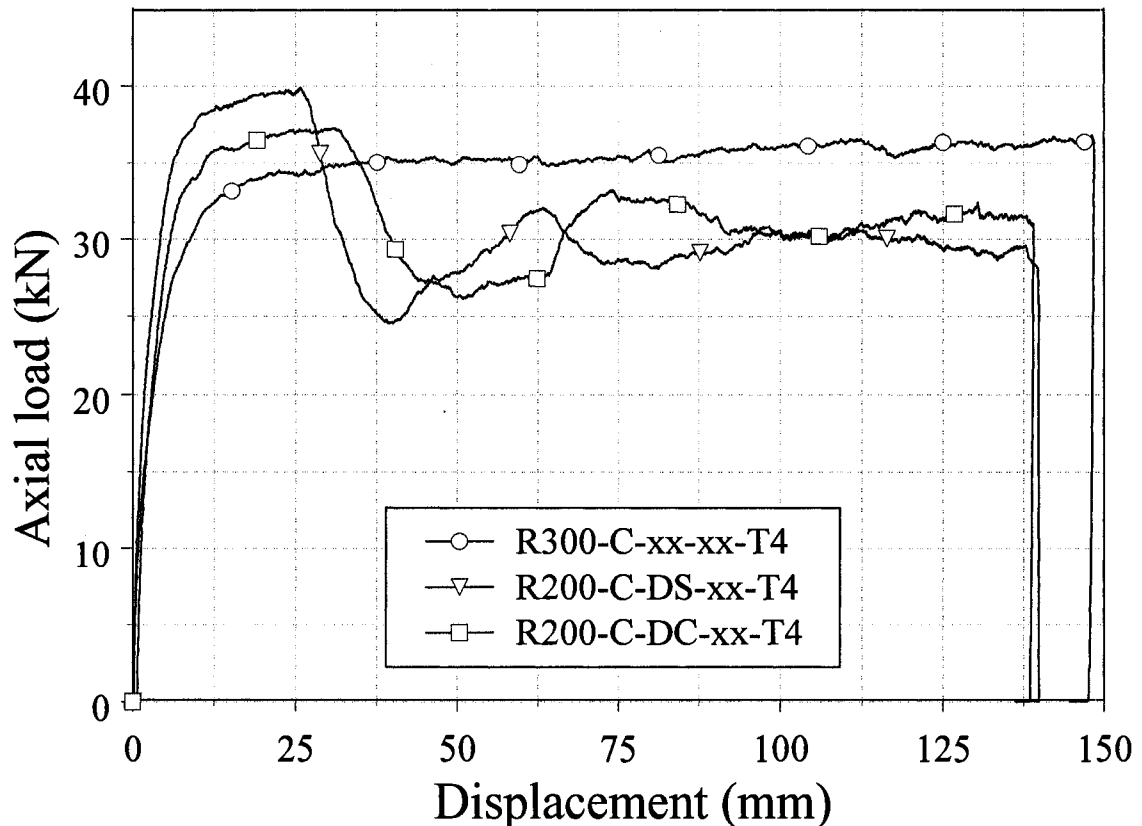


Figure 6.37. Comparison of the load/displacement responses among T4 round extrusions with a wall of thickness 3.175 mm in the presence and without the presence of deflectors.

Comparison of the load/displacement responses for extrusions with both wall thicknesses and the T6 and T4 tempers are utilizing the straight and curved deflector are illustrated in Figure 6.38 and 6.39 respectively. Figure 6.38 clearly demonstrates that similar trends in the load/displacement profiles were observed for the extrusions with wall thicknesses of 1.587 mm and 3.175 mm in presence of the curved deflector. However, the load/displacement profiles for the extrusions with wall thicknesses of 1.587 mm and 3.175 mm were not consistent during the transition period in the presence

of the straight deflector. The surge of cutting force as the result of the contact with wall and the straight deflector was not significant for the specimens with a wall thickness of 1.587 mm compared to the findings of extrusions with a wall thickness of 3.175 mm. In the steady state region (crosshead displacement of 70 mm to the end of the test) the profile of all load/displacement responses were observed to be similar. The fluctuation of the load/displacement responses for extrusions with a wall thickness of 1.587 mm was occurred due to fracture of petalled side walls and also “back and forth” folding of the cut petalled side walls during the cutting. The load/displacement profiles for specimens with both wall thicknesses and the T4 temper followed very similar path in presence of both the straight and curved deflector as shown in Figure 6.39. The mean cutting force after the transition period was observed to be two times larger for the extrusions with a wall thickness of 3.175 mm compared to the specimens with a wall thickness of 1.587 mm.

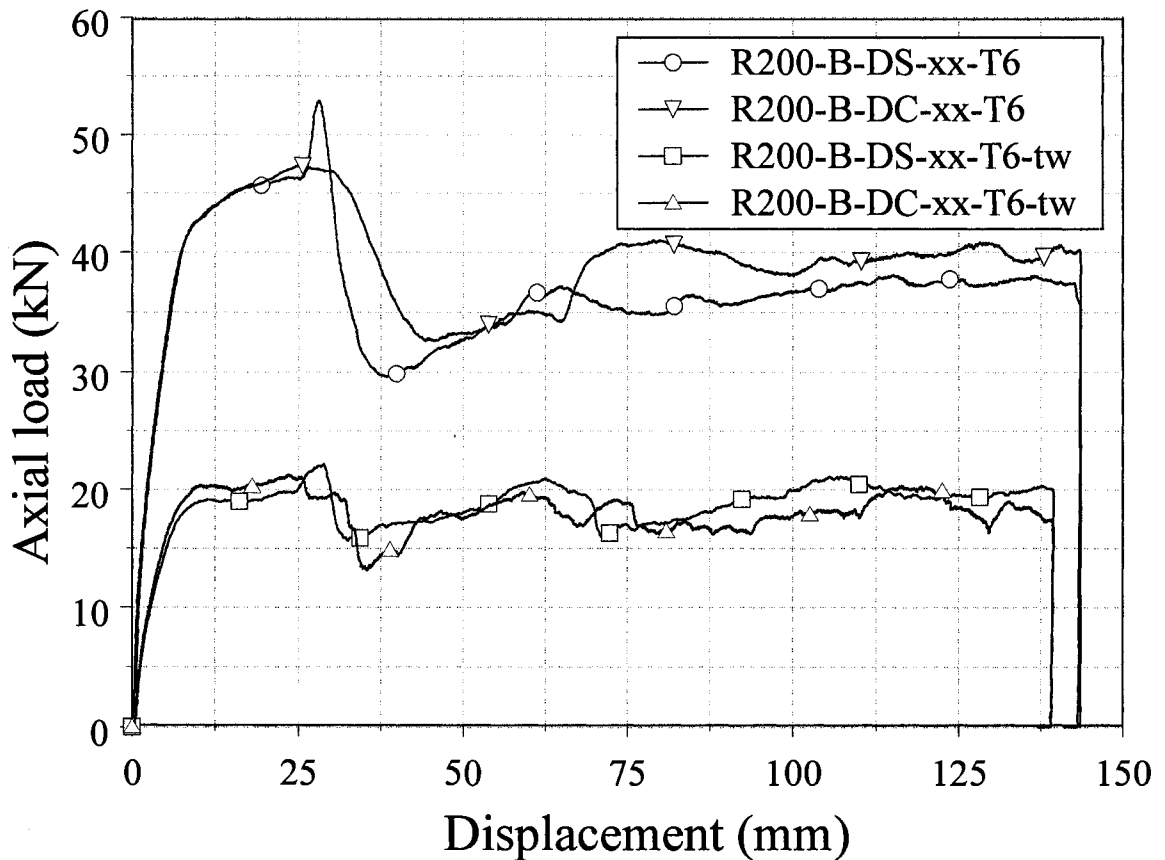


Figure 6.38. Comparison of load/displacement responses for the specimens with both wall thicknesses and T6 temper in presence of the straight and the curved deflectors.

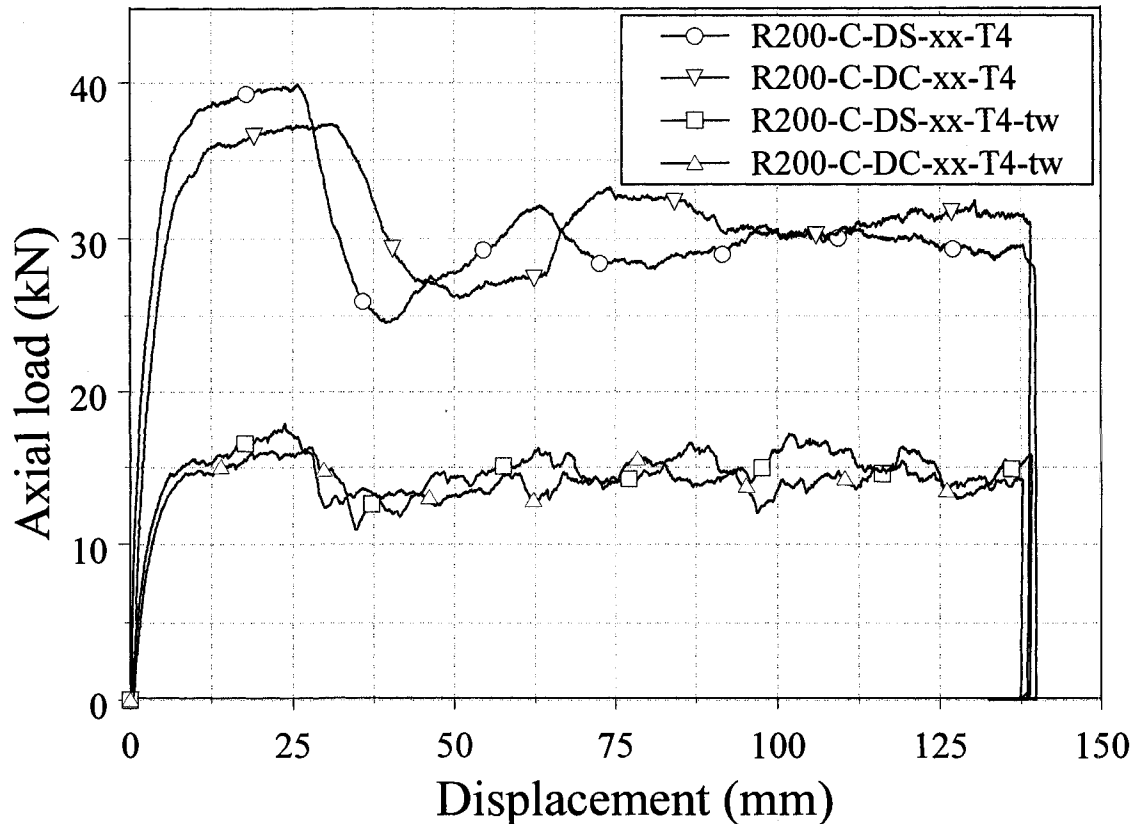


Figure 6.39. Comparison of the load/displacement responses for the specimens with both wall thicknesses and T6 temper in presence of the straight and the curved deflectors.

6.3.14 Comparison of crush performance parameters

This section compares the crush performance parameters of each group considered in this research. For each specimen tested, the crushing force and crosshead displacement were recorded. Post-testing data analysis was completed to determine the peak crush load, the mean crush force, CFE, total energy absorption, SEA and the energy-absorbing effectiveness factor. The mean values of crush parameters for each group utilizing only the cutters are presented in Table 6.4. Table 6.5 summarises the mean values of crush parameters for each group utilizing the cutter as well as straight/curved deflectors.

Table 6.4. Calculated average values of the crush parameters for each group utilizing different cutter sides, extrusions tempers and wall thicknesses.

Group	Specimen ID	Average P_m (kN)	Average P_{max} (kN)	Average CFE (%)	Average TEA (kJ)	Average SEA (kJ/kg)	EF ψ
c-1	R300-A-xx-xx-T4	25.00	28.06	89.07	3.47	9.03	0.109
c-2	R300-B-xx-xx-T4	29.89	32.21	92.70	4.26	10.34	0.120
c-3	R300-C-xx-xx-T4	34.21	36.40	93.97	4.76	12.38	0.131
c-4	R300-D-xx-xx-T4	29.96	32.26	92.80	4.26	11.06	0.130
c-5	R300-A-xx-xx-T6	42.21	45.40	93.08	6.04	15.69	0.181
c-6	R300-B-xx-xx-T6	43.76	46.66	93.80	6.22	15.76	0.154
c-7	R300-C-xx-xx-T6	44.69	47.14	94.80	6.35	16.50	0.159
c-8	R300-D-xx-xx-T6	42.01	44.07	95.32	5.94	16.02	0.158
c-9	R200-A-xx-xx-T4-tw	14.41	16.30	88.35	2.00	15.09	0.178
c-10	R200-B-xx-xx-T4-tw	14.58	18.15	80.63	2.04	15.41	0.181
c-11	R200-C-xx-xx-T4-tw	15.90	18.40	86.47	2.21	16.68	0.199
c-12	R200-D-xx-xx-T4-tw	14.61	16.69	87.50	2.04	15.37	0.185
c-13	R200-A-xx-xx-T6-tw	18.44	21.62	85.24	2.55	19.27	0.191
c-14	R200-B-xx-xx-T6-tw	19.26	21.86	88.05	2.68	20.19	0.202
c-15	R200-C-xx-xx-T6-tw	20.50	22.83	89.84	2.83	21.36	0.208
c-16	R200-D-xx-xx-T6-tw	20.00	21.65	92.34	2.79	21.07	0.206
c-17	R400-A-xx-xx-T4-tw	15.28	16.94	90.20	2.14	8.33	0.095
c-18	R400-A-xx-xx-T6-tw	19.88	22.19	89.6	2.79	10.52	0.102

Table 6.5. Calculated average values of the crush parameters for each group utilizing the cutters and the straight or curved deflector.

Group	Specimen ID	Average P_m (kN)	Average P_{max} (kN)	Average CFE (%)	Average TEA (kJ)	Average SEA (kJ/kg)	EF ψ
d-1	R200-A-DS-xx-T6	35.59	53.38	66.80	5.14	19.91	0.196
d-2	R200-B-DS-xx-T6	36.47	52.31	69.72	5.25	20.47	0.199
d-3	R200-C-DS-xx-T6	37.15	51.46	72.20	5.18	24.28	0.238
d-4	R200-D-DS-xx-T6	36.51	58.15	62.80	5.27	20.53	0.200
d-5	R200-A-DC-xx-T6	36.58	44.97	81.34	5.28	20.60	0.203
d-6	R200-B-DC-xx-T6	38.50	46.94	82.04	5.59	21.79	0.211
d-7	R200-C-DC-xx-T6	39.80	49.93	79.70	5.79	22.57	0.218
d-8	R200-D-DC-xx-T6	37.07	45.76	81.00	5.38	20.98	0.207
d-9	R200-A-DS-xx-T4	23.56	29.74	79.23	3.35	13.08	0.153
d-10	R200-B-DS-xx-T4	21.87	27.47	79.63	3.10	12.08	0.146
d-11	R200-C-DS-xx-T4	28.12	39.91	76.47	3.67	18.57	0.227
d-12	R200-D-DS-xx-T4	26.54	33.65	78.90	3.71	14.47	0.175
d-13	R200-A-DC-xx-T4	24.56	28.59	85.90	3.50	13.63	0.172
d-14	R200-B-DC-xx-T4	26.68	31.10	85.80	3.79	14.79	0.181
d-15	R200-C-DC-xx-T4	29.62	36.19	81.90	4.12	16.06	0.199
d-16	R200-D-DC-xx-T4	27.72	33.46	82.93	3.88	15.13	0.188
d-17	R200-A-DS-xx-T6-tw	18.22	22.38	81.43	2.53	19.06	0.189
d-18	R200-B-DS-xx-T6-tw	18.25	22.14	82.43	2.54	19.14	0.190
d-19	R200-C-DS-xx-T6-tw	18.81	23.40	80.53	2.61	19.67	0.193
d-20	R200-D-DS-xx-T6-tw	20.55	25.06	82.00	2.85	21.49	0.212
d-21	R200-A-DC-xx-T6-tw	17.74	21.01	84.67	2.48	18.66	0.185
d-22	R200-B-DC-xx-T6-tw	17.88	21.13	84.67	2.49	18.78	0.182
d-23	R200-C-DC-xx-T6-tw	19.04	22.09	86.33	2.65	19.98	0.194
d-24	R200-D-DC-xx-T6-tw	18.87	21.65	87.13	2.62	19.79	0.196
d-25	R200-A-DS-xx-T4-tw	13.02	15.24	85.50	1.81	13.65	0.162
d-26	R200-B-DS-xx-T4-tw	13.03	15.40	84.60	1.81	13.66	0.161
d-27	R200-C-DS-xx-T4-tw	14.20	17.01	83.57	1.97	14.90	0.178
d-28	R200-D-DS-xx-T4-tw	13.07	16.00	81.73	1.82	13.69	0.167
d-29	R200-A-DC-xx-T4-tw	13.21	15.11	87.40	1.83	13.83	0.165
d-30	R200-B-DC-xx-T4-tw	13.76	16.16	85.30	1.91	14.38	0.172
d-31	R200-C-DC-xx-T4-tw	13.96	16.53	84.63	1.93	14.57	0.175
d-32	R200-D-DC-xx-T4-tw	13.48	15.85	85.03	1.89	14.21	0.168

6.3.14.1 The peak crush force and the mean crush force

The maximum peak and the mean cutting forces were observed for specimens (with both temper and a wall thickness of 3.175 mm) which underwent cutting with side C with blade tip width of 1.17 mm. Similar findings were also observed for the specimens with a wall thickness of 1.587 mm as illustrated in Table 6.4. These findings demonstrate the influence of cutter blade tip width on crush performance of aluminum extrusions. A higher cutting force can be achieved by increasing cutter blade tip width. The maximum peak and the mean cutting forces were observed to be 47.14 kN and 44.69 kN respectively for the T6 temper specimens with a wall thickness of 3.175 mm. Similar specimens with a T4 temper experienced the peak cutting force of 36.40 kN and the mean cutting force of 34.21 kN. The reduction of the peak and the mean cutting forces by approximately 30% for the T4 temper extrusions can be attributed towards lower strength of the material in T4 temper. The maximum peak and the mean cutting forces for specimens with a wall thickness of 1.587 mm and T6 temper were observed to be 22.83 kN and 20.50 kN respectively. Identical specimens with the T4 temper experienced the peak cutting force of 18.40 kN and the mean cutting force of 15.90 kN.

The maximum peak cutting force was observed to be 51.4 kN for the T6 temper extrusions in the presence of the straight deflector but the maximum mean cutting force was found to be 44.6 kN in the presence of only the cutter. For the identical extrusions with the T4 temper experienced almost the same peak cutting force with or without the presence of the straight/curved deflector but the highest mean cutting force was observed to 34.21 kN utilizing only the cutter. Findings for the 1.587 mm wall thickness extrusions with the T6 temper were not consistent with the findings for extrusions with a wall thickness of 3.175 mm. The maximum peak and the mean cutting forces were observed to 25.06 kN and 20.65 kN for the T6 temper extrusion in presence of the straight deflector utilizing cutter side D with blade tip width of 1.02 mm. However, the findings for the T4 temper extrusions with a wall thickness of 1.587 mm were inline with the findings from identical extrusions with the T6 temper.

6.3.14.2 Total energy absorption and crush force efficiency

The total energy absorption for specimens with the T6 temper ranging from 5.94 kJ to 6.35 kJ and the maximum value was observed utilizing cutter side C. The specimens with the T4 temper, TEA ranging from 3.47 kJ to 4.76 kJ and similar to the T6 temper extrusions the maximum total energy absorption was found using cutter side C. A high CFE ranging from 93.08% to 95.32% was observed for all the specimens with the T6 temper. The CFE observed for the T4 temper was ranging from 89.07% to 93.97%. The findings for the specimens with a wall thickness of 1.587 mm were inline with the findings from identical extrusions with a wall thickness of 3.175 mm as illustrated in Table-6.4. The observed TEA for the T6 temper specimens was ranging from 2.55 kJ to 2.83 kJ and for the T4 temper extrusions ranging from 2.00 kJ to 2.21 kJ. The maximum TEA was observed utilizing cutter side C for both temper conditions. The CFE observed ranging from 85.24% to 92.34% for the T6 temper extrusions and 80.63% to 88.35% for the specimens with the T4 temper.

6.3.14.3 Specific energy absorption and effectiveness factor

The specific energy absorption for the T6 tempered extrusions with a wall thickness of 3.175 mm was ranging from 15.44 kJ/kg to 16.50 kJ/kg. Geometrically identical extrusions but with the T4 tempered, the observed *SEA* was ranging from 9.03 kJ/kg to 12.38 kJ/kg. Incorporating deflectors increased *SEA* by approximately 33% and 35% for the T6 tempered specimens with a wall thickness of 3.175 mm utilizing the straight deflector and the curved deflector respectively. A increase of *SEA* was noticed in presence of the straight and the curved deflector ranging from 36% to 39% for the similar wall thickness extrusions but with the T4 tempered. A higher specific energy observation of approximately 30% was observed for the specimens with a wall thickness of 1.587 mm compared to the identical tempered specimens with a wall thickness of 3.175 mm. The effectiveness factor for the T6 specimens with a wall thickness of 3.175 mm was observed ranging from 0.154 to 0.236. The specimens with the T4 temper, the effectiveness factor was found ranging from 0.109 to 0.227.

6.3.15 Cutting force analysis and comparison with the theoretical prediction

This section details the analysis of steady state cutting forces and compare the experimental findings with the theoretical model developed by Zheng and Wierzbicki [23] as well as Simonsen and Wierzbicki [24]. The flat-plate cutting process utilized in references [23, 24] was generated by a sharp tip wedge, and crack propagation was observed during these tests. However, the present circular tube cutting testing was penetrated by four blunt nose tips of the cutters, and chips instead of crack propagation were found to develop at the tips of the cutter blades. In order to determine the proportion of energy dissipation associated with each mechanism, the circumferential and longitudinal radii of the deformed petalled sidewalls were measured. A circumferential membrane stretching with a deformed average radius of 27.2 mm and a petalled sidewall bending with a deformed average radius of 618.4 mm were observed in the round AA6061-T6 tube cutting tests. However, for AA6061-T4 extrusions a circumferential membrane stretching with a deformed average radius of 26.1 mm and a petalled sidewall outward bending with a deformed average radius of 813 mm were observed. The petalled sidewall bending was mostly due to the eccentric membrane stretching generated by the pushing forces from the contact of cutter blades and the split petalled sidewall, which was not significant compare with the cutting mechanism in consideration of energy dissipation. Although the flat-plate wedge-cutting deformation mode [23, 24] and the present tube cutting deformation bear their own characteristics, the main energy-dissipation systems have much in common. Therefore, the theoretical predictions of the cutting force for the flat-plate wedge cutting are introduced to this research for comparison purposes.

The majority of the cutting tests conducted in this study can be considered stable or clean curling cut. Moreover, the majority of the load/displacement profiles observed in this study appear to be an ideal cutting force response typical of a stable or clean curling cut. The experimentally observed crosshead displacement for the initial transient stage of the cutting process was estimated to be approximately 15 mm for all specimens which exhibited stable or clean curling cutting utilizing cutters only. After that, an average constant cutting force was maintained in the steady-state cutting stage. The

constant cutting force was observed to be dependent upon extrusion temper condition, and cross-sectional geometry. Four energy dissipation mechanisms were observed, namely, a near blade tip cutting deformation mechanism (material separation or fracture in the vicinity of the blade tip), circumferential membrane stretching, petalled sidewall plastic bending and friction due to the interaction between the extrusion and the cutter.

Zheng and Wierzbicki [23] developed a closed form solution for the reaction force after steady-state cutting is reached. The resistance force is given by:

$$F = \left(1.268 \frac{R}{t} \cos \theta \frac{\sigma_0 t^2}{4} + 2 \frac{R+B}{R} \frac{\sigma_0 t^2}{4} + 1.28 \theta^2 \frac{(R+B)^2}{Rt} \cos(\theta/2) \frac{\sigma_0 t^2}{4} \right) \cdot (1 + \mu \cot \theta) \quad (6.1)$$

where R is the rolling radius expressed in equation (6.2),

$$R = B \sqrt{\frac{2(t/B) + 1.28 \theta^2 \cos(\theta/2)}{1.268 \cos \theta + 1.28 \theta^2 \cos(\theta/2)}} \quad (6.2)$$

In equation (6.2), B is one-half of the wedge shoulder width.

Simonsen and Wierzbicki [24] conducted a closed form solution similar to Zheng and Wierzbicki [23] for the reaction force after steady-state cutting is obtained. The resistance force was found to be:

$$F = \left(\frac{0.64}{\sqrt{3}} \sigma_0 t R \cos^2 \theta (1 + 0.55 \theta^2) + \frac{\sigma_0 t^2 (B+R)}{\sqrt{3} R \cos \theta} + \frac{2}{\sqrt{3}} \sigma_0 t B \theta \right) \cdot \left(1 - \frac{\mu}{\sin \theta + \mu \cos \theta \cos(\theta/2)} \right)^{-1} \quad (6.3)$$

with the roll radius R determined through equation (6.4)

$$R = \sqrt{\frac{Bt}{0.64(1 + 0.55 \theta^2) \cos^3 \theta}} \quad (6.4)$$

With respect to the current study, the first two terms in the first parentheses of the expressions (6.1) and (6.3) are cutting resistance forces associated with the near blade tip cutting mechanism (or fracture) and circumferential membrane stretching. The third term in the first parentheses is the far field flap bending, which was not observed in the current

research and is assumed to be negligible. The term in the second parentheses is a factor due to the friction energy dissipation mechanism.

Energy associated with the outward plastic bending of the petalled sidewalls can be estimated by assuming an elastic perfectly plastic material behaviour. The fully plastic bending moment was calculated as:

$$M_o = \frac{2\pi(r)\sigma_o t^2}{4} \quad (6.5)$$

where r is the central radius and t is the thickness. Hence, the cutting resistance force associated with the outward plastic bending of the petalled sidewalls can be estimated using the following expression:

$$F = \frac{2\pi(r)\sigma_o t^2}{R_l} \quad (6.6)$$

where R_l is the longitudinal radius of the petalled sidewall after bending.

The theoretical predictions and the experimental findings of the mean cutting resistance force at the steady state condition for AA6061-T4 and -T6 round tubes are presented in Table 6.6. It should be noted that T4 temper extrusions with a wall thickness of 1.587 mm exhibited characteristics of braided cutting, which are not applicable to the theory presented above and hence have not been presented. To the best of the authors' knowledge there exists no theory to predict the cutting force for braided cutting. It can be found that the theoretical predictions agree well with the experimental findings for clean cutting.

In order to determine the proportion of energy dissipation associated with each mechanism, the circumferential and longitudinal radii of the deformed petalled sidewalls were measured. Based upon these measurements, combined with the theory presented in equations (6), (8), and (11), the proportion of energy dissipation is presented in Table 6.7 for the different material tempers and wall thicknesses considered. The coefficient of friction used in the analyses completed was 0.3.

It is expected to find that the percentage contribution of material fracture to the total energy dissipation for AA6061-T4 is lower than that for AA6061-T6 primarily due to the lower yield strength and greater work hardening characteristics of AA6061 T4. It is believed that the same material characteristics is also a result of the larger proportional value associated with the circumferential stretching for AA6061-T4 compared to the AA6061-T6 material. The proportional value of the petalled sidewall plastic bending for specimens with a T4 temper is almost equal to that for specimens with a T6 temper.

Table 6.6. Steady state cutting resistance force comparison between experimental findings and theoretical predictions.

Research group	P_m (kN)			
	6061-T4 (3.175mm)	6061-T6 (3.175mm)	6061-T4 (1.587mm)	6061-T6 (1.587mm)
Zheng and Wierzbicki [23]	32.89	40.77	Braided	13.38
Simonsen and Wierzbicki [24]	35.92	44.58	cutting	15.08
Present study	31.32	45.58	observed	19.55

Table 6.7. Proportion energy dissipation for each mechanism.

Energy dissipation mechanism	Percentage energy dissipation (%)			
	6061-T4 (3.175mm)	6061-T6 (3.175mm)	6061-T4 (1.587mm)	6061-T6 (1.587mm)
Material fracture	8.1	5.4	Braided	1.5
Circumferential stretching	59.2	29.5	cutting	74.7
Friction	32.3	64.6	observed	23.3
Petalled sidewall bending	0.4	0.5		0.5

6.4 Cutting tests results and discussion utilizing dual cutter configuration

In order to enhance the cutting resistance force, an investigation into the load/displacement and energy dissipation characteristics of AA6061-T4 and -T6 extrusions has been completed by imposing a two stage cutting process on the concentric extrusions. Additionally, to control the onset of the second stage of the two stage cutting process, research into the use of some degree of spacing between cutters has also been completed. Finally, to control cut sidewall bending during the two stage cutting process, use of deflectors, with curved and straight profiles, have also been employed. Although three experimental tests were completed for each group listed in Table 6.8 and Table 6.9 and two tests were completed for each group listed in Table 6.10 except groups s-4, s-7 and s-8, the load/displacement observations for all specimens within each group were fairly consistent. For this reason and for greater clarity, only a representative specimen from each group was selected for illustration and discussion purposes. The load/displacement profiles of all three tests within groups m-1, m-4, m-7, m-11, n-1, n-4, n-7, n-10, s-2 and s-5 are presented in Appendix A to demonstrate repeatability of the tests.

6.4.1 Cutting test results for the specimens in groups m-1 through m-3

The observed load/displacement profiles for representative AA6061-T6 specimens from groups m-1 through m-3 are illustrated in Figure 6.40. Photographs of the experimental cutting process for a representative AA6061-T6 specimen from group m-2 are illustrated in Figure 6.41(a)-(d). The load/displacement observations for the corresponding images in Figure 6.41(a)-(d) are presented in Figure 6.42.

The experimental tests showed that the cutter penetrated through the sidewall of the specimens and develop highly localized plastic deformation in the vicinity of the cutting blades where cutting chips were formed. It is evident from the force/displacement profiles that the cutting phenomena can be referred to stable or clean curling cut [24]. No crack propagation was observed in any tests. As cutting progressed, petalled sidewalls bent slightly outwards as a result of the interaction between the first cutter blades

shoulder and the tube sidewalls. After approximately 20 mm crosshead displacement, equal to the thickness of the cutter, the cut petalled side walls contacted the second cutter blades and the total cutting load surged to approximately twice the steady-state cutting load for a single cutter configuration. The load/displacement responses in Figure 6.52 clearly demonstrate that the dual stage cutting appears to be the superposition of two single stage cutting processes. The cutter side combination CA (1.17 mm and 1.01 mm) demonstrated approximately 8% higher cutting force compared to other two cutter side combinations during the first stage of cutting process. However, the magnitude of the cutting force in the second stage was observed to be very consistent amongst all cutter side combinations. The steady-state cutting was achieved after 32 mm of crosshead displacement and the average steady state cutting force was found to be approximately 90 kN.

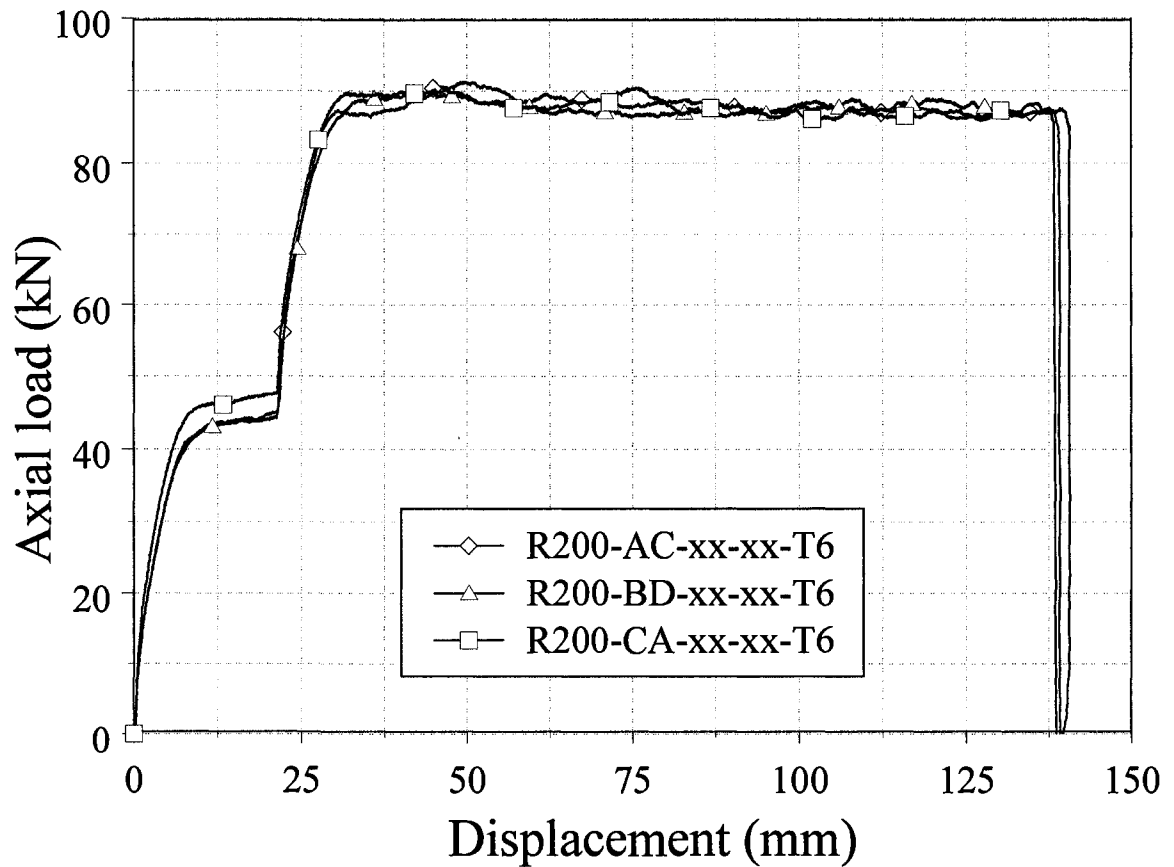


Figure 6.40. Experimentally observed load/displacement responses for representative specimens from Groups m-1 through m-3.

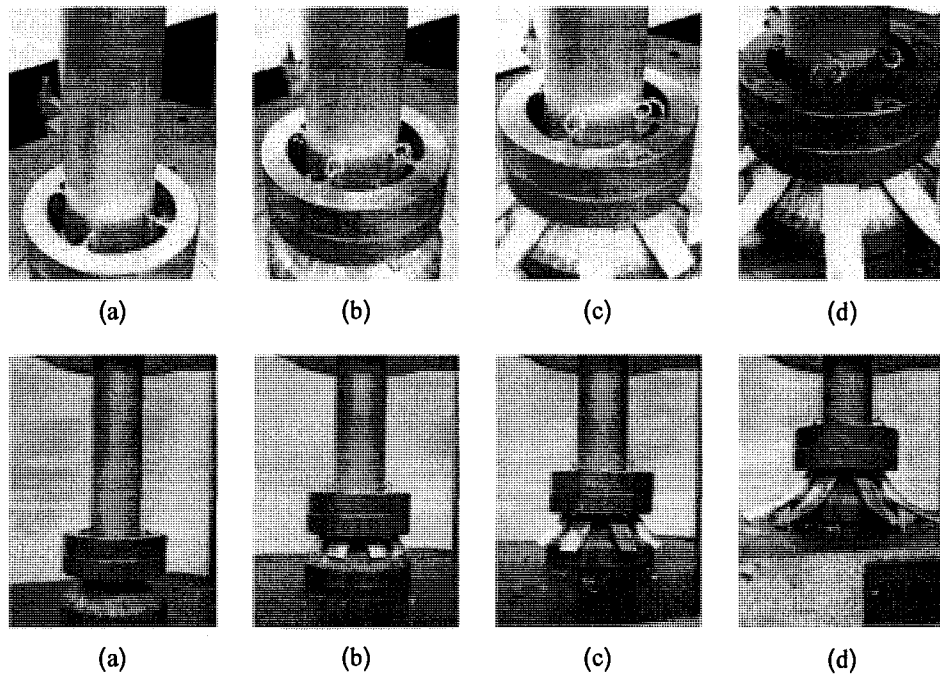


Figure 6.41. Photographs illustrating the experimental cutting process for a representative specimen in Group m-2 (top and bottom views).

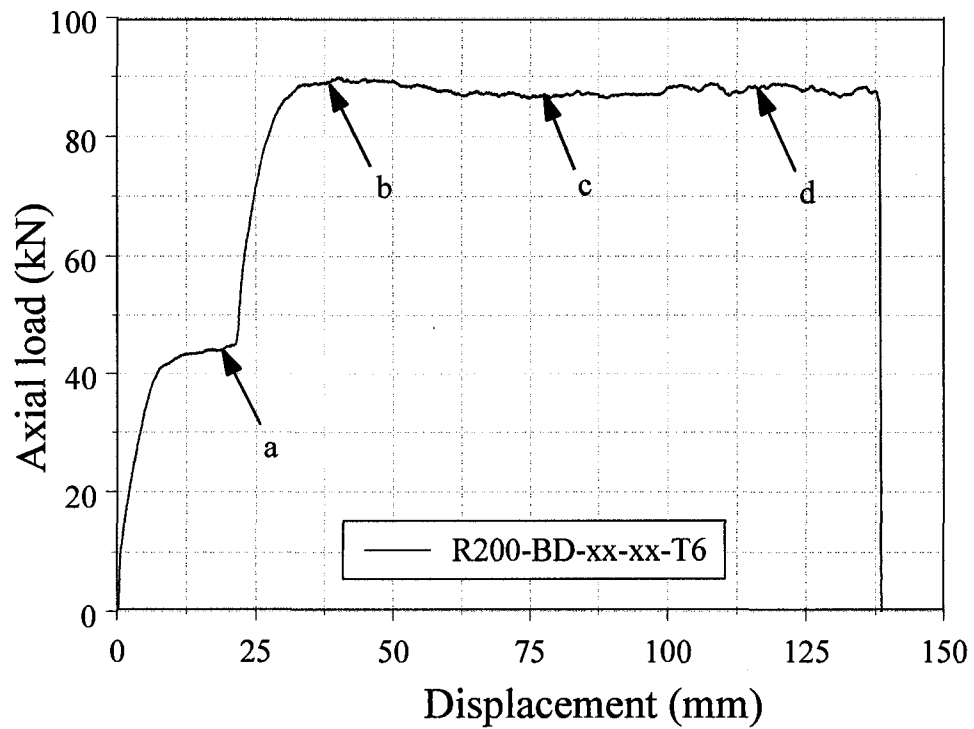


Figure 6.42. Experimentally obtained load/displacement profile for the representative specimen in Group m-2, positions a, b, c and d correspond to photographs in Figure 6.41.

6.4.2 Cutting test results for the specimens in groups m-4 through m-6

Specimens used in groups m-4 through m-6 were identical to the specimens utilized in groups m-1 through m-3. In addition to cutters, a straight deflector was incorporated to study the influence of deflector on the load/displacement response. The force/displacement profiles for representative specimens of each group are shown in Figure 6.43. Photographs of the experimental cutting process for a representative AA6061-T6 specimen from group m-4 are illustrated in Figure 6.44(a)-(d). The load/displacement observations for the corresponding images in Figure 6.44(a)-(d) are presented in Figure 6.45.

The stability of the cutting process and the load/displacement profiles for the specimens in groups m-4 through m-6 appeared to be very similar to the observations from the specimens in groups m-1 through m-3. However, a sharp rise in cutting force was observed at 52 mm crosshead displacement when cut petalled side walls hit the straight deflector. This increase in the load was observed to be within the range from 8 kN to 10 kN for all specimens, was a result of the additional force necessary to initiate flaring process of the vertical cut sidewalls. A gradual reduction of cutting force from the peak cutting force was observed over the displacement of approximately 58 mm to 86 mm. The cutting force was observed to increase slightly after a crosshead displacement of approximately 87 mm until 105 mm, consistent to the single stage cutting process after side walls/ deflector contact is fully completed. Finally, the deformation process reached a steady state cutting phase after a crosshead displacement of approximately 106 mm with an approximate resistance force of 90 kN for all tests considered with the straight deflector.

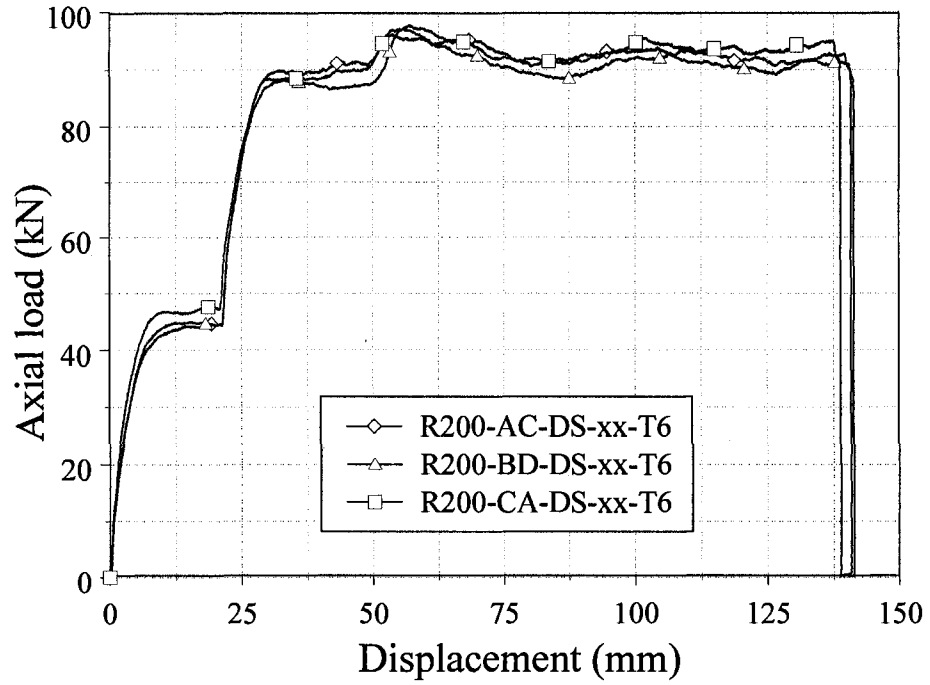


Figure 6.43. The load/displacement profiles for the representative specimens from Groups m-4 through m-6 in presence of the straight deflector.

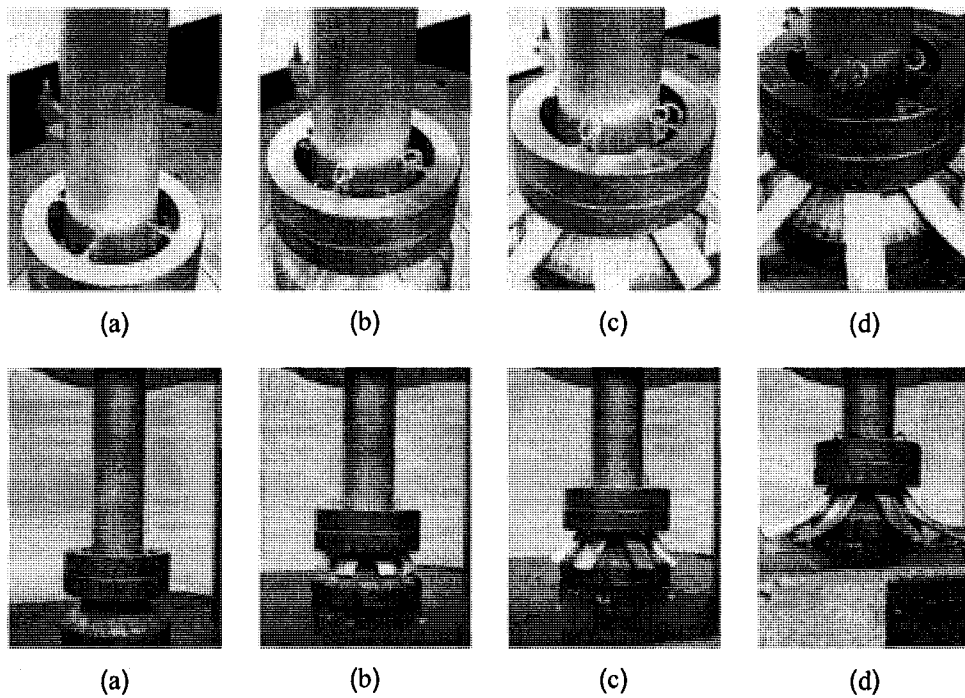


Figure 6.44. Photographs illustrating the experimental cutting process for a representative specimen in Group m-2 (top and bottom views).

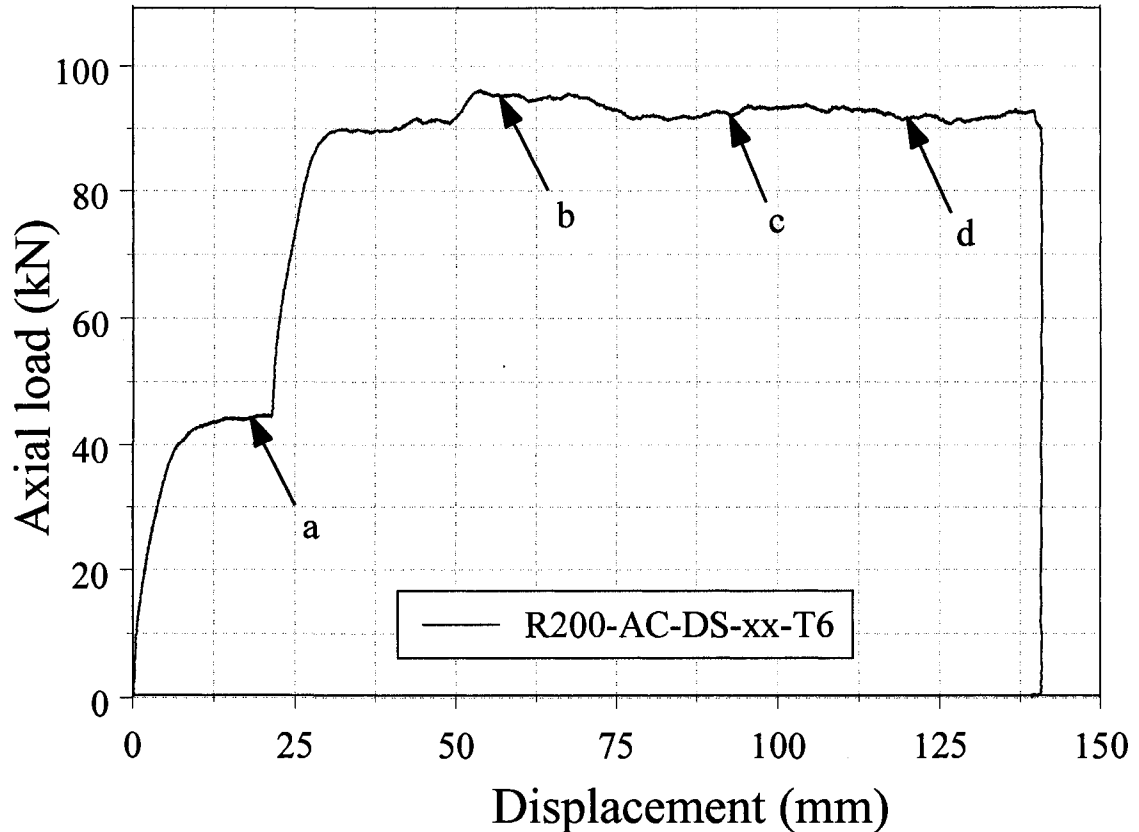


Figure 6.45. The load/displacement response for the representative specimen from Group m-4, positions a, b, c and d correspond to photographs in Figure 6.44.

6.4.3 Cutting test results for the specimens in groups m-7 through m-9

Fairly consistent load/displacement responses up to crosshead displacement of 50 mm were observed for specimens within the groups m-7 through m-9. A minor inconsistency in the load/displacement profiles were noticed in between 52 mm to 85 mm displacement domain. Consistency in findings was again observed after 90 mm displacement to the end of the test. Figure 6.46 illustrates the load/displacement behaviour of representative specimens within group m-7 through m-9. Photographs of the experimental cutting process for a representative specimen from group m-7 are illustrated in Figure 6.47(a)-(d). The load/displacement observations for the corresponding images in Figure 6.47(a)-(d) are presented in Figure 6.48.

Specimens in groups m-7 through m-9 exhibited similar load/displacement responses and cutting phenomenon to the specimens in groups m-4 through m-6. However, it was observed that the significant increase in cutting force previously observed in groups m-4 through m-6, when contact with the deflector was initiated, reduced considerably with the use of the curved deflector. The reduction of the cutting force was caused by the curvature associated with the curved deflector. In addition, the reduction in cutting force after initial contact with the deflector occurred over a longer displacement with the curved deflector compared to the straight deflector. Flaring of the specimens within groups m-7 through m-9 were more gradual than observed for the specimens within groups m-4 through m-6. The cutting process reached a steady-state phase after a crosshead displacement of approximately 95 mm with an approximate resistance force of 90 kN for all the specimens within these groups. The cutting force was maintained constant until testing was completed.

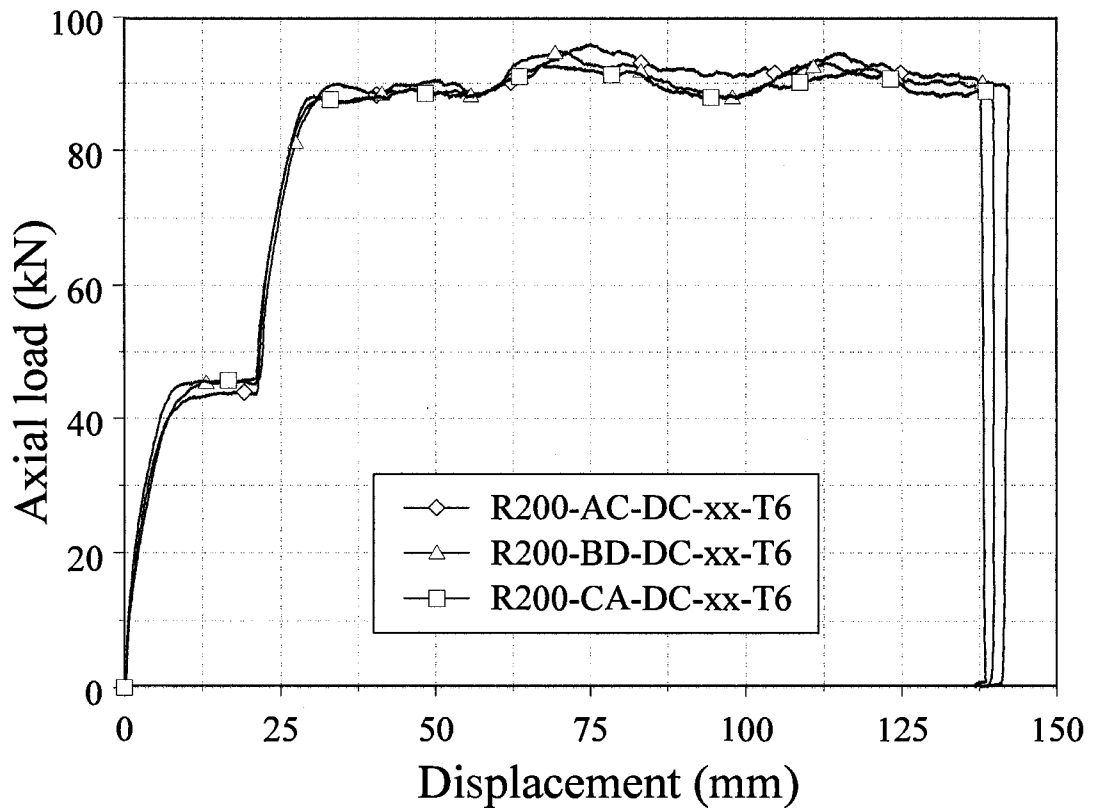


Figure 6.46. The load/displacement profiles for the representative specimens from Groups m-7 through m-9 in the presence of curved deflector.

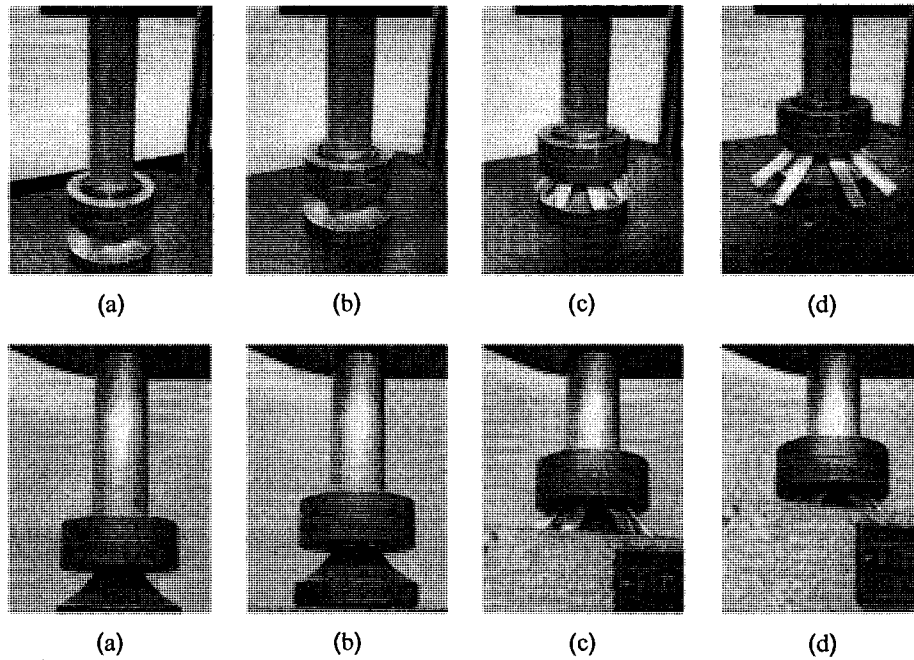


Figure 6.47. Photographs illustrating the experimental cutting process for a representative specimen in Group m-7 (top and bottom views).

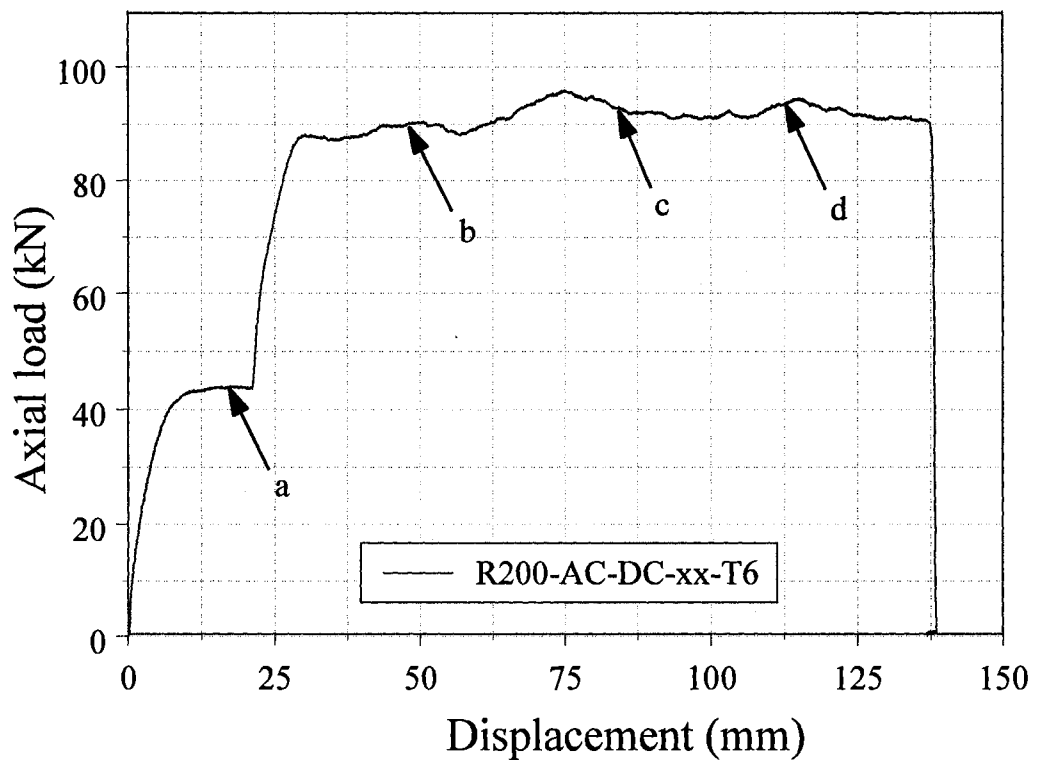


Figure 6.48. The load/displacement response for the representative specimen from Group m-7, positions a, b, c and d correspond to photographs in Figure 6.47.

6.4.4 Cutting test results for the specimens in groups m-10 through m-12

The load/displacement profiles for representative specimens of each group are shown in Figure 6.49. Photographs of the experimental cutting process for a representative AA6061-T4 specimen from group m-10 are illustrated in Figure 6.50(a)-(d). The load/displacement observations for the corresponding images in Figure 6.50(a)-(d) are presented in Figure 6.51.

No significant variations in the load were observed to occur over the first stage of cutting process. However, the extrusions without presence of the straight/curved deflector completely failed to go through the second stage cutting. This failure may be associated with shifting of the cutters or an instability during the cutting process. Incorporating the straight/curved deflector improved stability of the cutting process and the extrusions in groups m-11 and m-12 completed the second stage cutting process. The cutting force surged to 84 kN from 76 kN at 60 mm crosshead displacement when cut petalled side walls contacted the straight deflector. The increase in cutting force in the presence of the curved deflector was relatively less compared to the straight deflector and the increase took place over a longer displacement. After approximately 80 mm crosshead displacement, responses were observed to be very consistent.

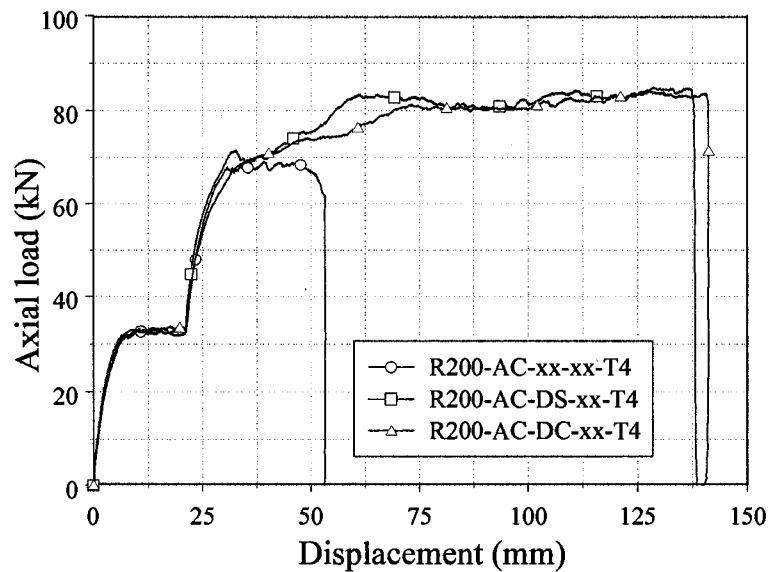


Figure 6.49. The load/displacement profiles for the representative specimens from Groups m-10 through m-12.

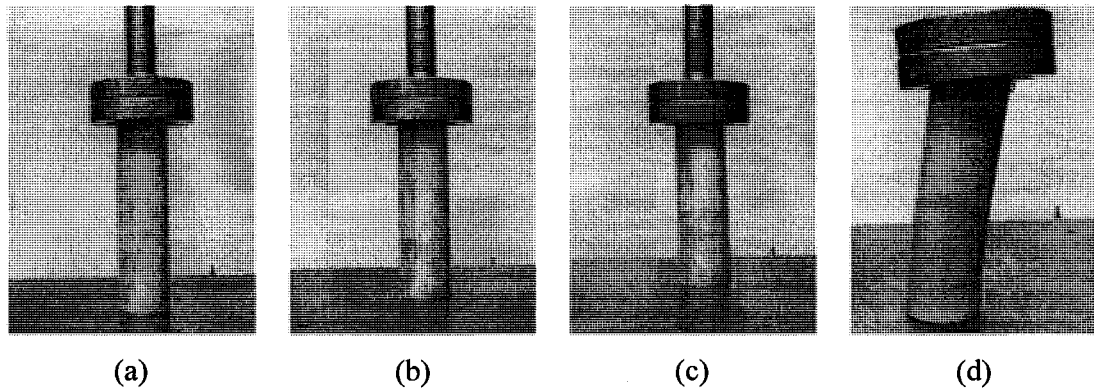


Figure 6.50. Photographs illustrating the experimental cutting process for a representative specimen in Group m-10.

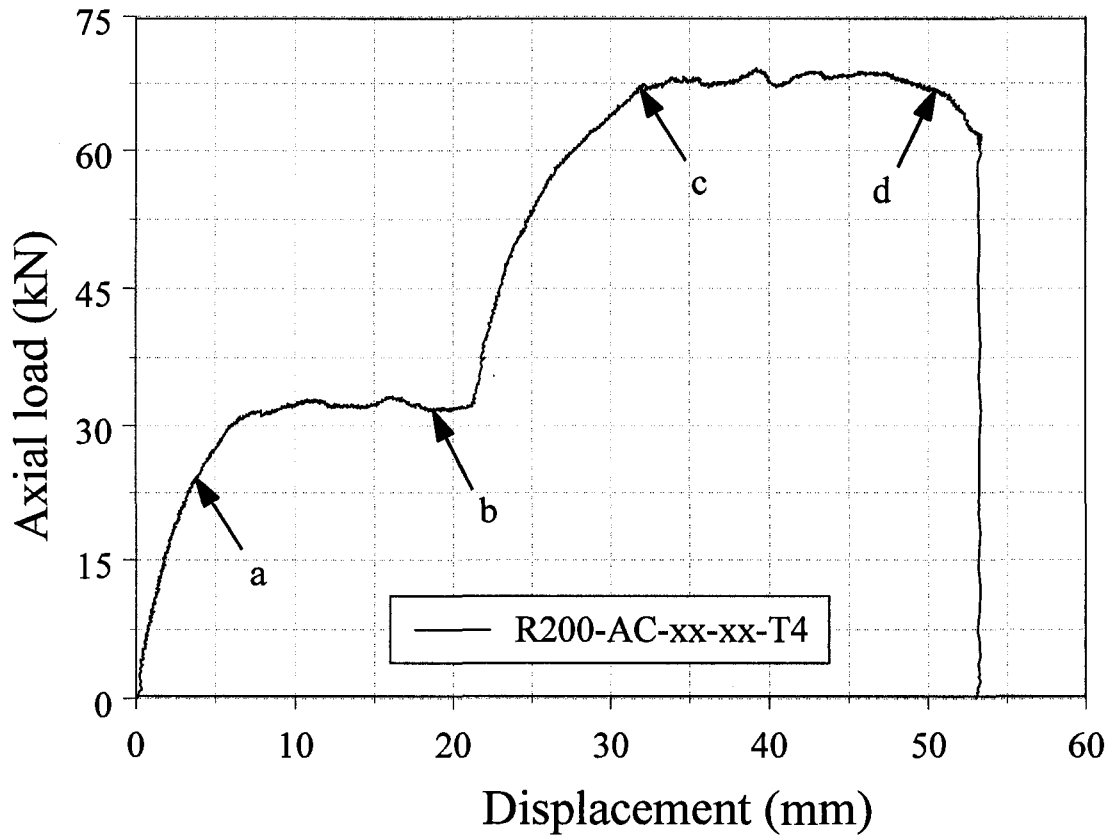


Figure 6.51. The load/displacement profile for the representative specimen from Group m-10, positions a, b, c and d correspond to photographs in Figure 6.50.

6.4.5 Cutting test results for the specimens in groups m-13 through m-15

The observed load/displacement responses for representative specimens of AA6061-T6 extrusions with a wall thickness of 1.587 mm in groups m-13 through m-16 are illustrated in Figure 6.52. Photographs of the cutting process for specimen in presence of the straight deflector from group m-13 are illustrated in Figures 6.53(a)–(d). The load/displacement observations for the corresponding images in Figures 6.53(a)–(d) are presented in Figure 6.54. Photographs of the deformation process illustrated in-word and out-word bending as well as twisting of the cut petalled side walls. After approximately 30 mm crosshead displacement the load/displacement profiles in Figure 6.52 clearly demonstrates inconsistency in cutting force for all specimens in groups m-13 through m-16. The cutting deformation behaviour was more representative of braided cut [24] with ‘back and forth’ folding of cut side walls. The fluctuation of cutting force after 30 mm displacement may be associated with very thin extrusion wall thickness of 1.587 mm.

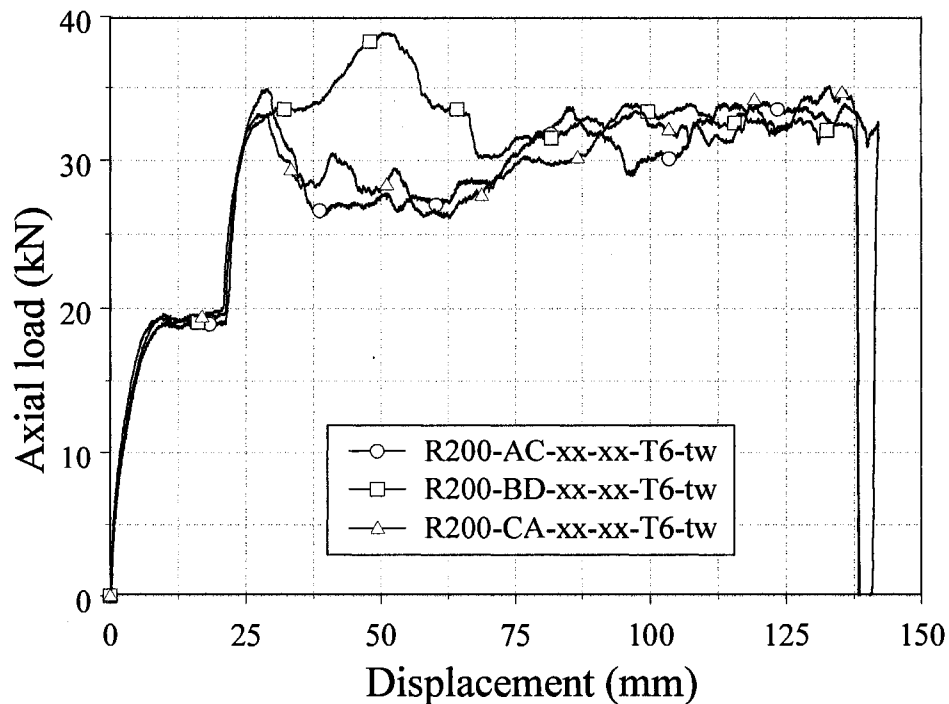


Figure 6.52. The load/displacement profiles for the representative specimens from Groups m-13 through m-15.

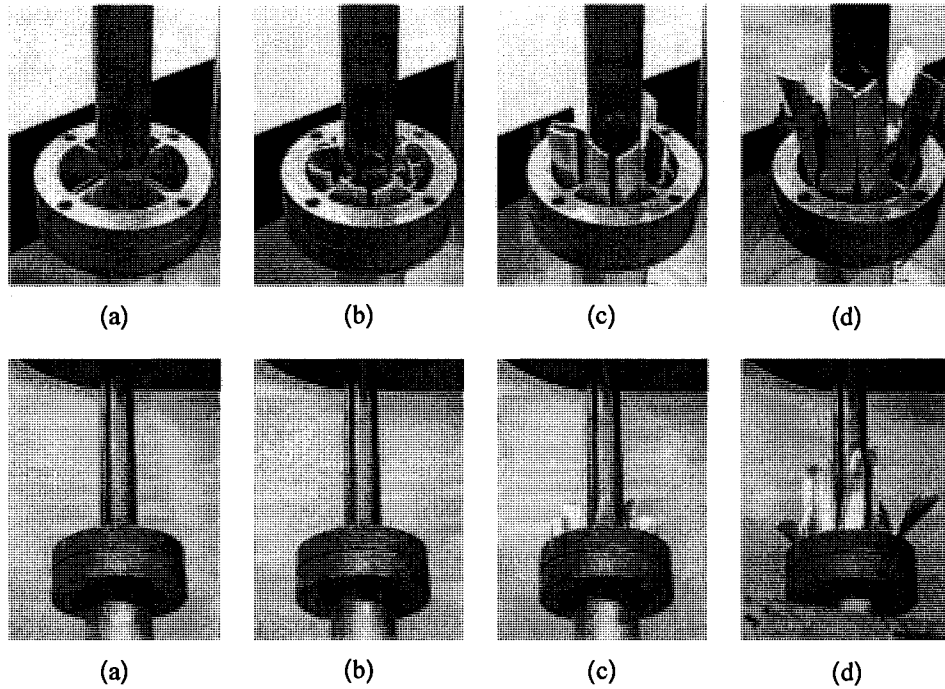


Figure 6.53. Photographs illustrating the experimental cutting process for a representative specimen in Group m-13 (top and bottom views).

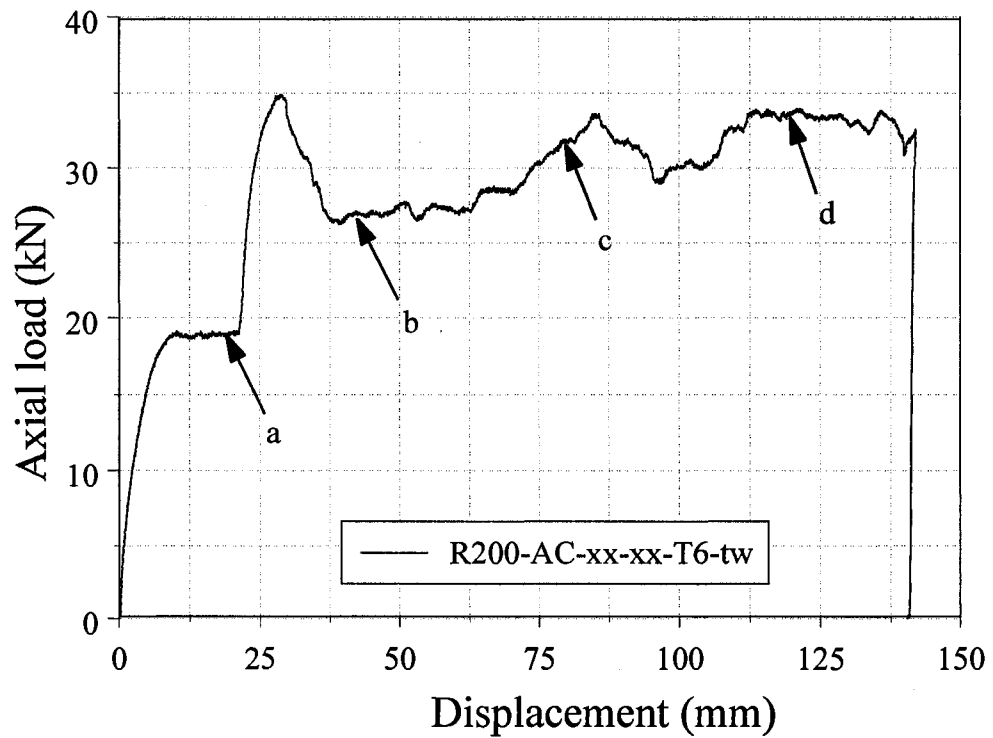


Figure 6.54. The load/displacement profile for the representative specimen from Group m-13, positions a, b, c and d correspond to photographs in Figure 6.53.

6.4.6 Cutting test results for specimens in groups m-16 through m-18

A straight deflector was incorporated in edition to cutters in these tests to observe whether edition of deflector can improve the profile of cutting force. But inconsistent load/displacement responses were again observed for specimens within the groups m-16 through m-18. After 30 mm of crosshead displacement, fluctuation of cutting force was observed until end of the test for all specimens in group m-16 through m-18. The force/displacement profiles for representative specimens of each group are shown in Figure 6.55. Photographs of the experimental cutting process for a representative from group m-17 are illustrated in Figure 6.56(a)-(d). The load/displacement observations for the corresponding images in Figure 6.56(a)-(d) are presented in Figure 6.57.

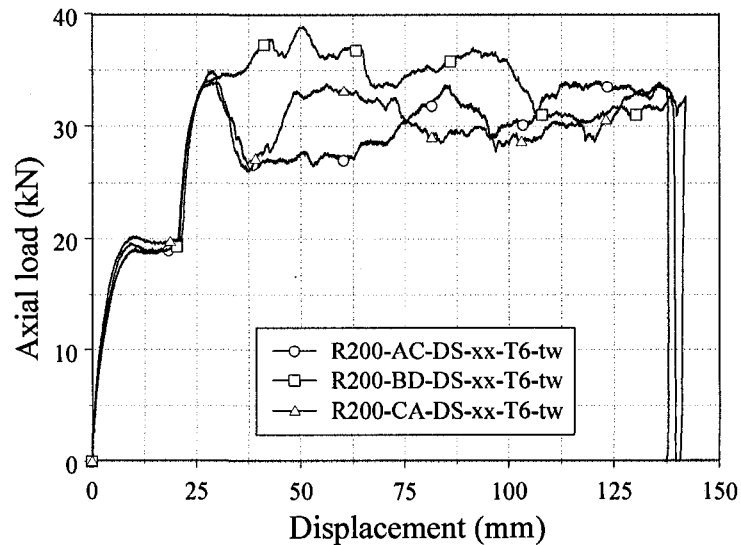


Figure 6.55. Experimentally obtained load/displacement profiles for the specimens in Group m-16 through m-18.

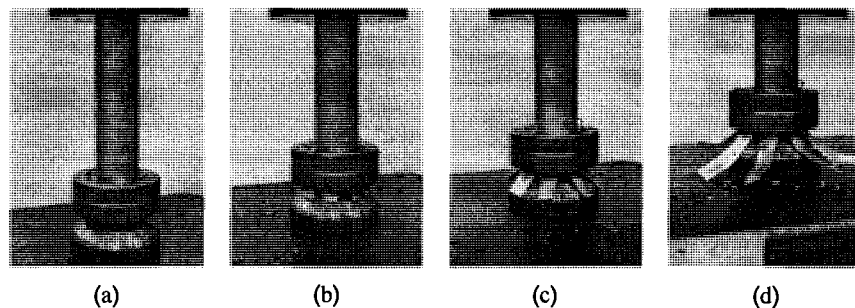


Figure 6.56. Photographs illustrating the experimental cutting process for a representative specimen in Group m-17.

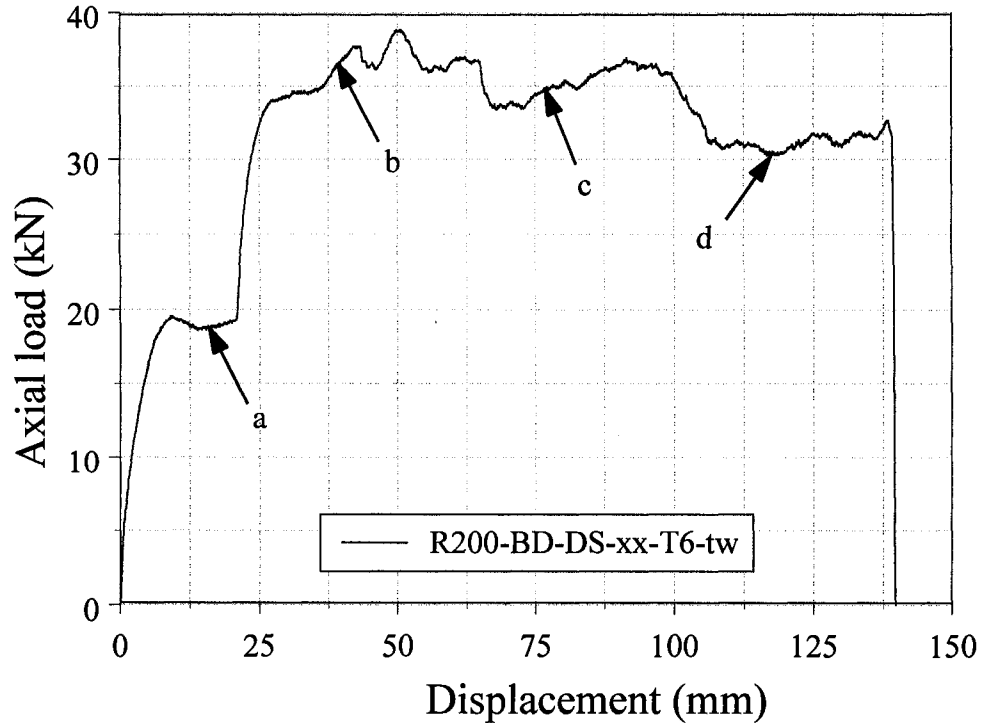


Figure 6.57. The load/displacement profile for the representative specimen from Group m-17, positions a, b, c and d correspond to photographs in Figure 6.56.

6.4.7 Cutting test results for specimens in groups m-19 through m-21

The observations from groups m-19 through m-21 in the presence of the curved deflector were identical to the observation in the presence of the straight deflector mentioned in section 6.4.6. The observed load/displacement profiles for representative specimens from groups m-19 through m-21 are illustrated in Figure 6.58. Photographs of the experimental cutting process for a representative from group m-20 are illustrated in Figure 6.59(a)-(d). The load/displacement observations for the corresponding images in Figure 6.59(a)-(d) are presented in Figure 6.60. Massive twisting of the cut petalled side walls was observed for all specimens as illustrated in photographs in Figure 6.59. The first stage of cutting process was observed to be very consistent. However, when cut petalled side walls from first stage cutting went through second stage cutters, the cutting force exhibited significant fluctuations. The load bearing capability of the cut side walls of 1.587 mm wall thickness extrusions was significantly lower compared to cut side walls of 3.175 mm extrusions.

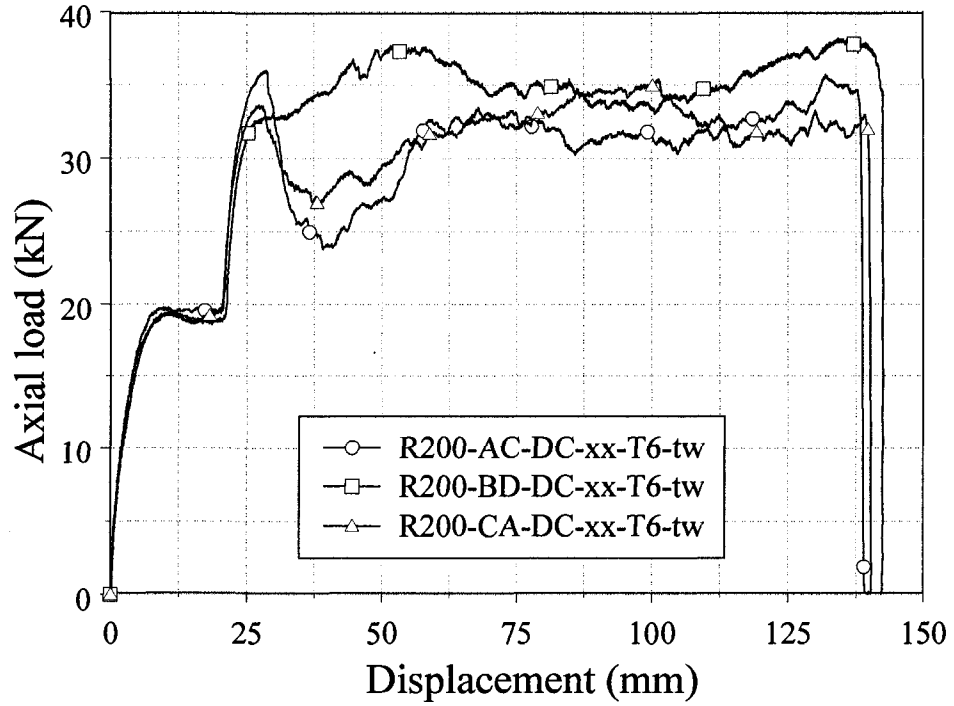


Figure 6.58. Experimentally obtained load/displacement responses for specimens in Groups m-19 through m-21.

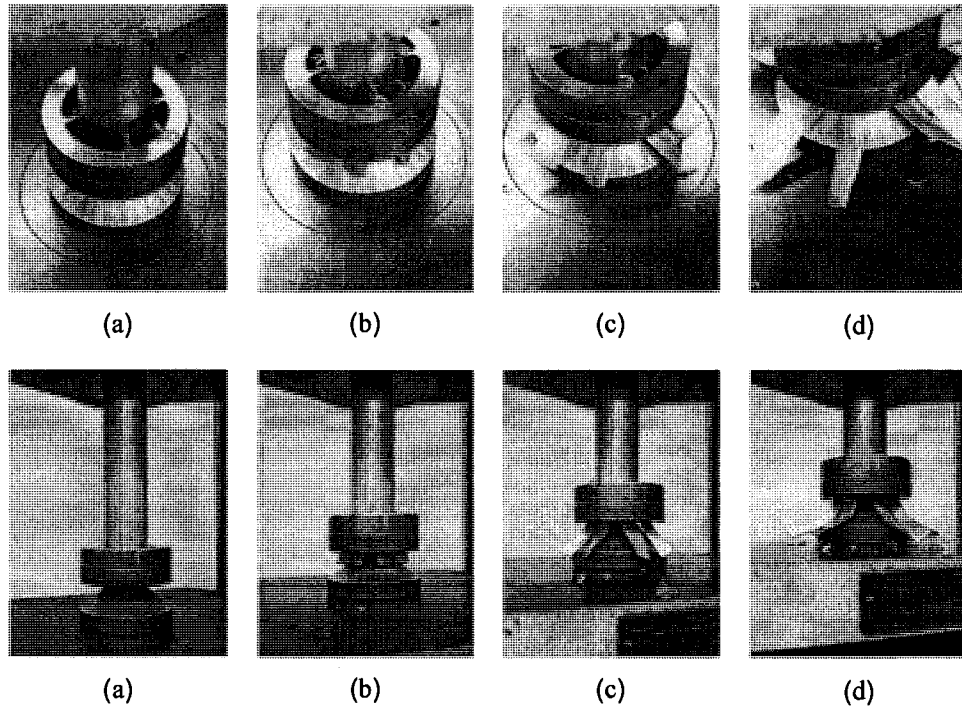


Figure 6.59. Photographs illustrating the experimental cutting process for a representative specimen in Group m-21 (top and bottom views).

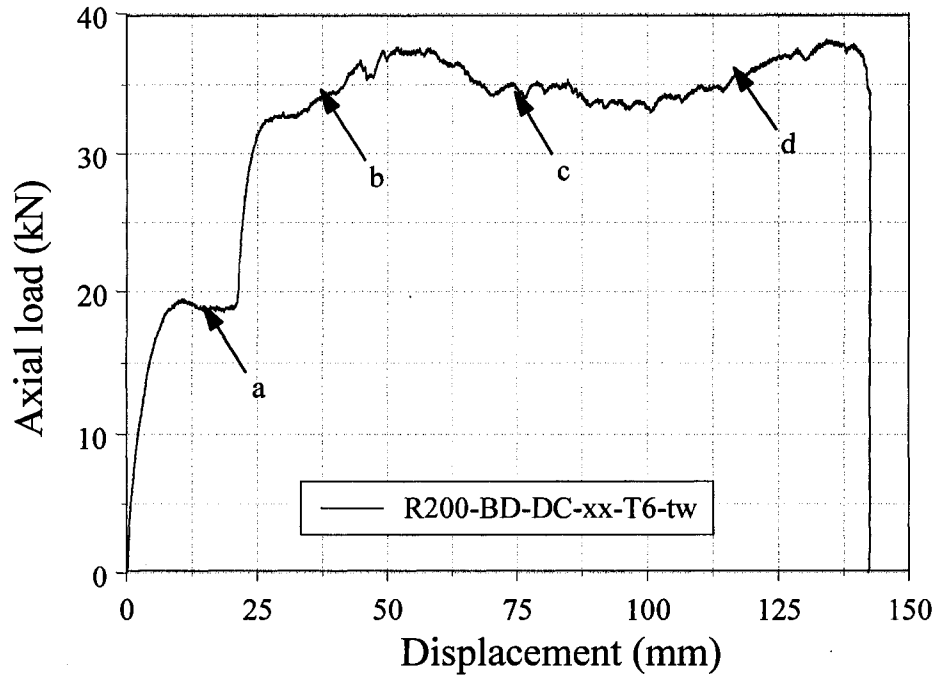


Figure 6.60. The load/displacement profile for the representative specimen from Group m-21, positions a, b, c and d correspond to photographs in Figure 6.59.

6.4.8 Cutting test results for the specimens in groups m-22 through m-24

The force/displacement responses for representative specimens of AA6061-T4 round extrusions with 1.587 mm wall thickness in the presence of straight or curved deflector as well as only the cutters are shown in Figure 6.61. Photographs of the experimental cutting process for a representative from group m-22 are illustrated in Figure 6.62(a)-(d). The load/displacement observations for the corresponding images in Figure 6.62(a)-(d) are presented in Figure 6.63. The photographs clearly demonstrate that the cut petalled side walls from the first cutting stage failed to go through the second cutting stage and the deformation mode switched from cutting to progressive folding. After 30 mm crosshead displacement all specimens in groups m-22 through m-24 exhibited similar deformation behaviour. Strain hardening of the T4 temper material reduced the material strength and significantly reduced the load bearing capability. The specimen portion from ahead of the cutting blade could not support the additional increase in the cutting force and subsequently the extrusion portion ahead of the cutter underwent progressive folding.

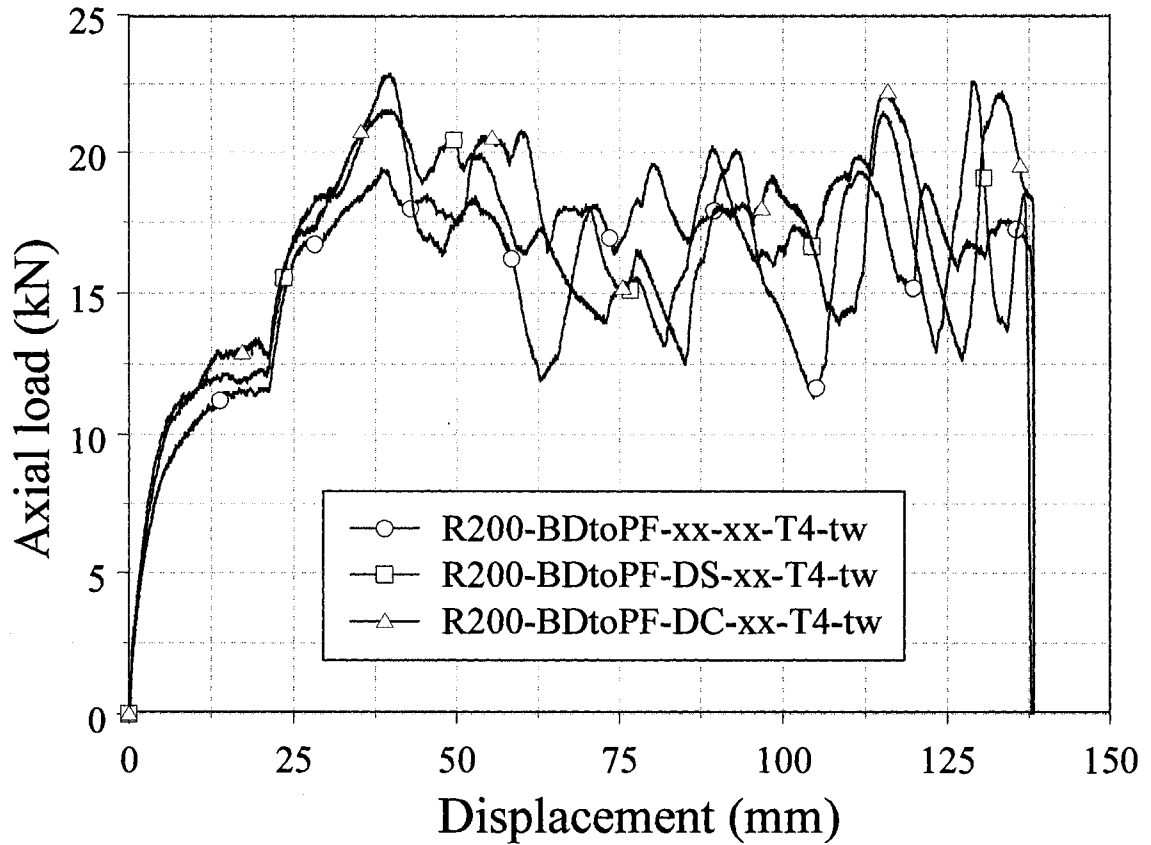


Figure 6.61. Experimentally obtained load/displacement responses for specimens in Groups m-22 through m-24.

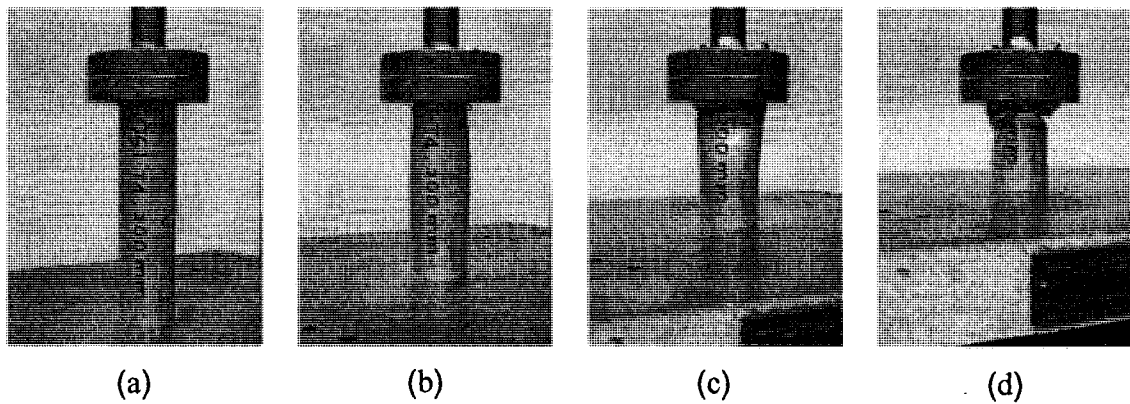


Figure 6.62. Photographs illustrating the experimental cutting process for a representative specimen in Group m-22.

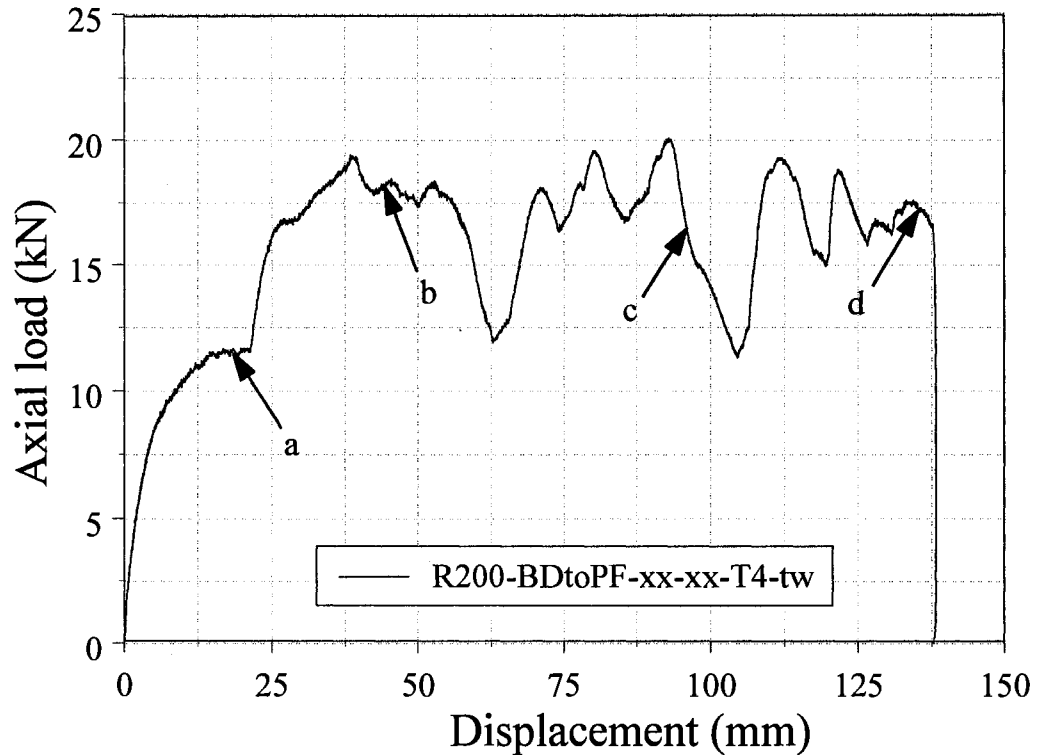


Figure 6.63. The load/displacement profile for the representative specimen from Group m-22, positions a, b, c and d correspond to photographs in Figure 6.62.

6.4.9 Cutting test results for specimens in groups s-1 through s-4

The force/displacement profiles for representative specimens of each group utilizing different spacer geometries and cutter side combinations are shown in Figure 6.64. The addition of spacers in between the two cutters resulted in a greater degree of separation (in the displacement domain) between the first portions of the steady state response to the initiation of the second cutting stage. The load/displacement responses in Figure 6.64 clearly illustrate that cutter side combination has very minor influence on first-stage cutting process. Cutter side combination CA (1.17 mm and 1.01 mm blade tip width) experienced approximately 5% higher cutting load compared to cutter side combination BD (1.00 mm and 1.02 mm blade tip width) in the first stage cutting. There is a limitation on length of spacing can be used in between two cutters. As shown in Figure 6.64, the cut petalled side walls from the first cutting stage failed to go through the second stage cutters when 30 mm spacer were used. As spacing between the cutters

increased the stability of the cutting progress degraded due to contact between the cut petalled sidewalls (resulting from excessive bending of the sidewalls in the first cutting process) and regions of the second cutter away from the blade tip. For this investigation limiting spacer size was observed to be 20 mm.

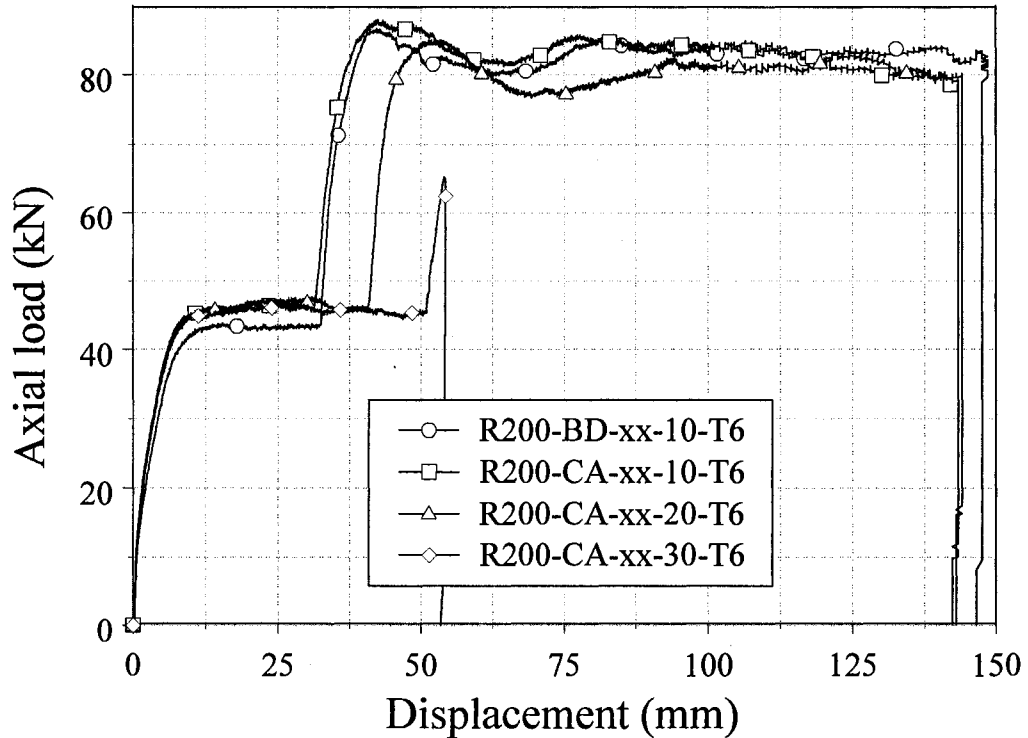


Figure 6.64. The load/displacement responses for representative specimen from Groups s-1 through s-4 utilizing spacers of different lengths.

6.4.10 Cutting test results for the specimens in groups s-5 through s-8

The load/displacement behaviour of representative specimens from groups s-5 through s-8 in the presence of straight or curved deflectors with spacing of 10 mm and 20 mm in between cutters are presented in Figure 6.65. Consistent load/displacement response was observed for all the tests completed within groups s-5 through s-8. No significant difference in the load/displacement profiles was observed incorporating straight/curved deflector compared to cutters only tests. A minor but notable increase of cutting force was observed at 72 mm crosshead displacement when cut petalled side

walls hit straight/curved deflector in the event of incorporating 10 mm spacer. However, no notable increase of cutting force was observed using 20 mm spacers when cut petalled side walls contacted straight/curved deflector. As the spacing length increased cut petalled side walls bended further outward and when hit deflector no significant resistance force exhibited.

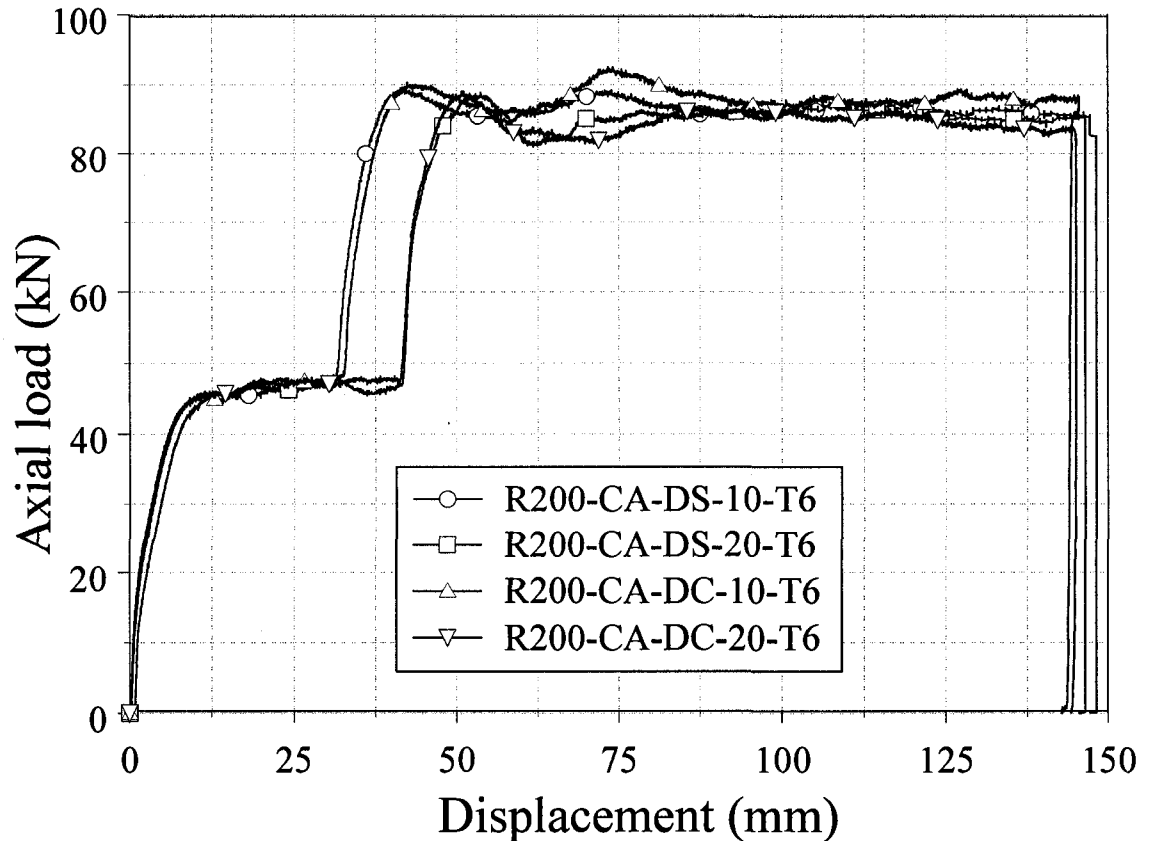


Figure 6.65. The load/displacement responses for the representative specimen from Groups s-5 through s-8 utilizing spacers of different lengths and straight/curved deflector.

6.4.11 Cutting test results among all specimens

A comparison of the load/displacement responses among specimens without using any spacing in between two cutters and incorporating different spacer profiles are presented in Figure 6.66. A stable load/displacement response was observed for the tests without use of any spacer between two cutters. Stability of the cutting progress degraded

using 10 mm spacing between two cutters. The least stable load/displacement response was observed utilizing 20 mm spacing as contact between the cut petalled sidewalls (resulting from the first cutting process) and regions of the second cutter further away from the blade tip. The mean cutting force during the first cutting stage for all the specimens was observed to be approximately 48 kN. However, during the second cutting stage, the specimens without use of spacers exhibited the mean cutting force of approximately 88 kN and the specimens incorporating 10 mm and 20 mm spacers exhibited the mean cutting forces of approximately 84 kN and 80 kN respectively. This findings demonstrate that the mean cutting force during the second cutting stage reduced with the increased of spacing between two cutters. The load/displacement profiles in Figure 6.66 demonstrate that the length of onset after the first cutting stage may be moved forward equivalent to the spacing incorporated in between two cutters.

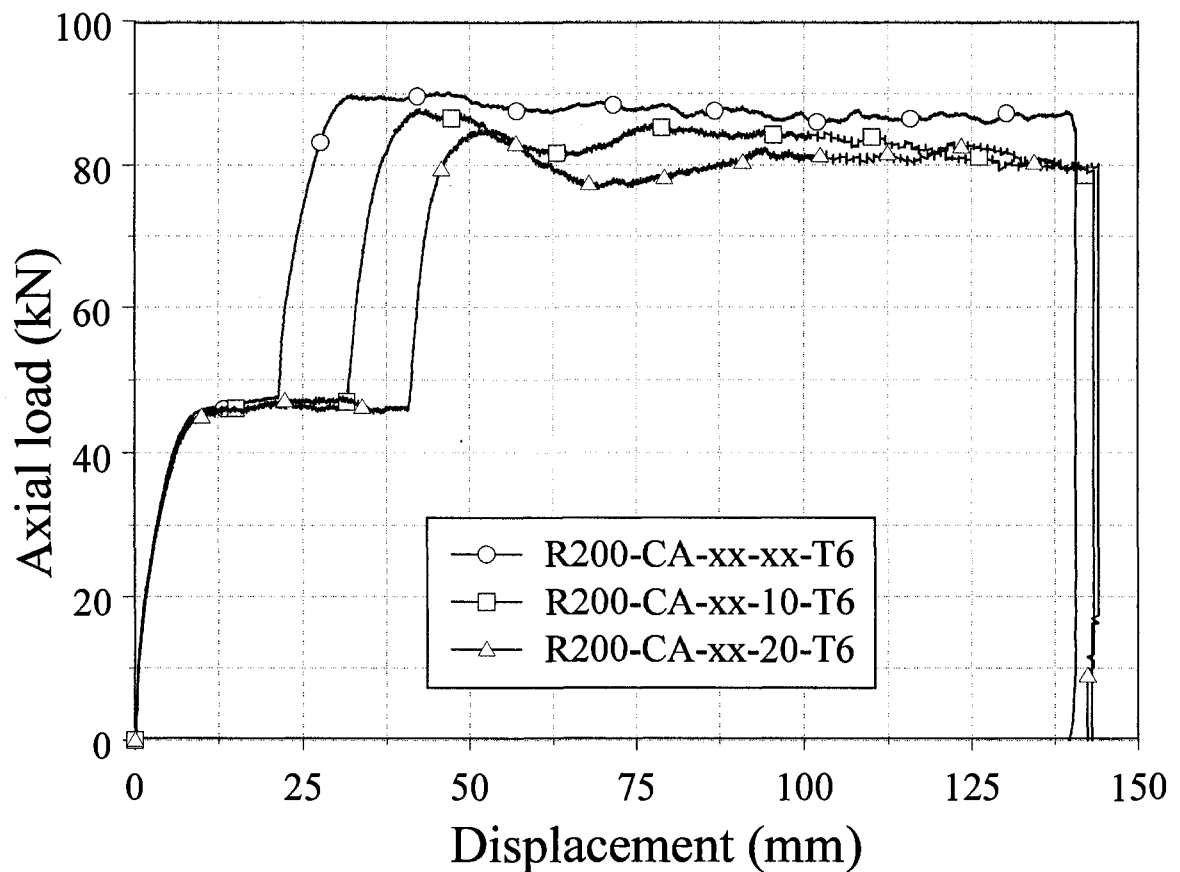


Figure 6.66. Comparison of the load/displacement responses among specimens without using any spacing and incorporating spacing of different lengths.

6.4.12 Comparison of crush performance parameters

This section compares the crush performance parameters of each group considered in this research. For each specimen tested, the crushing force and crosshead displacement were recorded. Post-testing data analysis was completed to determine the peak crush load, mean crush force, CFE, total energy absorption, SEA and the effectiveness factor. The mean values of crush parameters for each group utilizing different combination of cutters and deflectors are presented in Table 6.8 and Table 6.9. The mean values of crush parameters for each group using spacing of different lengths between two cutters are presented in Table 6.10.

Table 6.8. Calculated average values of the crush parameters for each group in the dual stage cutting process using specimens with wall thicknesses of 1.587 mm and 3.175 mm.

Group	Specimen ID	Average P_m (kN)	Average P_{max} (kN)	Average CFE (%)
m-1	R200-AC-xx-xx-T6	78.53	90.60	86.70
m-2	R200-BD-xx-xx-T6	77.95	88.73	87.50
m-3	R200-CA-xx-xx-T6	78.56	89.25	88.03
m-4	R200-AC-DS-xx-T6	82.16	95.07	86.43
m-5	R200-BD-DS-xx-T6	81.41	97.27	83.70
m-6	R200-CA-DS-xx-T6	81.84	96.46	84.87
m-7	R200-AC-DC-xx-T6	81.89	95.29	85.93
m-8	R200-BD-DC-xx-T6	80.85	94.43	85.60
m-9	R200-CA-DC-xx-T6	80.70	93.24	86.57
m-10	R200-AC-xx-xx-T4	44.90	70.67	63.47
m-11	R200-AC-DS-xx-T4	69.29	84.10	82.37
m-12	R200-AC-DC-xx-T4	68.86	83.03	82.93
m-13	R200-AC-xx-xx-T6-tw	28.03	34.92	80.20
m-14	R200-BD-xx-xx-T6-tw	29.02	36.48	79.73
m-15	R200-CA-xx-xx-T6-tw	26.45	33.82	78.17
m-16	R200-AC-DS-xx-T6-tw	28.37	35.35	79.50
m-17	R200-BD-DS-xx-T6-tw	30.48	38.07	80.07
m-18	R200-CA-DS-xx-T6-tw	29.84	35.87	83.17
m-19	R200-AC-DC-xx-T6-tw	28.69	35.85	80.03
m-20	R200-BD-DC-xx-T6-tw	31.35	38.59	81.47
m-21	R200-CA-DC-xx-T6-tw	30.11	36.51	82.50
m-22	R200-BDtoPF-xx-xx-T4-tw	15.03	20.93	71.93
m-23	R200-BDtoPF-DS-xx-T4-tw	15.49	22.66	68.33
m-24	R200-BDtoPF-DC-xx-T4-tw	16.36	22.86	71.60

Table 6.9. Calculated average values of TEA, SEA and the effectiveness factor.

Group	Specimen ID	Average <i>TEA</i> (kJ)	Average <i>SEA</i> (kJ/kg)	Average <i>EF</i> ψ
m-1	R200-AC-xx-xx-T6	10.85	42.29	0.413
m-2	R200-BD-xx-xx-T6	10.68	41.63	0.408
m-3	R200-CA-xx-xx-T6	11.23	43.77	0.423
m-4	R200-AC-DS-xx-T6	11.74	45.76	0.440
m-5	R200-BD-DS-xx-T6	11.32	44.13	0.429
m-6	R200-CA-DS-xx-T6	11.56	44.08	0.426
m-7	R200-AC-DC-xx-T6	11.27	43.93	0.427
m-8	R200-BD-DC-xx-T6	11.40	44.46	0.432
m-9	R200-CA-DC-xx-T6	11.17	43.57	0.426
m-10	R200-AC-xx-xx-T4	2.68	10.47	0.116
m-11	R200-AC-DS-xx-T4	9.56	37.97	0.442
m-12	R200-AC-DC-xx-T4	9.74	37.06	0.453
m-13	R200-AC-xx-xx-T6-tw	4.01	30.22	0.282
m-14	R200-BD-xx-xx-T6-tw	4.01	30.25	0.291
m-15	R200-CA-xx-xx-T6-tw	3.66	27.61	0.265
m-16	R200-AC-DS-xx-T6-tw	3.94	29.70	0.298
m-17	R200-BD-DS-xx-T6-tw	4.26	32.12	0.310
m-18	R200-CA-DS-xx-T6-tw	4.13	31.17	0.309
m-19	R200-AC-DC-xx-T6-tw	3.99	30.14	0.294
m-20	R200-BD-DC-xx-T6-tw	4.47	33.73	0.328
m-21	R200-CA-DC-xx-T6-tw	4.23	31.92	0.312
m-22	R200-BDtoPF-xx-xx-T4-tw	1.56	11.75	0.157
m-23	R200-BDtoPF-DS-xx-T4-tw	2.01	15.18	0.193
m-24	R200-BDtoPF-DC-xx-T4-tw	2.26	17.02	0.201

Table 6.10. Calculated average values of the crush parameters for each group in the dual stage cutting process using spacers of various geometries.

Group	Specimen ID	Average P_m (kN)	Average P_{max} (kN)	Average <i>CFE</i> (%)	Average <i>TEA</i> (kJ)	Average <i>SEA</i> (kJ/kg)	Average <i>EF</i> ψ
s-1	R200-BD-10-T6	72.91	86.32	84.45	10.51	40.96	0.405
s-2	R200-CA-10-T6	73.61	88.90	82.85	10.62	41.39	0.407
s-3	R200-CA-20-T6	69.42	86.40	80.35	9.95	38.77	0.376
s-4	R200-CA-30-T6	44.41	73.14	61.07	2.41	9.02	0.089
s-5	R200-CA-DS-10-T6	76.69	90.14	85.05	11.34	44.21	0.437
s-6	R200-CA-DS-20-T6	71.46	87.10	82.05	10.47	40.81	0.405
s-7	R200-CA-DC-10-T6	77.28	92.46	83.50	11.21	43.70	0.426
s-8	R200-CA-DC-20-T6	72.28	88.97	81.20	10.46	40.96	0.405

6.4.12.1 Peak crush force and mean crush force

The magnitude of the peak and the mean cutting forces were very close in the presence of straight or curved deflector for both temper specimens. Use of the deflectors in the cutting process illustrated a slight increase in the cutting force. The T6 temper specimens which under went cutting deformation mode in the presence of straight or curved deflector experienced approximately 5.2% and 4.6% higher peak and mean cutting forces respectively compared to specimens utilized cutters only. The extrusions with T6 temper in the presence of straight or curved deflector exhibited 13.3% and 18.2% higher peak and mean cutting forces respectively compared to identical extrusions with T4 temper specimens. The reduction of the peak and the mean cutting forces for the T4 temper extrusions can be attributed towards the reduced material strength. Similar findings were also observed for the specimens with 1.587 mm wall thickness and both temper. The specimens with T6 temper and wall thickness of 3.175 mm experienced 160% and 180% higher peak and mean cutting forces compared to identical temper specimens but 1.587 mm wall thickness.

The highest peak and the mean cutting forces of 92.46 kN and 77.28 kN respectively were exhibited using 10 mm spacing in presence of the curved deflector. The tests utilizing 10 mm spacing demonstrated 5.2% and 6.0% higher peak and mean cutting forces compared to tests using 20 mm spacing. Similar finding were also observed in presence of straight/curved deflector.

6.4.12.2 Total energy absorption and crush force efficiency

A fairly consistent CFE was observed among all specimens tested in groups m-1 through m-12 except group m-10. Specimens in group m-10 failed to go through second stage cutting process. The CFE observed ranges from 82.37% to 88.07% for all specimens with both temper and wall thickness of 3.175 mm. The maximum total energy absorption was observed to be 11.74 kJ for specimens with T6 temper in presence of straight deflector. The CFE observed for specimens with T6 temper and a wall thickness of 1.587 mm ranges from 78.17% to 82.5%. The observed TEA for identical extrusions

ranges from 3.66 kJ to 4.47 kJ. Specimens with a T4 temper with a wall thickness of 1.587 mm switched deformation mode from cutting to progressive folding during the second cutting stage.

A better degree of consistency in the crush force efficiencies was observed for the various spacer thicknesses considered. The observed CFE ranging from 86.32% to 92.46% for all tests completed except test using 30 mm spacing in which cut petalled side walls failed to go through second stage cutter. The energy absorption was found to be dependent upon the degree of spacing in between the cutters blade tips, however, in this investigation the energy absorption was observed ranging from 9.95 kJ to 11.46kJ.

6.4.12.3 Specific energy absorption and effectiveness factor

A higher specific energy observation of approximately 40% was observed for specimens with the T6 temper and a wall thickness of 3.175 mm compared to the identical specimens but a wall thickness of 1.587 mm. Incorporating the straight or curved deflector resulted in approximately 9% increase in SEA compared to tests using only the cutters. A reduction of specific energy absorption of approximately 21% was noticed for specimens with the T4 temper and a wall thickness of 3.175 mm compared to that for geometrically identical extrusion but with the T6 temper. The effectiveness factor observed for specimens with T6 temper and a wall thickness of 3.175 mm ranges from 0.408 to 0.440. The observed effectiveness factor for the extrusions with identical temper but a wall thickness of 1.587 mm ranges from 0.265 to 0.328. A higher effectiveness factor of approximately 6% was observed for the specimens with a wall thickness of 3.175 mm and a T4 temper compared to the extrusion having similar geometry but with a T6 temper. A reduction in the effectiveness factor was noticed with the increase of spacing between the cutters.

6.5 Controlling the load/displacement response

Although two experimental tests were completed for each group except groups starting with letter e, the load/displacement observations for both specimens within each group were fairly consistent. For this reason and for greater clarity, only a representative specimen from each group was selected for illustration and discussion purposes. The load/displacement profiles of both tests within group a-T4 are presented in Appendix A to demonstrate repeatability of the tests.

6.5.1 Cutting test results for the specimens in groups a-T6 through d-T6

The observed force/displacement profiles for the representative specimens in groups a-T6 through d-T6 are presented in Figure 6.67. Photographs of the cutting process for specimen a-T6-1 are illustrated in Figure 6.68 which corresponds to the annotated letters in Figure 6.69. Note that Figure 6.68(e) illustrates the extrusion after the test was completed. Photographs of the cutting deformation illustrate that the cutter penetrated through the sidewall of the specimens and developed highly localized plastic deformation in the vicinity of the cutting blades. Cutting chips were observed to be formed. No crack propagation was observed in any tests. As the cutting progressed, petalled sidewalls bent slightly outwards most likely due to the interaction between the cutter blade shoulder and the tube sidewalls. With the variation in the tube wall thickness, no significant difference in the degree of bending was observed. The cutting process was observed to be stable and consistent for all specimens in groups a-T6 through d-T6.

After approximately 10 mm of cutting, an almost constant force was observed during the deformation with a minimal degree of hardening for specimens in group a-T6. Consistent with the transition from the reduced wall thickness to the original nominal tube thickness at displacement of 42 mm an increase in the cutting force to a value of approximately 42 kN was observed. A reduction in the cutting force occurred over the displacement domain from approximately 70 mm to 85 mm indicating some degree of influence on reduced wall thickness (after axial distance of 84 mm) on the cutting load prior to this value of position. This should be expected as a significant zone of plasticity occurs ahead of the cutter blade tip. The cutting force observed over the displacement

domain from approximately 85 mm to 125 mm was consistent with the cutting load observed from displacement ranging from 10 mm to 40 mm. Cutting loads after displacement of 125 mm were consistent with expected values of 42 kN which were also observed for the displacement ranging from 42 mm to 70 mm. This should be expected as a result of the consistent wall thickness in these ranges of the extrusion.

The force/displacement responses of the specimens in group a-T6 (Figure 6.67) generally changed accordingly to the variations of the extrusion wall thicknesses as shown in Figure 4.7(a). Though no significant difference in the force/displacement profiles was observed for specimens within group a-T6, variations from the expected results can be explained as a result of the large plasticity zone ahead of the cutter blade tip and the influence of a geometrical stress concentration as a result of the stepped wall thickness. The deformation behaviour of specimens in groups b-T6 through d-T6 were consistent to the characteristics observed in group a-T6. Similarly to group a-T6, the cutting force/displacement responses of the specimens in groups b-T6 through d-T6 (Figure 6.67) changed accordingly to the variations of the extrusion wall thicknesses and provided abrupt or ramped changes in the cutting load for increases in cutter displacement. No significant difference in the force/displacement profiles was observed for specimens within each group, however, minor variations at values of x corresponding to locations of stress concentration, due to wall thickness transitions, were found.

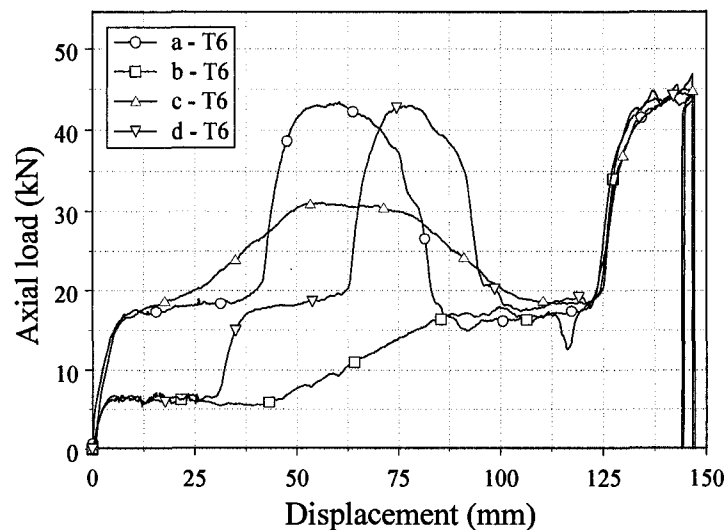


Figure 6.67. Experimentally obtained load/displacement profiles for representative specimens from Groups a-T6 through d-T6.

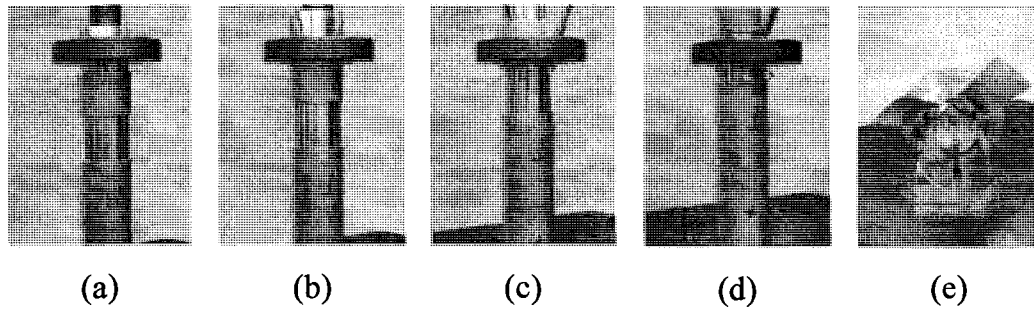


Figure 6.68. Photographs illustrating the cutting process for specimen a-T6-1.

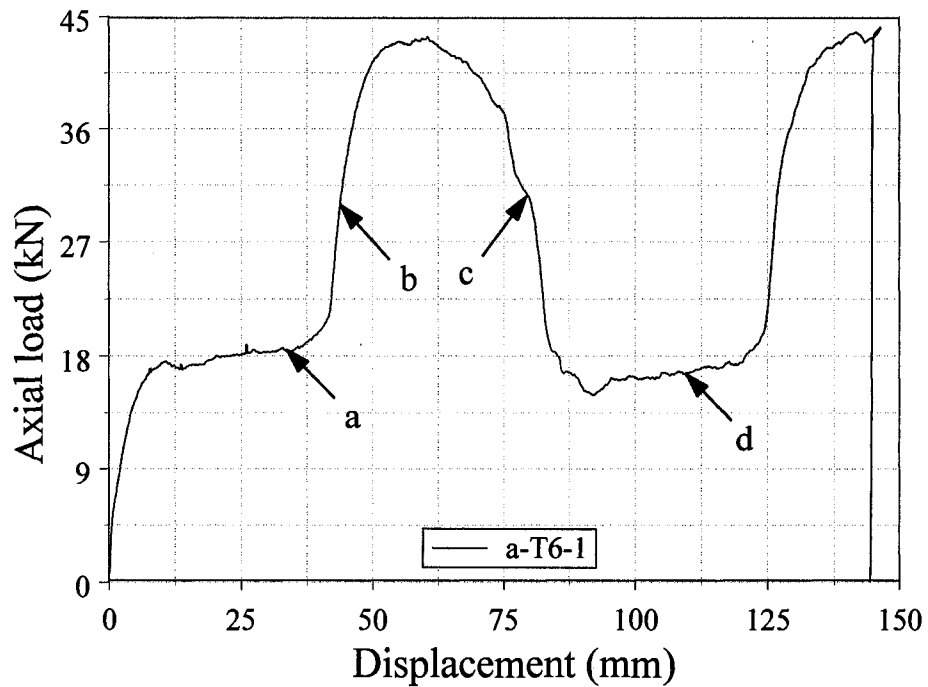


Figure 6.69. The load/displacement profile for the representative specimen from Group a-T6-1, positions a, b, c and d correspond to photographs in Figure 6.68.

6.5.2. Cutting test results for specimens in groups e-1-T6 through e-4-T6

The observed force/displacement responses for the specimens in groups e-1-T6 through e-4-T6 are presented in Figure 6.70. Only a single specimen with a specific value of W (indicated in Figure 4.7(e)) was tested as the observed load/displacement profiles were in excellent agreement to expected results. The deformation process was consistent with previous testing.

After a transient cutting process corresponding to approximately 10 mm of platen displacement, the cutting force ramped linearly to a constant steady state cutting load of approximately 42 kN at displacement of 125 mm for specimens e-1-T6 through e-3-T6. Independent of the taper associated with each tube all specimens illustrated a cutting force of 42 kN over displacement from 125 mm up to the end of the test. Actually, the constant cutting load was observed to occur prior to displacement of 125 mm at approximately displacement of 117 mm. This observation indicates that, for specimens in groups e-1-T6 through e-4-T6, the load/displacement response is dependent upon extrusion geometry at approximately 8 mm ahead of the cutter blade tip. Specimen e-4-T6 obtained a constant cutting load at displacement of 10 mm and greater. The force/displacement responses of the specimens in groups e-1-T6 through e-4-T6 were observed to change accordingly to the variations of the extrusion wall thicknesses.

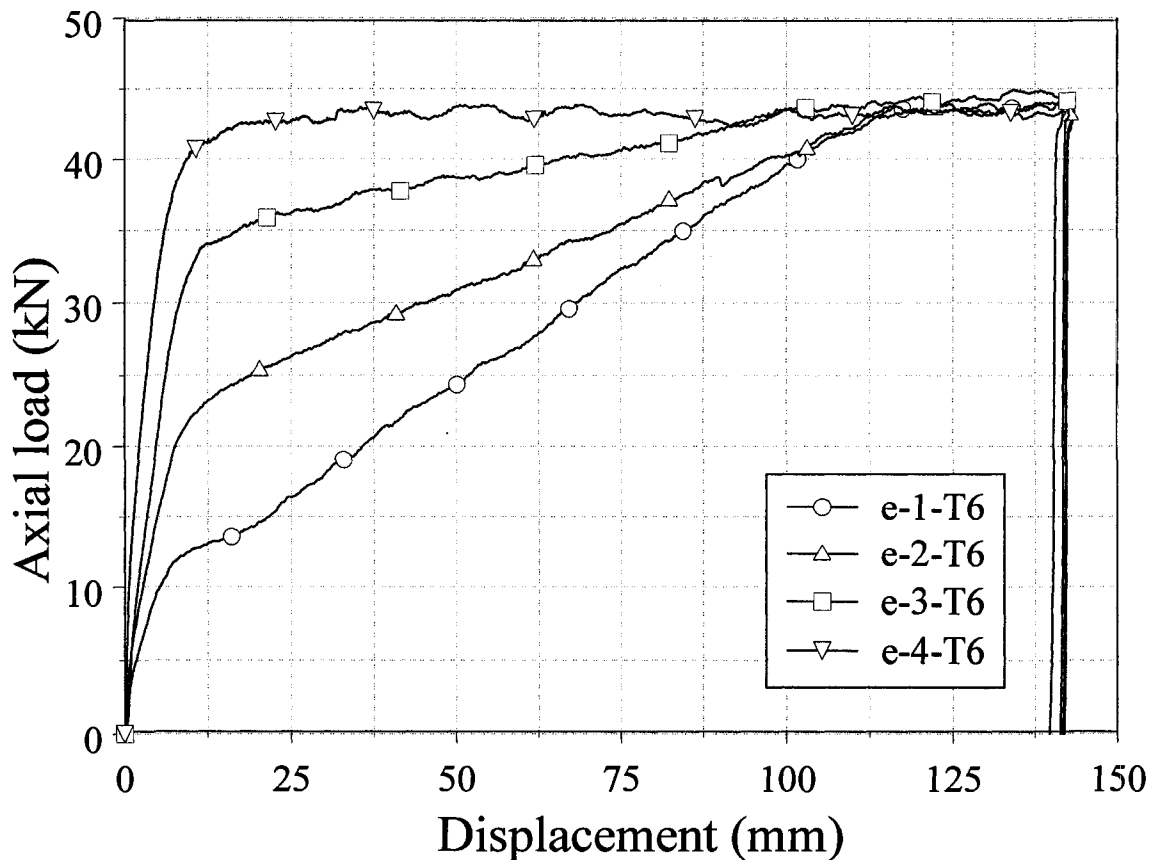


Figure 6.70. Experimentally obtained load/displacement profiles for representative specimens from Groups e-1-T6 through e-4-T6.

6.5.3. Cutting test results for the specimens in groups a-T4 through d-T4

The observed force/displacement profiles for the representative specimens in groups a-T4 through d-T4 are presented in Figure 6.71. With the variation in the tube wall thickness, no significant difference in the degree of bending was observed. The cutting process was observed to be stable and consistent for all specimens in groups a-T4 through d-T4. The load/displacement profiles observed for T4 temper specimens followed similar profile observed T6 specimens in groups a-T6 through d-T6. However, the magnitude of the cutting force for the T4 temper extrusions were observed to be approximately 34% lower compared to identical extrusions with T6 temper. The force/displacement responses of the specimens in group a-T4 (Figure 6.71) generally changed accordingly to the variations of the extrusion wall thicknesses as shown in Figure 4.7(a). Similarly to group a-T4, the cutting force/displacement responses of the specimens in groups b-T4 through d-T4 (Figure 6.71) changed accordingly to the variations of the extrusion wall thicknesses and provided abrupt or ramped changes in the cutting load for increases in cutter displacement.

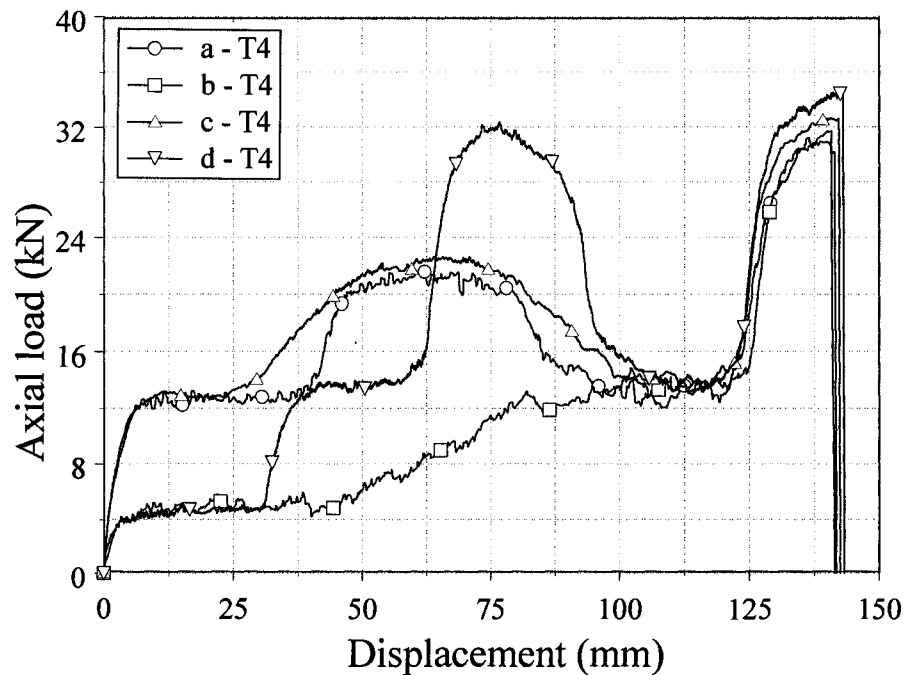


Figure 6.71. Experimentally obtained load/displacement profiles for representative specimens from Groups a-T4 through d-T4.

6.5.4. Cutting test results for specimens in groups e-1-T4 through e-4-T4

Figure 6.72 illustrates the observed load/displacement responses for the specimens in groups e-1-T4 through e-4-T4. Only a single specimen with a specific value of W (indicated in Figure 4.7(e)) was tested as the observed load/displacement profiles were in excellent agreement to expected results. The load/displacement profiles observed for T4 temper specimens followed similar profile observed T6 specimens in groups e-1-T6 through e-4-T6. However, fluctuation in cutting force was observed during cutting test with T4 temper extrusions. This fluctuation of force may be due to 'back and forth' folding of cut petalled side walls observed during experimental tests. The force/displacement responses of the specimens in groups e-1-T6 through e-4-T6 were observed to change accordingly to the variations of the extrusion wall thicknesses. The magnitude of the cutting force for T4 temper specimens observed to be approximately 35.7% lower compared to identical extrusion with T6 temper.

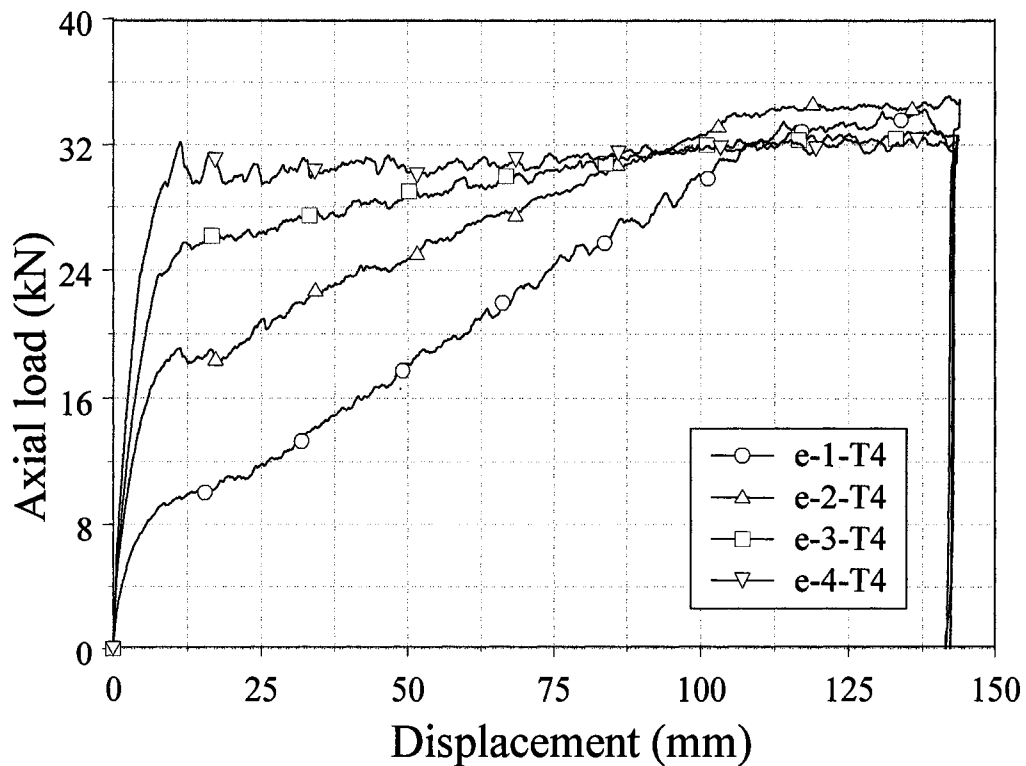


Figure 6.72. Experimentally obtained load/displacement profiles for representative specimens from Groups e-1-T4 through e-4-T4.

6.5.5. Cutting test results amongst all specimens

The load/displacement profiles of specimens with tapered and stepped wall with both T6 and T4 temper followed very similar profile as clearly demonstrated in Figure 6.73. The difference of cutting force between T6 and T4 temper specimens gradually increased with the increase of wall thickness. At 20 mm crosshead displacement, T6 temper extrusions demonstrated approximately 3.5 kN higher cutting force compared to T4 temper specimens, however, the difference in cutting force was observed to be approximately 10.5 kN at 110 mm crosshead displacement. It is evident from the force/displacement profiles that the cutting phenomena for T6 extrusions can be referred to stable or clean curling cut [24] but T4 temper specimens exhibited braided cutting phenomenon.

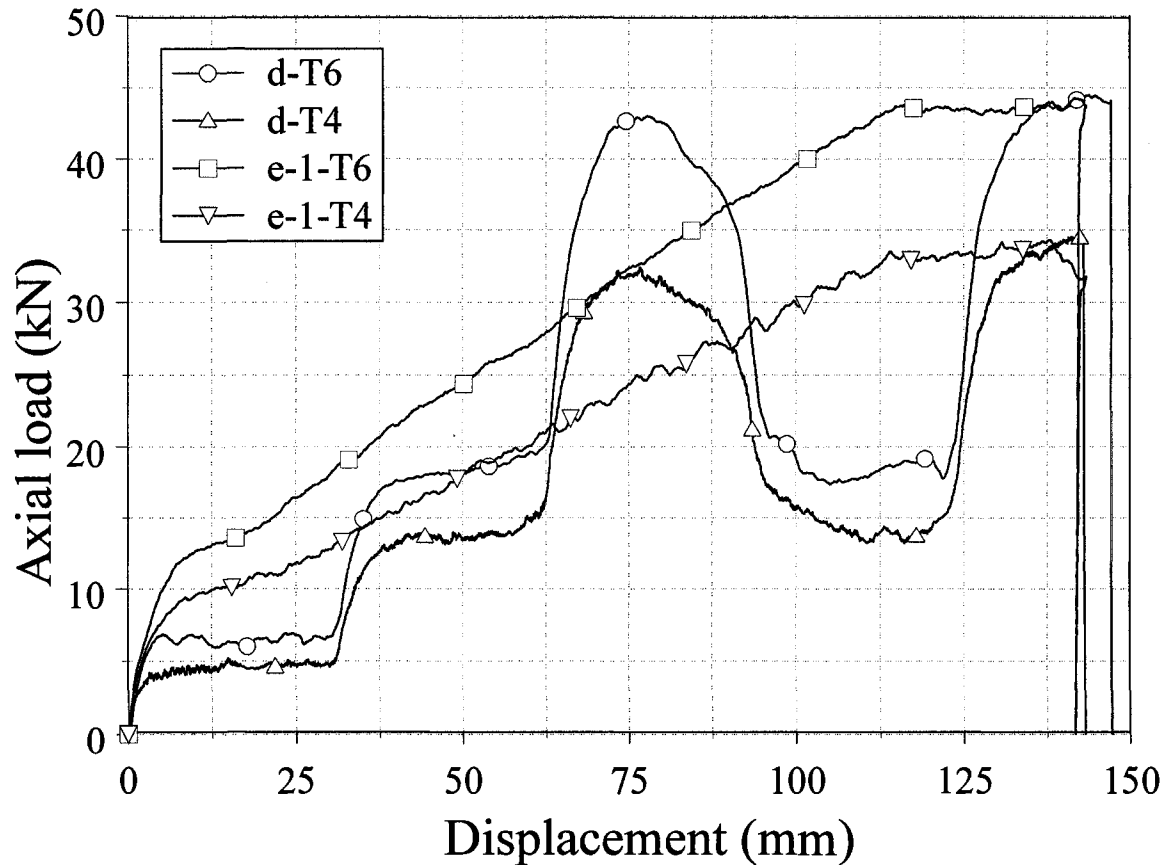


Figure 6.73. Comparison of load/displacement profiles for representative specimens from Group d and Group e-1 with T6 and T4 temper conditions.

6.5.6. Comparison of crush performance parameters amongst all specimens

This section compares the crush performance parameters of each group considered in this research. Table 6.11 summarizes the average peak and mean crushing forces as well as the CFE, TEA, SEA and the effectiveness factor (ψ) for each specimen groups considered in this investigation.

Table 6.11 Specimen grouping information and crush parameters for the specimens in group a through d and groups e-1 through e-4 with both temper.

Group	Average P_m (kN)	Average P_{max} (kN)	Average CFE (%)	Average TEA (kJ)	Average SEA (kJ/kg)	EF ψ
a-T6	25.88	42.81	60.5	3.75	11.40	0.081
b-T6	15.06	44.74	33.7	2.17	7.72	0.050
c-T6	25.47	44.46	57.3	3.71	11.66	0.084
d-T6	22.61	43.54	52.0	3.29	10.49	0.064
e-1-T6 ($W = t/4$)	29.90	44.36	67.4	4.31	13.36	0.124
e-2-T6 ($W = t/2$)	33.94	44.18	76.8	4.88	14.22	0.109
e-3-T6 ($W = 3t/4$)	39.72	45.38	87.5	5.85	16.09	0.148
e-4-T6 ($W = t$)	41.60	44.0	94.4	5.90	15.30	0.150
a-T4	18.26	36.52	50.0	2.60	7.91	0.081
b-T4	10.66	31.06	34.3	1.53	5.44	0.047
c-T4	19.09	33.83	56.4	2.76	8.66	0.085
d-T4	16.67	34.69	48.2	2.44	7.78	0.075
e-1-T4 ($W = t/4$)	22.29	34.43	64.7	3.20	9.93	0.121
e-2-T4 ($W = t/2$)	27.21	35.27	77.2	3.95	11.52	0.098
e-3-T4 ($W = 3t/4$)	28.76	32.72	87.9	4.16	11.44	0.128
e-4-T4 ($W = t$)	30.29	32.81	92.3	4.36	11.34	0.134

6.5.6.1. Peak crush force and mean crush force

Good consistency for the peak crush force was observed for all specimens in groups a through d with T6 temper and minor variation was noticed among specimens in different groups with T4 temper. The peak cutting force varied between 42.81 kN and

44.74 kN for T6 tempered specimens, however, the peak cutting force for T4 tempered specimens ranges from 31.06 kN to 36.52 kN .

Although the load/displacement response of the extrusion was dependent upon the variation in wall thickness through the axial direction the mean cutting force ranged from 15.06 kN to 25.88 kN and 10.66 kN to 19.09 kN for T6 and T4 tempered specimens respectively. Very minor variations in the cutting force within a group were noticed which most likely the result of differences in manual alignment of the cutter to the extrusions prior to the test. Geometrical and material differences between specimens could also result in load/displacement variations amongst specimens within a group.

Again, a fair consistency for the peak crush force was observed for all specimens in groups e-1 through e-4 with T6 temper and minor variation was noticed within specimens in different groups with T4 temper. The variation of peak cutting force was observed between 44.0 kN to 45.38 kN and 32.72 kN to 35.27 kN for T6 and T4 tempered specimens respectively. The maximum cutting force was consistent with the steady state cutting force of the specimen e-4 which had no geometrical modifications. The mean cutting force observed ranged from 29.90 kN to 41.60 kN and 22.29 kN to 30.29 kN for the T6 and the T4 tempered specimens respectively.

6.5.6.2. Total energy absorption and crush force efficiency

The total energy absorption for specimens with the T6 and the T4 temper was observed to range from 2.17 kJ to 3.75 kJ and 1.53 kJ to 2.76 kJ respectively. A significant reduction in CFE compared to original wall thickness extrusions was observed for all specimens tested in this study. CFE was observed to range 33.7% to 60.5% for all specimens in groups a through d including both temper materials. However, higher CFE was observed to increase for both tempered extrusions as reduction of wall thickness reduced. The CFE depends upon the load/displacement response. The load/displacement profiles in this investigation were not ideal as focus was to control the load/displacement response. For the extrusion geometries considered in this research the TEA was observed to range from 2.05 kJ to 5.90 kJ for T6 temper extrusions.

7. FINITE ELEMENT MODELLING AND SIMULATION METHOD

This chapter describes the FE modeling and simulation of the experimental axial cutting of round aluminum alloy extrusions. Two different models were developed utilizing Eulerian and Smoothed Particle Hydrodynamics (SPH) technique to predict the deformation behaviour of AA6061-T6 aluminum extrusions under axial cutting mode in the presence of straight and curved deflectors.

The first stage of the model development (pre-processing) involved the creation and discretization of the specimen, cutter blade and deflector as well as the implementation of boundary conditions. This was accomplished through using the pre-processing software package Finite Element Model Builder (FEMB). The FEMB was then used to output an analysis code file, to which the material models were added. The completed analysis file was then input to LS-DYNA, an explicit non-linear FE solver. The solution results were then viewed and analyzed in the post-processing software package LS-PREPOST.

7.1 Eulerian FE formulation

Lagrangian FE formulations are the most common in the majority of numerical simulations employing the FE method. However, in large deformation processes the massive mesh distortion of Lagrangian type elements will lead to significant numerical error. Raczy [65] investigated extensively on Lagrangian element formulation for orthogonal cutting and found less predictive capability of Lagrangian element formulation during large deformation. An alternative element selection for large deformation processes is Eulerian or Arbitrary Lagrangian/Eulerian (ALE) element formulations. In the Eulerian element formulation the material coordinates and spatial coordinates of the FE mesh are disassociated and the material moves through the FE mesh. In the explicit time integration scheme, during every cycle (time step) of the simulation each Eulerian element completes a Lagrangian analysis, however, prior to the next cycle the spatial coordinates of the FE mesh is remapped to its original position in a process referred to as advection. While the FE mesh is remapped to its original position,

the material coordinates are not and will move through the FE mesh. Therefore, in the implementation used in this research, an airmesh must surround the original material location of the extrusion material for evaluation of the deformed material state. At the start of the simulation, the airmesh contains no material and its only purpose is to accommodate deformed material. Special care must be taken in modeling the airmesh large enough to account for any possible material deformation during the simulation yet allow a fine enough mesh geometry to appropriately predict deformation.

Although most research involving FE analysis of axial crushing of tubular extrusions has been conducted using Lagrangian FE formulation, an Eulerian FE formulation was employed in the present study in order to simulate the cutting process accurately. Some disadvantages may arise by using an Eulerian FE formulation, such as larger CPU costs, however it is beneficial especially in dealing with the large plastic deformation processes and numerical instabilities associated with severe mesh distortion. The extrusions, cutter and deflector were modelled with accordance to the experimental set-up. A summary of the input files compiled for cutting process in presence of curved deflector is enclosed in Appendix B. The most pertinent parts of the input files are contained in the text within following sub-sections and other details can be found in LS-DYNA Keyword User's Manual [66].

7.1.1 Model geometry and discretization

FEMB was used to generate the mesh for the AA6061-T6 aluminum extrusions with circular geometry, the airmesh, the straight deflector, the curved deflector and the cutter blade. Due to the symmetry observed in the experimental quasi-static cutting process of these specimens, only one quarter of the tubular specimen, one quarter of the deflector and one corresponding cutter blade were considered in these models. Moreover, only approximately 100 mm length of the tubular specimen was considered during modeling to minimize computational cost as it was observed during experimental tests that a steady-state cutting process was achieved after a cutter displacement of approximately 60 mm. The geometry of the cutter and the deflectors were identical to the nominal geometry of the cutter apparatus.

The discretization of the tubular extrusion, airmesh, the deflectors, and the cutter is shown in Figure 7.1 with the straight deflector. A single point quadrature Eulerian element was selected for extrusion and airmesh. As shown in Figure 7.1, the mesh density of the tube in the vicinity of the region of contact between the cutter and extrusion was finer than all other regions. Higher discretization was completed to ensure an accurate approximation of the stress distribution and deformation near the contact region. Chip formation of the extrusion material was observed in all experimental tests with an approximate thickness of 1 mm. In an attempt to appropriately predict the deformation behaviour and chip formation, the Eulerian mesh of the extrusion and airmesh were discretized with a smallest dimension of 0.27 mm employing an aspect ratio of 1.5 in the region of contact between the extrusion and cutter. Twelve Eulerian elements through the thickness of the tube near the contact region were utilized. Transition elements were introduced between the finer mesh and coarser mesh in three directions. The airmesh was modeled with an 8 mm radial offset from the inner and outer surfaces of sidewall of the tube in the contact region. In all other regions a 2.2 mm radial offset from the inner and outer surfaces of the tube sidewalls was employed. The airmesh in the axial direction was offset 1.3 mm from the top surface of the tube. The dimensions of the airmesh were estimated based upon the extent of extrusion deformation observed in the experimental tests.

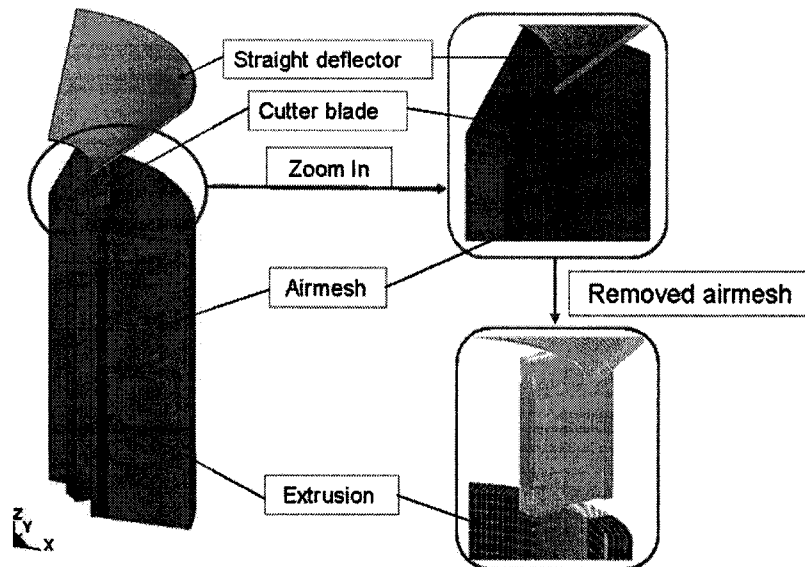


Figure 7.1. Discretization of the AA6061-T6 specimen, the tube airmesh, the cutter blade and the straight deflector.

A constant stress (single point integration) Lagrangian element formulation was used to model the cutter blade and the deflectors (either curved or straight) as shown in Figure 7.1. The mesh geometry used for these elements was identical to the extrusion and airmesh in the vicinity of contact. The thickness of the cutter varied linearly from the cutter shoulder to the cutter tip. The widths of the cutter shoulder and cutter tip were 6.0 mm and 1.0 mm respectively. The length of the cutter, in the tapered region, was 7.0 mm and the entire length of the cutter was 12.8 mm. This geometry for these entities was identical to the experimental apparatus.

7.1.2 Modeling contact

Contact between the Eulerian extrusion and airmesh and the Lagrangian FE cutter blade was completed through Eulerian/Lagrangian coupling by employing a single ‘CONSTRAINED_LAGRANGE_IN_SOLID’ contact definition available within LS-DYNA. A penalty type contact formulation was employed in the normal direction through a 3x3x3 point grid representing virtual nodes located at the Gauss points of the extrusion/airmesh. Relative motion at the interfaces was modeled using a coefficient of friction specified as 0.3. Within this contact algorithm only a single constant value of the coefficient of friction may be defined.

7.1.3 Application of boundary conditions

The axial cutting process of the tubular specimens was modeled by prescribing a constant velocity of 7 m/s in the axial direction of the tube (the negative Z-direction in Figure 7.1). Jones [13] noted that crushing speeds on the order of 10 m/s or less can be considered quasi-static. This facilitates the comparison of the FE results to the experimental quasi-static cutting test results. Furthermore, an analysis of the kinetic and internal (strain) energies during the axial cutting simulations illustrated that the kinetic energy was, on average, approximately 0.04% of the internal energy through the simulation. This observation indicates that the numerical simulations are quasi-static in nature and comparisons between the experimental and numerical testing methods are appropriate.

At the lower end of the extrusion, full boundary constraints were applied to all nodes. Also, in order to ensure that the symmetry conditions were met, nodes lying in the symmetry planes at the boundaries of the quarter-structure model were constrained to move only within the symmetry planes as illustrated in Figure 7.1.

7.1.4 Material models

An elastic-plastic-hydrodynamic material model (referred to as *MAT_ELASTIC_PLASTIC_HYDRO within LS-DYNA) was selected for the extrusion and airmesh. Although the airmesh is initially void of material, through the course of the simulation, the extrusion material may pass into the airmesh and hence this material definition was applied to the airmesh. This material model allows for appropriate modeling of an elastic-plastic hydrodynamic material and requires for input the density, shear modulus, yield strength and a piecewise linear approximation to the true stress/true effective plastic strain behaviour of the material. The experimental tensile testing conducted on extrusion stock material provided the majority of data for input into this material definition.

This material model requires an equation of state to describe the bulk characteristics of the material. A linear polynomial equation of state, which requires coefficients to describe the pressure/volume relationship as a high order polynomial, was utilized. All terms except for the linear coefficient were specified as zero. The linear term was specified as the elastic bulk modulus of the AA6061-T6 alloy. A rigid material definition was applied to the cutter blade and deflector as no apparent deformation of the 4140 steel alloy was observed in the cutter during the experimental testing.

7.1.5 Simulation procedure

The simulations of the axial cutting of round extrusions in presence of the straight/curved deflector were completed utilizing LS-DYNA version 970 release 6763 on a personal computer with dual 2.0 GHz AMD Opteron processors and 4 GB of dynamic random access memory. The time duration to complete a simulation utilizing an Eulerian element formation for the FE model was approximately 160 hours.

7.2. Smooth particle hydrodynamics (SPH) mesh free approach

Smoothed Particle Hydrodynamics is a mesh-free Lagrangian numerical technique, which is a possible alternative to numerical techniques currently used to analyze large deformation events. The technique has some special advantages over the traditional grid-based numerical methods, the most significant one among which is the adaptive nature of the SPH method. This adaptability of SPH is achieved at the very early stage of the field variable approximation that is performed at each time step based on a current local set of arbitrarily distributed particles. Because of this adaptive nature of the SPH approximation, the formulation of SPH is not affected by the arbitrariness of the particle distribution. Therefore, it can naturally handle problems with extremely large deformation.

7.2.1 Model geometry and discretization

Discretization of the cutter and deflector were identical to the models of these entities used in the Eulerian simulation studies. Element formulations selected for these entities was identical to previous simulations.

Discretization of the extrusion was completed by utilizing 13 SPH particles through the thickness of the extrusion side wall. This resulted in an approximate distance of 0.26 mm between particles in the radial direction. A similar distance between particles was also considered in the transverse direction. In the axial direction of the extrusion, particle separation distance was approximately 0.42 mm. These spacing dimensions are consistent with what was utilized in the discretization of the extrusion and airmesh in the Eulerian studies. In total 435487 SPH particles were utilized to discretize the extrusion. In addition, the default particle approximation theory within LS-DYNA was implemented for all SPH particles.

The default value for the smoothing length of the SPH particles was utilized in simulations employing the particle formulation. In addition, values for the minimum and maximum scale factors for the smoothing length were specified as 0.2 and 2.0. Finally, the initial number of neighbours per particle was altered to 300 from the default value of

150. As an example Figure 7.2 illustrates the FE model incorporating the SPH particle formulation for the extrusion with a curved deflector and cutter blade.

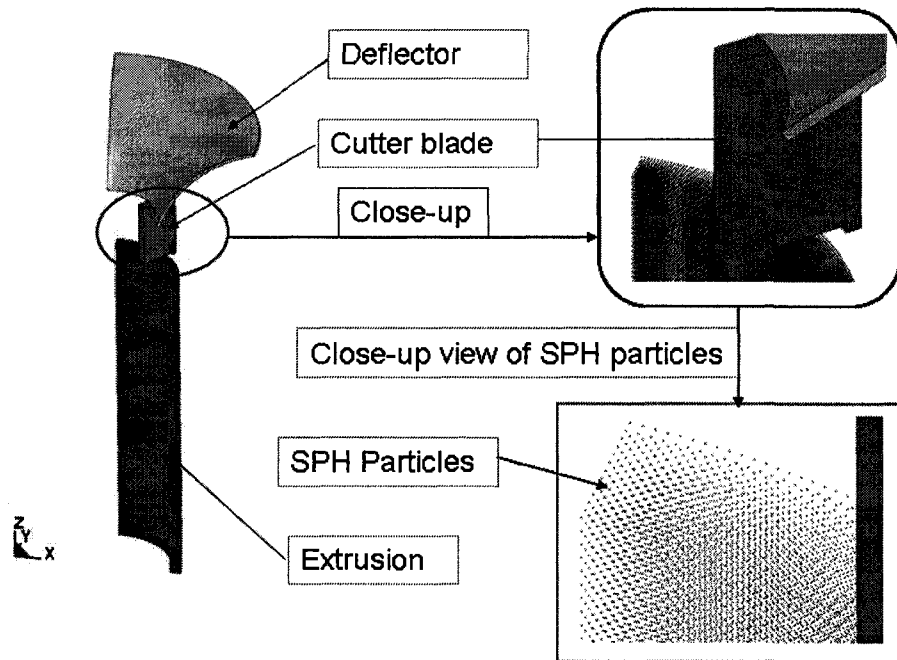


Figure 7.2. Discretization of the AA6061-T6 specimen, the tube airmesh, the cutter blade and the curved deflector.

7.2.2 Modeling contact

A penalty based contact algorithm (*CONTACT_NODES_TO_SURFACE) was used to numerically model the interaction between the extrusion and both the cutter and deflector. Values for the static and dynamic coefficients of friction were specified as 0.20 and 0.15 respectively. Furthermore, a soft constraint contact formulation was implemented.

7.2.3 Application of boundary conditions

Boundary conditions, applied to the SPH particles of the extrusion, were consistent with the boundary conditions imposed in previous simulations incorporating Eulerian element formulations.

7.2.4 Material models

The identical material model and equation of state, previously detailed in the numerical simulations employing the Eulerian formulation for the extrusion and airmesh, were prescribed for the extrusion SPH particles.

7.2.5 Simulation procedure

The amount of time necessary to complete simulation of the SPH extrusion cutting process was approximately 112 hours. The simulation procedure was otherwise identical to the approach taken in the Eulerian FE modeling process.

8. FINITE ELEMENT ANALYSIS RESULTS AND DISCUSSION

The results of the FE simulations of the experimental cutting test of AA6061-T6 round aluminum alloy extrusions in presence of the cutter and the straight or curved deflector are presented and discussed in this chapter. The results of FE simulation in the form of load/displacement profiles employing both Eulerian and SPH formulations in presence of the straight and the curved deflectors are discussed in sections 8.1 and 8.2 respectively. These profiles are overlaid with the experimental load/displacement response in order to illustrate the predictive capabilities of the FE models. In addition, deformed geometry plots are shown for selected simulations along with pictures taken during the experimental quasi-static cutting tests in order to illustrate the ability of the FE models to predict the cutting mode of the extrusion. In section 8.3, the numerically predicted total energy absorption and *CFE* of each FE formulation in presence of the straight and curved deflectors are compared with experimental results. Section 8.4 compares the numerically found the peak and the mean cutting forces with corresponding experimentally obtained the peak cutting force and the mean cutting force. A table summarizing results of all the crush parameters from the FE simulation and the experimental tests is also presented in section 8.4.

8.1 FE Simulation results and discussion in presence of the straight deflector

The load/displacement profile from FE simulation utilizing Eulerian and SPH formulations along with the experimental findings in presence of the straight deflector are presented in Figure 8.1. The load/displacement profiles illustrated in Figure 8.1 indicated that the Eulerian FE model predicted the steady state cutting process well. However, under-predictions of the peak load occurring during initial sidewall contact with the deflector and over-prediction of loads during the second transient cutting process by approximately 33% (averaged over the displacement range of 35 mm to 60 mm) were observed. The steady-state cutting/deflecting forces from the Eulerian FE (after approximately 65 mm) were within 5% of the experimental observations.

The presence of the crack formations in the SPH FE model significantly reduced the loads necessary to permit cutter penetration into the extrusion. The extrusion provided less resistance to penetrate the cutter as indicated in Figure 8.1. The ‘tensile instability’ [56, 57] associated with SPH technique may be a possible reason. The SPH analysis formulation results became suspect when there was significant bending and membrane stretching occurred.

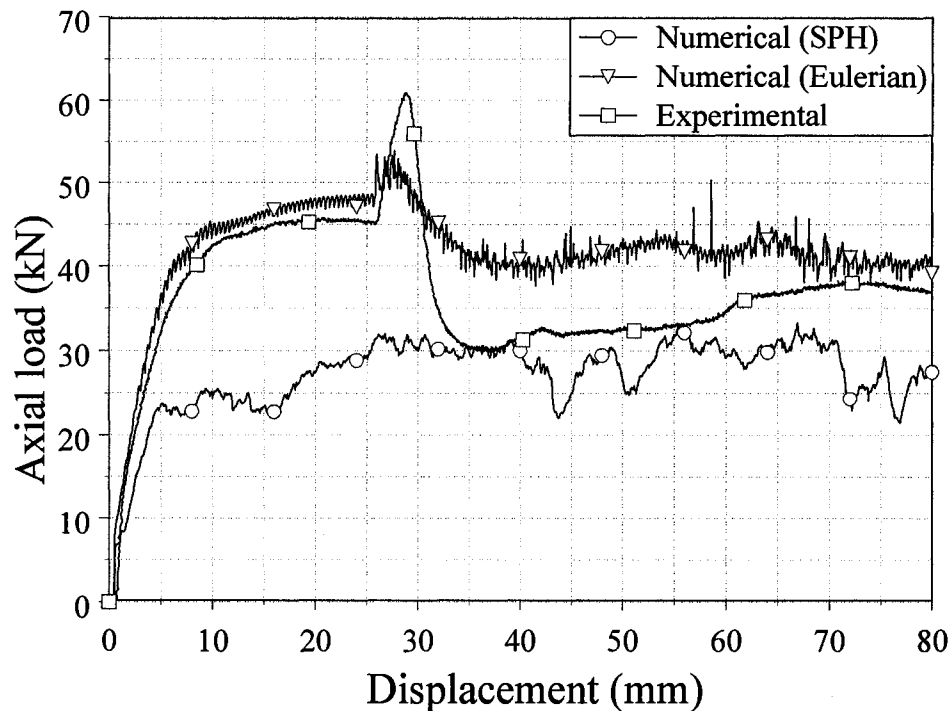
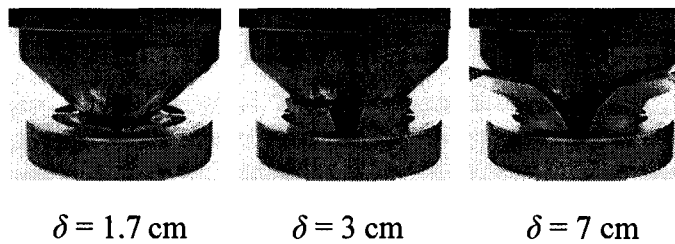


Figure 8.1. The load/displacement behaviour from experimental testing and numerical simulation of axial cutting in presence of the straight deflector.

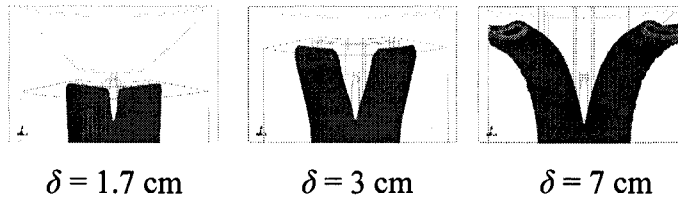
Images in Figure 8.2 illustrate the cutting behaviour and approximate cutter penetration through the aluminum extrusions during experimental tests and numerical simulations with the presence of a straight deflector. Photographs of the deformation process utilizing the straight deflector in Figure 8.2 illustrated that the cutter penetrated through the sidewall of the specimens and developed highly localized plastic deformation in the vicinity of the cutting blades where cutting chips were formed. No crack propagation was observed during the experimental cutting process. Similar findings were observed for the numerical simulations employing an Eulerian element formulation,

however random crack propagation was observed for the SPH numerical model of the extrusion. As the cutting process proceeded, the petalled sidewalls contacted the deflector and flared outward and formed a continuous region of contact with the deflector. Circumferential stretching of the tube was observed to occur after cutting but prior to contact with the deflector. After contact between the deflector and petalled sidewalls commenced a combination of circumferential stretching and large bending was observed to occur within the petalled sidewall.

(a) Experimental



(b) Numerical using Eulerian Model



(c) Numerical using SPH model

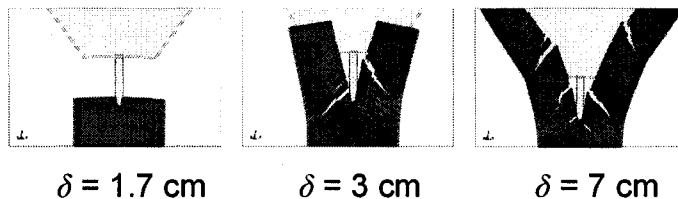


Figure 8.2. Experimental (a) and numerical (b and c) axial cutting of the AA6061-T6 extrusions under cutting deformation mode in presence of the straight deflector.

8.2 FE Simulation results and discussion in presence of curved deflector

Figure 8.3 illustrates the observed load/displacement responses from experimental and numerical testing utilizing a curved deflector. The Load/displacement profiles in Figure 8.3 illustrate that the Eulerian FE model predicted both the steady state and

transient cutting processes well. However, an over-estimation to the cutting/deflecting force in the displacement range of approximately 30 mm to 70 mm was observed. FE simulations of the SPH extrusion also illustrated similar findings to the load/displacement under-predictions previously noted for the straight deflector.

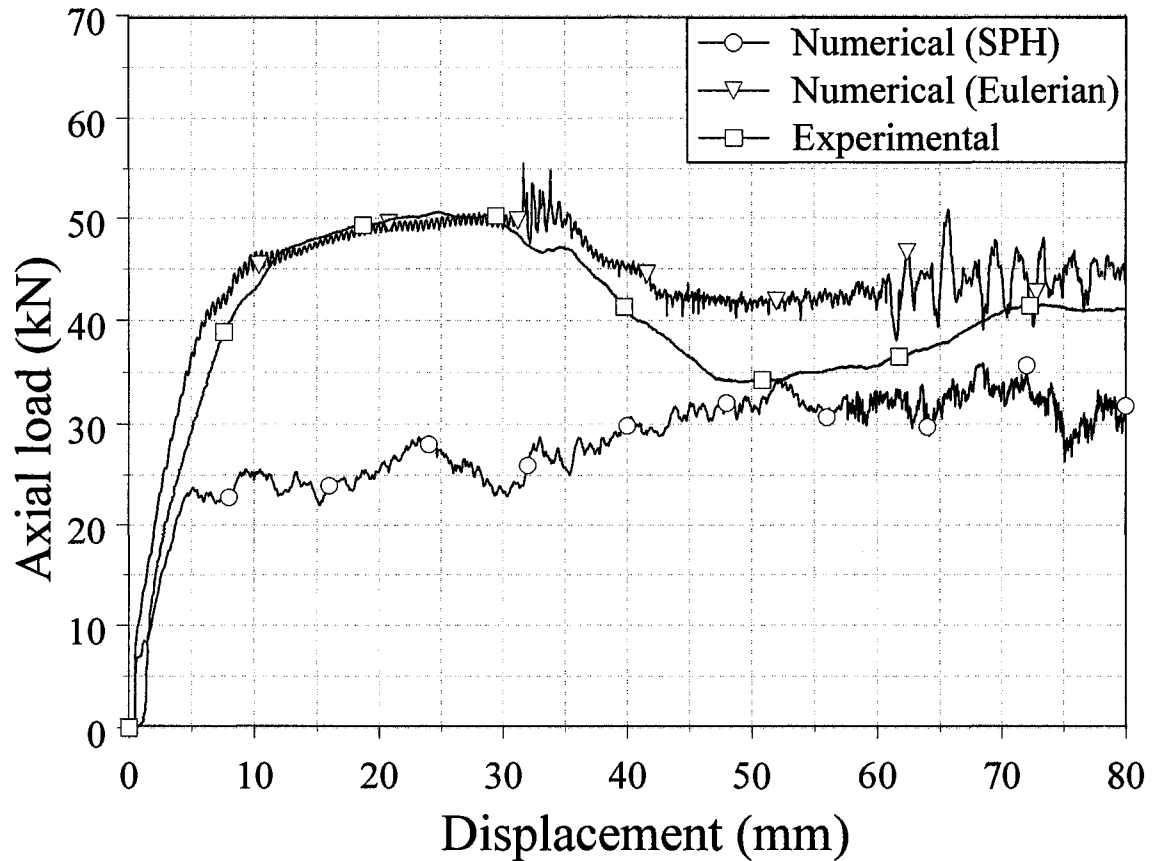
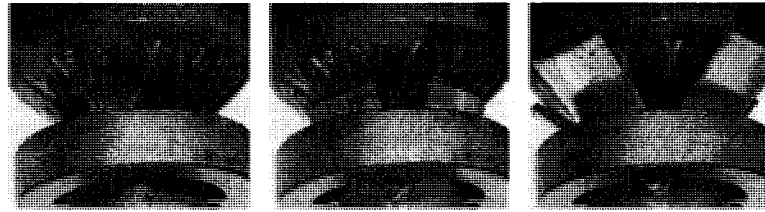


Figure 8.3. The load/displacement behaviour from experimental testing and numerical simulation of the axial cutting in presence of the curved deflector.

Figure 8.4 illustrates the cutting behaviour and approximate cutter penetration through the aluminum extrusions during experimental tests and numerical simulations in presence of a curved deflector. As observed in previous simulations, crack propagation was observed in the simulation utilizing the SPH element formulation for the extrusion.

(a) Experimental

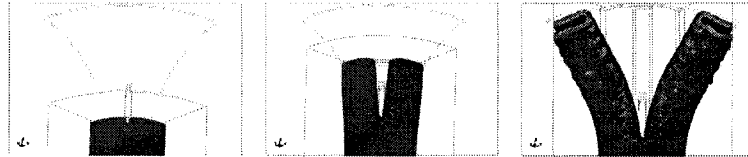


$\delta = .5 \text{ cm}$

$\delta = 3 \text{ cm}$

$\delta = 6 \text{ cm}$

(b) Numerical using Eulerian Model

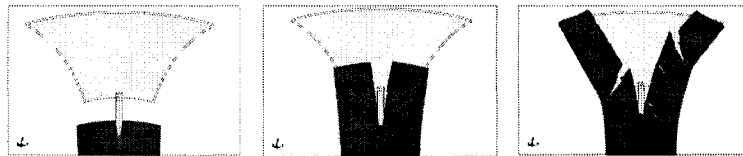


$\delta = .5 \text{ cm}$

$\delta = 3 \text{ cm}$

$\delta = 6 \text{ cm}$

(c) Numerical using SPH model



$\delta = .3 \text{ cm}$

$\delta = 3 \text{ cm}$

$\delta = 6 \text{ cm}$

Figure 8.4. Experimental (a) and numerical (b and c) axial cutting of AA6061-T6 extrusions under cutting deformation mode in presence of the curved deflector.

8.3 Total energy absorption and crush force efficiency

Figure 8.5 and 8.6 illustrate generally linear energy absorption versus displacement relationships after approximately 40 mm and 50 mm of cutter displacement in presence of straight and curved deflector respectively. These findings are expected as a result of the almost constant cutting force after this cutter displacement. The Eulerian FE simulation over predicted TEA approximately 14% and 8% higher compared to experimental findings in presence of straight and curved deflector respectively. However, FE simulations results employing SPH technique failed to predict TEA within acceptable range.

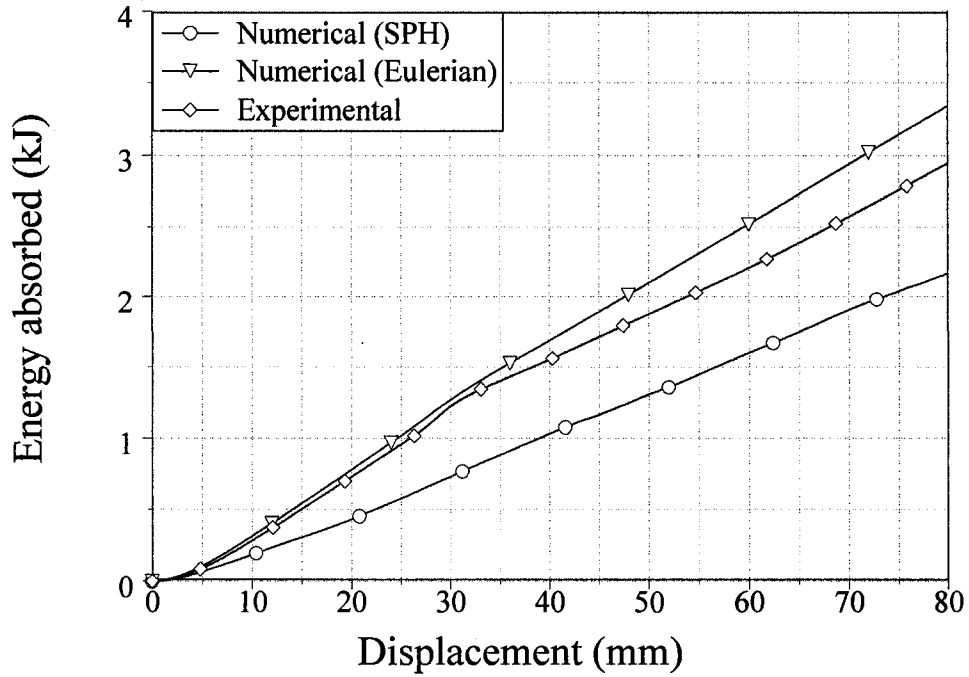


Figure 8.5. Energy absorbed versus displacement behaviour from experimental testing and numerical simulation of axial cutting with the presence of the straight deflector.

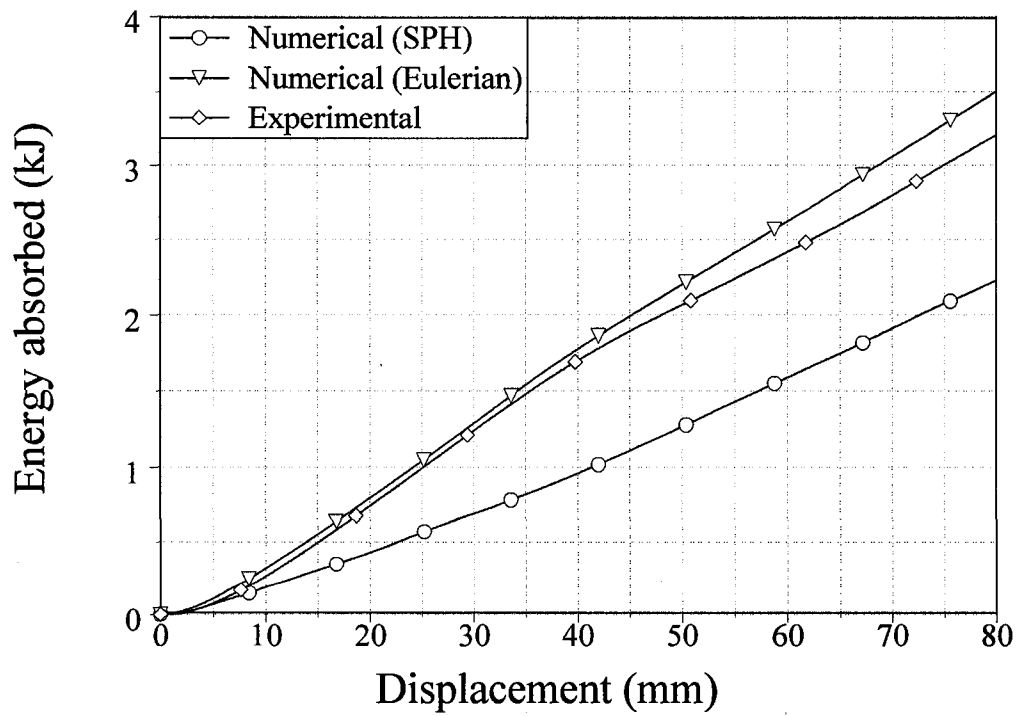


Figure 8.6. Energy absorbed versus displacement behaviour from experimental testing and numerical simulation of axial cutting with the presence of the curved deflector.

8.4 Mean cutting force and peak cutting force

The FE simulation employing Eulerian technique in presence of straight deflector under predicted the peak cutting force by approximately 14% but over predicted the mean cutting force by approximately 11.7%. However, Eulerian technique over predicted both peak and mean cutting forces by approximately 2% and 10% respectively in presence of curved deflector. The SPH formulation significantly under predicted both the peak and mean cutting forces in both cases as material showed less resistance during penetration of cutter due to tensile instability associated with SPH formulations.

Table 8.1 Cutting characteristics for the AA6061-T6 extrusions summarized from experimental testing and numerical simulations in the presence straight and curved deflector.

	P_m (kN)	P_{max} (kN)	CFE	TEA (kJ)
Experimental test with straight deflector	37.16	52.48	0.71	5.18
Experimental test with curved deflector	39.94	49.93	0.82	5.79
Simulation with straight deflector (Euler)	41.74	53.85	0.78	3.34
Simulation with curved deflector (Euler)	43.71	55.51	0.79	3.50
Simulation with straight deflector (SPH)	27.03	33.26	0.81	2.16
Simulation with curved deflector (SPH)	27.78	35.82	0.78	2.22

9. CONCLUSIONS

A significant amount of information regarding the energy absorption capabilities and deformation modes of circular aluminum alloy structural members under axial compressive loading condition have achieved through the experimental tests and numerical simulations conducted in this research. The relationship between the extrusion geometry and material properties of AA6061-T4 and -T6 tubes under cutting deformation mode provides in depth knowledge on improving crush performance and achieving desired force/displacement response utilizing specially designed cutters, deflectors and spacers. Based upon the observations and through analysis of the experimental and numerical data, the following conclusions can be made.

9.1 Conclusions for quasi-static axial crushing tests

1. The CFE for AA6061-T6 specimens considered in this research ranged from 8.3% to 70% as a result of the global bending and progressive folding deformation modes. For specimens with a T4 temper the CFE ranged from 16% to 74% with lower values a result of global bending and higher values due to the progressive folding deformation behaviour.
2. The average TEA for the AA6061-T6 extrusions, with a wall thickness of 3.175 mm, which experienced the progressive folding and global bending deformation modes was approximately 13.71 kJ and 4.05 kJ respectively. The specimens with the same temper but a reduced wall thickness of 1.587 mm illustrated TEA of approximately 3.70 kJ and 0.79 kJ for progressive folding and global bending deformations respectively. The extrusions with a T4 temper and wall thickness of 3.175 mm, which experienced the progressive folding and global bending deformation modes, exhibited TEA of 9.46 kJ and 3.37 kJ respectively. Identical extrusions with wall thickness of 1.587 mm illustrated TEA of approximately 3.25 kJ and 0.71 kJ for progressive folding and global bending deformations respectively.
3. The specimens with T6 temper and 3.175 mm wall thickness experienced approximately 40% higher mean crushing force compared to similar extrusions

with T4 temper for progressive folding deformation mode. However, this difference was reduced to approximately 18.5% for extrusions with reduced wall thickness of 1.587 mm. Similar observations were also found for the peak crushing force.

4. All the specimens with T6 temper and wall thickness of 1.587 mm illustrated significant local plasticity during the formation of folds which resulted in material failure and the generation of a large number of fragmented pieces of the extrusion. However, no material failure was observed for similar specimens with T4 temper.

9.2 Conclusions for cutting deformation mode utilizing single cutter

1. The cutting deformation mode initiated by the use of the cutter appeared to be stable, repeatable and controllable. Specimens with a wall thickness of 3.175 mm and both temper conditions as well as extrusions with a wall thickness of 1.587 mm and T6 temper condition illustrated a stable or clean curling cut deformation mode with a constant load during cutting after crosshead displacement of about 20 mm. Specimens with a T4 temper and wall thickness of 1.587 mm illustrated a braided cut deformation pattern. The cutting load remained constant until approximately 50 mm crosshead displacement. Significant fluctuations in the cutting force were observed after this crosshead displacement.
2. The slight variation in cutter blade tip width thickness among cutter sides A, B, C and D had a minor but notable influence on the load/displacement responses for all cutting deformation observed in this research. The extrusions with T4 temper utilizing cutter side C, which had blade tip width of 1.17 mm, experienced approximately 14.5% and 9% higher cutting force compared to cutting force exhibited using cutter side with blade tip width of 1.00 mm for wall thickness of 3.175 mm and 1.587 mm respectively. Similar findings were also observed for extrusions with T6 temper but with relatively lower range of approximately 2.2% and 6.4% for extrusions with 3.175 mm and 1.587 mm wall thicknesses respectively.

3. No significant dependency on extrusion length for the load/displacement behaviour of the AA6061-T4 and -T6 specimens was found during the cutting process.
4. The average CFE for the AA6061-T4 extrusions, with a wall thickness of 3.175 mm, which experienced the cutting deformation mode was approximately 92%. Specimens with the same temper but a reduced wall thickness of 1.587 mm illustrated a CFE of 86%. The extrusions with a T6 temper exhibited CFE of 94.5% and 89% for wall thickness of 3.175 mm and 1.587 mm respectively. The average energy absorption for the extrusions with a wall thickness of 3.175 mm which experienced the cutting mode of deformation was 4.2 kJ and 6.1 kJ for T4 and T6 temper respectively. For specimens which also experienced cutting deformation with a reduced wall thickness of 1.587 mm in T4 and T6 temper conditions, the average total energy absorption was found to be 2.1 kJ and 2.7 kJ respectively.
5. A consistent force/displacement responses were observed incorporating deflectors with straight and curved profile along with cutter. The load/displacement relationship was observed to be almost constant after a crosshead displacement of approximately 60 mm for the cutting deformation in presence of the straight deflector and a crosshead displacement of approximately 70 mm for the cutting deformation incorporating the curved deflector.
6. The average CFE for extrusions with 3.175 mm wall thickness, which experienced the cutting deformation mode in presence of the straight deflector, was approximately 68% and 81.6% with T6 and T4 temper respectively. Specimens with a reduced wall thickness of 1.587 mm and with T6 and T4 temper utilizing similar deflector exhibited CFE of approximately 78.6% and 83.9% respectively. The average CFE for the AA6061-T6 extrusions, with a wall thickness of 3.175 mm in presence of the curved deflector was approximately 81%. The extrusions with similar wall thickness but with T4 temper showed average CFE of approximately 84%. However, the specimens with 1.587 mm and both temper illustrated similar *CFE* of 85.6%.

7. The average total energy absorption for the extrusions with a wall thickness of 3.175 mm in presence of straight deflector was 5.21 kJ and 3.38 kJ for T4 and T6 temper respectively. For the specimens, which also utilized the straight deflector with a reduced wall thickness of 1.587 mm in T4 and T6 temper conditions, the average total energy absorption was found to be 2.63 kJ and 1.85 kJ respectively. The specimens with wall thickness of 3.175 mm, which experienced cutting deformation mode in presence of the curved deflector, exhibited approximately 6% and 13% higher TEA compared to the straight deflector for T6 and T4 temper respectively.
8. The AA6061-T6 extrusions, with a wall thickness of 3.175 mm, experienced approximately 17.5% higher peak cutting force in presence of straight deflector compared to that with no deflector. However, the peak cutting force for identical specimens in presence of curved deflector illustrated only 2.4 % increase over the cutting force without use of deflector. Consistent peak cutting force with or without presence of straight or curved deflector was observed for specimens with T4 temper.
9. For the extrusions which experienced the cutting deformation mode, four energy-dissipating mechanisms were observed, namely, a near blade tip cutting deformation mechanism, a circumferential membrane stretching, a far field petalled sidewall outward bending and friction. The bending mechanism was most probably formed due to the eccentric pushing forces generated from the contact of cutter blades and the split petalled sidewall, which was not significant compared with the vertical cutting mechanism.

9.3 Conclusions for dual stage cutting

1. The dual stage cutting is the superposition of two single stage cutting processes. A constant force/displacement response for AA6061-T6 extrusions with 3.175 mm wall thickness was observed after 30 mm crosshead displacement using no deflector and after approximately 80 mm in presence of straight or curved deflector. However, fluctuation in cutting force after extrusions passed through second stage cutter, with or without presence of deflectors, was noticed

for identical extrusions but reduced wall thickness of 1.587 mm. The specimens with T4 temper and 1.587 mm wall thickness switched deformation mode from cutting to progressive folding as strength of the material reduced.

2. The average CFE for AA6061-T6 extrusions with 3.175 mm wall thickness ranged from 83.7% to 88.03% with different combinations of cutter sides. The CFE for identical extrusions but with T4 temper was ranged from 63.5% to 83%. The lower value of CFE associated with T4 temper extrusions was due to switching deformation mode from cutting to global bending during second stage cutting process. Specimens with a reduced wall thickness of 1.587 mm and with T6 temper illustrated CFE ranged from 78% to 83%.
3. Incorporating deflectors with cutters increased stability of the dual stage cutting process. The extrusions with T6 temper and wall thickness of 3.175 mm predicted mean cutting force 4.4% higher in presence of straight deflector and 3.6% higher in presence of curved deflector compared to the mean cutting force using no deflector. However, a consistent mean and peak cutting forces were observed with identical extrusions but reduced wall thickness of 1.587 mm.
4. A minor influence of cutter side combination was observed during first stage cutting process for extrusions with 3.175 mm wall thickness, however, this influence was not noticed during cutting process of specimens with reduced wall thickness of 1.587 mm. The cutter side combination CA (1.17 mm and 1.01 mm) demonstrated approximately 8% higher cutting force compared to other two cutter side combinations during the first stage of cutting process.
5. The addition of spacers in between the two cutters resulted in a greater degree of separation between the first portions of the steady state response from the first cut to the initiation of the second stage cutting process. There is a limitation on length of spacing can be used in between two cutters. The experimental observations illustrated a maximum 20 mm spacing between two cutters can be utilized. As spacing between the cutters increased the stability of the cutting progress degraded due to contact between the cut petalled sidewalls (resulting from the first cutting process) and regions of the second cutter away from the blade tip.

9.4 Conclusions for controlling load/displacement response

1. The cutting deformation mode, initiated within the extrusions by use of the cutter, appeared to be stable, repeatable and controllable. These findings indicate that the deformation appeared to exhibit characteristics of a stable (or clean curling) cutting mode.
2. The TEA observed in this experimental investigation ranged from 2.05 kJ to 5.90 kJ for T6 temper extrusions and 1.53kJ to 4.36 kJ for extrusions with T4 temper. The variation in TEA was strongly dependent upon the variation of wall thickness of the extrusion.
3. The profiles of the load/displacement curve exhibited a good correlation to the variations of wall thickness through the axial direction of the extrusion.

9.5 Conclusions for FE modeling

1. A good correlation was observed between the results of FE simulations utilizing Eulerian FE formulation and the results of quasi-static cutting tests prior to side wall contact with either straight or curved deflector. The Eulerian FE formulation under predicted the experimental peak cutting force in presence of straight deflector, however, over predicted the cutting load approximately 12% from 30 mm to 70 mm cross-head displacement.
2. SPH FE formulation failed to predict experimental result in both instances. A significant reduction in material resistance during penetration of cutter through the extrusions may be attributed towards tensile instability associated with SPH formulation.

9.6 Future work

Future work in this area may include the experimental axial cutting tests under impact loading conditions as well as quasi-static and impact testing on oblique loading. Furthermore, numerical simulations of cutting process under both quasi-static and impact loading may be helpful in this research.

REFERENCES

1. <http://www.iihs.org/ratings/rating.aspx> , Insurance Institute for Highway Safety, Accessed on June 2008.
2. <http://www.worldautosteel.org/>, International Iron and Steel Institute, Accessed on June 2008.
3. <http://www.autoaluminum.org/main/index> , The Aluminum Association Inc., Accessed on June 2008.
4. Abramowicz, W. and Jones, N., '*Dynamic axial crushing of square tubes*', International Journal of Impact Engineering 1984, 2(2), pp.1979-2008.
5. Guillow, S.R., Lu, G. and Grzebieta, R.H., '*Quasi-static axial compression of thin-walled circular aluminium tubes*', International Journal of Mechanical Sciences 2001, 43(9), pp. 2103-2123.
6. Abramowicz, W. and Jones, N., '*Dynamic progressive buckling of circular and square tubes*', International Journal of Impact Engineering 1986, 2, pp.243-269.
7. Langseth, M. and Hopperstad, O.S., '*Static and dynamic axial crushing of square thin-walled aluminum extrusions*', International Journal of Impact Engineering 1996, 18(7-8), pp.949-968.
8. Singace, A.A., '*Axial crushing analysis of tubes deforming in the multi-lobe mode*', International Journal of Mechanical Sciences 1999, 41, pp. 869-890.
9. Hsu, S.S. and Jones, N., '*Quasi-static and dynamic axial crushing of thin-walled circular stainless steel, mild steel and aluminium alloy tubes*', International Journal of Crashworthiness 2004, 9(2), pp.195-217.
10. Miscow, F.P.C. and Al-Qureshi, H.A., '*Mechanisms of static and dynamic inversion processes*', International Journal of Mechanical Sciences 1997, 39(2), pp. 147-161.
11. Alghamdi, A.A.A., '*Collapsible impact energy absorbers: an overview*', Thin-Walled Structures 2001, 39, pp.189-213.
12. Leu, D.K., '*The curling characteristics of static inside-out inversion of metal tubes*', International Journal of Machine Tools & Manufacture 2000, 40(1), pp. 65-80.

13. Rosa, P.A.R., Rodrigues, J.M.C. and Martins, P.A.F., '*External inversion of thin-walled tubes using a die: experimental and theoretical investigation*', International Journal of Machine Tools & Manufacture 2003, 43(8), pp. 787-796.
14. Kitazawa, K., '*Criteria for outward curling of tubes*', Journal of Engineering for Industry Trans. 1993, ASME 115, pp. 466-471.
15. Al-Hassani, S.T.S., Johnson, W. And Lowe, W.T., '*Characteristics of inversion tube under axial loading*', Journal of Mechanical Engineering Science 1972, 14, pp. 370-381.
16. Stronge, W.J., Yu, T.X. and Johnson, W., '*Long stroke energy dissipation in splitting tubes*', International Journal of Mechanical Sciences 1983, 25(9-10), pp. 637-647.
17. Reddy, T.Y. and Reid, S.R., '*Axial splitting of circular metal tubes*', International Journal of Mechanical Sciences 1986, 28(2), pp. 111-131.
18. Lu, G., Ong, L.S., Wang, B. and Ng, H.W., '*An experimental study on tearing energy in splitting square metal tubes*', International Journal of Mechanical Sciences 1994, 36(12), pp. 1087-1097.
19. Huang, X., Lu, G. and Yu, T.X., '*On the axial splitting and curling of circular metal tubes*', International Journal of Mechanical Sciences 2002, 44(11), pp. 2369-2391.
20. Huang, X., Lu, G. and Yu, T.X., '*Energy absorption in splitting square metal tubes*', Thin-Walled Structures 2002, 40(2), pp. 153-165.
21. Cheng, Q. and Altenhof, W., '*Load/displacement and energy absorption performances of AA6061-T6 tubes under a cutting deformation mode*', International Journal of Crashworthiness 2005, 10(6), pp. 621-633.
22. Jin, S.Y., Altenhof, W. and Kapoor, T., '*An experimental investigation into the cutting deformation mode of AA6061-T6 round extrusions*', Thin-Walled Structures 2006, 44(7), pp. 773-786.
23. Zheng, Z.M. and Wierzbicki, T., '*A theoretical study of steady-state wedge cutting through metal plates*', International Journal of Fracture 1996, 78(3/4), pp. 45-66.
24. Simonsen, B.C. and Wierzbicki, T., '*Plasticity, fracture and friction in steady-state plate cutting*' International Journal of Impact Engineering 1998, 21(5), pp. 387-411.

25. Jin, S.Y. and Altenhof, W., 'Experimental observations of AA6061-T6 round extrusions under a cutting deformation mode with a deflector', *International Journal of Crashworthiness* 2008, 13(2), pp. 127-132.
26. Kim, H.S. and Wierzbicki, T., 'Effect of the cross-sectional shape on crash behavior of a three dimensional space frame', *International Journal of Vehicle Design* 2001, 25(4), pp. 283-304.
27. Kim, H.S. and Wierzbicki, T., 'Effect of the cross-sectional shape of hat-type cross-section on the crash resistance of an 'S' frame', *Thin-Walled Structures* 2001, 39(7), pp. 535-554.
28. Kim, H.S., 'New extruded multi-cell aluminum profile for maximum crash energy absorption and weight efficiency', *Thin-Walled Structures* 2002, 40(4), pp. 311-327.
29. Abramowicz, W. and Jones, N., 'Transition from initial global bending to progressive buckling of tubes loaded statically and dynamically', *International Journal of Impact Engineering* 1997, 19(5-6), pp. 415-437.
30. Langseth, M. and Hannsen, A., 'Lecture Notes on Crashworthiness of Aluminum Structures', Department of Structural Engineering, Norwegian University of Science & Technology, 2002.
31. Kim, D.K. and Lee, S., 'Impact energy absorption of 6061 aluminum extruded tubes with different cross-sectional shapes', *Materials and Design* 1999, 20, pp. 41-49.
32. Arnold, B. and Altenhof, W., 'Finite element modeling of the axial crushing of AA6061 T4 and T6 and AA6063 T5 structural square tubes with circular discontinuities', *SAE Transactions: Journal of Materials & Manufacturing* 2006, 114(5), pp. 300-315.
33. Gupta, N.K. and Gupta, S.K., 'Effects of annealing, size and cut-outs on axial collapse behaviour of circular tubes', *International Journal of Mechanical Sciences* 1993, 35(7), pp. 597-613.
34. Krauss, C.A. and Laananen, D.H., 'A parametric study of crush initiators for a thin-walled tube', *International Journal of Vehicle Design* 1994, 15(3/4/5), pp. 385-401.
35. Abah, L., Limam, A. and Dejeammes, M., 'Effects of cutouts on static and dynamic behaviour of square aluminum extrusions', *Fifth International Conference on Structures Under Shock and Impact* 1998, Greece, June 24-26.

36. Lee, S., Hahn, C., Rhee, M. and Oh, J., '*Effect of triggering on the energy absorption capacity of axially compressed aluminum tubes*', Materials and Design 1999, 20(1), pp. 31-40.
37. Kitagawa, Y., Hagiwara, I. and Tsuda, M., '*Development of a collapse mode control method for side members in vehicle collisions*', SAE paper # 910809.
38. Arnold, B. and Altenhof, W., '*Experimental observations on the crush characteristics of AA6061 T4 and T6 structural square tubes with and without circular discontinuities*', International Journal of Crashworthiness 2004, 9(1), pp. 73-87.
39. Cheng, Q., Altenhof, W. and Li, L., '*Experimental investigations on the crush behaviour of AA6061-T6 aluminum square tubes with different types of through-hole discontinuities*', Thin-Walled Structures 2006, 44(4), pp. 441-454.
40. Han, H., Taheria, F. and Pegg, N., '*Quasi-static and dynamic crushing behaviors of aluminum and steel tubes with a cutout*', Thin-Walled Structures 2007, 45(3), pp.283-300.
41. Ohkubo, Y., Akamatsu, T. and Shirasawa, K., '*Mean crushing strength of closed-hat section members*', Society of Automotive Engineers 1974, Paper No. 740040.
42. Wierzbicki, T., '*Crushing behaviour of plate intersections*', Structural Crashworthiness 1983, Chapter 3, pp. 66-95.
43. Hayduk, R.J. and Wierzbicki, T., '*Extensional collapse modes of structural members*', Computers and Structures 1994, 18(3), pp. 447-458.
44. Wierzbicki, T. and Abramowicz, W., '*On the crushing mechanics of thin-walled structures*', Journal of Applied Mechanics 1983, 50, pp. 727-739.
45. Krauthammer, T., Jenssen, A., and Langseth, M., '*Precision testing in support of computer code validation and verification*', Norwegian Defence Construction Service Work-Shop, Fortifikatorisk notat NR 234/96.
46. Langseth, M., Hopperstad, O. and Berstad, T., '*Crashworthiness of aluminum extrusions: validation of numerical simulation, effect of mass ratio and impact velocity*', International Journal of Impact Engineering 1999, 22(9-10), pp. 829-854
47. Berstad, T., Hopperstad, O. and Langseth, M., '*Elasto-viscoplastic constitutive models in the explicit finite element code LS-DYNA3D*', Second International LS-DYNA3D Conference 1994, Paper Number 2ILSD3D113.

48. Hanssen, A., Hopperstad, O., Langseth, M. and Ilstad, H., '*Validation of constitutive models applicable to aluminum foams*', International Journal of Mechanical Sciences 2002, 44(2), pp. 359-406.
49. Yamazaki, K. and Han, J., '*Maximization of the crushing energy absorption of tubes*', Structural Optimization 1998, 16, pp. 37-46.
50. Han, J. and Yamazaki, K., '*A study on maximization of dynamic crushing energy absorption of square tubes with and without stiffener*', Japan Society of Mechanical Engineers 2000, 43(2), pp.138-145.
51. Mamalis, A.G., Manolakos, D.E., Ioannidis, M.B., Kostazos, P.K. and Dimitriou, C., '*Finite element simulation of the axial collapse of metallic thin-walled tubes with octagonal cross-section*', Thin-Walled Structures 2003, 41(10), pp. 891-900.
52. Jin, S.Y. and Altenhof, W., '*Crush characteristics of AA6061-T6 round tubes during a cutting deformation mode*', SAE Paper # 2007-01-0985, SAE World Congress 2007, Detroit, MI, USA (also accepted for SAE Transactions 2007).
53. Lucy, L. B., '*Numerical approach to the testing of the fission hypothesis*', The Astronomical Journal 1977, 82, pp.1013-1024.
54. Gingold, R. A. and Monaghan, J. J., '*Smoothed particle hydrodynamic: theory and application to non-spherical star*', Monthly Notices of the Royal Astronomical Society 1977, 181, pp. 375-389.
55. Limidoa, J., Espinosaa, C., Salauna, M. and Lacombe, J.L., '*SPH method applied to high speed cutting modelling*', International Journal of Mechanical Sciences 2007, 49(7), pp. 898-908.
56. Schwer, L.E., '*Preliminary Assessment of Non-Lagrangian Methods for Penetration Simulation*', 8th International LS-DYNA User Conference 2004.
57. Schwer, L.E., Hacker, K. and Poe, K., '*Perforation of Metal Plates: Laboratory Experiments and Numerical Simulations*', 9th International LS-DYNA User Conference 2006.
58. '*Atlas of Stress-Strain Curves*', ASM International, Second Edition.
59. ASTM E8M '*Standard Test Methods for Tension Testing of Metallic Materials*', ASTM International, Annual Book of ASTM standards 2002, 03.01, pp. 60-81.

60. ASTM B918 '*Standard Practice for Heat Treatment of Wrought Aluminum Alloys*', ASTM International, Annual Book of ASTM standards 2002, 02.02, pp. 622-635.
61. Jones, N., '*Structural Impact*', Cambridge, Cambridge University Press 1989.
62. '*Machinery's hand book*', Industrial Press Inc. 2000, 26th edition.
63. Magee, C.L. and Thornton, P.H., '*Design Consideration in Energy Absorption by Structural Collapse*', Society of Automotive Engineers 1978, Paper No. 780434.
64. Mahmood, H.F. and Paluszny, A., '*Design of Thin Wall Columns for Crash Energy Management - Their Strength and Mode of Collapse*', 4th SAE International Conference on Vehicle Structural Mechanics 1981, Paper No. 811302.
65. Raczy G. A., '*An Eulerian Finite Model for Determination of Deformation State of a Copper Subjected to Orthogonal Cutting*', M.A.Sc. Thesis 2004, University of Windsor.
66. LS-DYNA Keyword User's Manual, Version 970, Livermore Software Technology Corporation, April 2003.

APPENDIX A:

EXPERIMENTAL LOAD VERSUS DISPLACEMENT PROFILES

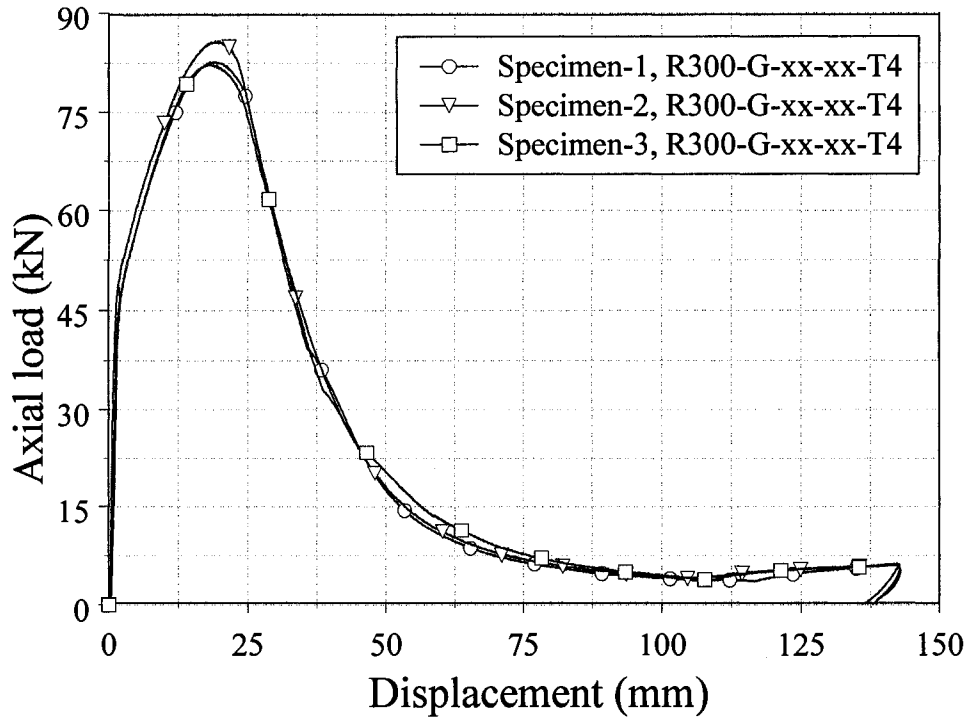


Figure A.1. The force/displacement responses for AA6061-T4 circular specimens with a wall thickness of 3.175 mm in Group 4.

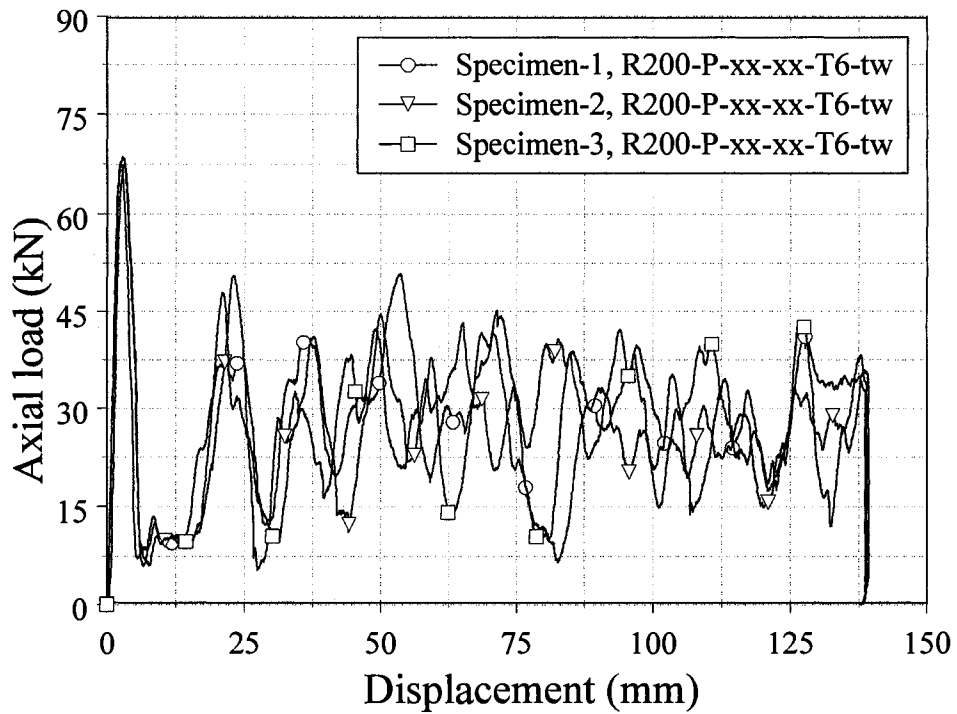


Figure A.2. The force/displacement profiles for AA6061-T6 round specimens with a wall thickness of 1.587 mm in Group 5.

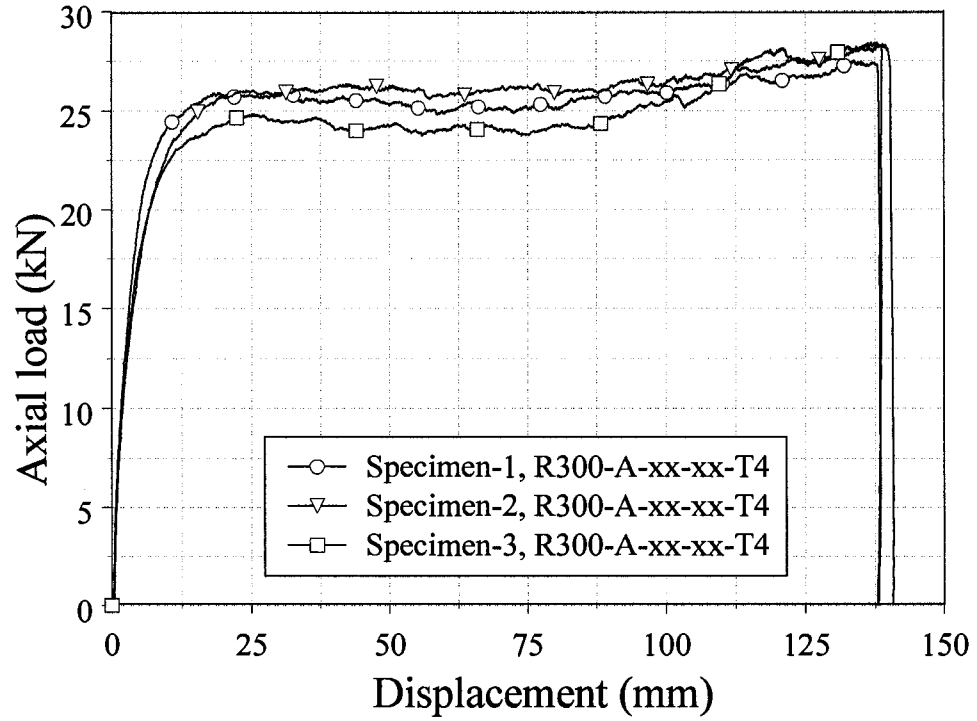


Figure A.3. The experimental load/displacement curves for AA6061-T4 round specimens with a wall thickness of 3.175 mm in Group c-1.

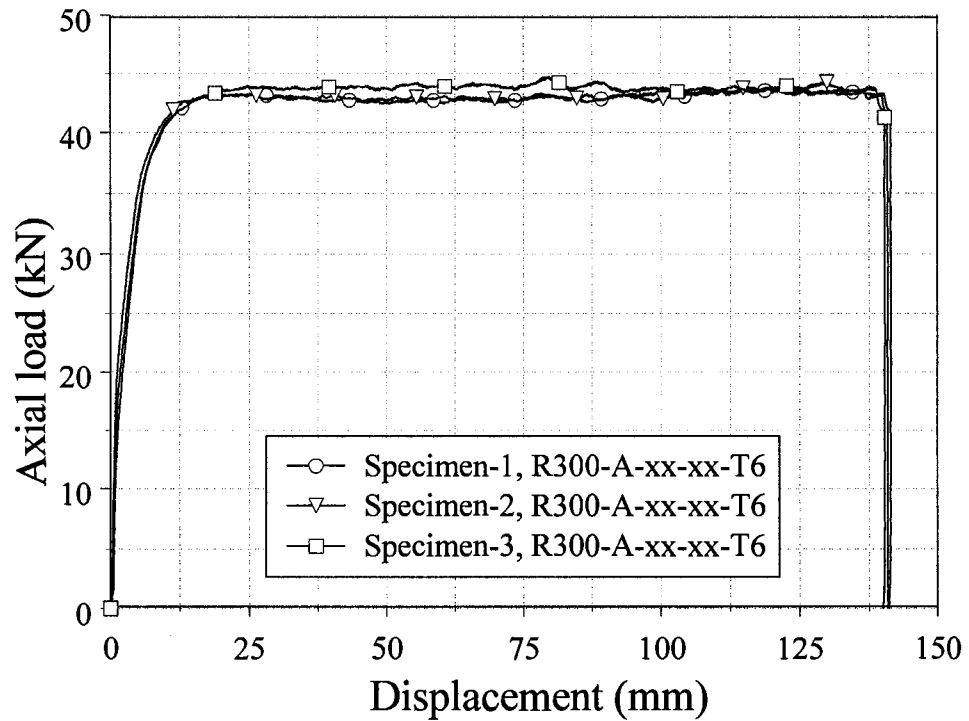


Figure A.4. The experimental load/displacement curves for AA6061-T6 round specimens with a wall thickness of 3.175 mm in Group c-5.

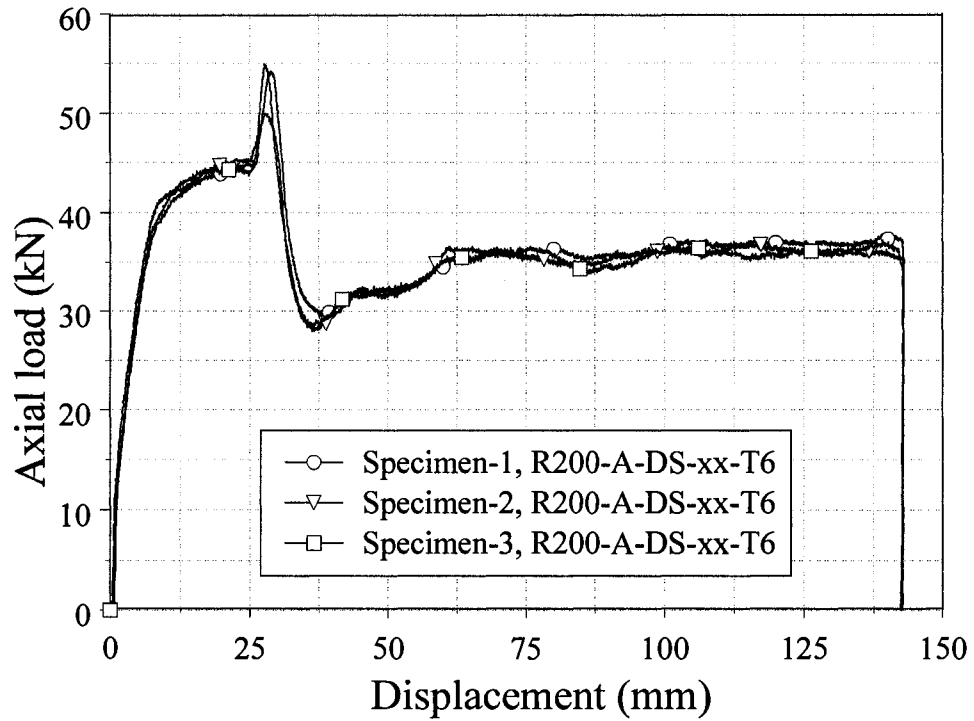


Figure A.5. The load/displacement profiles for AA6061-T6 extrusions with a wall thickness of 3.175 mm in the presence of straight deflector in Group d-1.

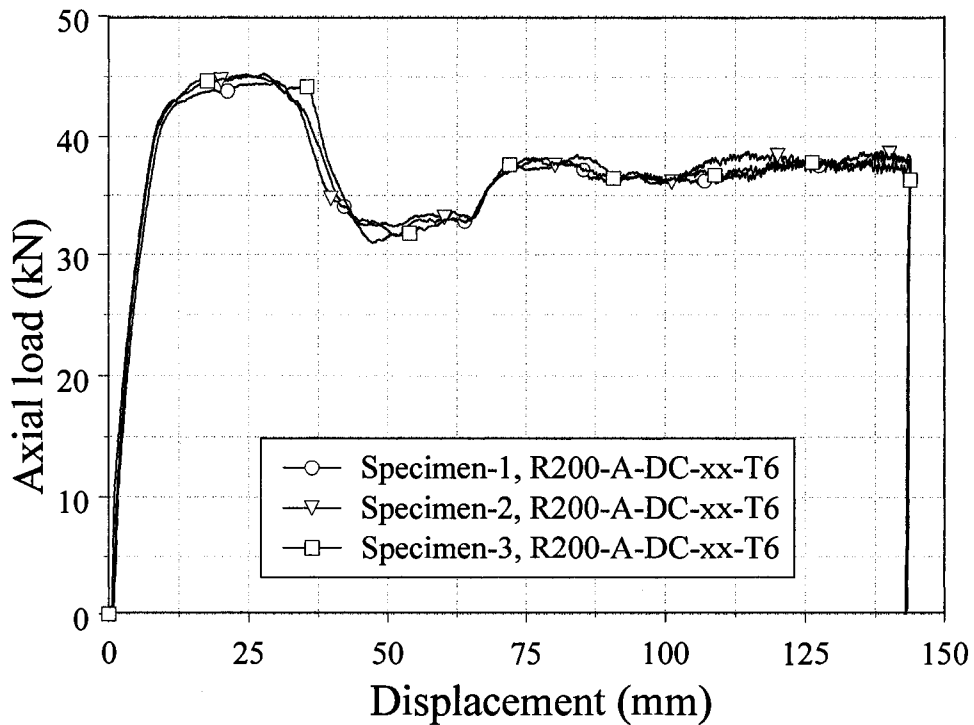


Figure A.6. The load/displacement profiles for AA6061-T6 extrusions with a wall thickness of 3.175 mm in the presence of curved deflector in Group d-5.

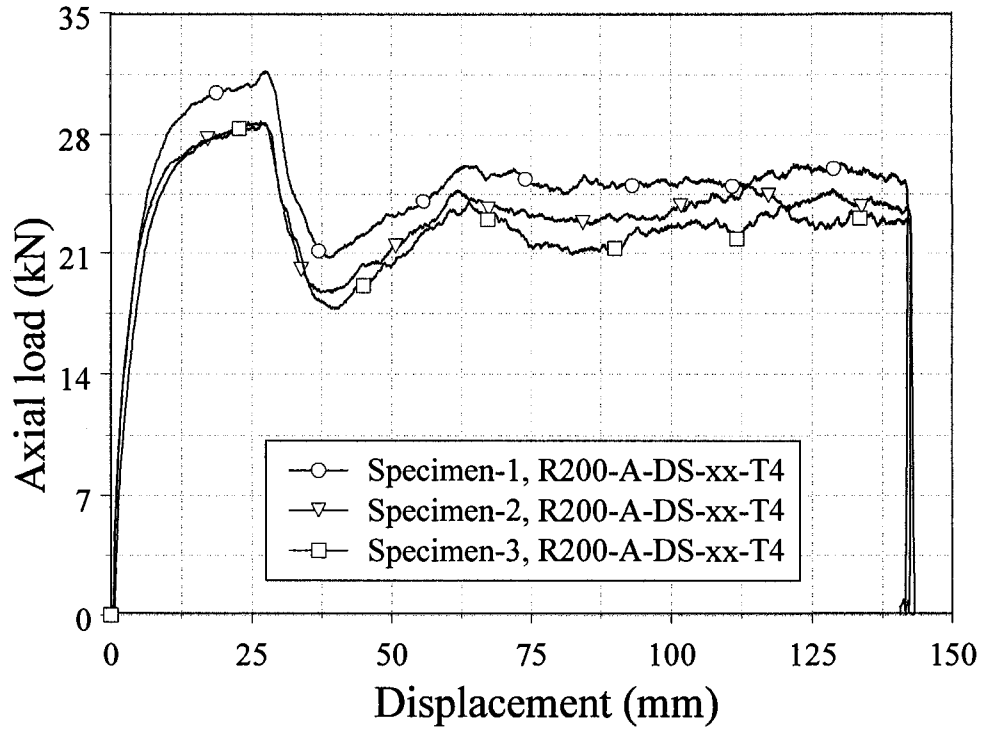


Figure A.7. The load/displacement responses for AA6061-T4 extrusions with a wall thickness of 3.175 mm in the presence of straight deflector in Group d-9.

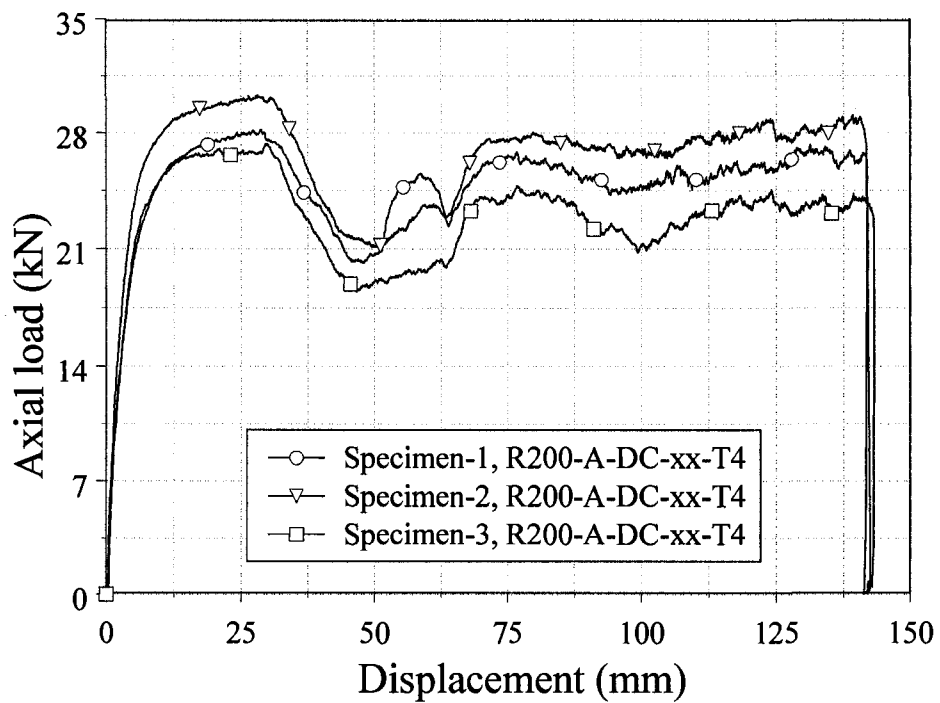


Figure A.8. The load/displacement responses for AA6061-T4 extrusions with a wall thickness of 3.175 mm in the presence of curved deflector in Group d-13.

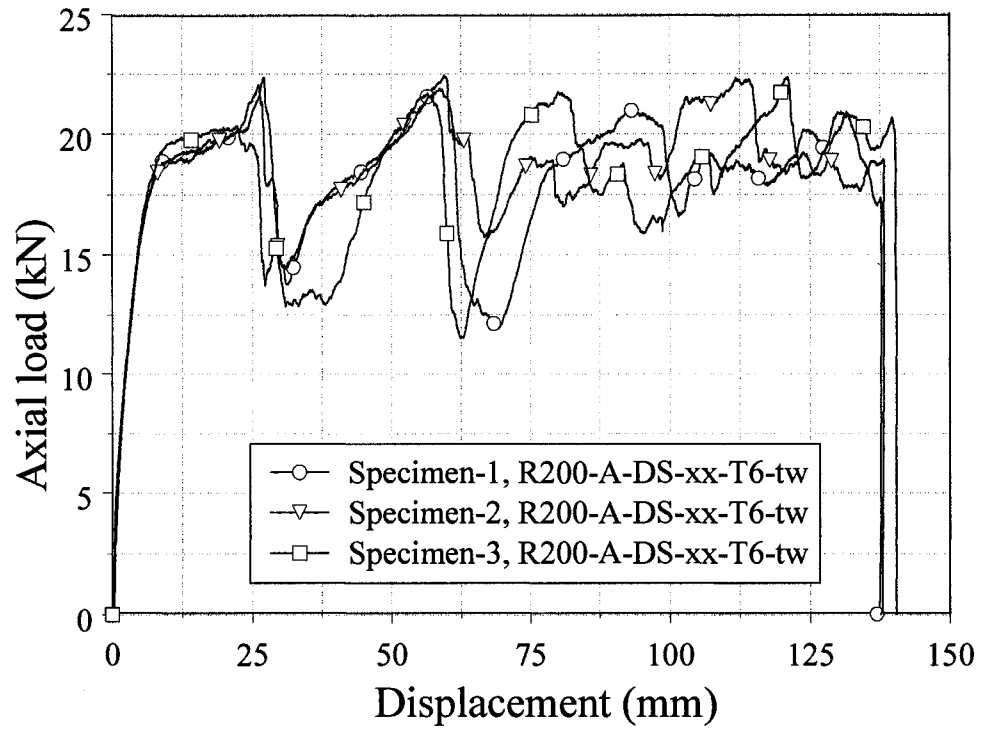


Figure A.9. The load/displacement profiles for AA6061-T6 extrusions with a wall thickness of 1.587 mm in the presence of straight deflector in Group d-17.

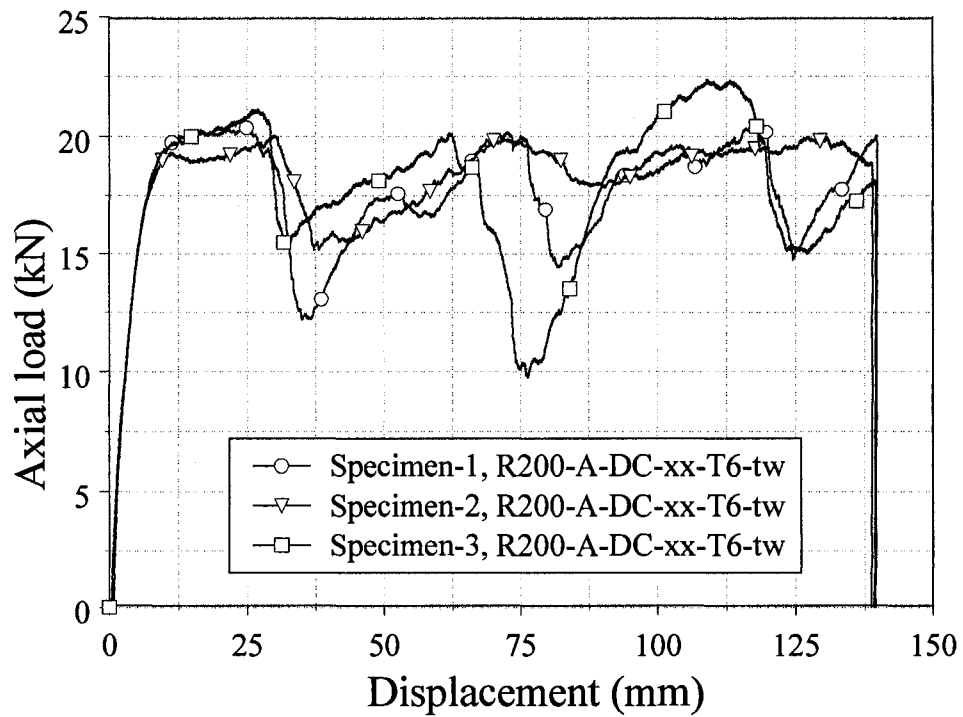


Figure A.10. The load/displacement profiles for AA6061-T6 extrusions with a wall thickness of 1.587 mm in the presence of curved deflector in Group d-21.

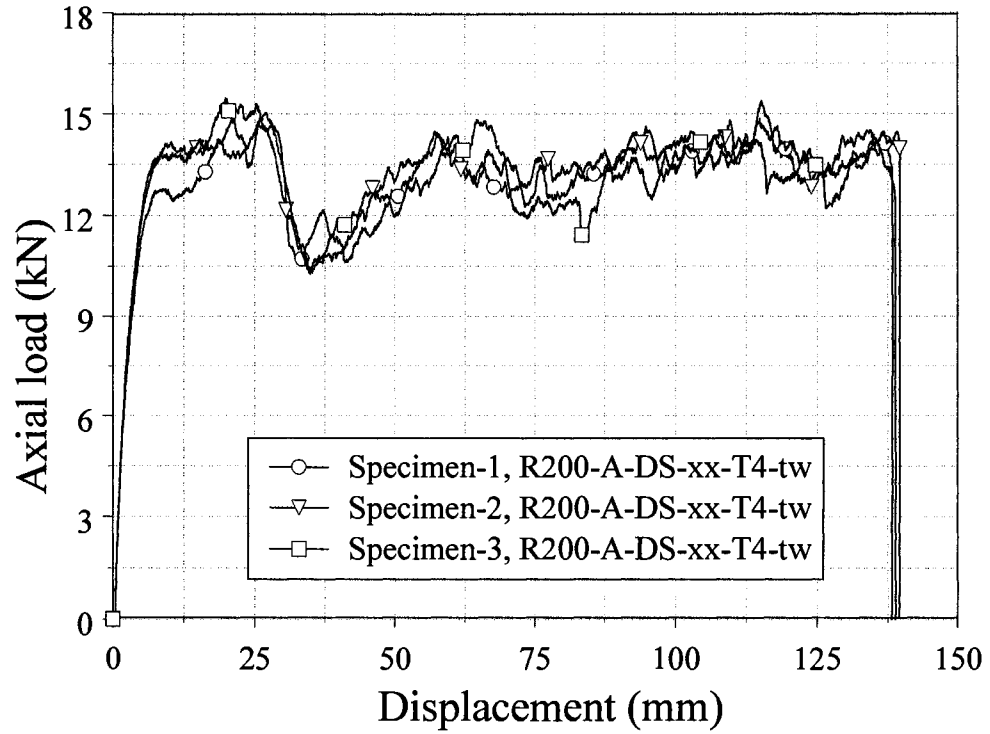


Figure A.11. The load/displacement curves for AA6061-T4 extrusions with a wall thickness of 1.587 mm in the presence of straight deflector in Group d-25.

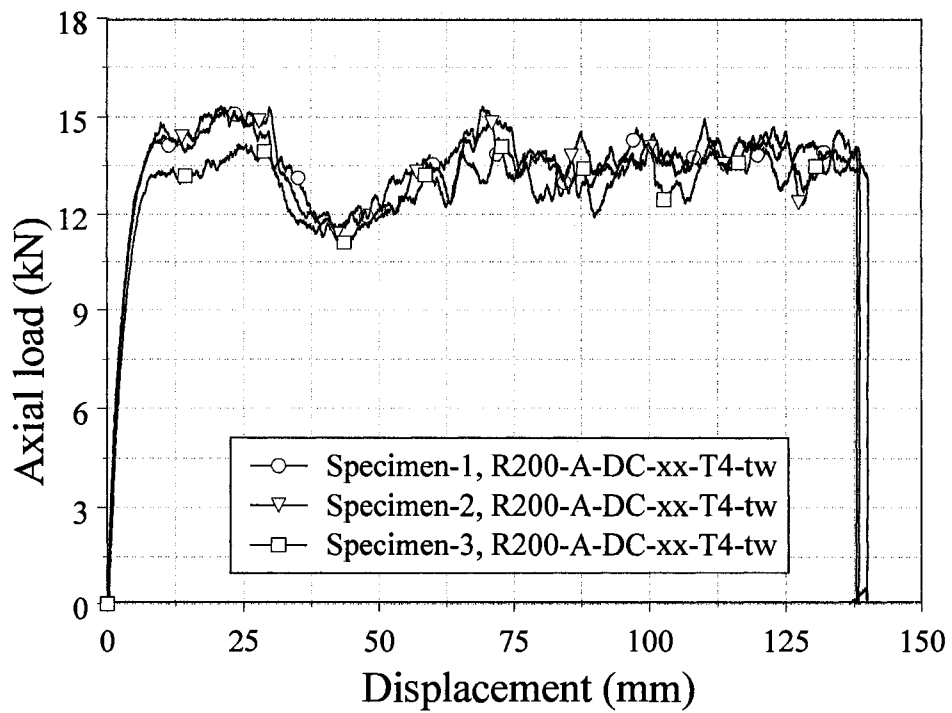


Figure A.12. The load/displacement curves for AA6061-T4 extrusions with a wall thickness of 1.587 mm in the presence of curved deflector in Group d-29.

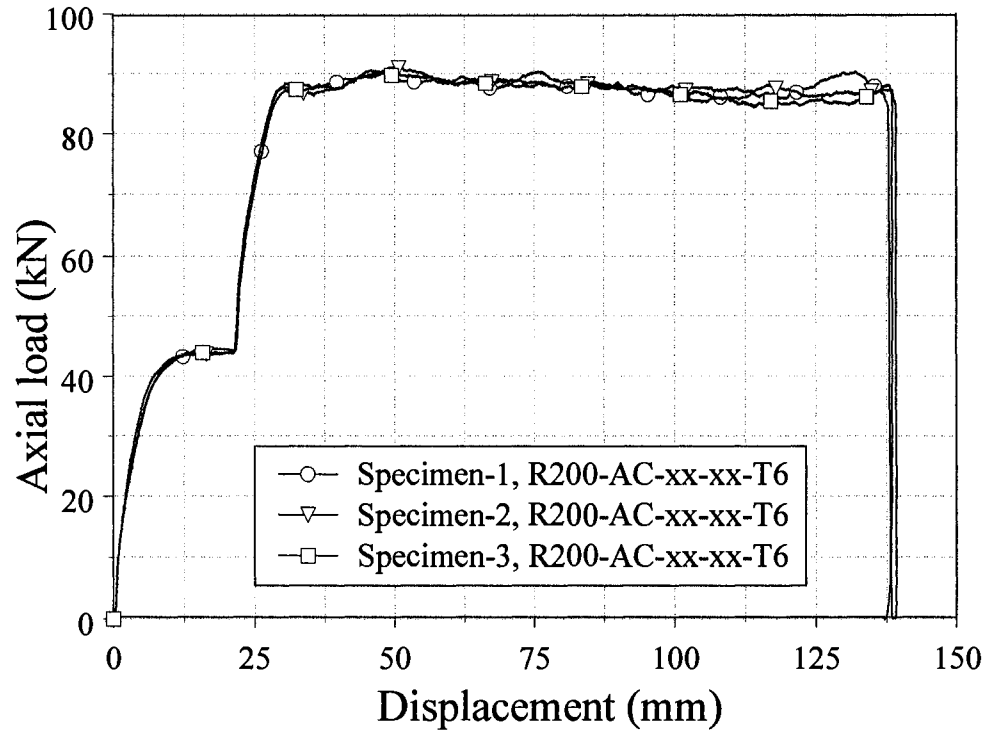


Figure A.13. The force/displacement profiles of AA6061-T6 round extrusions with a wall thickness of 3.175 mm under dual stage cutting from Group m-1.

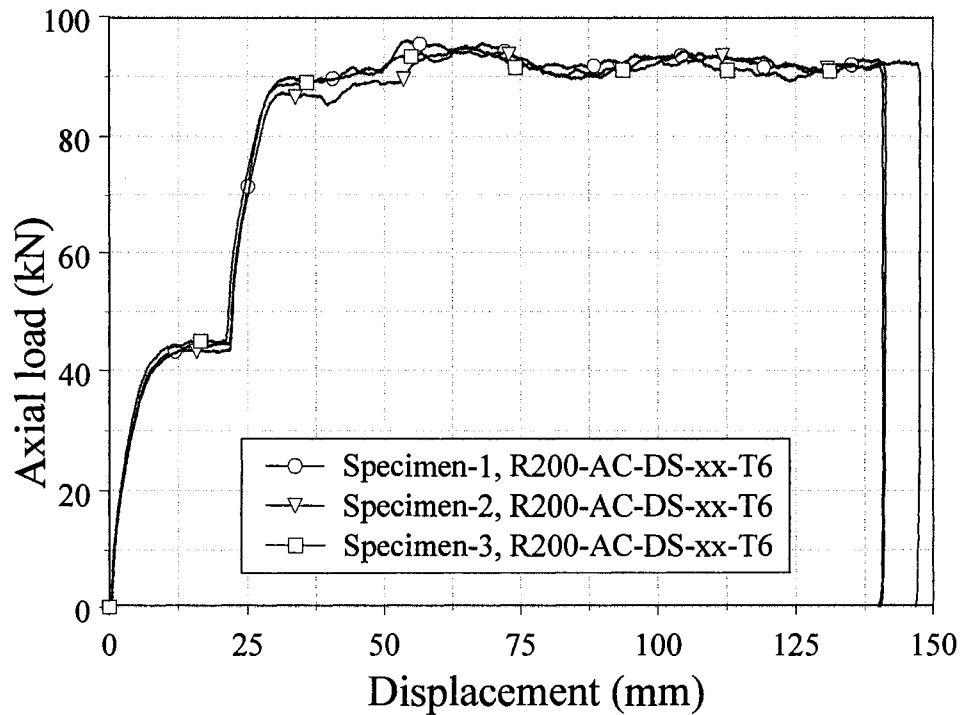


Figure A.14. The force/displacement profiles of AA6061-T6 round extrusions with a wall thickness of 3.175 mm under dual stage cutting from Group m-4.

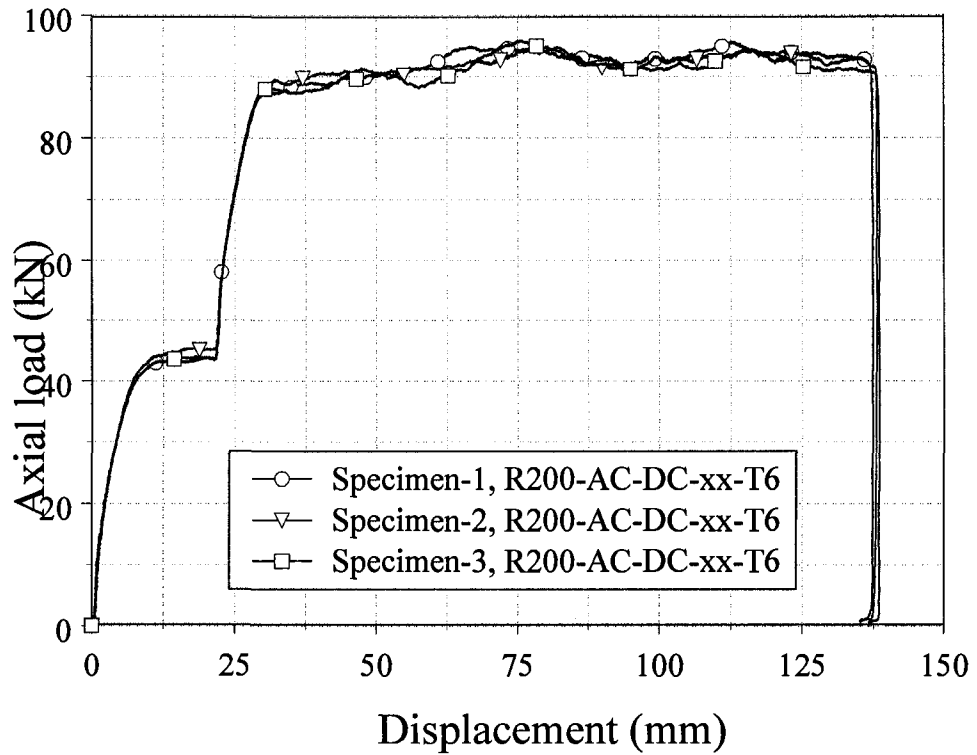


Figure A.15. The force/displacement profiles of AA6061-T6 round extrusions with a wall thickness of 3.175 mm under dual-stage cutting from Group m-7.

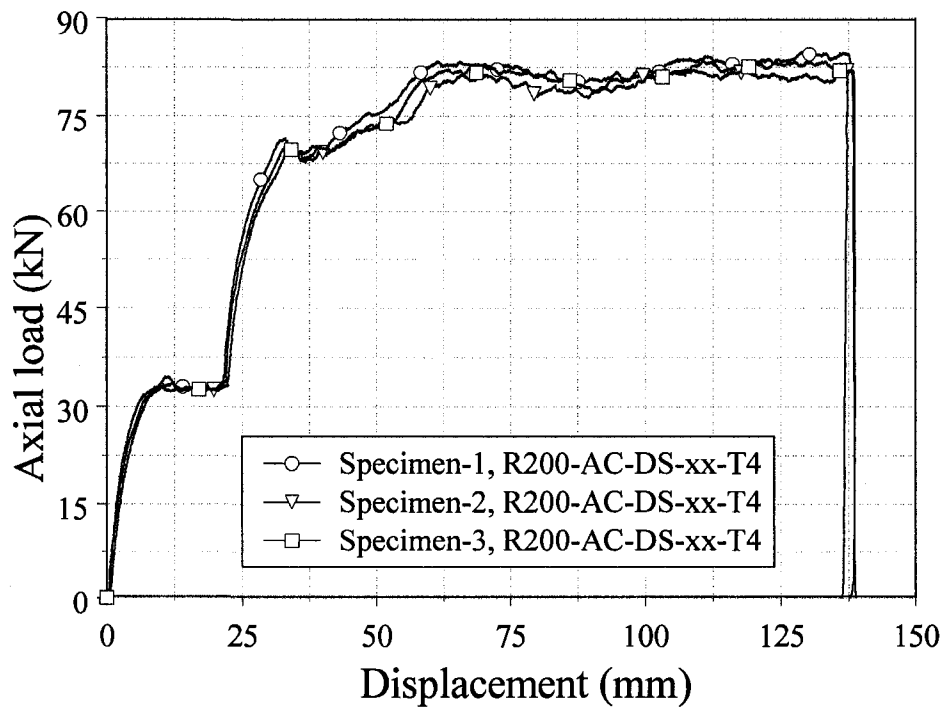


Figure A.16. The force/displacement profiles of AA6061-T4 round extrusions with a wall thickness of 3.175 mm under dual stage cutting from Group m-11.

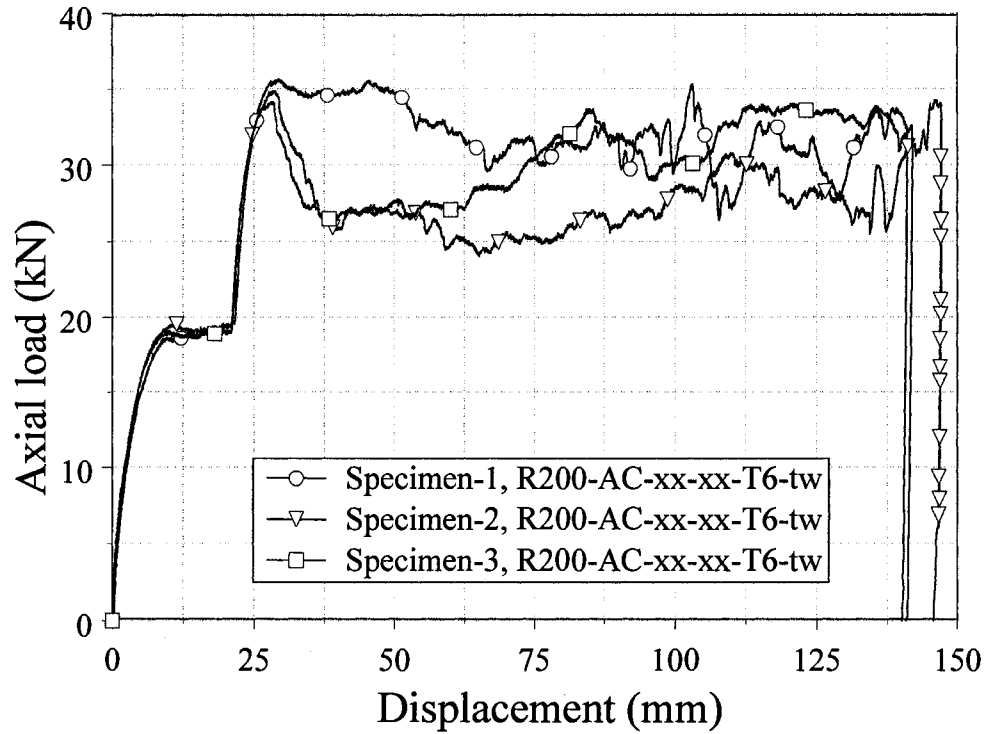


Figure A.17. The force/displacement responses of AA6061-T6 round specimens with a wall thickness of 1.587 mm under dual stage cutting from Group m-13.

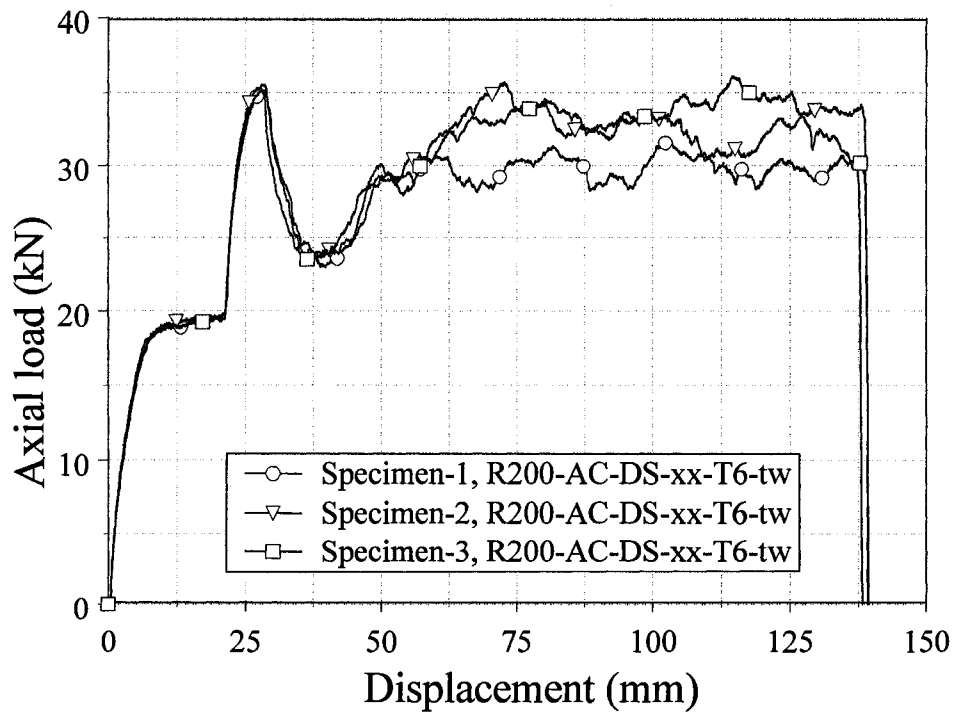


Figure A.18. The force/displacement profiles of AA6061-T6 round specimens with a wall thickness of 1.587 mm under dual stage cutting from Group m-16.

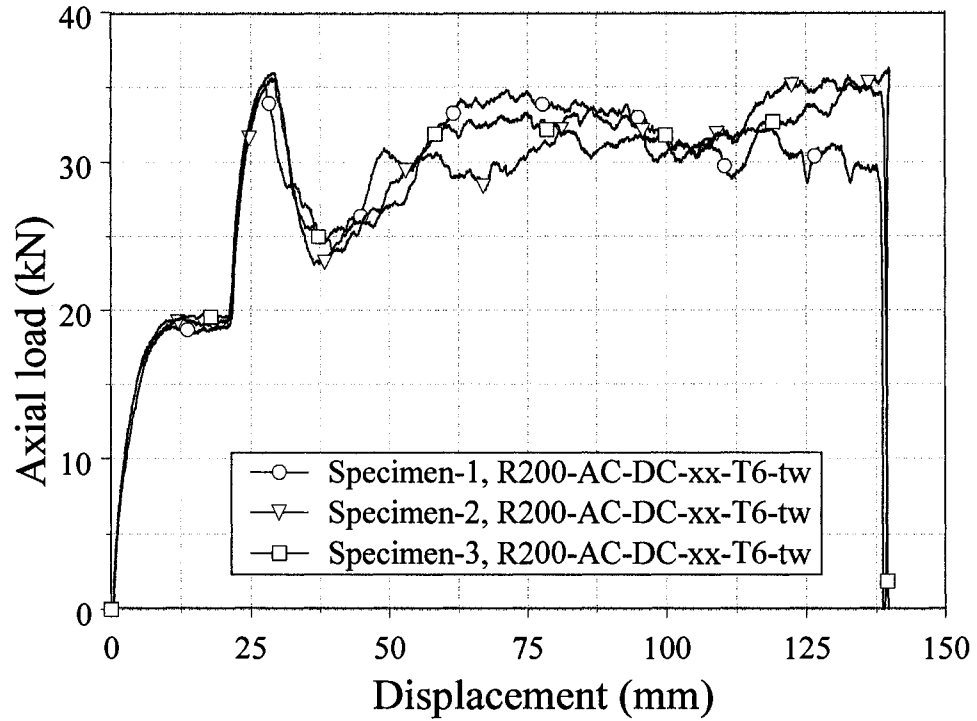


Figure A.19. The force/displacement profiles of AA6061-T6 round specimens with a wall thickness of 1.587 mm under dual stage cutting from Group m-19.

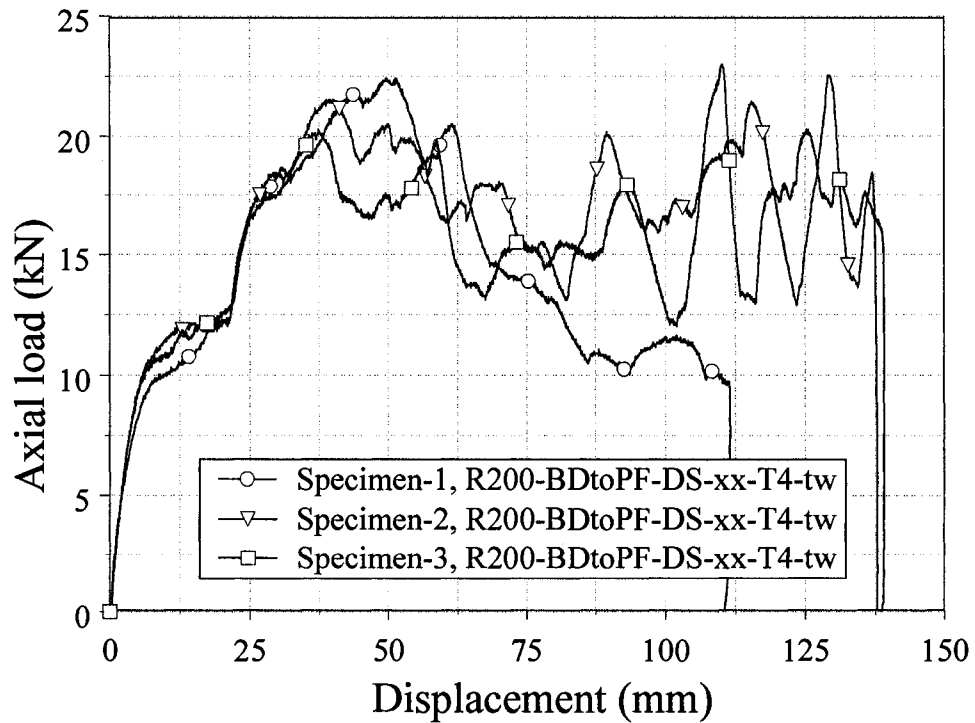


Figure A.20. The force/displacement profiles of AA6061-T4 round specimens with a wall thickness of 1.587 mm under dual stage cutting from Group m-23.

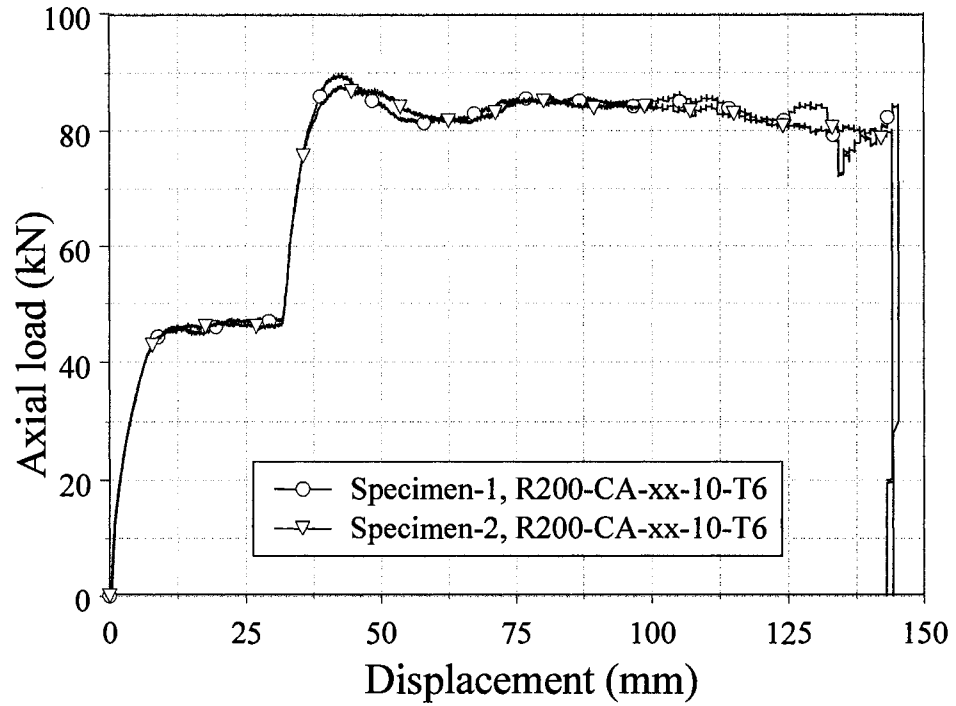


Figure A.21. The force/displacement profiles of the AA6061-T6 round specimens under the dual stage cutting using a 10 mm spacing between cutters in Group s-2.

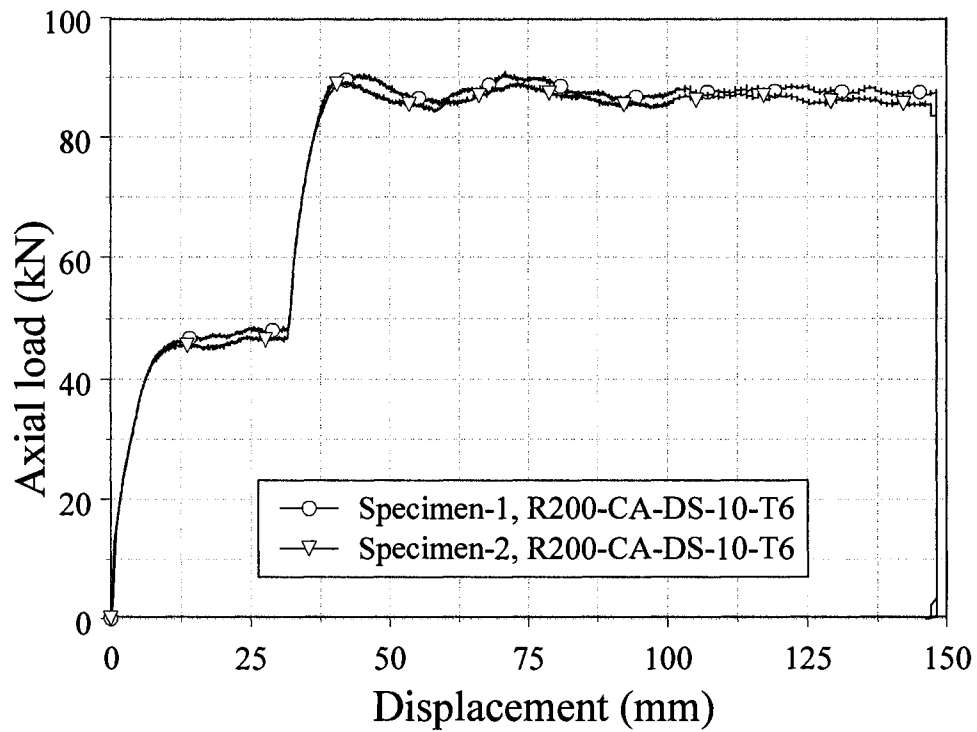


Figure A.22. The force/displacement profiles of the AA6061-T6 round specimens using a 10 mm spacing between cutters in presence of the straight deflector in Group s-5.

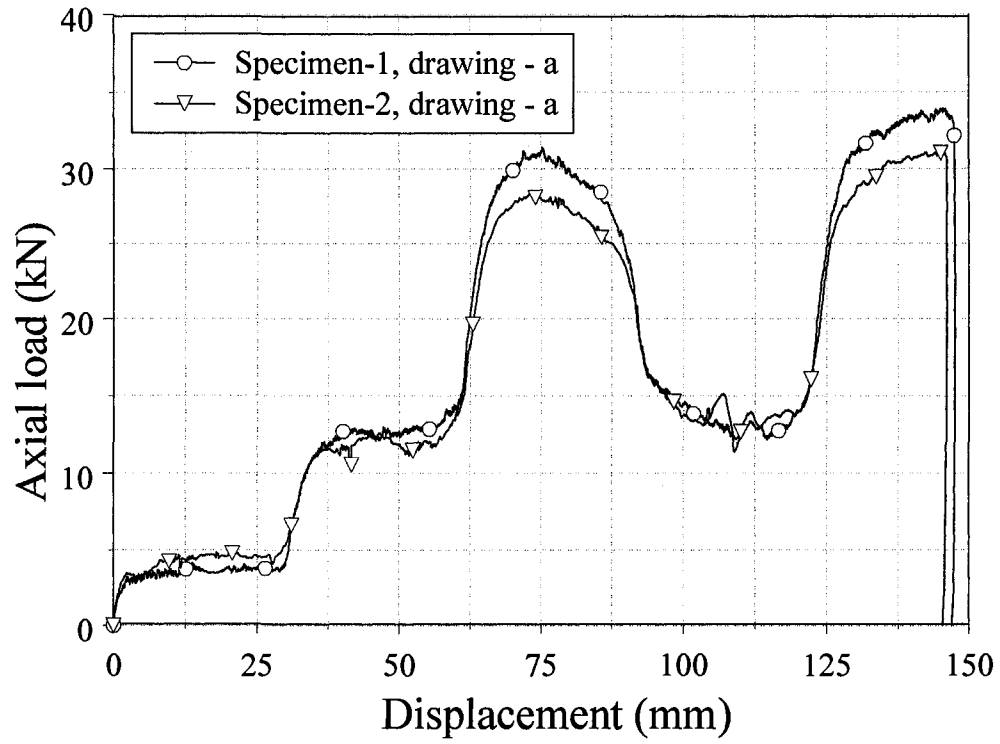


Figure A.23. The force/displacement profiles of the AA6061-T4 round specimens with stepped wall in Group a-T4.

APPENDIX B:

PARTIAL INPUT USED IN FE SIMULATION

B.1 Partial Input for Cutting of AA6061-T6 Round Extrusions in Presence of Straight or Curved Deflector Utilizing Eulerian FE Formulation

```

$-----1-----2-----3-----4-----5-----6-----7-----8
$
$                                     MATERIALS CARD
$
$-----1-----2-----3-----4-----5-----6-----7-----8
*MAT_ELASTIC_PLASTIC_HYDRO
$ This material model for the AA6061-T6 aluminum alloy
$   MID      RO      G      SIGY      EH      PC      FS
$   10.00000273.2880E+7 271600.0
$   EPS1     EPS2     EPS3     EPS4     EPS5     EPS6     EPS7     EPS8
$   0.0 0.000214 0.000611 0.001289 0.002246 0.003483 0.0050 006797
$   EPS9     EPS10    EPS11    EPS12    EPS13    EPS14    EPS15    EPS16
$   0.008873 0.016783 0.019979 0.061336 0.067331 0.086994 0.101501 .117129
$   ES1      ES2      ES3      ES4      ES5      ES6      ES7      ES8
$   271564.3 276939.4 283788.0 288361.2 291531.0 293903.9 295856.3 97639.3
$   ES9      ES10     ES11     ES12     ES13     ES14     ES15     ES16
$   299423.7 305662.2 308138.6 337897.1 341386.6 350660.1 356244.6 58802.2
$-----1-----2-----3-----4-----5-----6-----7-----8
$
$                                     SECTION CARDS
$
$-----1-----2-----3-----4-----5-----6-----7-----8
*SECTION_SOLID
$   SECID    ELFORM      AET
$   1        12
$-----1-----2-----3-----4-----5-----6-----7-----8
$
$                                     EOS CARD
$
$-----1-----2-----3-----4-----5-----6-----7-----8
*EOS_LINEAR_POLYNOMIAL
$   EOSID    C0      C1      C2      C3      C4      C5      C6
$   1        0.07.563E+07 0.0      0.0      0.0      0.0      0.0
$   E0      V0
$   0.0      1.0
$-----1-----2-----3-----4-----5-----6-----7-----8
$
$                                     MATERIALS CARD
$
$-----1-----2-----3-----4-----5-----6-----7-----8
*MAT_RIGID_TITLE
$ This material model for the Cutter and Deflector
$   MID      RO      E      PR      N COUPLE      M      ALIAS
$   10 0.0010757.200E+07 0.30
$   CMO      CON1      CON2
$   1.0      4.0      7
$LCO_ORAL      A2      A3      V1      V2      V3

```

```

$---+---1-----2-----3-----4-----5-----6-----7-----8
$
$                               SECTION CARDS                               $
$
$---+---1-----2-----3-----4-----5-----6-----7-----8
*SECTION_SOLID
$  SECID  ELFORM      AET
    10      1
$---+---1-----2-----3-----4-----5-----6-----7-----8
$
$                               CONSTRAINED RIGID BODIES CARDS                               $
$
$---+---1-----2-----3-----4-----5-----6-----7-----8
*CONSTRAINED_RIGID_BODIES
$  PIDM  PIDS
    12    10
$---+---1-----2-----3-----4-----5-----6-----7-----8
$
$                               BOUNDARY PRESCRIBED CARDS                               $
$
$---+---1-----2-----3-----4-----5-----6-----7-----8
*BOUNDARY_PRESCRIBED_MOTION_RIGID
$  PID  DOF  VAD  LCID  SF  VID  DEATH  BIRTH
    12   3   2   10  -80.0
$---+---1-----2-----3-----4-----5-----6-----7-----8
$
$                               LOAD CURVE CARDS                               $
$
$---+---1-----2-----3-----4-----5-----6-----7-----8
*DEFINE_CURVE
$  LCID  SIDR  SFA  SFO  OFFA  OFFO  DATYYP
    10      0
$
$                A1                O1
$                0.0                0.0
$                0.020                2.0
$---+---1-----2-----3-----4-----5-----6-----7-----8
$
$                               CONSTRAINED LAGRANGE IN SOLID CARDS                               $
$
$---+---1-----2-----3-----4-----5-----6-----7-----8
*CONSTRAINED_LAGRANGE_IN_SOLID
$  SLAVE  MASTER  SSTYP  MSTYP  NQUAD  CTYPE  DIREC  MCOUP
    11      1      0      0      -3      4      2      0
$  START  END  PFAC  FRIC  FRCMIN  NORM  NORMTYP  DAMP
$                .20  0.30
$  CQ  HMIN  HMAX  ILEAK  PLEAK  LCIDPOR

```

B.2 Partial Input for Cutting of AA6061-T6 Round Extrusions in Presence of Straight or Curved Deflector Utilizing SPH FE Formulation

Material models used for extrusion, cutter, deflector in SPH FE formulation were identical to that utilized in Eulerian FE formulation

```

$---+---1-----2-----3-----4-----5-----6-----7-----8
$
$                                $
$                                $
$                                $
$---+---1-----2-----3-----4-----5-----6-----7-----8
*CONTROL_SPH
$  NCBS      BOXID      DT      IDIM  MEMORY  FORM  START  MAXV
$    1              3      300
$  CONT      DERIV
$
$---+---1-----2-----3-----4-----5-----6-----7-----8
$
$                                $
$                                $
$                                $
$---+---1-----2-----3-----4-----5-----6-----7-----8
*SECTION_SPH
$  SECID     CSLH      HMIN     HMAX  SPHINI  DEATH  START
$    3       1.2     0.20     2.0   0.01.000E+20  0.0

```

APPENDIX C:

COPYRIGHT PERMISSION

C.1 Copyright Permission from Elsevier

From: "Williams, Lucy (ELS-OXF)" <Lu.Williams@elsevier.com>
Subject: RE: Request for copyright permission
Date: Tue, 5 Aug 2008 15:39:31 +0100
To: "Majumder A" <majumd2@uwindSOR.ca>

Dear Amitabha

We hereby grant you permission to reprint the material detailed below at no charge in your thesis subject to the following conditions:

1. If any part of the material to be used (for example, figures) has appeared in our publication with credit or acknowledgement to another source, permission must also be sought from that source. If such permission is not obtained then that material may not be included in your publication/copies.

2. Suitable acknowledgment to the source must be made, either as a footnote or in a reference list at the end of your publication, as follows:

“This article was published in Publication title, Vol number, Author(s), Title of article, Page Nos, Copyright Elsevier (or appropriate Society name) (Year).”

3. Your thesis may be submitted to your institution in either print or electronic form.

4. Reproduction of this material is confined to the purpose for which permission is hereby given.

5. This permission is granted for non-exclusive world English rights only. For other languages please reapply separately for each one required. Permission excludes use in an electronic form other than submission. Should you have a specific electronic project in mind please reapply for permission.

6. Should your thesis be published commercially, please reapply for permission.

This includes permission for the Library and Archives of Canada to supply single copies, on demand, of the complete thesis. Should your thesis be published commercially, please reapply for permission.

This includes permission for UMI to supply single copies, on demand, of the complete thesis. Should your thesis be published commercially, please reapply for permission.

Yours sincerely

Lucy Williams

Rights Assistant | ELSEVIER | The Boulevard| Langford Lane | Kidlington | Oxford OX5
1GB |

Tel: 01865 843398| Fax: 01865 853333

lu.williams@elsevier.com

From: "Majumder A" <majumd2@uwindsor.ca>
Subject: Request for copyright permission
Date: Thu, 24 Jul 2008 13:12:30 -0400
To: permissions@elsevier.com

Dear Mrs. Truter,

I have been writing my thesis for my Master of Applied Science degree in Mechanical Engineering at the University of Windsor, Ontario, Canada. Within the literature review chapter of my thesis I would like to use the following attached figures published by your company to illustrate research and/or experimental testing done by other researchers in my research area. I am requesting your permission to use these figures in my literature review part. My thesis would be printed in five copies. Two copies would be deposited in the University of Windsor Library, one copy would be deposited in the Mechanical Engineering Department and the remaining two copies would be given to individuals. Would you please respond to this mail as soon as possible?

Thank you very much!

Best regards,

Amitabha Majumder

M.A.Sc. Candidate

Department of Mechanical, Automotive and Materials Engineering

University of Windsor

Windsor, Ontario, Canada

Email: majumd2@uwindsor.ca

Figures:

- (1) Figure 13 from: Guillow, S.R., Lu, G. and Grzebieta, R.H., 'Quasi-static axial compression of thin-walled circular aluminium tubes', *International Journal of Mechanical Sciences* 2001, 43(9), pp. 2103-2123.
- (2) Figure 7 and Figure 19(b) from: Langseth, M. and Hopperstad, O.S., 'Static and dynamic axial crushing of square thin-walled aluminum extrusions', *International Journal of Impact Engineering* 1996, 18(7-8), pp.949-968.
- (3) Figure 4(a) from: Singace, A.A., 'Axial crushing analysis of tubes deforming in the multi-lobe mode', *International Journal of Mechanical Sciences* 1999, 41, pp. 869-890.
- (4) Figure 2 from: D.K., 'The curling characteristics of static inside-out inversion of metal tubes', *International Journal of Machine Tools & Manufacture* 2000, 40(1), pp. 65-80.
- (5) Figure 2 and Figure 3 from: Miscow, F.P.C. and Al-Qureshi, H.A., 'Mechanisms of static and dynamic inversion processes', *International Journal of Mechanical Sciences* 1997, 39(2), pp. 147-161.
- (6) Figure 5(a) from: Reddy, T.Y. and Reid, S.R., 'Axial splitting of circular metal tubes', *International Journal of Mechanical Sciences* 1986, 28(2), pp. 111-131.
- (7) Figure 1 from: Lu, G., Ong, L.S., Wang, B. and Ng, H.W., 'An experimental study on tearing energy in splitting square metal tubes', *International Journal of Mechanical Sciences* 1994, 36(12), pp. 1087-1097.
- (8) Figure 1, Figure 3 and Figure 5 from: Huang, X., Lu, G. and Yu, T.X., 'On the axial splitting and curling of circular metal tubes', *International Journal of Mechanical Sciences* 2002, 44(11), pp. 2369-2391.
- (9) Figure 2 and Figure 3 from: Huang, X., Lu, G. and Yu, T.X., 'Energy absorption in splitting square metal tubes', *Thin-Walled Structures* 2002, 40(2), pp. 153-165.
- (10) Figure 10 from: Jin, S.Y., Altenhof, W. and Kapoor, T., 'An experimental investigation into the cutting deformation mode of AA6061-T6 round extrusions', *Thin-Walled Structures* 2006, 44(7), pp. 773-786.
- (11) Figure 28 from: Kim, H.S. and Wierzbicki, T., 'Effect of the cross-sectional shape of hat-type cross-section on the crash resistance of an 'S' frame', *Thin-Walled Structures* 2001, 39(7), pp. 535-554.

- (12) Figure 7, Figure 8 and Figure 9 from: Kim, H.S., 'New extruded multi-cell aluminum profile for maximum crash energy absorption and weight efficiency', *Thin-Walled Structures* 2002, 40(4), pp. 311-327.
- (13) Figure 6 and Figure 10(a) from: DiPaolo, B.P., Monteiro, P.J.M. and Gronsky, R., 'Quasi-static axial crush response of a thin-wall, stainless steel box component', *International Journal of Solids and Structures* 2004, 41(14), pp. 3707-3733.
- (14) Figure 9 from: Abramowicz, W. and Jones, N., 'Transition from initial global bending to progressive buckling of tubes loaded statically and dynamically', *International Journal of Impact Engineering* 1997, 19(5-6), pp. 415-437.
- (15) Figure 2 and Figure 7 from: Kim, D.K. and Lee, S., 'Impact energy absorption of 6061 aluminum extruded tubes with different cross-sectional shapes', *Materials and Design* 1999, 20, pp. 41-49.
- (16) Figure 1, Figure 2 and Figure 4(a) from: Lee, S., Hahn, C., Rhee, M. and Oh, J., 'Effect of triggering on the energy absorption capacity of axially compressed aluminum tubes', *Materials and Design* 1999, 20(1), pp. 31-40.
- (17) Figure 1, Figure 5 and Figure 14 from: Cheng, Q., Altenhof, W. and Li, L., 'Experimental investigations on the crush behaviour of AA6061-T6 aluminum square tubes with different types of through-hole discontinuities', *Thin-Walled Structures* 2006, 44(4), pp. 441-454.
- (18) Figure 12(a) from: Abramowicz, W. and Jones, N., 'Dynamic axial crushing of square tubes', *International Journal of Impact Engineering* 1984, 2(2), pp. 1979-2008.
- (19) Figure 2 from: Langseth, M., Hopperstad, O. and Berstad, T., 'Crashworthiness of aluminum extrusions: validation of numerical simulation, effect of mass ratio and impact velocity', *International Journal of Impact Engineering* 1999, 22(9-10), pp. 829-854.
- (20) Figure 4 from: Limidoa, J., Espinosaa, C., Salauna, M. and Lacombeb, J.L., 'SPH method applied to high speed cutting modelling', *International Journal of Mechanical Sciences* 2007, 49(7), pp. 898-908.

C.2 Copyright Permission from SAE

From: "Kelly, Terri" <Terri.Kelly@sae.org>
Subject: RE: Request for copyright permission
Date: Tue, 12 Aug 2008 15:39:31
To: "Majumder A" <majumd2@uwindsor.ca>

Dear Mr. Majumder:

Permissions to include the figures in a thesis for your Master of Applied Science degree in Mechanical Engineering at the University of Windsor, Ontario, Canada, is hereby granted, and we request that the following credit statement appear directly below each figure:

“Reprinted with permission from SAE paper number * (c) 200_** Society of Automotive Engineers, Inc.”

(please insert the appropriate paper number and **year of publication)

I understand that you will produce 5 printed copies of your thesis for distribution to the university library, your supervisor and for yourself.

Thank you for contacting SAE for this permission.

Sincerely,
Terri Kelly
SAE Publishing

From: "Majumder A" <majumd2@uwindsor.ca>
Subject: Request for copyright permission
Date: Thu, 24 Jul 2008 13:19:41 -0400
To: copyright@sae.org

Dear Sir/Madam,

I have been writing my thesis for my Master of Applied Science degree in Mechanical Engineering at the University of Windsor, Ontario, Canada. Within the Literature Review chapter of my thesis I would like to use the following attached figures published by SAE to illustrate research and/or experimental testing done by other researchers in my research area. I am requesting your permission to reprint these figures in my literature review part.

Would you please respond to this as soon as possible?

Thank you very much!

Best regards,

Amitabha Majumder
M.A.Sc. Candidate
Department of Mechanical, Automotive and Materials Engineering
University of Windsor
Windsor, Ontario, Canada
Email: majumd2@uwindsor.ca

Figures:

- (1) Figure 3, Figure 18 and Figure 20 from: Arnold, B. and Altenhof, W., 'Finite element modeling of the axial crushing of AA6061 T4 and T6 and AA6063 T5 structural square tubes with circular discontinuities', SAE Transactions: Journal of Materials & Manufacturing 2006, 114(5), pp. 300-315.
- (2) Figure 4 and Figure 6 from: Jin, S.Y. and Altenhof, W., 'Crush characteristics of AA6061-T6 round tubes during a cutting deformation mode', SAE Transactions: Journal of Materials & Manufacturing 2007, 116(5).

C.3 Copyright Permission from Springer

Powered by **RIGHTSLINK**  [Home](#) [Account Info](#)
COPYRIGHT CLEARANCE CENTER, INC.



Title: A theoretical study of steady-state wedge cutting through metal plates
Author: Z. M. Zheng
Publication: International Journal of Fracture
Publisher: Springer
Date: Mar 1, 1996
Copyright © 1996, Springer Netherlands

Logged in as:
Amitabha Majumder

[LOGOUT](#)

Order Completed

Thank you very much for your order.

This is a License Agreement between Amitabha Majumder ("You") and Springer ("Springer"). The license consists of your order details, the terms and conditions provided by Springer, and the payment terms and conditions.

Get the printable license.

Order Details	Billing & Contact Info
License Number	2000211084465
License date	Aug 01, 2008
Licensed content publisher	Springer
Licensed content publication	International Journal of Fracture
Licensed content title	A theoretical study of steady-state wedge cutting through metal plates
Licensed content author	Z. M. Zheng
Licensed content date	Mar 1, 1996
Volume number	78
Issue number	1
Pages	45 - 66
Type of Use	Thesis / Dissertation
Details of use	Print
Portion of the article	Figures
Title of your thesis / dissertation	Characteristics of AA6061-T4 and T6 Extrusions Under Cutting Deformation
Expected completion date	Aug 2008
Total	0.00 USD

Copyright © 2008 Copyright Clearance Center, Inc. All Rights Reserved. Privacy statement. Comments? We would like to hear from you. E-mail us at customer care@copyright.com

SPRINGER LICENSE TERMS AND CONDITIONS

Aug 01, 2008

Introduction:

The publisher for this copyrighted material is Springer Science + Business Media. By clicking "accept" in connection with completing this licensing transaction, you agree that the following terms and conditions apply to this transaction (along with the Billing and Payment terms and conditions established by Copyright Clearance Center, Inc. ("CCC"), at the time that you opened your Rightslink account and that are available at any time at <http://myaccount.copyright.com>).

Limited License:

With reference to your request to reprint in your thesis material on which Springer Science and Business Media control the copyright, permission is granted, free of charge, for the use indicated in your enquiry. Licenses are for one-time use only with a maximum distribution equal to the number that you identified in the licensing process.

This License includes use in an electronic form, provided it is password protected or on the university's intranet, destined to microfilming by UMI and University repository. For any other electronic use, please contact Springer at (permissions.dordrecht@springer.com or permissions.heidelberg@springer.com)

The material can only be used for the purpose of defending your thesis, and with a maximum of 100 extra copies in paper.

Copyright Notice:

Please include the following copyright citation referencing the publication in which the material was originally published. Where wording is within brackets, please include verbatim.

"With kind permission from Springer Science+Business Media: <book/journal title, chapter/article title, volume, year of publication, page, name(s) of author(s), figure number(s), and any original (first) copyright notice displayed with material>."

Warranties: Springer Science + Business Media makes no representations or warranties with respect to the licensed material.

No Transfer of License:

This license is personal to you and may not be sublicensed, assigned, or transferred by you to any other person without Springer Science + Business Media's written permission.

C.4 Copyright Permission from Taylor and Francis

Powered by **RIGHTSLINK** 
COPYRIGHT CLEARANCE CENTER, INC.

[Home](#) [Account Info](#)



Taylor & Francis
Taylor & Francis Group

Title: Load/displacement and energy absorption performances of AA6061-T6 tubes under a cutting deformation mode

Author: Q. Cheng, W. Altenhof

Publication: International Journal of Crashworthiness

Publisher: Taylor & Francis

Date: Jan 6, 2005

Copyright © 2005 Taylor & Francis

Logged in as:
Amitabha Majumder

Account #:
3000144108

[LOGOUT](#)

Taylor & Francis is pleased to offer reuses of its content for a thesis or dissertation free of charge contingent on resubmission of permission request if work is published.

Powered by **RIGHTSLINK** 
COPYRIGHT CLEARANCE CENTER, INC.

[Home](#) [Account Info](#)



Taylor & Francis
Taylor & Francis Group

Title: Experimental observations of AA6061-T6 round extrusions under a cutting deformation mode with a deflector

Author: Shun Yi Jin, William Altenhof

Publication: International Journal of Crashworthiness

Publisher: Taylor & Francis

Date: Jan 4, 2008

Copyright © 2008 Taylor & Francis

Logged in as:

Amitabha Majumder

Account #:
3000144108

[LOGOUT](#)

Thesis/Dissertation Reuse Request

Taylor & Francis is pleased to offer reuses of its content for a thesis or dissertation free of charge contingent on resubmission of permission request if work is published.

[BACK](#)

[CLOSE WINDOW](#)



Taylor & Francis
Taylor & Francis Group

Title: Experimental observations on the crush characteristics of AA6061 T4 and T6 structural square tubes with and without circular discontinuities

Author: B. Arnold, W. Altenhof

Publication: International Journal of Crashworthiness

Publisher: Taylor & Francis

Date: Jan 1, 2004

Copyright © 2004 Taylor & Francis

Logged in as:
Amitabha Majumder
Account #:
3000144108

LOGOUT

Thesis/Dissertation Reuse Request

Taylor & Francis is pleased to offer reuses of its content for a thesis or dissertation free of charge contingent on resubmission of permission request if work is published.

BACK

CLOSE WINDOW

Copyright © 2008 Copyright Clearance Center, Inc. All Rights Reserved. Privacy statement. Comments? We would like to hear from you. E-mail us at customer@copyright.com



C.5 Copyright Permission from ASME

From: "Beth Darchi" <DarchiB@asme.org>
Subject: Re: ASME PUBLICATIONS PERMISSION REQUEST FORM
SUBMISSION
Date: Wed, 30 Jul 2008 15:05:28 -0400
To: <majumd2@uwindsor.ca>
Cc: "Michelle DeBlasi" <DeBlasiM@asme.org>

Dear Mr. Majumder,

It is our pleasure to grant you permission to publish the following ASME

Figure 3 from "Criteria for outward curling of tubes", by Kitazawa, K., Journal of Engineering for Industry Transactions, Vol. 115, 1993, pp 466-471, cited in your letter for inclusion in a Literature Review chapter of your master thesis to be published by the University of Windsor, Ontario, Canada. As is customary, we request that you ensure proper acknowledgment of the exact sources of this material, the authors, and ASME as original publisher.

Thank you for your interest in ASME publications.

Sincerely,

Beth Darchi
Copyrights & Permissions
ASME International
Three Park Avenue
New York, NY 10016
P: 212-591-7700
F: 212-591-7292
E: darchib@asm

ASME PUBLICATIONS PERMISSION REQUEST FORM

Please indicate the ASME content you wish to use:

NOTE: This form is only for requesting permission to reprint all or part of ASME copyrighted material for books, journals, and conference proceedings.

All fields with * are required.

Not all ASME Journal papers are © ASME. Please indicate if the paper has ASME written as copyright holder. *

Yes No

ASME Publication Title: *

Complete List of Authors: *

Paper Title (Conference/Journal): *

Paper Number (Conference):

Volume Number (Journal) if any: *

Page(s) in the publication of the permission request (when applicable):

Year of Publication: *

I would like to...*

Portion to be used*

List Figure Numbers if any (ex. 1, 2, 3...)

List Table Numbers if any (ex. 1, 2, 3...)

Number of Copies (or users if electronic)

Usage*

Title of outside publication:*
(Please put the title of the publication you wish to use the ASME works in.)

Outside Publisher:*

Comments:

Check Box if: you are the author of the ASME paper

Please fill out the necessary contact information:

First Name: *	Amitabha
Last Name: *	Majumder
Address Line 1:*	401 Sunset Avenue
Address Line 2:	
City:*	Windsor
State:*	Ontario
Zip:	N9B3P4
Phone:*	519 560 798
Fax:	
Email:*	majumd2@uwindsor.ca

<input type="submit" value="Submit"/>	<input type="submit" value="Reset"/>
---------------------------------------	--------------------------------------

Form Submission Statement:

ASME International does not sell, give or provide email addresses gathered from these forms to any other party.
For Non-US customers, personal data that is submitted on this form will be transferred to the United States.
By pressing the submit button, customers consent to this transfer.

C.6 Copyright Permission from IIHS

From: Permissions <permissions@iihs.org>
Subject: RE: Request for copyright permission
Date: Mon, 28 Jul 2008 09:09:44 -0400
To: "majumd2@uwindsor.ca" <majumd2@uwindsor.ca>

Hello,

You may use these Insurance Institute for Highway Safety images.

From: "Majumder A" <majumd2@uwindsor.ca>
Subject: Request for copyright permission
Date: Thu, 24 Jul 2008 13:45:01 -0400
To: permissions@iihs.org

Dear Sir/Madam,

I have been writing my thesis for my Master of Applied Science degree in Mechanical Engineering at the University of Windsor, Windsor, Ontario, Canada. Within the Literature Review chapter of my thesis I would like to use the attached image downloaded from your website (<http://www.iihs.org/ratings/rating.aspx>) to illustrate research and/or experimental testing done by other researchers in my research area. I am requesting your permission to reprint these images in my literature review part to show the effect of good structure on improving vehicle crashworthiness.

Would you please respond to this as soon as possible?

Thank you very much!

Best regards,

Amitabha Majumder
M.A.Sc. Candidate
Department of Mechanical, Automotive and Materials Engineering
University of Windsor
Windsor, Ontario, Canada
Email: majumd2@uwindsor.ca

Attachment: Images_IIHS.doc (1331Kbytes)

C.7 Copyright Permission from IISI



About IISI > Copyright

Terms and conditions of use

By accessing, visiting or using worldsteel.org you agree to these terms and conditions. You also acknowledge and accept that the terms and conditions may be amended without notice from time to time.

Intellectual property rights

All information available on worldsteel.org is the property of the International Iron and Steel Institute (IISI), its affiliated companies or third parties. The material is protected by copyright and neighbouring rights or other proprietary rights.

Information on this site may be quoted as long as the source of the information is acknowledged. Please use either of the following terms of acknowledgement:

- Source: International Iron and Steel Institute (IISI)
- Source: worldsteel.org (IISI)

worldsteel.org

[contact form](#) | [copyright](#) | [worldautosteel](#) | [extranet.worldsteel.org](#) | [worldstainless](#) |
[livingsteel](#) | [steeluniversity](#)

VITA AUCTORIS

Amitabha Majumder was born in 1971 in Bangladesh. He graduated from Bangladesh University of Engineering and Technology (BUET), Dhaka, Bangladesh where he obtained B.A.Sc. in Mechanical Engineering in 1995. He also received Bachelor of Science Honors Mechanical Engineering with distinction from University of Windsor in 2006. He is currently a candidate for the Master's degree in Mechanical Engineering at the University of Windsor and hopes to graduate in Summer 2008.